Numerical methods for radiative and ideal relativistic hydrodynamics applied to the study of gamma-ray bursts

Julio David Melon Fuksman

Department of Physics

University of Rome “La Sapienza”

This dissertation is submitted for the degree of

Doctor of Philosophy

IRAP PhD program

Supervisor: Dr. Carlo L. Bianco

September 2019

A Julio y Elena

Acknowledgements

I am obliged to express my gratitude towards a number of people who have helped me in different ways throughout the last three and a half years, making this work possible.

First of all, I would like to thank the organizers of the IRAP PhD Program for the financial support throughout the time of my PhD. I also thank my advisor, Carlo L. Bianco, and Professors Jorge A. Rueda and Gregory V. Vereshchagin for their guidance and the many fruitful discussions we had. I thank the entire staff of Sapienza and ICRANet, in particular Cinzia Di Niccolo, Federica Di Berardino, Cristina Adamo, Silvia Latorre, Gabriele A. Brandolini, and Elisabetta Natale, for being so helpful and kind to me ever since my arrival in Pescara.

I would like to thank all of the members of the Thesis Comittee and the external evaluators for aiding me in the final stage of my PhD by taking the time to read this thesis and express their judgement.

Among the scientists I have met since I arrived in Italy, I must especially mention Andrea Mignone. I am indebted to you for welcoming my interest to work together and consistently trusting it would lead to a good place. Above all, however, I thank you deeply for your support in the last year, and for always finding some time to talk when I needed advice. You are an example to follow both as a scientist and as a person.

I would also like to thank all of the students of the ICRANet group I have met in these years, starting with Daria Primorac and Andreas Krut. We have shared so many adventures, some of them rather extreme, and we survived them all. I treasure the amazing experiences we lived together and the times we have stood up for each other. As well, I thank José Fernando Rodríguez Ruiz and Margarita Velandia Avendaño for their continued support and friendship. You are amazing people and many moments throughout this PhD were made easier thanks to you. I must also mention Rahim Moradi and Yu Wang, who welcomed me into the group in Pescara, as well as Marco Muccino and Giovanni Pisani, who did the same in Rome. I thank Yerlan Aimuratov, Laura Becerra, Stefano Campion, Diego Cáceres Uribe, Gabriel Guimarães Carvalho, Vahagn Harutyunyan, Mile Karlica, Miloš Kovačević, Iarley Pereira Lobo, Clément Stahl, Juan David Uribe Suárez, and Ronaldo Vieira Lobato for the great moments we shared. Lastly, I thank Rafael Ignacio Yunis for the mates and his (always very Argentinian) words of encouragement.

During my years at Sapienza I have met several people outside of my group that have brought countless cheerful moments into the day-by-day experience of my PhD, starting with

the students of Stanza 117. In particular, I want to thank José Manuel Ruiz Franco for his daily Maradonian encouragement in the worst and best moments of the PhD. No me alcanzan todos los alfajores del planeta para agradecerte lo que me has bancado estos años. Gracias por tantos cafés compartidos (que casi nunca me has dejado pagar), por los partidos de fútbol, las birras, y las juntadas en tu casa. Mil gracias también a Carmen por estas últimas. I must also thank Nicolás García for being so welcoming to me when I first arrived to the Physics Department, and for bringing me to the RCAI. I thank my irmão Jorge Henrique Nogueira for his support, and for the many great moments and trips we shared. In this sense, I also thank Gabriela Navarro, Nazanin Davari, and Francesco De Santis.

A great deal of my stress during these years was relieved thanks to the football group I helped organize together with Matt Starr, Jan Delshad, and Alan Daventry. I thank the three of you for your amazing friendship and for building such a wonderful community that has brought together so many people who, like us, were far from home.

Agradezco de corazón a mis amigos de toda la vida, esos que son mi familia y me lo hacen sentir cada vez que vuelvo a la Argentina, en particular a Ana Ailén Armanelli, Daniela Giraldez, Ramiro Manuel Monzón Herrera, Nicolás Gabriel Ojea, Lisandro Parodi, y Matías Pérez Rojas, por bancarme y quererme, literalmente, siempre. Agradezco a Cintia Buonzerio por los mismos motivos y por algunos otros que los dos sabemos. Agradezco también a Lucas Javier Albornoz, Nahuel Almeira, Rodrigo Bonazzola, Ignacio Ferreiro, Paloma Machain y Nicolás Vattuone, los integrantes de La Casa. Pese a estar desperdigados por el mundo, nos hemos acompañado a la distancia, y las veces que he podido verlos, ya sea en Argentina o en algún lugar del norte, hemos vuelto a esa fantástica atmósfera que creamos juntos en Bariloche. Agradezco también a Octavio Cabrera Morrone por confiar en mis capacidades y sacarme de la vorágine del doctorado para divertirnos un poco y pensar juntos otro tipo de problemas.

I am deeply indebted to Courtney Ann Pereira for her incredible support, especially in moments when I could do nothing but work day and night. You consistently brought happiness and tranquility into my mind in the darkest days. You are an amazing person, and this work was largely possible thanks to you.

Finalmente agradezco a mi familia, en particular a mis padres, Elena Margarita Fuksman y Julio César Melon. Gracias por bancarse todos estos años lejos de casa, y por venir a visitarme cada vez que han podido. A ustedes debo no solo su eterno cariño y apoyo, sino también mi curiosidad y mis eternas ganas de aprender más sobre el mundo. En definitiva, ustedes son el motor de todo. Agradezco por último el cariño de mi abuela, Olga Anunciada Pirro, que siempre entendió que estuviera acá y me acompañó desde donde pudo, sin saber bien qué estaba haciendo yo del otro lado del mar.

Abstract

This thesis is devoted to the application of high-resolution numerical methods for relativistic hydrodynamics (RHD) to the study of gamma-ray bursts (GRBs), as well as to the development of new schemes able to describe radiative transfer in relativistic magnetized and unmagnetized flows.

On one side, we have performed RHD simulations of relativistic plasma outbursts within the binary-driven hypernova model, developed throughout the last years in the International Center of Relativistic Astrophysics Network (ICRANet[1]). This model is based on the so-called induced gravitational collapse scenario, proposed to explain the observed temporal coincidence of GRBs and supernovae (SN) of type Ic. This scenario considers a carbon-oxigen star ($CO_{\rm core}$) forming a tight binary system with a companion neutron star (NS). When the collapse of the $CO_{\rm core}$ produces a type Ic SN, part of the ejected material is accreted by the NS, which in turn collapses and forms a black hole (BH). It has been proposed, although the details of this process are a matter of current research, that this collapse creates an optically thick electron-positron plasma around the BH that expands due to its own internal pressure and originates a GRB. Our work in this context has focused on the description of such expanding plasma and its interaction with the surrounding SN ejecta, for which we have followed a hydrodynamical approach using the open-source code `PLUTO`. This allowed us to study this process in high-density regions that had not been explored thus far, and to perform consistency checks of the model taking into account both theoretical and observational constraints such as the system's size, the initial plasma energy, the observed timing and the Lorentz factor of the outbursts. Three different scenarios are here considered: (I) the expansion of the plasma in low-density regions, proposed to produce most of the GRB emission in the prompt phase; (II) a model in which X-ray flares are produced due to the breakout of shocks created when the plasma interacts with high-density regions of the SN ejecta; and (III) a model for the emission of secondary bursts due to the creation of reflected waves caused by the same interaction.

The second part of this thesis is devoted to the main part of our work, which consists in the development of a numerical code for radiative transfer integrated in `PLUTO`. Our implementation is able to solve the equations of relativistic radiation magnetohydrodynamics (Rad-RMHD) under the so-called M1 closure, which allows the radiation transport to be handled in both the free-streaming and diffusion limits. Since we use frequency-averaged opacities, this approach is unable to describe frequency-dependent phenomena; instead,

[1] https://www.icranet.org/

the main focus is put on the transport of total energy and momentum. To avoid numerical instabilities arising due to the possibly large timescale disparity caused by the radiation–matter interaction terms, the Rad-RMHD equations are integrated following implicit–explicit (IMEX) schemes. In this way, interaction terms are integrated implicitly, whereas transport and all of the remaining source terms are solved explicitly by means of the same Godunov-type solvers included in PLUTO. Among these, we have introduced a new Harten–Lax–van Leer–contact (HLLC) solver for optically thin radiation transport. The code is suitable for multidimensional computations in Cartesian, spherical, and cylindrical coordinates using either a single processor or parallel architectures. Adaptive grid computations are also made possible by means of the CHOMBO library. We explain in this work the implementation of all of these methods, after which we show the code's performance in several problems of radiative transfer in magnetized and unmagnetized flows. We pay particular attention to the behavior of the solutions in the free-streaming and diffusion limits, and show the efficiency and scalability properties of the code as compared with its usual nonradiative implementation. Finally, we show an application of this code to the mentioned model for X-ray flares.

Table of contents

Chapter 1

Introduction

1.1 Gamma-Ray Bursts

1.1.1 A brief history

Gamma-ray bursts (GRBs) are intense pulses of gamma rays observed in the sky. In particular, they are famous for being the brightest known sources of electromagnetic (EM) radiation in the universe, reaching isotropic luminosities of the order of 10^{54} erg/s [1], with estimated emitted energies in the range $10^{48} - 10^{55}$ erg if the emission is isotropic [2]. On the contrary, in models where the emission is beamed, these values get reduced to up to $\sim 10^{52}$ erg [3–5], which is in the order of magnitude of the energy emitted by the brightest supernovae throughout several months [6]. Even considering collimation, this means that some of these events release, in just a few seconds, the amount of energy that the Sun will have radiated by the end of its entire ten-billion years lifetime. It is therefore no wonder that the mechanisms that produce such violent events continue to puzzle the scientific community to this day.

GRBs were serendipitously discovered in 1967 in a series of observations made by the *Vela* satellites, an US project led by the Los Alamos laboratory whose only purpose was to monitor hypothetical nuclear weapon tests by the Soviet Union in outer space. By that time, atmospheric, underwater, and outer-space nuclear tests had been prohibited through the joint signing by the Soviet Union, the United Kingdom, and the United States of the *Nuclear Test Ban Treaty*, an international attempt that failed to halt the growth of the nuclear arms race but successfully reduced the atmospheric radioactive contamination [7]. On July 2, 1967, the gamma-ray detectors on board the *Vela* 3A, 3B, 4A, and 4B satellites detected a signal consisting of two peaks; the first of these lasted an eigth of a second (the time resolution of Vela 4), and the second one was observed for two seconds, a behavior that could not be explained as a result of nuclear detonations [8]. The discovery of GRBs was

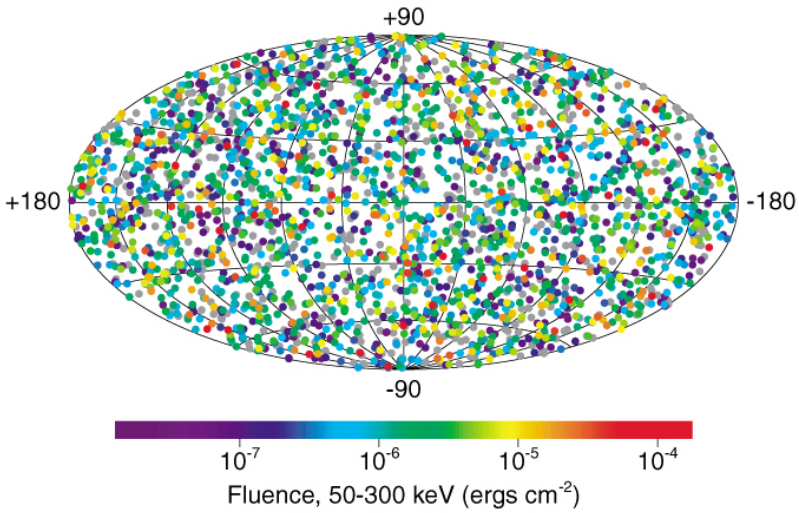

Fig. 1.1 Fluence and location on the sky of the 2704 GRBs detected by BATSE between 1991 and 2000. Source: CGRO-BATSE home page (https://heasarc.gsfc.nasa.gov/docs/cgro/cgro/batse_src.html).

finally published in 1973 in [9], where it was reported that 16 bursts of photons in the energy range $0.2 - 1.5$ MeV lasting between 0.1 and 30 s had been observed by the *Vela* 5A, 5B, 6A, and 6B satellites between 1969 and 1972[1]. In the same article, a study of the arrival time differences between different satellites ruled out both the Earth and the Sun as the sources of the observed radiation.

Since their discovery, several scientific campaigns have been launched with the purpose of better understanding GRBs. The first one to achieve a breakthrough in this direction was the NASA *Compton Gamma-Ray Observer* (CGRO), a space observatory that from 1991 to 2000 detected photons in the 20 keV-30 GeV energy range [11]. The most important instrument on board of this satellite was the *Burst and Transient Source Experiment* (BATSE), that consisted of a series of eight detectors placed in different positions in order to provide the location of the observed GRBs, apart from their temporal and spectral properties. During those nine years, BATSE detected 2704 GRBs and showed that their locations were isotropically distributed on the sky (see Fig. 1.1), instead of being preferentially located in the galactic plane [11]. Furthermore, the observations made by the CGRO showed that the number of detected sources as a function of their flux f deviated from the Euclidean count $N(> f) \propto f^{-3/2}$ [12–14]. These two discoveries convinced most astronomers that GRBs originated either in an extended galactic halo or at cosmological distances [14, 15]. The confirmation of the latter hypothesis

[1] Needless to say, the military purposes of the *Vela* project are not mentioned in that article. Instead, the project is justified in the search for gamma-ray emission during the early stages of supernovae, that had been predicted in [10].

was only obtained after the launching in 1996 of the *BeppoSAX* satellite, that covered a broad range of energies between 0.1 and 300 keV and provided enough angular resolution for optical and radio astronomers to search for lower-energy counterparts of these explosions. The observation of GRB 970228[2] by this satellite led in 1997 to the first detection of an X-ray *afterglow* following a GRB [17] and the first identification of a host galaxy, whose redshift was later identified to be $z = 0.695$ [18]. In the same year, the absorption features observed in the afterglow of GRB 970508 led to the measurement of a redshift of $z = 0.835$. Later observations have confirmed the hypothesis that GRBs arrive from cosmological distances, sometimes with z values as large as 9 [15].

Further advancements were achieved in the last 20 years thanks to the observations made by several gamma- and X-ray satellites, and the follow-up observations carried out by numerous ground-based optical, infrared, mm and radio observatories [15]. In the next Section, we will review some of the most important observational features of GRBs known to this day, with the goal of providing an overview of GRB physics that sets the ground for the models explored in this thesis.

1.1.2 Observational features

GRB events are typically divided into two main parts: the prompt emission, consisting of the initial emission of gamma- and X-ray photons, and the afterglow phase, a lower energy emission occurring right after the prompt phase in an energy range between gamma-rays and radio waves.

Prompt emission light curves have in general the property of being irregular, diverse and complex, which makes their modelling rather challenging (see Fig. 1.2). This phase is usually composed of individual pulses, each of them exhibiting a FRED (fast rise and exponential decay) behavior. The total duration of the prompt emission is generally determined by the parameteter T_{90}, defined as the time interval between the moments in which 5% and 95% of the total fluence is observed, and whose value ranges from milliseconds to tenths of thousands of seconds. As pointed out in [15] and [19], this definition is quite limited for several reasons: (I) it depends on the energy range and sensitivity of the detector; (II) some GRBs exhibit long gaps between emission episodes, and hence T_{90} may overestimate the duration of the source's activity; (III) this parameter does not distinguish the prompt emission from the early afterglow and can include episodes originated in different physical phenomena, which reduces

[2]GRBs are named after the date they are published, following the convention GRB YYMMDD. If more than one GRB is published on the same day, the form GRB YYMMDDX is adopted, where X is a letter that identifies the order of publication of the burst (A for the first one, B for the second one and so forth). Since 2010, a letter A is added even if no second burst is published that day [16].

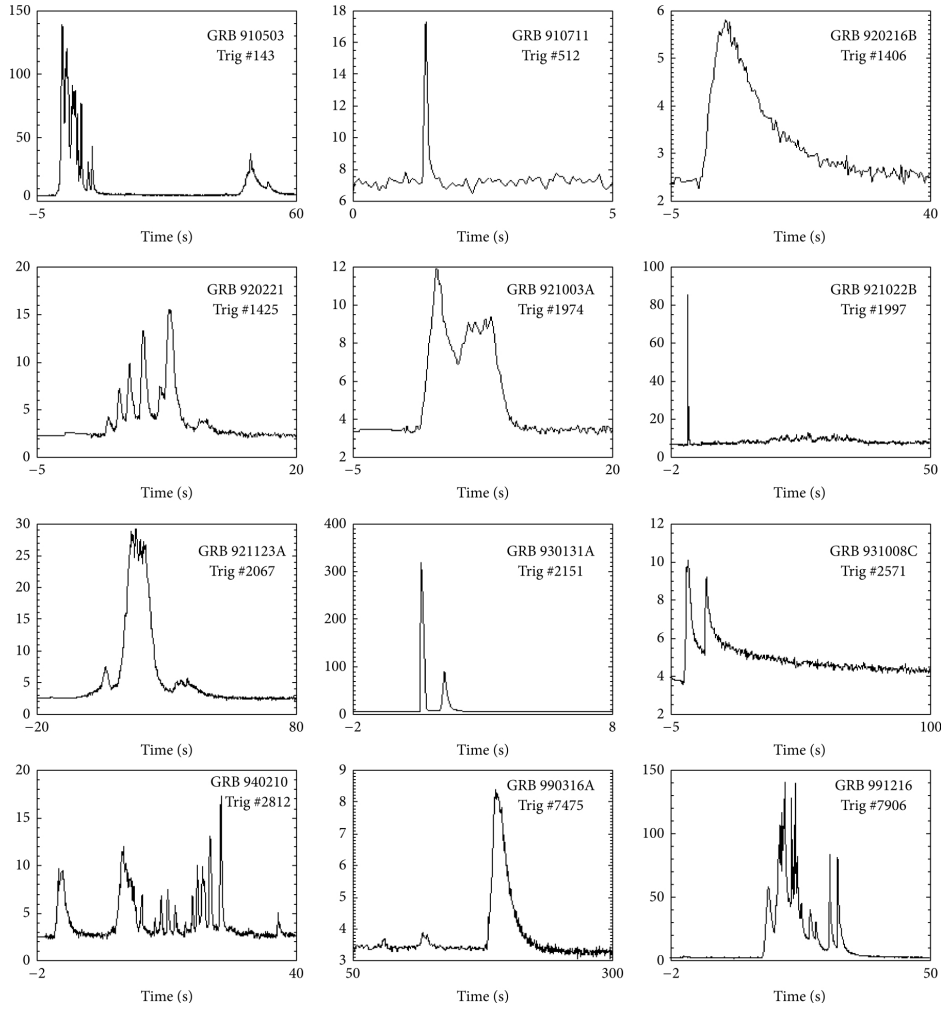

Fig. 1.2 Light curves of 12 different GRBs (reproduced from [19]), created by Daniel Perley with data from the public BATSE archive (http://gammaray.msfc.nasa.gov/batse/grb/catalog/).

its physical significance; and (IV) its definition is based on the observation time, and hence it does not take into account the differences in the redshift of different souces, which can be important. Despite these issues, this parameter brings some light to the general behavior of GRBs. When considering many GRB sources, it can be seen that T_{90} follows a bimodal distribution, leading to a division into two main groups (see Fig. 1.3). About 25% of GRBs in the BATSE catalog[3] are classified as *short*, with an average T_{90} between 0.2 and 0.3 s, while the rest of them are *long*, with an average T_{90} between 20 and 30 s [22, 23]. The boundary between the two distributions is usually set at 2 s. On top of this, short GRBs have in general a harder spectrum than long ones, with a mean peak energy of ~ 600 and ~ 200 keV for short

[3]This observation was later confirmed by the *Swift* and *Fermi* satellites, with a slightly smaller proportion of short GRBs (18%) [21].

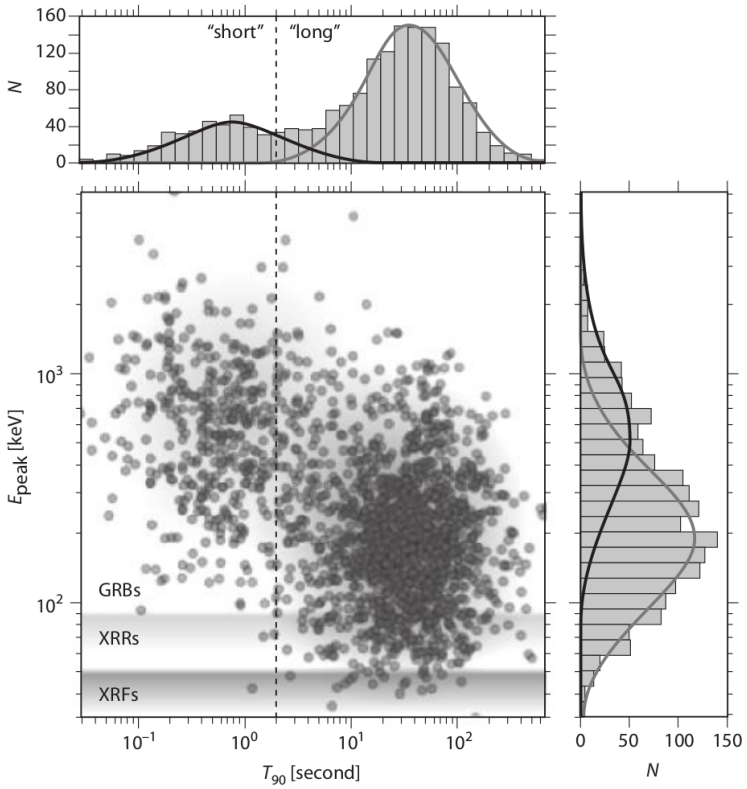

Fig. 1.3 Histograms of T_{90} and $E_{\rm peak}$ and scatter plot of $E_{\rm peak}$ vs. T_{90} for several GRBs observed by BATSE, where the bimodality of both distributions can be seen. Reproduced from [20].

and long GRBs respectively [20]. These features seem to indicate that long and short GRBs are originated by different physical mechanisms, as discussed in Section 1.2. An additional clue for this is given by the observed spatial and temporal coincidence between some long GRBs and core collapse supernovae of type Ib/c [24–30], that is not observed for short GRBs. Most evidence in this direction points to an association between long GRBs and broad-lined type Ic SN, named *hypernovae* (HN) due to their uncommonly large kinetic energy when compared with other SNe Ic [31, 32]. In particular, broad spectral lines reveal unusually large velocities for the ejected material ($\lesssim 10^{-1}\,c$; see [32]).

Contrarily to the erratic behavior seen in the prompt emission, the afterglow usually presents a smoother and simpler pattern. The understanding of this phase was radically improved after the launch of the Neil Gehrels *Swift* Observatory in 2004, which allowed for the first time for a rapid localization and coverage (within the first ~ 100 s after the gamma-ray trigger) of GRB afterglows in the γ, X, and optical bands [34, 35]. As shown in [33, 36] using data from *Swift*'s X-Ray Telescope (XRT), afterglow light curves can be schematized in a canonical form that generally includes five components (see Fig. 1.4): (I) an early time

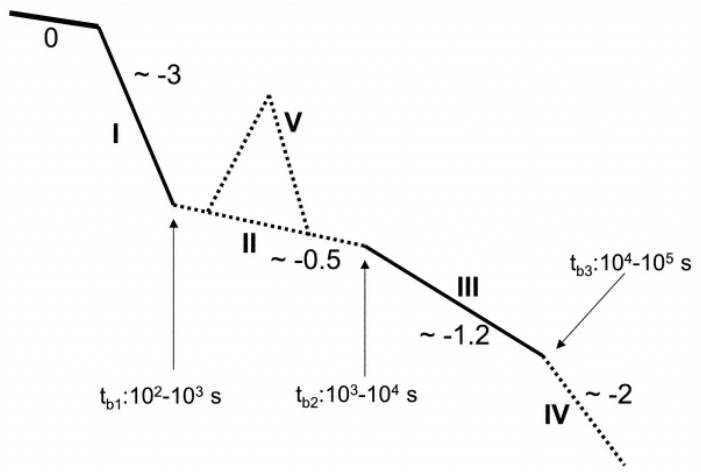

Fig. 1.4 Scheme of the typical behavior of an early afterglow, showing the early time steep decay phase (I), the plateau (II), the two decay phases after the plateau (III and IV), and an X-ray flare (V). Reproduced from [33].

steep decay phase, typically proportional to t^{-3} or steeper; (II) a shallow decay or *plateau*, usually proportional to $t^{-1/2}$ except in few cases where the light curve is flat or even rises in the beginning of this phase; (III) a normal decay phase, approximately proportional to t^{-1}; (IV) a late steep decay phase, usually decaying as t^{-2} and not always observed; and (V) X-ray flares, which are sudden increases in the flux observed in roughly $1/3$ of GRB X-ray afterglows. After these initial stages, the late decay of the afterglow is sometimes observed to last up to several years [37].

Another feature shared by a few GRBs is the appearance of a *precursor*, a typically softer and weaker emission that precedes the main burst by $10 - 100$ s. This phenomenon is observed in roughly 10% of GRBs [38], although this number depends on the definition of the precursor, and ranges generally between 3% [39] and 20% [40]. Most precursors are observed to be shorter than the main burst, as shown in [38], and no statistical correlation is found between the features of the main episode in the prompt emission and the existence of a precursor event [40, 41]. In some GRBs, the properties of the precursor are similar to those of the main-episode emission [38, 40, 41].

More information about the general behavior of GRBs and the mechanisms that produce them can be obtained from the measurement of their spectral energy distributions (SEDs), either time-integrated over the entire duration of the bursts or time-resolved. Spectra are generally observed to be nonthermal, and their time-integrated functional forms can typically be optimally fitted by a phenomenological model consisting in two smoothly connected power laws. This model, introduced by David Band et al. in [42] and hence called the *Band* model,

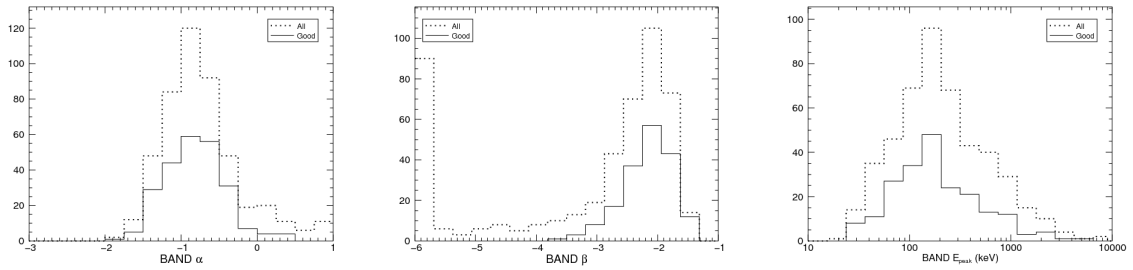

(a) (b) (c)

Fig. 1.5 Histograms of the parameters of the Band model, corresponding to the low-energy slope α (a), the high-energy slope β (b), and the peak energy of the $E^2N(E)$ distribution $E_{\rm peak}$ (c). Data are extracted from 3800 spectra, derived from the 487 GRBs in the first *Fermi*/GBM catalogue. Dashed lines represent results obtained for all GRBs in the catalogue, while solid lines show only those that satisfy goodness criteria based on the χ^2 distribution. Reproduced from [43].

is given by the following function:

$$N(E) = \begin{cases} A\left(\frac{E}{100\,\mathrm{keV}}\right)^{\alpha} \exp\left(-\frac{E}{E_0}\right), & E < (\alpha-\beta)E_0 \\ A\left(\frac{E}{100\,\mathrm{keV}}\right)^{\beta} \left(\frac{(\alpha-\beta)E_0}{100\,\mathrm{keV}}\right)^{\alpha-\beta} \exp\left(\beta-\alpha\right), & E \geq (\alpha-\beta)E_0 \end{cases}, \tag{1.1}$$

where $N(E)$ is defined in such a way that $N(E)dE$ is the number of photons per unit area measured in the energy interval $(E, E+dE)$. This function has four free parameters: the low– and high–energy spectral slopes α and β, the break energy E_0, and the normalization constant A. In [43], using data of 487 GRBs detected by the *Fermi*[4] Gamma-ray Burst Monitor (GBM), it is shown that the low-energy spectral slope is roughly in the range $[-1.5, 0.5]$ and averages at $\alpha \approx -1$ (see Fig. 1.5), while β is typically smaller than -1.3 and can sometimes take very small values ($\lesssim -3$), which is consistent with an exponential cutoff [19]. The distribution of the parameter E_0 is represented in Fig. 1.5c in terms of the peak energy of the $E^2N(E)$ distribution, given by $E_{\rm peak} = (2+\alpha)E_0$, which peaks around ~ 150 keV and ranges from ~ 20 keV up to ~ 2 MeV.

The Band model is not the only one usually implemented to fit GRB spectra, and often a combination of several components is used. To this date, there is evidence for the existence of up to three separate components in the observed spectra: (I) a nonthermal component, fitted as a Band function with $E_{\rm peak} \sim 1$ MeV; (II) a quasi-thermal component fitted by either

[4] The Fermi Gamma-ray Space Telescope, launched in 2008 with a detection energy range between 8 keV and 300 GeV and still in activity, was the first instrument to study the behavior of GRBs in such high energies [44].

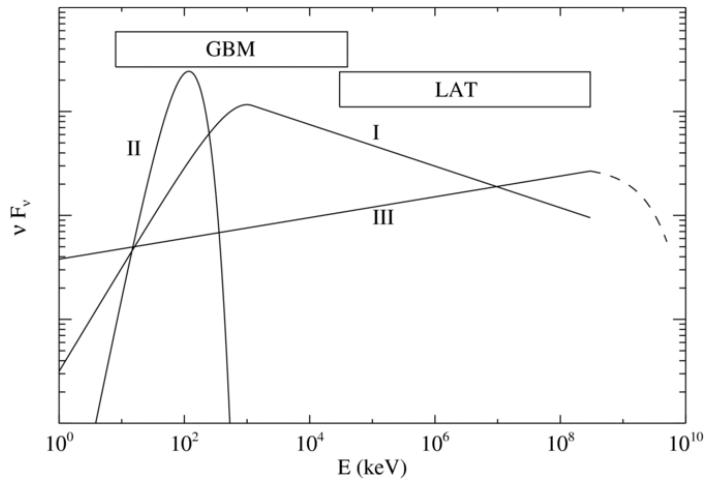

Fig. 1.6 Scheme of the three components of GRB spectra considered in [45], showing a nonthermal component (I), a quasi-thermal component (II), and an extra power-law component that extends to high energies (III). The bandwidths of the LAT and GBM detectors of *Fermi* are shown for comparison. Reproduced from [45].

a blackbody or multicolor blackbody model, typically peaking at ~ 100 keV; and (III) an extra power-law component at very high energies (> 100 MeV) [45, 46] (see Fig. 1.6). The determination of an optimal fitting model is not always clear, as frequently more than one can fit the data equally well. This must be taken into account when developing theoretical frameworks aimed to explain each of the observed components. For instance, the fraction of GRBs that show clear evidence for the existence of a thermal component is not clear, since such value is quite sensitive to the analysis method [19].

In general, determining the photon spectrum emitted in different time windows gives valuable information about the processes originating each of the emission episodes in a GRB. Unfortunately, due to the amount of photons required in each temporal bin to achieve a good statistical significance, time-resolved spectra can only be obtained for the brightest GRBs. Nevertheless, this method is nowadays broadly used due to the high sensitivity of the *Fermi* satellite. An interesting feature that can only be observed in this way is the variation of the value of $E_{\rm peak}$ in individual GRB pulses, which either shows a hard-to-soft evolution, in which $E_{\rm peak}$ decreases from the beginning of the pulse [47], or a tracking behavior, in which $E_{\rm peak}$ follows variations of the flux [48]. On the other hand, observations made by *Fermi*/LAT have shown that in most cases high energy photons (> 100 MeV) are detected with a delay of a few seconds with respect to the lower energy emission ($\lesssim 1$ MeV) [45, 49, 50].

In the next section, we will outline a series of astrophysical models proposed in the literature to explain the origin and behavior of GRBs, paying particular attention to those explored in this thesis.

1.2 Models for GRB emission

1.2.1 Generally accepted ingredients

Despite the years of work dedicated to understanding the processes that lead to the emission of GRBs, there is no universally accepted model that explains all of their observed features. Before going into details about the different scenarios proposed in the literature, we will enumerate a few common features shared by most of them and summarized in [19, 51]:

1. Practically all GRB models involve relativistic motion with Lorentz factors $\gamma > 100$. Initially, this was theoretically proposed to solve the *compactness problem*: assuming Newtonian dynamics, the estimated photon densities required to emit the observed energies with a time variability of ~ 10 ms are high enough to efficiently produce pairs out of photon-photon interaction, which makes the source optically thick. Relativistic motion solves this issue by reducing the photon energy by a factor γ in the source's frame and the size of the source by a factor γ^2, which as a result makes the source optically thin for $\gamma \gtrsim 100$. This theoretical prediction was later on experimentally supported [52–54]. To this day there is no consensus on the mechanisms that accelerate matter to such velocities: while some models consider a radiation–dominated expansion [55, 56], in others matter dynamics is dominated by magnetic fields [57].

2. The energy radiated in both the prompt and afterglow phases are generally explained through a dissipation process that enables the conversion of bulk kinetic energy into random motion of highly energetic particles. Some mechanisms proposed in the literature are diffusive shock acceleration [58], collisional heating [59], magnetic reconnection [60], and heating by neutron decay [59, 61]. In particular, there is a rather general agreement in the association of GRB afterglows with the dissipation of energy generated by the interaction of the burst and the circumburst medium (CBM). The processes that lead to the gamma-ray emission differ according to the model, the most widely considered ones being synchrotron emission, inverse Compton effect, and photospheric emission.

3. Most GRB models consider that the energy emission is highly collimated, with an opening angle $\theta_j \lesssim 10^\circ$ (see, e.g., [5, 62]), which drastically reduces the energy budget required to explain observations. Moreover, a jet with Lorentz factor γ being slowed down by the CBM will produce a steepening in the afterglow light curve when $\theta_j \sim 1/\gamma$ for two main reasons. Firstly, the flux emitted from the jet is beamed within an angle $\theta_b = 1/\gamma$, which means that an observer along the jet axis will see a steeper decrease

of the flux as soon as $\theta_b > \theta_j$, which would not be observed if emission was isotropic [3, 4, 63, 64]. Secondly, as shown in [3, 4, 65], the jet starts spreading sideways as soon as it reaches the same condition, which also leads to a steepening of the flux. The combination of these two phenomena provides the most widely accepted interpretation of the frequently observed flux steepening observed in GRB afterglows (between phases III and IV in Fig. 1.4), usually denominated *jet break*. According to this model, jet breaks must be *achromatic*, i.e., they must be observed in all frequency bands. Evidence for achromatic jet breaks was found e.g. in [66, 67], whereas evidence for chromatic breaks occurring in the X-ray band but not in the optical was found in [68]. In particular, a consistent lack of achromatic breaks has been observed in GRB afterglows since the beginning of the *Swift* mission, sometimes attributed to off-axis observations [69] or to misinterpretation of low-quality data [70]. Such lack of evidence is argued in [71, 72] to support the model considered in this thesis, in which the GRB emission is produced isotropically (see Section 1.2.3).

4. GRBs are generally associated with the death of massive stars and the birth of compact objects. The most important indication for this is the large amount of energy released in these processes (up to $\sim 10^{52}$ erg if the emission if collimated), since no other kinds of sources are known to release that much energy in such short times. In the case of long GRBs, this is additionally supported by their association with SN Ic.

We will now describe two models for GRB emission proposed in the literature. In Section 1.2.2 we will focus on the so-called *fireball* model, widely regarded as a standard model of GRBs, while in Section 1.2.3 we will discuss the main features of the alternative *fireshell* model.

1.2.2 The fireball model

To this day, the most widely accepted scenario for the emission of GRBs is the fireball model, in which GRBs are associated with the sudden release of a large amount of gravitational energy (of the order of a solar mass) by a stellar size object, which receives the generic name of *central engine* [73]. The model does not make any particular assumption of the nature of this object, and focuses instead on the dissipation processes that produce the GRB emission. In this scenario, a small fraction of the total released energy[5] ($\sim 10^{-3} - 10^{-2}$) is transformed into a high-temperature (~ 1 MeV) plasma containing electrons, protons, photons and baryons, known as fireball [55]. This plasma is produced within a volume of

[5] In such a process, most of the energy should be converted into thermal neutrinos with typical energies $10 - 30$ MeV and gravitational waves with frequencies in the range $10^2 - 10^3$ Hz [73].

radius $R_0 \sim 10^7$ cm, which makes it initially optically thick to Compton scattering due to its high density of positrons and electrons. Depending on the emission mechanism, the internal energy of a fireball can either be radiation–dominated or magnetically dominated. We will mostly discuss the first of these scenarios, which is the most commonly regarded one among the two of them.

Let us consider a radiation–dominated fireball (see Fig. 1.7) produced through the injection from the central engine of mass and internal energy at the rates $\dot{M}$ and $\dot{E}$. As studied in [74–76], such an outflow undergoes an initially adiabatic expansion (acceleration phase) until all of its internal energy has been transformed into bulk kinetic energy, and the flow expands at constant velocity (coasting phase). For constant $\dot{M}$ and $\dot{E}$, we can obtain a limit to the maximum velocity reached by the fireball by imposing energy conservation [75, 77], which gives a maximum Lorentz factor $\gamma_{\max} = \eta$, where $\eta = \dot{E}/\dot{M}c^2$. In particular, the condition $\gamma \gtrsim 100$ gives an upper limit on the total baryon load of the fireball, defined as $B = Mc^2/E$, where E and M are respectively the total injected energy and mass, which must therefore satisfy $B < 10^{-2}$. During the acceleration phase, the bulk Lorentz factor of the outflow grows as $\gamma \propto r$, and the coasting phase is reached at the saturation radius given by $R_s \sim \eta R_0$.

At some point during this evolution, at the so-called *photospheric radius* $R_{\rm ph}$, the fireball becomes optically thin, which allows radiation to escape freely. After that stage, each layer continues to expand without changing its speed, and radiation streams freely through the *photosphere*, i.e., the optically thin region located at $r \gtrsim R_{\rm ph}$ [78, 79]. Some of these photons are scattered by the highly energetic electrons in the ejected plasma, as explained below. This process is proposed in the fireball model to explain the quasithermal component observed in the spectra of several GRBs, whose spectrum depends on the several dissipation mechanisms occurring both at $r > R_{\rm ph}$ and $r \lesssim R_{\rm ph}$ [80]. In particular, it is proposed in [81] that the transition between the optically thick and thin regimes produces a precursor with a quasithermal spectrum.[6] This model explains a class of GRB precursors with smooth and FRED-shaped light curves and quasithermal spectra, but is at odds with the predominantly nonthermal spectrum observed in most GRB precursors[7] [40, 85].

In the radiation–dominated fireball model, dissipation is explained through *internal* and *external* shocks. The first of these are caused by fluctuations in the energy injection rate at the early stages of the expansion, which lead to different values of η and consequently to variations in $\gamma_{\max}$. As discussed in [87], such fluctuations cannot be smoothed out in spatial

[6] Some alternative models to this one involve are the breakout of the fireball through the surface of a massive star [82, 83] and the formation of weak jets caused by magnetohydrodynamical processes preceding the main emission episode [84]. In particular, nonthermal emission would be emitted only in the latter of these scenarios.

[7] In principle, the nonthermal appearance could be explained through a convolution of blackbody emission at different temperatures and locations in the outflow. However, this does not explain why the spectral indices of precursors are on average similar to those of the main event [41].

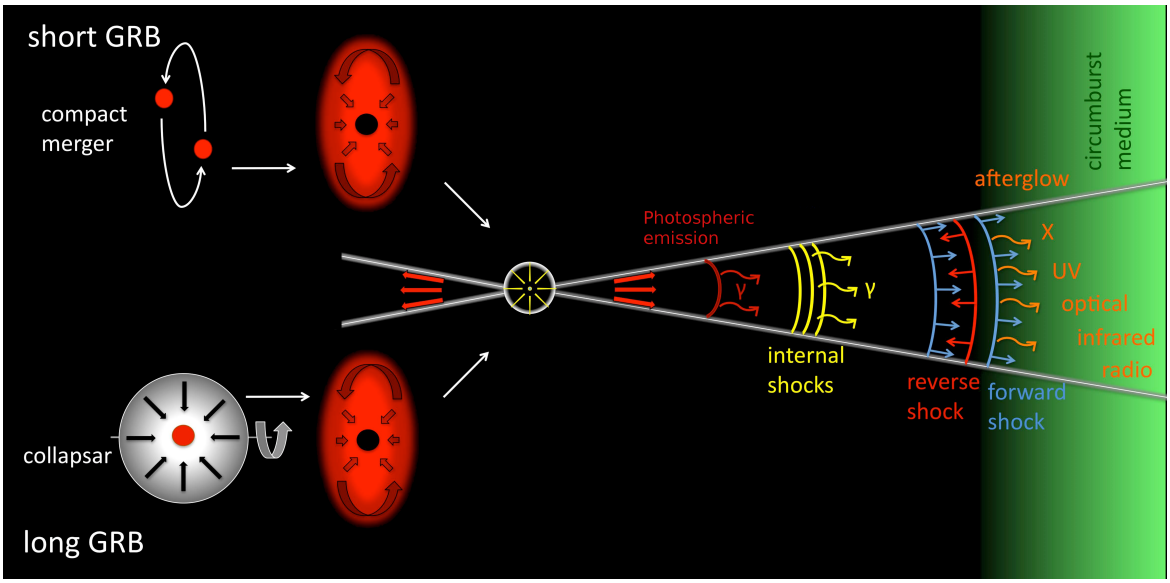

Fig. 1.7 Schematic representation of the different emission mechanisms involved in a radiation–dominated fireball model. Reproduced from [86] with modifications.

scales bigger than R_0, and hence the outflow is formed by a series of independent shells with typical thickness $\sim R_0$. In particular, spreading due to gradients in γ within individual shells start occurring for $r \gtrsim 2\eta^2 R_0$ [19, 88]. Approximately at the same radius, the interaction of shells with different velocities becomes possible. As faster shells catch up with slower ones, internal shocks are generated within the plasma. Due to its low density, the ejected plasma is collisionless, which enables the acceleration of electrons to high energies through diffusive shock acceleration[8] (Fermi process). Such electrons can then emit part of their energy, either through synchrotron emission or by inverse Compton scattering. In this picture, the fast variability during the prompt phase of GRBs is naturally explained through energy dissipation occurring at several internal shocks. However, this model has the drawback of predicting a low overall efficiency in the conversion of kinetic to internal energy unless the Lorentz factor changes considerably from side to side of the shocks[9] [19, 90, 91]. On the other hand, external shocks produced when the fireball is slowed down by the CBM are proposed in this model to produce the afterglow [92, 93]. Such a scenario predicts a slower time variability with respect to the prompt phase [94], and explains the shallow decay during the plateau by

[8] It is likely that the acceleration mechanisms are related to magnetic field amplification close to the shocks via plasma instabilities, which is a matter of current research. Efforts in this direction have been made in the past years through particle-in-cell (PIC) simulations (see, e.g., [89]). However, further advancements are limited by the lack of computational power required to resolve both the electron skin depth and the dynamical length scales of astrophysical systems.

[9] Alternatively, dissipation mechanisms due to collisional processes and the decay of neutrons in the outflow are considered in [59].

means of a prolonged energy injection into the external shocks [36]. As well, the interaction with the CBM may produce reverse shocks, which are expected to produce a lower-energy emission that could explain the optical flashes observed in several GRB afterglows [95].

If the energy release is entirely explained through synchrotron emission, i.e., assuming that dissipation produces enough energetic electrons, the emitted spectrum can be computed by assuming that such electrons are injected for $\gamma_e > \gamma_{\min}$ with a distribution proportional to γ_e^{-p}, where γ_e is the electron Lorentz factor, $\gamma_{\min}$ is the minimum γ_e of the distribution, and where $p > 2$ [96, 97].[10] The characteristic energy $h\nu_s$ of observed synchrotron photons depends in general on the Lorentz factors γ and γ_e of the emitting material and the energetic electrons, as well as on the magnetic field. The behavior of the emitted spectrum of an electron changes depending on whether γ_e is larger or smaller than the value γ_c, above which electrons emit practically their entire kinetic energy during a single synchrotron period. The observed spectrum can consequently be expected to be different in the regimes characterized by $\gamma_{\min} > \gamma_c$ (fast cooling) and $\gamma_{\min} < \gamma_c$ (slow cooling). In the fast cooling regime, all of the electrons satisfy $\gamma_e > \gamma_c$, which results in the following observed flux:

$$F_\nu = F_{\nu,\max} \begin{cases} (\nu/\nu_c)^{1/3}, & \nu < \nu_c \\ (\nu/\nu_c)^{-1/2}, & \nu_c < \nu < \nu_m \\ (\nu_m/\nu_c)^{-1/2}(\nu/\nu_m)^{-p/2}, & \nu_m < \nu \end{cases}, \tag{1.2}$$

where $\nu_c = \nu_s(\gamma_c)$ and $\nu_m = \nu_s(\gamma_{\min})$. Conversely, in the slow cooling regime, we have

$$F_\nu = F_{\nu,\max} \begin{cases} (\nu/\nu_m)^{1/3}, & \nu < \nu_m \\ (\nu/\nu_m)^{-(p-1)/2}, & \nu_m < \nu < \nu_c \\ (\nu_c/\nu_m)^{-(p-1)/2}(\nu/\nu_c)^{-p/2}, & \nu_c < \nu \end{cases}. \tag{1.3}$$

In particular, fast cooling must take place during the prompt phase in order to produce an efficient emission of photons. On the other hand, it is expected that during the afterglow phase there will be a transition from fast to slow cooling [53, 92, 98–100].

The synchrotron model gives an explanation for the broken power-law behavior of GRB spectra, commonly fitted by means of the Band function (Eq. (1.1)). Provided that the outflow is optically thin, the lowest part of the spectrum must verify $F_\nu \propto \nu^{1/3}$, which translates into $\alpha = -2/3$. This behavior is typical of synchrotron radiation [101–103] and does not depend on the energy distribution of the accelerated electrons. Taking fast cooling into

[10] This condition is imposed to guarantee that the total integrated energy is finite, although the same can be achieved by considering $1 < p < 2$ with an energy cutoff.

account, the lowest-energy spectral index α must be contained in the range $[-3/2, -2/3]$, which is not verified in several bursts[11] [106, 107]. This means that additional mechanisms must take place in those cases. For instance, if the scattering optical depth of the emitting material is of order unity, spectral indices of up to $3/2$ can be obtained [108–110]. On top of this, synchrotron self-aborption should produce a steep cut-off of the spectrum at lower frequencies; in particular, this happens if the photon frequency is lower than that for which the optical depth equals 1 for uncooled electrons (denoted ν_{ac}) and for all electrons (denoted ν_{sa}) [109, 110]. In that case, $F_\nu \propto \nu^2$ and $\nu^{11/8}$ for $\nu < \nu_{ac}$ and $\nu_{ac} < \nu < \nu_{sa}$ respectively. On the other hand, inverse Compton scattering can also change the spectrum even if the system is optically thin to this process. The effect of this phenomenon depends on the Compton parameter $Y = \gamma_e^2 \tau_e$, where τ_e is the optical depth to Compton scattering [51]. This process becomes important for $Y > 1$. Typically, a scattering of a photon by a relativistic electron boosts its energy by a factor γ_e^2, which should lead to the appearance of an ultrahigh-energy component in the GeV$-$TeV range of the observed spectra [111, 112]. In addition, inverse Compton speeds up the cooling of the emitting regions by shortening the cooling time by a factor Y [51].

An alternative mechanism for the emission of GRBs is given by magnetically dominated fireballs, in which most of the energy is released in the Poynting flux [113–115]. In this case, the dynamics of the ejected material depends on the magnetization parameter σ, defined as the Poynting to kinetic energy flux ratio, which verifies $\sigma \gg 1$. If absence of dissipation, such a magnetically driven outflow reaches a maximum Lorentz factor given by $\sigma_0^{1/3}$, where $\sigma_0 = \sigma(R_0)$ [15, 116]. It is proposed in this model that energy dissipation occurs in these outflows through reconnection of magnetic fluctuations on small scales. Although additional dissipation could be in principle caused by internal shocks, such mechanism is much less efficient in Poynting–dominated plasmas than in weakly magnetized plasmas (e.g. radiation–dominated fireballs) [117–119]. Jet acceleration can be driven by both adiabatic expansion and reconnection itself, if part of the dissipated energy is transferred to bulk kinetic energy. However, due to a lack of understanding of the reconnection process, it is not known in which proportion the dissipated energy is destined to heating and jet acceleration. Despite this drawback, this model counts with the advantage of predicting a high enough radiative efficiency, and is in good agreement with observed GRB spectra [120]. Another prediction made by this model comes from the fact that photons are mainly radiated by accelerated particles in an ordered magnetic field, which means that the emission should be largely polarized [121]. Although some studies indicate smaller polarization degrees than predicted

[11] This approach is critiqued in [104, 105], where it is argued that criteria based on the Band function tend to overreject synchrotron models, which are consistent with data in most GRBs if alternative physically motivated fitting functions are used instead.

by models of magnetically dominated fireballs (see, e.g., [122, 123]), both experimental and theoretical developments still need to be achieved in this direction.

Several models are proposed in the literature for the central engine responsible of the energy injection. In particular, temporal and energetic considerations suggest that GRBs are produced as a consequence of the accretion of a massive disk ($\sim 0.1 M_\odot$) by a compact object, most likely a newly born black hole (BH). It is generally considered that short GRBs originate from small disks produced by compact binary mergers, either of two neutron stars (NSs) or of a NS and a BH (see, e.g., [124]), whereas long GRBs originate in the gravitational collapse of massive stars (*collapsars*). In the first of these cases, the merger releases $\sim 10^{53}$ ergs, mainly in the form of low-energy neutrinos and gravitational waves [51], and the rest produces a jetted GRB emission. This scenario has been recently supported by the observation of GRB 170817A 1.7 s after the detection of the gravitational wave GW170817, whose signal was determined to be consistent with the merger of two NSs [125]. On the other hand, the most accepted explanation for the emission of long GRBs is given by the collapsar model, which involves the collapse of a massive, rapidly rotating Wolf-Rayet star with a core of $\sim 10\ M_\odot$. In this model, matter accretion on the newly created BH creates a low-density region close to the rotation axis of the latter, which leads to the formation of a jetted outflow that breaks through the star's surface. The mechanisms by which the rotational and gravitational energy of the system produce such jets in both of these models are not clear, and are a matter of current research. If the central engine is an accreting BH, three jet launching mechanisms are most commonly proposed in the literature: (I) neutrino-antineutrino annihilation in rapidly accreting disks, which can generate a hot $e^- e^+$ plasma with similar features to a radiation–dominated fireball [126, 127]; (II) the Blandford-Znajek mechanism, in which rotational energy and angular momentum are transferred from the BH to a Poynting–dominated outflow due to the frame dragging of the magnetic field lines supplied by the accretion disk [128]; (III) the launching of magnetic blobs from accretion disks [129]. An alternative possibility for the central engine is given by millisecond *magnetars*, which are rapidly spinning (period ~ 1 ms), highly magnetized ($B \gtrsim 10^{15}$ G) NSs [130–133]. The spindown of these objects powers the jetted emission of Poynting–dominated outflows, which release a large fraction of the stored magnetic and rotational energy in typical timescales of ~ 10 s (for this value of the magnetic field; see [19]). The energy budget for such emission is powered by the dynamo produced by the differential rotation of the NS. In this model, the fast variability and erratic behavior of the prompt phase are explained through magnetic dissipation instabilities [134, 135]. Following the main energy extraction, a residual rotation is proposed (e.g. in [132]) to power late time flaring or afterglow emission, giving a possible explanation for the occurrence of X-ray plateaus [136, 137].

1.2.3 The fireshell model

An alternative mechanism for the emission of GRBs is given by the *fireshell* model, proposed in [138] and further developed in [139–146]. As well as the fireball model, this one also involves the relativistic expansion of an optically thick baryon-loaded e^-e^+ plasma up to bulk Lorentz factors $\gamma \sim 100 - 1000$, but the emission process is radically different. Firstly, the expansion of the pair-baryon plasma is assumed to be isotropic, which increases the energy budget required for the observed GRB emission with respect to jet models. In addition, this model does not consider a prolongued activity of the inner engine, and dissipation is, at least in the early stages of the emission, explained through collisional mechanisms.

In this scenario, the initial creation of an e^-e^+ plasma is explained through vacuum polarization (Schwinger effect, [147]) due to the strong electric fields created during the collapse of a compact object to a BH [138, 148] (see [149] for a review). The region where electric fields are initially intense enough to allow such process, called *dyadosphere*, has a width $r_{\rm dyad} \sim 10^8 - 10^9$. The details of the creation of such strong electric fields are still a matter of current research: while initially this was explained through the collapse to a Kerr-Newman BH, some authors have rejected this possibility by arguing that the creation of e^-e^+ itself is an efficient mechanism for the discharge of the BH (see, e.g., [150]). The model has been changed in the last year by considering a configuration proposed in [151], in which strong electric fields are induced due to the rotation of an uncharged (Kerr) BH placed in an asymptotically uniform magnetic field [152].

Since the e^-e^+ plasma is initially optically thick, its evolution is well described by the already mentioned hydrodynamical models applied to the fireball model in [75, 77]: the expanding plasma forms an ultrarelativistic shell (hence the name fireshell) that accelerates as $\gamma \propto r$ due to the conversion of internal into kinetic energy, while maintaining its width approximately equal to $r_{\rm dyad}$ [139]. The expansion is slowed down by conservation of total momentum as the plasma engulfs the baryonic matter in the CBM, until acceleration stalls when most of the internal energy of the plasma has been converted into kinetic energy. This occurs when the shell has reached a bulk Lorentz factor $\gamma \sim 1/B$ [75, 77, 140]. From that moment on, the plasma continues to expand at constant speed until the electron density decreases below the point at which the material becomes optically thin. At this stage, photons decouple from the electrons and positrons in the shell, which produces an emission episode denominated proper GRB (P-GRB). Since the optical depth of electrons and positrons in the material is still significant during this emission, the spectrum of photons emitted in the P-GRB should be that of a Comptonized Doppler-shifted blackbody [142, 153]. Moreover, the spectrum can be further broadened if the comoving temperature varies significantly along the shell [142].

Once the P-GRB is emitted, the ejected material continues to expand, and interacts with the CBM. This interaction slows down the shell by dissipating part of its kinetic energy through collisional processes, and produces the afterglow. Hence, the prompt emission corresponds in this model to both the P-GRB and the initial stages of the afterglow. In particular, the fast time-variability of prompt GRB light curves is explained by considering that the CBM is formed of clumps of matter of size $\sim 10^{15} - 10^{16}$ cm, density contrast $\delta\rho/\rho \sim 0.1 - 10$, and mass between 10^{22} and 10^{24} g, which is supported by both observations of the CBM in novae (see, e.g., [154]) and theoretical models [155, 156]. Thus, in this scenario, fast changes in the structure of GRBs map abrupt changes in the density of the CBM[12]. In particular, light curves can be reproduced numerically by making a few assumptions about the geometry of the CBM and its interaction with the expanding shell. The approach adopted in the fireshell model consists in considering that the shell reaches instantaneous thermal equilibrium with the engulfed CBM matter, which allows for a description of the entire dynamics of the expanding shell by imposing energy-momentum conservation, provided the CBM density profile is known. This method is implemented by means of a 1D code that computes the interaction between a spherically symmetric shell with a constant width in the laboratory frame and an isotropic matter distribution that represents the CBM [140, 158]. For each observation time, a distant observer measures photons emitted at different locations on the shell and at different times in the source's rest frame, such that the arrival time is the same for all of them. This condition defines for each arrival time an *equitemporal surface* (EQTS), such that photons emitted from it arrive at the same time at the observation location. The geometry of each EQTS depends entirely on the shell's dynamics, and can be computed analytically as shown in [144, 145]. The observed light curve is thus computed by integrating the differential luminosity of the shell on each EQTS, assuming that the emitted photon distribution is at each point thermal, and taking into account the Doppler shift due to the relativistic motion of the emitting material. In order to take into account the filamentary, clumpy structure of the CBM, the local emitted power is multiplied by the ratio between the effective emitting area of the shell and the total visible area [158]. The time-resolved and time-integrated spectra of some low-energy GRBs can be explained through this model, where the nonthermal Band-like shape arises as a product of the integration of different thermal spectra on each EQTS[13]. In particular, the observed hard-to-soft spectral variation observed in individual pulses (see Section 1.1.2) is explained by the time decrease of both the comoving temperature and the bulk Lorentz factor. However, this model does not reproduce the spectra of some highly

[12] A similar model in the context of collisionless external shocks has been proposed in [157]. On the contrary, it is argued in [51] that such model is unable to explain the millisecond-scale time variability observed in several long GRBs.

[13] A similar idea is proposed in [159].

Class	Type	Number	*In-State*	*Out-State*	$E_{\rm p,i}$ (MeV)	$E_{\rm iso}$(erg)	$E_{\rm iso,GeV}$ (erg)	$\rho_{\rm GRB}$ (Gpc^{-3} yr^{-1})
Binary-driven	I	329	CO_{core}-NS	νNS-BH	$\sim$0.2–2	$\sim10^{52}$–10^{54}	$\gtrsim10^{52}$	$0.77^{+0.09}_{-0.08}$
hypernova	II	(30)	CO_{core}-NS	νNS-NS	$\sim$0.01–0.2	$\sim10^{50}$–10^{52}	–	100^{+45}_{-34}
(BdHN)	III	(19)	CO_{core}-NS	νNS-NS	$\sim$0.01	$\sim10^{48}$–10^{50}	–	–
	IV	5	CO_{core}-BH	νNS-BH	$\gtrsim$2	$>10^{54}$	$\gtrsim10^{53}$	$\lesssim0.77^{+0.09}_{-0.08}$
	I	18	NS-NS	MNS	$\sim$0.2–2	$\sim10^{49}$–10^{52}	–	$3.6^{+1.4}_{-1.0}$
Binary	II	6	NS-NS	BH	$\sim$2–8	$\sim10^{52}$–10^{53}	$\gtrsim10^{52}$	$\left(1.9^{+1.8}_{-1.1}\right)\times10^{-3}$
Merger	III	(1)	NS-WD	MNS	$\sim$0.2–2	$\sim10^{49}$–10^{52}	–	$1.02^{+0.71}_{-0.46}$
(BM)	IV	(1)	WD-WD	NS/MWD	$<$0.2	$<10^{51}$	–	–
	V	(0)	NS-BH	BH	$\gtrsim$2	$>10^{52}$	–	$\approx0.77^{+0.09}_{-0.08}$

Table 1.1 Summary of the 9 GRB subclasses considered in the approach outlined in Sections 1.2.3 and 1.2.4 (extracted from [72]). The nature of the initial binary is indicated, as well as the resulting state after the GRB emission (either a new binary or a merged compact object) and the amount of claimed observations with known redshifts (numbers in parenthesis indicate lower limits). Rest-frame peak spectral energies ($E_{\rm p,i}$) are indicated together with the isotropic energies in the 1 keV-10 MeV ($E_{\rm iso}$) and $0.1-100$ GeV ($E_{\rm iso,GeV}$) bands. Estimated rates for each type of event are shown in the last column.

energetic GRBs (such that their isotropic emitted energy $E_{\rm iso}$ exceeds $\sim 10^{54}$ erg), which is why it has been proposed in [160] that energy is not emitted thermally, but following a modified blackbody spectrum with a different low-energy power index, for which a physical explanation has not yet been proposed. However, further ingredients have been added to this model in the last two years, including the modelling of the early flaring activity and the synchrotron emission produced both at the central engine and the ejected magnetized material (see Section 1.2.4 and [161, 162]).

In this alternative approach, GRBs are to this date divided into 9 subclasses on top of their standard long-short categorization, classified according to their spectral peak energies, $E_{\rm iso}$ values in different energy bands, and occurrence rates (see Table 1.1). These subclasses are thoroughly reviewed in [72, 163]. In agreement with general models of GRBs, short bursts are proposed to originate from binary mergers (BM), and are therefore classified into BM of types I–V[14]. The other four subclasses correspond to long bursts, and are subdivided into *binary driven hypernovae* (BdHNe) of types I–IV [72]. In particular, part of this thesis consists in the modelling of type I BdHNe, which we discuss in Section 1.2.4.

1.2.4 The BdHN model

The BdHN model has been proposed in the past years to explain the observed temporal coincidence of long GRBs and type Ic SN mentioned in Section 1.1.2 [164–168]. This model considers a tight binary system composed by a NS and a carbon-oxygen star that has lost its

[14]Type III BM, however, have hybrid properties between short and long GRBs; see, e.g., [72].

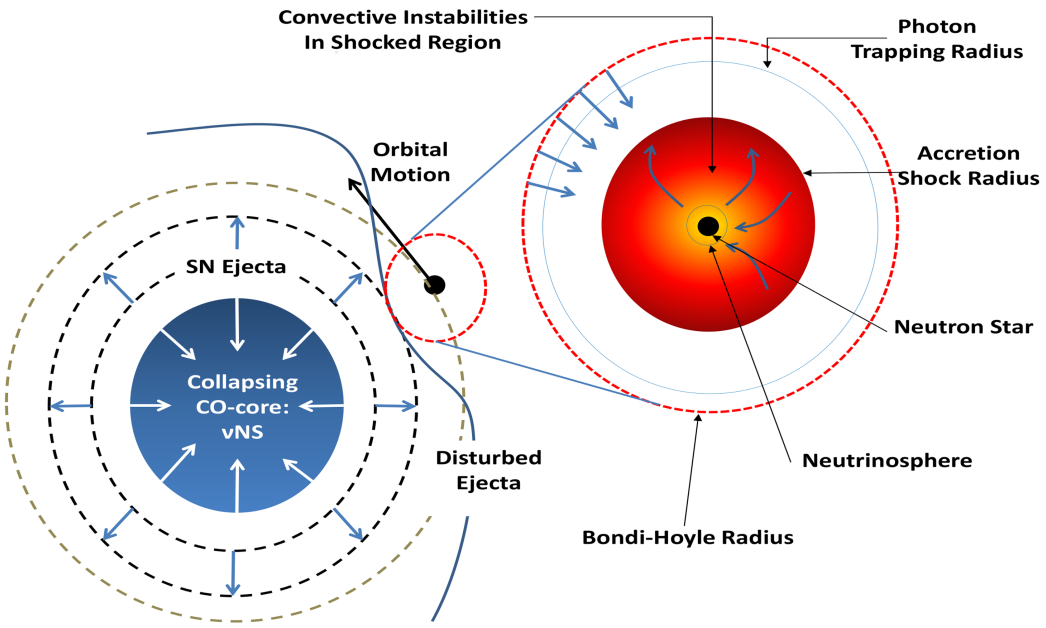

Fig. 1.8 Schematic picture of the IGC, extracted from [165]. The collapse of a CO_{core} produces a SN explosion that impacts the companion NS. Photons are trapped in the infalling flow, and temperatures are high enough to enable efficient neutrino emission close to the NS surface.

hydrogen and helium envelopes (CO_{core}), which explodes as a type Ic SN as portraited in Fig. 1.8. Part of the mass ejected during this explosion is directed towards the NS, which starts fastly accreting it at a high rate ($\dot{M} \gtrsim 10^{-3}\ M_\odot\ \mathrm{s}^{-1}$). If the binary system is tight enough (for orbital periods of a few minutes), this accretion process may become hypercritical. In this regime, the mass infall rates are so high that the emitted photons diffuse outward at a slower velocity than that of the accreting material, and are consequently trapped in the accreting flow. This causes the NS atmosphere to reach the high temperatures ($T \sim 10^{10}$ K) and densities ($\rho \gtrsim 10^6$ g cm^{-3}) required for neutrino-antineutrino cooling to become efficient. Consequently, the energy gained by the accreted material is mostly radiated via neutrino emission, and matter continues to fall onto the NS at a high rate without being stopped by photon pressure. If the NS reaches its critical mass, it can collapse into a BH, which gives this process the name of *induced gravitational collapse* (IGC). In particular, helium depletion plays a crucial role in this model, since carbon-oxygen stars lead to tight binaries and high opacities, which favors photon trapping [165]. It is argued in [165] that helium cores do not trigger enough hypercritical accretion onto the NS to produce its IGC, which explains in this model why GRBs are associated with SNe with totally absent or very little helium.

In general, there is a chance that the binary system may be disrupted due to the SN explosion, which depends on the mass loss and the kick imparted during the explosion (see,

e.g., [169]). If this is not the case, the IGC mechanism produces as a result a binary system composed by the collapsed BH and a newly formed NS (νNS) at the center of the SN. The BH rotates in the presence of the magnetic field of the νNS, which induces an electric field around it strong enough to efficiently create e^-e^+ pairs [72]. As outlined in Section 1.2.3, this process creates an e^-e^+ plasma around the BH, that expands isotropically and produces the emission of the different episodes seen in GRB light curves. The energy budget for the creation of such a plasma comes from the rotation of the BH, which consequently spins down until the induced electric field is insufficient for the creation of pairs. It has been hypothetized in the recent years that X-ray precursors can be explained by the emission of rising bubbles driven by the Rayleigh-Taylor instability during the initial phase of the accretion process [72, 165, 167], whereas a different explanation could be given by the emission produced at the SN shock breakout [72]. As well, it is proposed that the energy injection into the SN ejecta from the hypercritical accretion and the produced GRB tranforms the SN Ic into a more energetic broad-lined SN Ic or hypernova (see Section 1.1.2), which is observed in the optical band a few days after the GRB trigger [72, 170]. An additional energy release is proposed to occur due to the acceleration in the induced electric field of protons up to 10^{21} eV, which in turn produce synchrotron emission of GeV photons [168, 170]. Moreover, the synchrotron emission produced by relativistic electrons injected in the magnetized HN ejecta, and the νNS pulsar emission, are proposed to explain, respectively, the early and late X-ray afterglow [162].

Bursts produced in this way are characterized by an isotropic energy in the range $10^{52}-10^{54}$ erg and a rest-frame peak energy between 0.2 and 2 MeV, and are classified as type I BdHNe. On the other hand, if the system is not tight enough, the accretion onto the NS may be insufficient to induce its collapse to a BH. Such scenario produces bursts with a lower isotropic energy ($E_{\rm iso} \lesssim 10^{52}$ erg) and spectral peak energy ($E_p \lesssim 200$ keV), classified as a type II BdHNe (or X-ray flashes) if $E_{\rm iso}$ is in the range $10^{50} - 10^{52}$ erg, and as type III BdHNe if $E_{\rm iso} \lesssim 10^{50}$ erg [72]. Higher energies ($\gtrsim 10^{54}$ erg) are proposed to be reached when a similar process originates from $\mathrm{CO_{core}}$-BH binaries, in which case the BdHN is classified as type IV (see Table 1.1 and [72]).

During its evolution, the e^-e^+ plasma encounters different mass density profiles depending on the direction of expansion. This can be seen in Fig. 1.9, where the location of the BH and the νNS are shown on the equatorial plane of the binary system together with the mass distribution of the SN ejecta. In this scenario, the prompt emission occurs due to the ultrarelativistic expansion of the plasma in the lowest-density regions according to the fireshell model detailed in Section 1.2.3. On the other hand, the creation of shocks in the SN ejecta by its interaction with the plasma in higher-density regions, and the subsequent breakout of these shocks, are

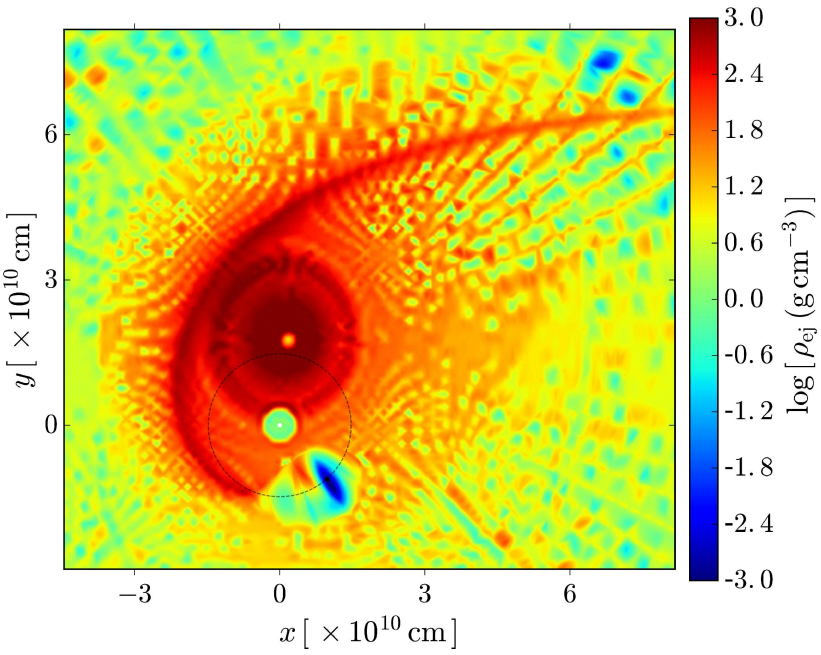

Fig. 1.9 Matter distribution of a BdHN in the equatorial plane of the binary system at the moment of the IGC of the NS, produced through N-body Newtonian simulations. The white and black circles indicate, respectively, the locations of the νNS and the newly born BH. Reproduced from [167].

proposed in this model to produce the early flaring activity observed in GRB afterglows (see Section 1.1.2). Additionally, the interaction of the e^-e^+ plasma with high-density regions of the SN ejecta can produce a reflected wave. Due to the baryon depletion caused by both the accretion process and the expansion of the plasma, a low-density optically thin region is created in the ejecta, which allows radiation to be emitted from the reflected wave towards a distant observer, producing a second burst following the main GRB emission. All of these processes are studied in this thesis by following a hydrodynamical approach. In particular, shock breakouts in high-density regions of the SN ejecta are also studied by means of radion hydrodynamics. We introduce both approaches in the next sections.

1.3 Hydrodynamics and radiative transfer

Fluid dynamics is one of the most powerful tools to understand astrophysical systems such as star and planet interiors, disks, winds, and even larger systems including the universe itself. Countless physical phenomena can be solved by following hydrodynamical and magnetohydrodynamical approaches, including flow instabilities, convection, and astrophysical dynamos. Even though high-energy phenomena such as accretion in BHs usually require the

consideration of general relativistic effects, some astrophysical phenomena involve relativistic flows far from strong gravitational fields. Some of those systems, as is the case for optically thick ejected flows in GRB models in far regions from the central engine, are well described by special relativistic hydrodynamics (RHD). Such is the approach followed in this thesis to explore the different episodes occurring in the BdHN model.

In most cases, the RHD equations must be solved numerically in order to produce realistic descriptions of astrophysical processes. The first numerical methods to solve the RHD equations were introduced by J. R. Wilson in the seventies [171–173]. The techniques implemented in this approach relied on explicit finite difference schemes, together with the introduction of artificial viscosity to handle shock waves. Although these methods became extremely popular at the time, they proved too inaccurate when describing relativistic flows with bulk Lorentz factors greater than ~ 2 [174]. Ever since, new techniques have been developed and larger and more accurate computations have been made possible, aided by the rapidly increasing technological advancements of the last decades and the possibility of running parallel simulations using thousands of processors. In the context of the BdHN model, the smoothed particle hydrodynamics (SPH) technique has been used by L. Becerra et al. [168] to perform an extensive study of the dynamical properties of the system and the conditions for the IGC to be possible. Although this technique is particularly well suited for some nonrelativistic problems such as SN explosions and star mergers (see, e.g., [175]), it is still in disadvantage with respect to other methods when describing shock waves, in particular when relativistic speeds are involved [176]. Nowadays, the most accurate option for the description of relativistic shocks, frequently involved in GRB emission models, is given by high-resolution shock capturing (HRSC) methods such as the Godunov-type[15] schemes described in Chapter 2 of this thesis. In particular, these methods are implemented in the open-source `PLUTO`[16] code, which has been used to produce the simulations presented in this work.

Maybe the most important condition required for the validity of any hydrodynamical approach is the the assumption of *local thermodynamic equilibrium* (LTE). This assumption consists in stating that the described system can be divided into a series of elementary volumes[17], in which all particles have equilibrium energy distributions at a common temperature. In many astrophysical scenarios, the most stringent condition for this to hold is given by the equilibrium between photons and material particles. Considering that the main exchange of

[15] This class of schemes is named after S. K. Godunov, who introduced them in [177].

[16] http://plutocode.ph.unito.it/

[17] Despite the definition of these volumes is rather ambiguous, it is enough to consider that they are large enough to contain a large number of particles and allow for a statistical kinetic description, and small enough to guarantee homogeneity in their interior [178].

internal energy between matter and radiation is dominated by absorption-emission processes [179], for LTE to be valid the absorption photon mean free path λ_a must be smaller than any characteristic length l in which the properties of the system change. Additionally, changes must be slow enough that these processes lead to thermal equilibrium in a much shorter time than any dynamical timescale of the system. If v is a typical mean velocity of the material, we can express such timescale $t_d \approx l/v$. Since the characteristic thermal equilibrium time is given by $t_a \approx \lambda_a/c$, the condition $t_a \ll t_d$ translates into $\lambda_a v/lc \ll 1$.

Despite the usefulness of the hydrodynamical approach to understand matter dynamics in astrophysical processes, the LTE assumption must be abandoned to explain the emission of EM radiation. Since radiative processes provide most of the information we have about the observable universe, their accurate description constitutes an important tool to do research in astrophysics, and is in particular one of the main goals of this thesis.

The problem of radiation transfer can be radically simplified if conditions are such that photons and matter particles are tightly coupled; for instance, in stellar interiors. In those cases, LTE can be assumed and radiation transport can often be treated as a diffusion problem (see Chapter 4). Contrarily, when densities are low enough that matter and radiation do not interact, they can be treated separately. The challenge arises when describing systems in which matter has a nonzero opacity but the condition $\lambda_a \ll l$ does not hold, and thus radiation–matter interaction occurs in nonequilibrium conditions. Such a situation is given in stellar atmospheres, where emitted photons constitute significant energy losses. Similarly, the assumption $\lambda_a/c \ll t_{\rm d}$ fails, for instance, in the vicinity of strong shocks, where the abrupt variation of the local properties of matter and radiation field produces regions in the shocked material that remain outside of equilibrium (see Chapter 4). As a consequence, the hydrodynamical approach fails to describe the dynamics of systems where radiation and matter are not in equilibrium. In particular, it is insufficient to describe several phenomena relevant for the understanding of GRB emission models, as is the case of the transition from optically thick to optically thin flows, and shock breakouts (see Chapters 3 and 5). Instead, such systems are most optimally described by methods that enable a description of matter and radiation separately, as well as their interaction. This caveat motivated the development of a radiative transfer module integrated in the `PLUTO` code, which constituted the main part of this work.

We overview in the next section different methods for radiative transfer commonly followed in the literature, and focus on the main features of the approach followed in this thesis.

1.4 Our approach to radiative transfer

Most modern treatments of the problem of radiation–matter interaction in astrophysics are based on different solutions of the *radiative transfer equation* (see, e.g., [179–194] and Chapter 4). In this approach, photons are treated as point-like wave packets that can be instantly emitted or absorbed. As detailed in [195], this rules out several effecs due to the wavelike nature of light, which we now summarize. Firstly, for this particle treatment to be valid, it is necessary that the spread of the wave packet, in both space and momentum, is small compared to any resolution of interest. Hence, the minimum possible resolution that can be described through this approach is determined by Heisenberg's uncertainty principle. Secondly, this treatment involves radiative intensities instead of wave amplitudes, and consequently it cannot describe any interference of photons among themselves. Thus, a different approach must be followed if the number density of photons is high enough that the overlap between their wavefunctions is not negligible[18]. However, this density cannot be arbitrarily small, since it must still be high enough to allow for a statistical treatment. Similarly, interference produced from waves arising from different scattering centers which scatter the same photon are is also neglected, and thus diffraction and reflection are also not contemplated. Refraction and dispersion are also not reproduced, since they also arise due to the wavelike nature of light. In addition, polarization of light is also neglected, and the computed intensity can be understood as an average of all polarization states. Finally, since it is assumed that the emission, absorption and scattering of photons are instantaneous, the timescales of these processes must be shorter than any described timescale.

In general, solving the frequency-dependent radiative transfer equation is a rather challenging task, since doing so requires an integration on many variables and a self-consistent simultaneous determination of the states of both matter and radiation fields, which is often only achievable in simplified cases. For this reason, several simplified schemes can be found in the literature. Typical examples are the post-processing of ideal hydrodynamical calculations, sometimes used in cases where radiation back-reaction can be neglected (see, e.g., [196]), and Monte Carlo methods [180, 181], where radiation densities and fluxes are computed by following the evolution of a large number of effective 'photon packets' along selected trajectories. In some particular cases, when dealing with optically thin environments which present some photon emission mechanism, it is also possible to account for radiative losses by simply adding cooling terms to the equations of fluid dynamics (see, e.g., [182]). A different approach is given by *discrete ordinate* methods, in which both the spatial domain and the photon propagation direction are discretized [183–186].

[18] This restriction can be relaxed, however, considering that photons with sufficiently different frequencies do not interfere even if they coincide spatially.

A generally faster alternative to these methods, followed in this thesis, is given by the moment approach to the radiative transfer equation. This consists in taking succesive angular moments of this equation, in the same fashion as the hydrodynamics (HD) and magneto-hydrodynamics (MHD) can be obtained from the collisional Boltzmann-Vlasov equation [197]. The resulting scheme provides an extension to relativistic and nonrelativistic MHD that can be used to compute the evolution of the total radiation energy density and flux while considering their interaction with a material fluid. In this work we focus on the relativistic case, to which we refer as relativistic radiation MHD (Rad-RMHD henceforth). The model involves a series of additional approximations:

1. We replace the opacity coefficients for a set of conveniently chosen frequency-averaged values, thus neglecting any physical effect caused by the frequency dependence of these coefficients. Consequently, our framework cannot be used to compute observables such as emission spectra, and instead can be used to describe dynamical processes depending on the total transport of energy and momentum of both matter and radiation. A similar approach that partially overcomes this limitation is given by multigroup methods, where the equations are solved in a set of selected frequency bands where opacities are averaged [198].

2. We consider the fluid to be a perfect conductor, and assume the validity of the equations of ideal relativistic MHD (RMHD) for the interaction between matter and EM fields.

3. As firstly done in [199], we close the system of equations by assuming that photons are transported isotropically in a certain reference frame. The assumption of the existence of such reference frame is generally known as M1 closure. As opposed to the Eddington approximation, which consists in assuming that the radiation field is isotropic in a chosen reference frame (typically the fluid's comoving frame; see e.g. [200]), this choice enables the description of systems in which photon transport has strong directional variations. In particular, it describes both the *free-streaming limit*, where photons are freely transported in a single direction without interacting with matter, and the *diffusion limit*, where the radiation flux is largely affected by radiation–matter interaction and the main transport mechanism is diffusion.

Our implementation of these methods in `PLUTO` makes use of several of the code's built-in capabilities. The new module is fully parallel, has been adapted to all available geometries (Cartesian, cylindrical and spherical) and supports calculations on adaptively refined grids

using the PLUTO-CHOMBO framework [201, 202]. This allows the code to capture and resolve localized features that evolve on a much shorter scale when compared to the rest of the computational domain, at a relatively low computational cost. In addition, we have introduced in this model a new Riemann solver suitable for optically thin radiation transport, based on the HLLC solver for RHD in [203] and designed to improve the code's ability to resolve contact discontinuities when compared to other schemes.

To integrate the transport terms of the equations of Rad-RMHD, our implementation employs the same sort of explicit methods used in PLUTO for the nonradiative case. However, gas-radiation interaction is treated differently, since this process may occur in times that are much shorter than the dynamical times; for instance, when matter is highly opaque. Hence, a direct explicit integration of the interaction terms would lead to prohibitively small time steps and inefficient calculations. For this reason, our method of choice relies on Implicit-Explicit (IMEX) Runge-Kutta methods [204] whereby spatial gradients are treated explicitly while point-local interaction terms are integrated via an implicit scheme. Such methods, commonly used to solve systems of differential equations with stiff source terms, have a significant effect on stability and make it possible to integrate the interaction terms without having to take extremely small time steps.

Similar approaches in the context of radiation HD and MHD have been followed in [187–194]. While some of the codes presented in these works use the Eddington approximation, others do not take into account relativistic corrections, and most of them are designed to work only in Cartesian coordinates. Apart from the increased accuracy of the new Riemann solver, the presented module counts with the comparative advantage of supporting adaptive mesh refinement (AMR), which is not included in most schemes for radiative transfer (in particular, in the mentioned references, it is only included in [188]).

1.5 Structure of this thesis

Chapter 2 is dedicated to a brief introductory review of the assumptions behind the RHD and RMHD equations, as well as a comprehensive description the methods followed to solve them.

In Chapter 3, we show the results of a series of RHD simulations of different episodes contemplated by the BdHN scenario. In Section 3.1, the acceleration stages of the fireshell are modelled through 1D RHD simulations and compared with results obtained following the constant-width approach described in Section 1.2.3. In Section 3.2 we study the expansion of shocks created by the e^-e^+ plasma in high-density regions of the SN ejecta and their subsequent breakout, in the context of a model for X-ray flares proposed in this scenario. The

dynamics of this process is again described through 1D RHD simulations, and estimates for the breakout velocity for different baryon loads are obtained and compared with estimates made for GRB 081008. A time and energy fit within this approach is made for GRB 160625B, and the plausibility and predictive power of the model are discussed. In Section 3.3, we study the possibility of explaining a particular peak in the light curve of GRB 190114C through a model for reflected waves created in the SN ejecta. A simplified analytical model is made for the interaction of the $e^{-}e^{+}$ and the SN material, and 2D RHD simulations of this phenomenon are shown. Estimates are given for the spectral properties of the observed radiation, and the predictive power of the model is discussed. In Section 3.4, we summarize the chapter's conclusions.

Chapter 4 is entirely devoted to the derivation and implementation of the numerical methods included in the Rad-RMHD module. An extensive discussion of the assumptions of our approach is made in Section 4.1, and the Rad-RMHD equations are derived. The employed numerical schemes are detailed in Section 4.2, while in Section 4.3 the code's performance is shown on several selected numerical benchmarks. Finally, Section 4.4 contains the chapter's conclusions.

In Chapter 5, we overview a few current and future applications of the Rad-RMHD module. In Section 5.1, we show preliminary results of an ongoing application to the model for X-ray flares studied in Section 3.2. We discuss these results in Section 5.2, and conclude by outlining further prospective developments.

Supplementary details and derivations not included in these chapters are shown in Appendices A–D.

1.6 List of publications

Published articles

- **J. D. Melon Fuksman** and A. Mignone, *A radiative transfer module for relativistic magnetohydrodynamics in the PLUTO code*. ApJS, 242:20 (2019). Chapter 4.

- R. Ruffini, L. Becerra, C. L. Bianco, Y. C. Chen, M. Karlica, M. Kovačević, **J. D. Melon Fuksman**, R. Moradi, M. Muccino, G. B. Pisani, D. Primorac, J. A. Rueda, G. V. Vereshchagin, Y. Wang, and S.-S. Xue, *On the Ultra-relativistic Prompt Emission, the Hard and Soft X-Ray Flares, and the Extended Thermal Emission in GRB 151027A*, ApJ, 869:151 (2018). Chapter 3

- R. Ruffini, Y. Wang, Y. Aimuratov, U. Barres de Almeida, L. Becerra, C. L. Bianco, Y. C. Chen, M. Karlica, M. Kovačević, L. Li, **J. D. Melon Fuksman**, R. Moradi, M. Muccino, A. V. Penacchioni, G. B. Pisani, D. Primorac, J. A. Rueda, S. Shakeri, G. V. Vereshchagin, and S.-S. Xue., *Early X-Ray Flares in GRBs*. ApJ, 852:53 (2018). Chapter 3.

- J. A. Rueda, Y. Aimuratov, U. Barres de Almeida, L. Becerra, C. L. Bianco, C. Cherubini, S. Filippi, M. Karlica, M. Kovacevic, **J. D. Melon Fuksman**, R. Moradi, M. Muccino, A. V. Penacchioni, G. B. Pisani, D. Primorac, R. Ruffini, N. Sahakyan, S. Shakeri and Y. Wang, *The binary systems associated with short and long gamma-ray bursts and their detectability*. International Journal of Modern Physics D, 26, 9, 1730016 (2017). Chapter 1.

Submitted articles

- R. Ruffini, **J. D. Melon Fuksman** and G. V. Vereshchagin, *On the role of a cavity in the hypernova ejecta of GRB 190114C*. Submitted to ApJ (2019), accepted. Preprint: https://arxiv.org/abs/1904.03163. Chapter 3.

- R. Ruffini, Liang Li, R. Moradi, J. A. Rueda, Yu Wang, S.-S. Xue, C. L. Bianco, S. Campion, **J. D. Melon Fuksman**, C. Cherubini, S. Filippi, M. Karlica, N. Sahakyan, *Self-similarity and power-laws in GRB 190114C*. Submitted to ApJ (2019). Preprint: https://arxiv.org/abs/1904.04162. Chapter 1.

- R. Ruffini, J. A. Rueda, R. Moradi, Y. Wang, S. S. Xue, L. Becerra, C. L. Bianco, Y. C. Chen, C. Cherubini, S. Filippi, M. Karlica, **J. D. Melon Fuksman**, D. Primorac, N. Sahakyan, G. V. Vereshchagin *The inner engine of GeV-radiation–emitting gamma-ray bursts*. Submitted to ApJ (2018). Preprint: https://arxiv.org/abs/1811.01839. Chapter 1.

Proceedings

- **J. D. Melon Fuksman**, L. Becerra, C. L. Bianco, M. Karlica, M. Kovačević, R. Moradi, M. Muccino, G. B. Pisani, D. Primorac, J. A. Rueda, R. Ruffini, G. V. Vereshchagin, and Y. Wang., *Evolution of an electron-positron plasma produced by induced gravitational collapse in binary-driven hypernovae*. In European Physical Journal Web of Conferences, 168, 04009 (2018). Chapter 3.

Chapter 2

Relativistic hydrodynamics and magnetohydrodynamics

This chapter has the twofold goal of presenting the numerical approach followed throughout Chapter 3 in the context of the BdHN model, and setting the ground for the methods implemented in Chapters 4 and 5 to solve the Rad-RMHD equations. After briefly discussing the main assumptions of both RHD and RMHD, we give an introduction to linear and nonlinear hyperbolic systems, paying particular attention to the solutions of discontinuous initial value problems. We then show how Godunov-type solvers can be constructed by making use of the knowledge of the behavior of such solutions, focusing on the way these methods are implemented in the `PLUTO` code.

2.1 Fluid dynamics

2.1.1 Relativistic hydrodynamics

As mentioned in the Introduction, the equations of RHD can be obtained by computing the first three moments of the collisional Boltzmann equation, in a similar way as the equations of Rad-RMHD can be derived from the radiative transfer equation (see Chapter 4). As in the radiative transfer treatment, the fluid description requires that the number density of particles is high enough to guarantee that the typical separation between them is much smaller than any relevant lengthscale (see, e.g., [178]). If this is true, the system can then be divided in a set of volume elements where local quantities are defined as volume averages. These elements must be both large enough to contain a high number of particles and small enough to guarantee homogeneity within them. In this context, we assume that the particles contained in each elementary volume are in thermal equilibrium in the *comoving frame*, i.e., a local reference

frame in which their average velocity is zero. The assumption of LTE thus defined holds as long as the mean free path of each particle species is smaller than all of the system's relevant lengthscales, provided that the system evolves in longer times than all thermal equilibrium timescales. This allows one to neglect the viscosity and thermal conduction terms that otherwise arise from the kinetic equations; i.e., we consider ideal hydrodynamics.

The aforementioned assumptions make it possible to describe a system of many particles as a single fluid, whose state is completely determined by a set of locally defined fields. In particular, in this work we follow the Eulerian description, in which the equations of motion are written in a chosen inertial reference frame to which we refer as *Eulerian* or *laboratory* frame. In this frame, we write the components of the total energy-momentum-stress tensor as

$$T^{\mu\nu} = \rho h u^{\mu} u^{\nu} + p_g \eta^{\mu\nu}, \tag{2.1}$$

where u^{μ} is the fluid's four-velocity and $\eta^{\mu\nu}$ is the Minkowski tensor (we use the $(-,+,+,+)$ sign convention), while ρ, h and p_g are, respectively, the fluid's matter density, specific entalphy, and pressure, measured in the comoving frame (our units are chosen so that $c = 1$). In this way, the conservation of energy and momentum in the system can be summarized as

$$\nabla_{\mu} T^{\mu\nu} = 0\,, \tag{2.2}$$

where the symbol ∇_{μ} denotes covariant derivation. Similarly, mass conservation reads

$$\nabla_{\mu} \left(\rho u^{\mu}\right) = 0\,. \tag{2.3}$$

Although this equation holds in general under the condition that particles are not created nor annihilated, it can still be considered if the mass variation caused by such processes is much smaller than the total mass. Writing Eqs. (2.2) and (2.3) using the explicit form of $T^{\mu\nu}$, we obtain the equations of RHD in the following form[1]:

$$\frac{\partial \left(\rho\gamma\right)}{\partial t} + \nabla \cdot \left(\rho\gamma \mathbf{v}\right) = 0 \tag{2.4}$$

$$\frac{\partial \mathcal{E}}{\partial t} + \nabla \cdot \left(\mathbf{m} - \rho\gamma \mathbf{v}\right) = 0 \tag{2.5}$$

$$\frac{\partial \mathbf{m}}{\partial t} + \nabla \cdot \left(\rho h \gamma^2 \mathbf{v}\mathbf{v}\right) + \nabla p_g = \mathbf{0}\,, \tag{2.6}$$

[1]This form of Eq. (2.5) is obtained by subtracting Eq. (2.3) to Eq. (2.2)

where $\gamma = 1/\sqrt{1-\mathbf{v}^2}$ is the Lorentz factor, $\mathbf{v}$ is the fluid's coordinate velocity, and $\mathbf{vv}$ denotes the outer product of $\mathbf{v}$ with itself. As well, we have here defined the fields

$$\mathbf{m} = \rho h \gamma^2 \mathbf{v} \tag{2.7}$$

and

$$\mathcal{E} = \rho h \gamma^2 - p_g - \rho\gamma\,, \tag{2.8}$$

which correspond, respectively, to the momentum and energy densities in the laboratory frame. The first of these is simply T^{0i}, whereas the second one results from subtracting $\rho\gamma$ to T^{00}. In this way, the comoving value of $\mathcal{E}$ corresponds to the fluid's internal energy in the comoving frame.

In order to completely define the system of Equations (2.4)–(2.6), it is necessary to include an additional set of relations between the considered fields. This can be achieved by imposing an *equation of state* (EoS) that relates the defined comoving thermodynamical quantities according to the microphysics of the considered fluid. In this work we consider two possible EoSs, which are the constant-Γ law

$$h = 1 + \frac{\Gamma}{\Gamma - 1}\,\Theta, \tag{2.9}$$

and the Taub-Mathews equation, introduced in [205],

$$h = \frac{5}{2}\Theta + \sqrt{1 + \frac{9}{4}\,\Theta^2}, \tag{2.10}$$

where $\Theta = p_g/\rho$. The Γ index in equation (2.9) can take values between $4/3$ and $5/3$, where these limits correspond respectively to a relativistic and a nonrelativistic gas. Equation (2.10) approximates within $\lesssim 4\%$ the equation of state of a single-species relativistic perfect gas, and so describes both limits: it coincides with equation (2.9) with $\Gamma = 4/3$ for $p_g \gg \rho$, and with $\Gamma = 5/3$ whenever $p_g \ll \rho$, while respecting the physical constraint $(\rho h - p_g)(\rho h - 4p_g) \geq 1$ (see [206]).

2.1.2 Relativistic magnetohydrodynamics

The equations of ideal RMHD, considered in Chapter 4, can be derived in a similar way by making a few additional conditions to those of RHD (see e.g. [207]). Firstly, we consider that the fluid is *quasineutral*, which means that the net charge averaged over each elementary volume is zero. Typically, this can be assumed as long as EM fields vary in timescales that are much longer than both $1/\omega_{pe}$ and $1/\omega_{ce}$, where ω_{pe} and ω_{ce} are, respectively, the electron

plasma frequency and synchroton frequency. Furthermore, relevant lengthscales must exceed simultaneously the length scales given by c/ω_{pe}, the electron Larmor radius, and the Debye length. In addition, we assume that typical dimensions are much larger than an ion gyro radius, and large enough to neglect resistive diffusion despite the high collisionality. If these conditions are fulfilled, we can safely assume that the electric field in the comoving frame is null, which yields the ideal nonresistive Ohm's law given by

$$\mathbf{E} + \mathbf{v} \times \mathbf{B} = \mathbf{0}\,, \tag{2.11}$$

where $\mathbf{E}$ and $\mathbf{B}$ are, respectively, the electric and magnetic fields. In this case, the total energy-momentum-stress tensor $T^{\mu\nu}$ includes the EM contribution as

$$T^{\mu\nu} = T^{\mu\nu}_g + T^{\mu\nu}_{em}\,, \tag{2.12}$$

where the components of $T^{\mu\nu}_g$ are defined in Eq. (2.1), while the EM part is defined as

$$T^{\mu\nu}_{em} = F^{\mu\alpha}F^{\nu}_{\alpha} - \frac{1}{4}\eta^{\mu\nu}F_{\alpha\beta}F^{\alpha\beta}\,. \tag{2.13}$$

We have here introduced the EM tensor $F^{\mu\nu}$, whose components are given by

$$F^{\mu\nu} = \begin{pmatrix} 0 & -E_1 & -E_2 & -E_3 \\ E_1 & 0 & -B_3 & B_2 \\ E_2 & B_3 & 0 & -B_1 \\ E_3 & -B_2 & B_1 & 0 \end{pmatrix}\,. \tag{2.14}$$

The components of $F^{\mu\nu}$ evolve according to Maxwell's equations, which can be written in covariant form as

$$\begin{aligned} \nabla_\mu \left(\epsilon^{\alpha\beta\mu\nu}F_{\mu\nu}\right) &= 0 \\ \nabla_\mu F^{\mu\nu} &= \mathcal{J}^\nu\,, \end{aligned} \tag{2.15}$$

where $\epsilon^{\alpha\beta\mu\nu}$ is the Levi-Civita symbol and $\mathcal{J}^\nu$ is the four-current.

Combining Equations (2.2), (2.3), and (2.15) using the expression for $T^{\mu\nu}$ given in Eq. (2.12), we obtain the RMHD equations:

$$\frac{\partial\left(\rho\gamma\right)}{\partial t}+\nabla\cdot\left(\rho\gamma\mathbf{v}\right)=0 \tag{2.16}$$

$$\frac{\partial\mathcal{E}}{\partial t}+\nabla\cdot\left(\mathbf{m}-\rho\gamma\mathbf{v}\right)=0 \tag{2.17}$$

$$\frac{\partial\mathbf{m}}{\partial t}+\nabla\cdot\left(\rho h\gamma^{2}\mathbf{v}\mathbf{v}-\mathbf{B}\mathbf{B}-\mathbf{E}\mathbf{E}\right)+\nabla p=\mathbf{0} \tag{2.18}$$

$$\frac{\partial\mathbf{B}}{\partial t}+\nabla\times\mathbf{E}=\mathbf{0}\,, \tag{2.19}$$

where we have introduced the quantities

$$p=p_{g}+\frac{\mathbf{E}^{2}+\mathbf{B}^{2}}{2}, \tag{2.20}$$

$$\mathbf{m}=\rho h\gamma^{2}\mathbf{v}+\mathbf{E}\times\mathbf{B}, \tag{2.21}$$

$$\mathcal{E}=\rho h\gamma^{2}-p_{g}-\rho\gamma+\frac{\mathbf{E}^{2}+\mathbf{B}^{2}}{2}, \tag{2.22}$$

which account, respectively, for the total pressure, momentum density, and energy density of matter and EM fields. In addition, the magnetic field must satisfy Gauss's law, given by

$$\nabla\cdot\mathbf{B}=0\,. \tag{2.23}$$

This system can be closed assuming an EoS like Eqs. (2.9) and (2.10) for the fluid fields, and using Eq. (2.11) to compute $\mathbf{E}$ in terms of $\mathbf{v}$ and $\mathbf{B}$. Due to the constraint given by Eq. (2.11), the first of Equations (2.15) is enough to obtain Eqs. (2.16)–(2.19) and (2.23), whereas the second one becomes irrelevant for the dynamics, and can be used solely to compute the value of $\mathcal{J}^{\mu}$. Finally, the nonmagnetic case is recovered by taking the limit $\mathbf{B}\to\mathbf{0}$ in the previous expressions, which yields the RHD equations.

2.2 Hyperbolic systems of partial differential equations

Both the equations of RHD and RMHD belong to a general class of systems of partial differential equations called *hyperbolic systems*. Systems of this type share well-known properties, that can be used to construct accurate numerical solutions of general initial value problems. In this section we review some of these properties, which will provide a theoretical

basis for the numerical methods implemented in this work. The definitions and results explained in this section follow mainly the book by Toro [208].

2.2.1 Linear and nonlinear systems

From Eqs. (2.4)–(2.6) and (2.16)–(2.6), we can see that both the RHD and RMHD equations can be cast as a conservation law of the form

$$\frac{\partial \mathcal{U}}{\partial t} + \nabla \cdot \mathsf{F}(\mathcal{U}) = 0 \tag{2.24}$$

where $\mathcal{U}$ is an array of *conserved fields*, while $\mathsf{F}(\mathcal{U})$ is a flux tensor. Applying the chain rule to the second term, this system of equations can be rewritten in cartesian coordinates as

$$\frac{\partial \mathcal{U}}{\partial t} + \sum_d J_d \frac{\partial \mathcal{U}}{\partial x^d} = 0\,, \tag{2.25}$$

where we have defined the Jacobian matrices of the system for each direction d as

$$J_d = \frac{\partial \mathsf{F}_d}{\partial \mathcal{U}} \equiv \begin{pmatrix} \partial \mathsf{F}^1_d/\partial \mathcal{U}^1 & \dots & \partial \mathsf{F}^1_d/\partial \mathcal{U}^n \\ \vdots & \ddots & \vdots \\ \partial \mathsf{F}^n_d/\partial \mathcal{U}^1 & \dots & \partial \mathsf{F}^n_d/\partial \mathcal{U}^n \end{pmatrix}\,, \tag{2.26}$$

while $\mathsf{F}_d = \mathsf{F} \cdot \hat{\boldsymbol{e}}_d$ are the flux components in the coordinate direction $\hat{\boldsymbol{e}}_d$. Equation (2.25) has the form of a homogeneous system of *quasi-linear* partial differential equations, which means that the matrices J_d depend in general on $\mathcal{U}$ (the system of equations is called linear otherwise, e.g., if J_d is a constant matrix). Such a system is said to be *hyperbolic* at a point $(t, \mathbf{x})$ if the matrices $J_d \in \mathbb{R}^{n\times n}$ have each n real eigenvalues $\lambda_1, \dots, \lambda_n$, and a corresponding set of n linearly independent right eigenvectors $\mathcal{K}^{(1)}, \dots, \mathcal{K}^{(n)}$ (such that $J_d\, \mathcal{K}^{(i)} = \lambda_i \mathcal{K}^{(i)}$, see [208]).

Some properties of this kind of systems can be intuitively illustrated by considering a one-dimensional linear hyperbolic system like the following:

$$\frac{\partial \mathcal{U}}{\partial t} + \mathcal{A}\, \frac{\partial \mathcal{U}}{\partial x} = 0\,, \tag{2.27}$$

where $\mathcal{A} \in \mathbb{R}^{n\times n}$ is a matrix of constant coefficients. The solution to the initial value problem given by this equation and the initial condition $\mathcal{U}(x, 0) = \mathcal{U}^{(0)}(x)$ can be written in terms of

the eigenvalues and eigenvectors of $\mathcal{A}$, as

$$\mathcal{U}(x,t) = \sum_{i=1}^{n} w_i^{(0)}(x - \lambda_i t)\, \mathcal{K}^{(i)} \,. \tag{2.28}$$

The functions $w_i^{(0)}(x)$ can be determined from the initial condition by inverting the relation

$$\mathcal{U}^{(0)}(x) = \sum_{i=1}^{n} w_i^{(0)}(x)\, \mathcal{K}^{(i)} \,, \tag{2.29}$$

which is always achievable due to the linear independence of $\left\{\mathcal{K}^{(i)}\right\}$. Therefore, the solution of any such initial value problem can be expressed as a sum of n independent waves, each of which move with constant speed λ_i (the eigenvalues λ_i are therefore called the *characteristic speeds* of the system). If, instead, the matrix $\mathcal{A}$ depends on $\mathcal{U}$, each mode $\mathcal{K}^{(i)}$ is in principle different for each point of space, and in particular, evolves with a different wave speed. To see the consequences that this can carry, let us consider an example where $n = 1$, in which the only eigenvalue λ satisfies $\lambda'(\mathcal{U}) > 0$. This condition means that higher values of $\mathcal{U}$ travel faster than lower values of $\mathcal{U}$, which creates expansive regions (corresponding to $\partial_x \lambda > 0$ for rightward-moving waves) and compressive regions ($\partial_x \lambda < 0$ for rightward-moving waves). In the considered example, compressive regions tend to steepen until eventually $\partial_x \mathcal{U}$ diverges, and a discontinuity is created within finite time. Wave steepening and shock development are distinctive features of nonlinear systems, which can be observed in nature in a vast number of physical scenarios (see, e.g., [209]).

2.2.2 The Riemann problem

Let us now consider a system like (2.27), with the following initial condition:

$$\mathcal{U}^{(0)}(x) = \begin{cases} \mathcal{U}_L & \text{if } x < 0 \\ \mathcal{U}_R & \text{if } x > 0 \end{cases} \,, \tag{2.30}$$

where $\mathcal{U}_L$ and $\mathcal{U}_R$ are two constant states. The solutions of this initial value problem, generally known as the *Riemann problem*, provides useful insights to understand the behavior of nonlinear systems, and as we shall see later, can be used to construct numerical schemes to solve them.

As shown in Section 2.2.1, we can solve this system by writing $\mathcal{U}^{(0)}(x)$ in terms of the eigenvectors of $\mathcal{A}$ (see Eq. (2.29)). We thus obtain that the resulting $w_i^{(0)}$ functions are of the

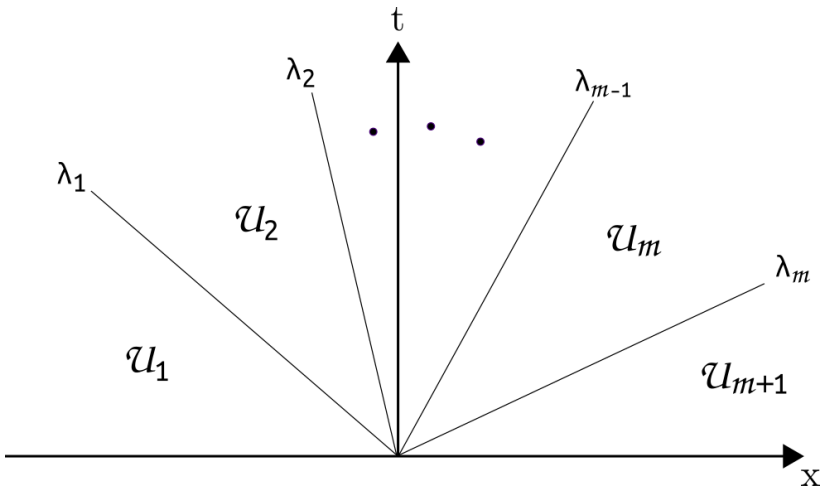

Fig. 2.1 Structure of the solution of the 1D linear Riemann problem for m different eigenvalues λ_i. The curves $x = \lambda_i t$ separate $m+1$ regions where $\mathcal{U}$ takes a constant value $\mathcal{U}_i$. Intermediate waves are represented with dots.

form

$$w_i^{(0)}(x) = \begin{cases} \alpha_i & \text{if } x < 0 \\ \beta_i & \text{if } x > 0 \end{cases} , \tag{2.31}$$

with $\alpha_i\,, \beta_i \in \mathbb{R}$. Consequently, the coefficients $w_i^{(0)}$ in the full solution of the Riemann problem (Eq. (2.28)) satisfy

$$w_i^{(0)}(x - \lambda_i) = \begin{cases} \alpha_i & \text{if } x - \lambda_i t < 0 \\ \beta_i & \text{if } x - \lambda_i t > 0 \end{cases} . \tag{2.32}$$

This expression states that, for each t and λ_i, the solution changes from one constant value to another in the boundary given by $x = \lambda_i t$. Consequently, if $\mathcal{A}$ has m different eigenvalues, the spatial domain is divided into $m + 1$ zones for each t, such that in each of them $\mathcal{U}(x, t)$ takes a constant value. Hence, the solution consists of m discontinuous waves (also called *jump discontinuities*), each of which propagate at a speed given by λ_i. The general structure of one such solution can be conveniently represented in the (x, t) plane by plotting the curves $x = \lambda_i t$, which separate the $m + 1$ regions of constant $\mathcal{U}(x, t)$. From this analysis, we can see that these solutions satisfy the property of *self-similarity*, as they depend solely on the ratio x/t. This is a direct consequence of the fact that both Eq. (2.27) and the initial condition in Eq. (2.30) are scale-invariant, i.e., they are invariant under the transformation $(x, t) \to (\alpha x, \alpha t)$ with $\alpha > 0$. Therefore, any solution of this problem should also satisfy this property, from which $\mathcal{U}(x, t) = \mathcal{U}(\alpha x, \alpha t)$, and hence $\mathcal{U}(x, t)$ can only be a function of x/t.

Let us now consider the nonlinear Riemann problem given by Eq. (2.24) with the initial condition in Eq. (2.30). This problem is also scale invariant, and therefore we should again expect to have self-similar solutions. Moreover, the general solution to the nonlinear problem shows again a pattern of m waves, each corresponding to a different eigenvalue, that divide $m+1$ constant states. The nature of these waves depends essentially on the behavior of the different functions $\lambda_i(\mathcal{U})$, and can be studied in terms of the so-called *characteristic curves* defined as the solutions of the equations $dx/dt = \lambda_i$. In short, these curves represent the direction in the (x,t) plane in which the data of a given mode is being transported from each point (x_0, t_0). This can be seen by considering the linearized problem defined in Eq. (2.25) approximating J_d as constant for small variations of $\mathcal{U}$, in which case the solution given by Eq. (2.28) holds locally.

The waves in the nonlinear Riemann problem can be thus classified into three main categories, depending on whether characteristic curves originated on different sides of the initial discontinuity converge, diverge, or are parallel when compared from side to side. If for a given mode i they converge, a compressive *shock wave* of speed S_i is formed, verifying

$$\lambda_i(\mathcal{U}_R) < S_i < \lambda_i(\mathcal{U}_L)\,, \tag{2.33}$$

where the subindices L and R denote each side of the discontinuity. Instead, if the characteristic curves at different sides of $x = 0$ diverge, i.e., if

$$\lambda_i(\mathcal{U}_R) > \lambda_i(\mathcal{U}_L)\,, \tag{2.34}$$

a *rarefaction wave* is formed. This kind of wave is characterized by a region of smooth transition between the L and R states, where characteristic curves diverge from each other. The third category is given by those jump discontinuities whose speed S_i verifies

$$S_i = \lambda_i(\mathcal{U}_L) = \lambda_i(\mathcal{U}_R)\,; \tag{2.35}$$

i.e., characteristic curves of both sides are parallel among each other. We shall refer to this category as *noncompressive* waves.[2]

The pattern followed by the solution of a given Riemann problem, also called *Riemann fan*, depends both on the initial condition and the functional form of $\mathsf{F}(\mathcal{U})$ (see Eq. (2.24)). For the RHD equations (see, e.g., [210]), each solution consists of a three-wave pattern, with two external waves that can be either shocks or rarefactions, and a middle noncompressive wave

[2] In the literature, these are usually called *contact waves*. However, that term is oftentimes applied to discontinuities in HD across which the pressure and normal velocity are continuous. To avoid confusion, we have chosen to give them a different name.

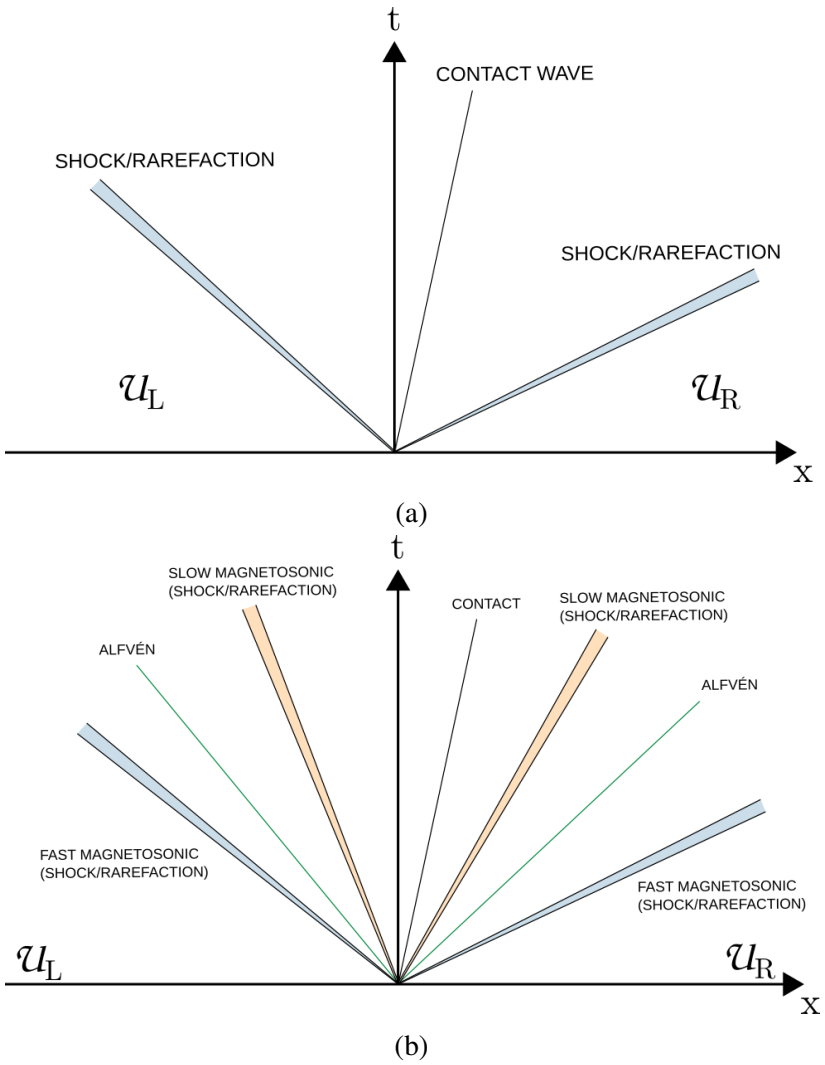

Fig. 2.2 Wave structure of the 1D Riemann problem for RHD (a) and RMHD (b).

moving at the fluid's velocity, across which the pressure and normal velocity are continuous (see Fig. 2.2a). The latter receives the name of *contact discontinuity*. On the other hand, in the Riemann problem for RMHD, up to seven waves can be formed (see Fig. 2.2b). These are two fast and two slow magnetosonic waves (either shocks or rarefactions), two so-called *rotational discontinuities* corresponding to Alfvén modes (noncompressive), and a middle contact wave, across which this time p_g, $\mathbf{v}$, and $\mathbf{B}$ are continuous (see [211]).

So far we see that the solutions of the Riemann problem exhibit a regular, predictable behavior despite the nonlinearity of the equations, which makes it an ideal benchmark to test numerical methods. In the next section we shall see how this regularity can also be used to construct approximate solutions (or *Riemann solvers*) that can be applied locally in cell boundaries to solve systems like Eq. (2.24) with arbitrary initial conditions. These

approximate solutions consist in replacing each of the above-mentioned waves with a jump discontinuity that moves at some guessed speed. Across each of these waves, a set of *jump conditions* relating the states left and right from the shock must be imposed for consistency. For any discontinuity that moves at a speed S, we can obtain a set of such relations by integrating Eq. (2.24) in an infinitesimal volume that includes the shock boundary. This yields the *Rankine-Hugoniot* jump conditions:

$$S\left[\mathcal{U}_R - \mathcal{U}_L\right] = \mathsf{F}(\mathcal{U}_R) - \mathsf{F}(\mathcal{U}_L)\,, \tag{2.36}$$

where again L and R denote each side of the shock. Additional conditions can be obtained from the particular form of the eigenvectors of J_d. For a noncompressive wave associated to the eigenvalue λ_i, for instance, it can be proven that

$$\frac{d\mathcal{U}_1}{\mathcal{K}_1^{(i)}} = \cdots = \frac{d\mathcal{U}_n}{\mathcal{K}_n^{(i)}}\,, \tag{2.37}$$

from which it can be obtained that the pressure and the normal component of the velocity are conserved across the shock. Thus, the mentioned approximate solutions of the Riemann problem can be constructed by applying Equations (2.36) and (2.37) on a set of approximate waves, as we will show in the next section.

2.3 Numerical approach

In this section we outline the numerical methods implemented in `PLUTO`, used in this work to solve the RHD and RMHD equations. These procedures are as well the basis of the methods used in Chapters 4 and 5 to solve the Rad-RMHD equations.

The `PLUTO` code solves hyperbolic systems of the form (2.24) by following a finite-volume approach. Instead of storing field values at specific points of space and time, as it is done in finite-difference schemes, in this formulation we follow the evolution of volume-averaged values of $\mathcal{U}$ computed within each cell in which the domain is divided. This approach is chosen due to its exceptional ability to accurately reproduce sharp discontinuities such as shock and contact waves (see, e.g., the discussion in Chapter 11 of [212]). This kind of method, usually called *shock-capturing* for that reason, guarantees as well that the correct jump conditions across each discontinuity are satisfied.

The full algorithm implemented in `PLUTO` is based on a standard Godunov-type *reconstruct-solve-update* strategy. In it, relevant fields are estimated at cell boundaries (*reconstruction step*) and used to compute the fluxes by means of approximate Riemann solvers (*solving step*),

after which flux differences are explicitly integrated in time (*update step*). We now describe each of these steps.

2.3.1 Reconstruction step

Let us consider the particular case of the RMHD equations, where our chosen set of conserved fields is

$$\mathcal{U} = (\rho\gamma, \mathcal{E}, \mathbf{m}, \mathbf{B})^\intercal \ . \tag{2.38}$$

We refer from now on to fields defined on computational grids, and therefore the notation $\mathcal{U}$ corresponds to cell-averaged values inside a given zone i, j, k (indices have been omitted to avoid cluttered notations). We define the set of *primitive fields* for this system as

$$\mathcal{V} = (\rho, p_g, \mathbf{v}, \mathbf{B})^\intercal \, . \tag{2.39}$$

These definitions are almost identical for the RHD equations, where the only difference is that $\mathbf{B}$ is not included.

The first part of the reconstruction step consists in computing $\mathcal{V}$ in each cell using the stored values of $\mathcal{U}$, for which Equations (2.20)–(2.22) must be inverted. This is achieved by means of root-finding algorithms, paying special attention to avoiding problems related to small number handling that arise when large Lorentz factors are involved. To perform this conversion, we follow the procedure detailed in [206].

Next, the obtained values of $\mathcal{V}$, assumed to be cell-centered, are interpolated to zone interfaces. This produces left and right discontinuous states adjacent to each interface, which we denote by $\mathcal{V}_L$ and $\mathcal{V}_R$. In order to avoid spurious oscillations next to discontinuities and steep gradients, reconstruction must use slope limiters in order to satisfy monotonicity constraints (see, e.g., [208, 213]). In more than one dimension, the interpolation is carried direction-wise. During this step, some physical constraints are imposed, such as gas pressure positivity and the upper boundary for the velocity given by $||\mathbf{v}|| < 1$. The imposition of these constraints is much simpler when applied on $\mathcal{V}$ than on $\mathcal{U}$, which is why the interpolation is carried over the former.

2.3.2 Solving step

Once reconstruction is finished, the states $\mathcal{V}_L$ and $\mathcal{V}_R$ are reconverted into the conserved fields $\mathcal{U}_L$ and $\mathcal{U}_R$, respectively. In an environment of each cell boundary, the solution of Equation (2.24) looks exactly like the nonlinear Riemann problem defined in Section 2.2.2. If we knew the exact solution to this problem in the general case, fluxes along each direction could be

computed at cell boundaries by means of a direct evaluation of such solution. However, this approach is too numerically expensive to be viable. Instead, we can use the integral form of Eq. (2.24) to obtain relations that allow us to make a good estimation of the fluxes.

With this purpose, let us assume that, knowing $\mathcal{U}_L$ and $\mathcal{U}_R$, we can produce a good estimation of the maximum and minimum wave speeds (λ_R and λ_L respectively) of the solution of the Riemann problem. Without loss of generality, we now consider only fluxes along the x-axis, since fluxes along the other directions can be computed in the exact same way. The resulting system takes the following form:

$$\frac{\partial \mathcal{U}}{\partial t} + \frac{\partial \mathcal{F}(\mathcal{U})}{\partial x} = 0\,, \tag{2.40}$$

where $\mathcal{F}(\mathcal{U})$ are the flux components in the $\hat{\boldsymbol{e}}_x$-direction.[3]

We now consider the case $\lambda_L \leq 0 \leq \lambda_R$, and place an initial discontinuity at $x = 0$. Following, e.g., [208], we can then integrate Eq. (2.40) in the region of the (x, t) plane given by $[\lambda_L T, \lambda_R T] \times [0, T]$ for a given time $T > 0$, which yields

$$\int_{\lambda_L T}^{\lambda_R T} \mathcal{U}(x, T)\, dx - \int_{\lambda_L T}^{\lambda_R T} \mathcal{U}(x, 0)\, dx + \int_0^T \mathcal{F}(\mathcal{U}(\lambda_R T, t))\, dt - \int_0^T \mathcal{F}(\mathcal{U}(\lambda_L T, t))\, dt = 0\,. \tag{2.41}$$

Some of these integrals can be easily evaluated noting that $\mathcal{U}(x, 0) = \mathcal{U}_L$ for $x < 0$ and $\mathcal{U}_R$ for $x > 0$. In the same way, $\mathcal{F}(\mathcal{U}(\lambda_R T, t)) = \mathcal{F}(\mathcal{U}_R) \equiv \mathcal{F}_R$ and $\mathcal{F}(\mathcal{U}(\lambda_L T, t)) = \mathcal{F}(\mathcal{U}_L) \equiv \mathcal{F}_L$. Inserting these relations into Eq. (2.41) and dividing both sides by $T(\lambda_R - \lambda_L)$, we obtain

$$\frac{1}{T(\lambda_R - \lambda_L)} \int_{\lambda_L T}^{\lambda_R T} \mathcal{U}(x, T)\, dx = \frac{\lambda_R \mathcal{U}_R - \lambda_L \mathcal{U}_L + \mathcal{F}_R - \mathcal{F}_L}{\lambda_R - \lambda_L}\,. \tag{2.42}$$

We hence see that the left-hand side of Equation (2.42) equals the space average of the full solution of the Riemann problem in the interval $[\lambda_L T, \lambda_R T]$ for any given time. This relation is exact and depends only on the correct estimation of λ_L and λ_R. Furthermore, the resulting averaged value of $\mathcal{U}$ does not depend on time, which is a consequence of the self-similarity of the solution. The cases $\lambda_L > 0$ and $\lambda_R < 0$ can be studied in a similar way, by integrating Eq. (2.40) in $[0, \lambda_R T] \times [0, T]$ and $[\lambda_L T, 0] \times [0, T]$ respectively. In both cases, this procedure leads again to Eq. (2.42).

We shall now use the above results to estimate the fluxes at the zone boundary, i.e., at the axis $x = 0$. For this, let us again consider the case $\lambda_L \leq 0 \leq \lambda_R$ and integrate

[3] In general, for any direction $\hat{\boldsymbol{e}}_d$, $\mathcal{F}^d(\mathcal{U}) = \hat{\boldsymbol{e}}_d \cdot \mathsf{F}(\mathcal{U})$, where $d = x, y, z$ in Cartesian coordinates or $d = r, \theta, \phi$ in spherical coordinates. In the derivation shown in this section, we have omitted the superindex x to avoid complicated notations.

Eq. (2.40) in $[\lambda_L T, 0] \times [0, T]$. Given that $\mathcal{F}(\mathcal{U}(x,t))$ is a function of x/t, we know that $\mathcal{F}(x=0) \equiv \mathcal{F}(\mathcal{U}(0,t))$ is constant. In this way, we obtain the following relation:

$$\mathcal{F}(x=0) = \mathcal{F}_L - \mathcal{U}_L - \frac{1}{T}\int_{\lambda_L T}^{0} \mathcal{U}(x,T)\,dx. \tag{2.43}$$

Our estimation of the flux will therefore depend on our estimation of the integral in the right-hand side of Eq. (2.43). An option for doing so, proposed in [214], is to replace $\mathcal{U}(x,T)$ in the intermediate zone $[\lambda_L T, \lambda_R T]$ by its averaged value $\mathcal{U}^*$, defined as the right-hand side of Eq. (2.42). This yields the following approximate flux at $x = 0$:

$$\mathcal{F}^* = \frac{\lambda_R \mathcal{F}_L - \lambda_L \mathcal{F}_R + \lambda_R \lambda_L \left(\mathcal{U}_R - \mathcal{U}_L\right)}{\lambda_R - \lambda_L}\,. \tag{2.44}$$

On the other hand, if $\lambda_L > 0$ ($\lambda_R < 0$), the solution at $x = 0$ for $T > 0$ corresponds to $\mathcal{U}_L$ ($\mathcal{U}_R$), and therefore the flux is $\mathcal{F}_L$ ($\mathcal{F}_R$). Therefore, this approximation leads to the Harten-Lax-van Leer (HLL) approximation to the intercell flux:

$$\mathcal{F}_{hll} = \begin{cases} \mathcal{F}_L & \text{if } \lambda_L > 0 \\ \mathcal{F}^* & \text{if } \lambda_L \le 0 \le \lambda_R \\ \mathcal{F}_R & \text{if } \lambda_R < 0\,. \end{cases} \tag{2.45}$$

We note that this treatment is equivalent to considering an approximate two-wave solution of the form

$$\mathcal{U}_{hll} = \begin{cases} \mathcal{U}_L & \text{if } \lambda_L > x/t \\ \mathcal{U}^* & \text{if } \lambda_L \le x/t \le \lambda_R \\ \mathcal{U}_R & \text{if } \lambda_R < x/t\,. \end{cases} \tag{2.46}$$

Applying the Rankine-Hugoniot conditions (Equation (2.36)) to the solutions left and right from both waves, we reobtain Equations (2.45). It must be noted that $\mathcal{F}^*$ and $\mathcal{U}^*$ represent approximate values, and in general $\mathcal{F}^* \neq \mathcal{F}(\mathcal{U}^*)$.

In the HLL solver implemented in `PLUTO`, λ_L and λ_R are estimated, respectively, as the minimum and maximum eigenvalues of both states $\mathcal{U}_L$ and $\mathcal{U}_R$; i.e.,

$$\begin{aligned} \lambda_R &= \max_{S=L,R} \max_i \left\{\lambda_i(\mathcal{U}_S)\right\} \\ \lambda_L &= \min_{S=L,R} \min_i \left\{\lambda_i(\mathcal{U}_S)\right\}\,. \end{aligned} \tag{2.47}$$

The way these speeds are calculated for both RHD and RMHD is detailed in Appendix A.

A simplified version of this solver is obtained when the maximum right- and left-going signal speeds are estimated as

$$\begin{aligned} \lambda_R &= \lambda_{max} \\ \lambda_L &= -\lambda_{max}\,, \end{aligned} \tag{2.48}$$

with

$$\lambda_{max} = \max_{S=L,R} \max_i \left\{ |\lambda_i(\mathcal{U}_S)| \right\}. \tag{2.49}$$

The result of this choice is the Lax-Friedrichs-Rusanov (LFR) solver (see [208, 215]), where the flux is computed as follows:

$$\mathcal{F}_{LFR} = \frac{1}{2}\left[\mathcal{F}_L + \mathcal{F}_R - \lambda_{max}\left(\mathcal{U}_R - \mathcal{U}_L\right)\right]. \tag{2.50}$$

This is the simplest flux estimation included in `PLUTO`, but also the most diffusive.

A more accurate estimation is given by the HLL-contact (HLLC) solver, which consists in a three-wave approximate solution. As before, two shocks of speeds λ_L and λ_R are considered, with the addition of a middle constant discontinuity of speed λ^*, with $\lambda_L \le \lambda^* \le \lambda_R$. This approximate solution takes the form

$$\mathcal{U}_{hllc} = \begin{cases} \mathcal{U}_L & \text{if } \lambda_L > x/t \\ \mathcal{U}_L^* & \text{if } \lambda_L \le x/t < \lambda^* \\ \mathcal{U}_R^* & \text{if } \lambda^* \le x/t \le \lambda_R \\ \mathcal{U}_R & \text{if } \lambda_R < x/t\,. \end{cases} \tag{2.51}$$

where now we have considered two intermediate states, $\mathcal{U}_L^*$ and $\mathcal{U}_R^*$, separated by the mentioned contact wave. This solution leads to the following approximate flux:

$$\mathcal{F}_{hllc} = \begin{cases} \mathcal{F}_L & \text{if } \lambda_L > 0 \\ \mathcal{F}_L^* & \text{if } \lambda_L \le 0 < \lambda^* \\ \mathcal{F}_R^* & \text{if } \lambda^* \le 0 \le \lambda_R \\ \mathcal{F}_R & \text{if } \lambda_R < 0\,. \end{cases} \tag{2.52}$$

The strategy followed to compute the approximate fluxes $\mathcal{F}_L^*$ and $\mathcal{F}_R^*$ consists in applying the Rankine-Hugoniot jump conditions (Eq. (2.36)) to the three considered waves. If $\mathcal{U}$ has n components, these relations provide $3n$ equations for the $4n+1$ unknowns given by $\mathcal{U}_{L/R}^*$, $\mathcal{F}_{L/R}^*$ and λ^*. Therefore, additional constraints must be imposed. A natural choice for this is given by the properties satisfied by the exact solution, such as the continuity of p_g and β_x along the contact wave in the RHD case. In addition, any approximate solution must satisfy

the constraint given by $\lambda_L \leq \lambda^* \leq \lambda_R$. The way this is achieved in the RHD and RMHD modules of PLUTO is described in [203, 216], and will not be discussed here. Instead, we will go back to HLLC solvers in Chapter 4, where we will show the full derivation of a solver of this type for the equations of radiation transport, which follows analogous steps to those shown in [203].

As we will show in Chapter 4, HLLC solvers are less diffusive than HLL and LFR solvers, and have a higher accuracy when reproducing contact waves. One could therefore ask whether it is possible to increase the accuracy of these methods by including more waves in the approximate Riemann solver. Since the solutions of the RHD equations exhibit a pattern of three waves, it seems natural to consider a three-wave solver. On the other hand, the solutions of the RMHD equation exhibit up to 7 waves, and therefore it is reasonable to increase the number of intermediate states in the approximate solutions. Such is the case of the HLLD solver, introduced in [217] and included in PLUTO. However, we consider in this work solvers which include up to three waves.

2.3.3 Update step

Once fluxes are estimated on every cell interface, their values are used to compute an operator $\mathcal{R}$ that approximates the value of $(-\nabla \cdot \mathsf{F})$, which is then integrated in time (see Equation (2.24)). For each cell, the value of $\mathcal{R}$ is computed by calculating all flux differences taking into account the cell's geometry. The contribution along each direction d is obtained as

$$\mathcal{R}_d = -\frac{1}{\Delta V^d}\left(A_+^d \mathcal{F}_+^d - A_-^d \mathcal{F}_-^d\right) + \mathcal{S}_e^d, \tag{2.53}$$

where $A_\pm^d$ are the cell's right $(+)$ and left $(-)$ interface areas and ΔV^d is the cell volume in that direction [213]. Here $\mathcal{S}_e^d(\mathcal{U})$ accounts for geometrical terms that arise when the divergence is written in different coordinate systems. These can be obtained at the cell center or following the approach outlined in [218]. The full operator $\mathcal{R}$ is in the end computed as $\sum_d \mathcal{R}_d$.

Among the integration schemes included in PLUTO, we shall focus on three particular *semidiscrete* methods. In these, time evolution is considered to be independent on the spatial discretization, and therefore Equation (2.24) is discretized as an ordinary differential equation (see [213]). The simplest case is given by the *Euler* discretization, which consists in the following method of first order in time:

$$\mathcal{U}^{n+1} = \mathcal{U}^n + \Delta t^n \mathcal{R}^n\,, \tag{2.54}$$

where n denotes the current step number and Δt^n is the current time step. Higher orders can be achieved by evolving $\mathcal{U}$ in intermediate time steps, as in the total variation diminishing[4] (TVD) Runge-Kutta schemes by Gottlieb & Shu [220]. In its second-order version (RK2), this method reads:

$$\begin{aligned} \mathcal{U}^{(1)} &= \mathcal{U}^n + \Delta t^n \mathcal{R}^n \\ \mathcal{U}^{n+1} &= \frac{1}{2}\mathcal{U}^n + \frac{1}{2}\left(\mathcal{U}^{(1)} + \Delta t^n \mathcal{R}^{(1)}\right) . \end{aligned} \tag{2.55}$$

Similarly, the third-order method of this kind (RK3) has the following steps:

$$\begin{aligned} \mathcal{U}^{(1)} &= \mathcal{U}^n + \Delta t^n \mathcal{R}^n \\ \mathcal{U}^{(2)} &= \frac{3}{4}\mathcal{U}^n + \frac{1}{4}\left(\mathcal{U}^{(1)} + \Delta t^n \mathcal{R}^{(1)}\right) \\ \mathcal{U}^{n+1} &= \frac{1}{3}\mathcal{U}^n + \frac{2}{3}\left(\mathcal{U}^{(2)} + \Delta t^n \mathcal{R}^{(1)}\right) . \end{aligned} \tag{2.56}$$

Once the update of the conserved variables is completed, the time step is changed using the maximum signal speed computed in the previous step, according to the Courant-Friedrichs-Lewy condition [221] given by

$$\Delta t^{n+1} = C_a \min_d \left(\frac{\Delta l^d_{\min}}{\lambda^d_{\max}} \right) , \tag{2.57}$$

where $\Delta l^d_{\min}$ and $\lambda^d_{\max}$ are, respectively, the minimum cell width and maximum signal speed along the direction d, and C_a, the Courant factor, is a user-defined parameter.

Finally, we must recall that finite-volume schemes do not maintain in general the condition $\nabla \cdot \mathbf{B} = 0$ when magnetic fields are included, which can lead to instabilities due to the unphysical acceleration parallel to field lines that occurs when monopoles are created (see e.g. [222]). In the modules of `PLUTO` regarded in this thesis, this constraint can be enforced by either using the constrained transport method ([223] and [224]) or hyperbolic divergence cleaning (see [225], [226], [227]).

[4] TVD schemes guarantee that the total variation of the numerical solution of Eq. (2.24), defined for 1D as the L_1 norm of $\partial\mathcal{U}/\partial x$, does not increase in time, which is a property that must be satisfied by monotonicity-preserving schemes (see, e.g., [219]).

2.3.4 Parallelization and AMR

We now provide a brief description of the parallelization and AMR routines included in PLUTO, which are applied in Chapter 3 and adapted to the radiative transfer module in Chapter 4.

In PLUTO, AMR is based on an implementation of the CHOMBO library [202]. The strategy consists in locally increasing the resolution of all regions of the domain where a given function χ of the conserved variables and its derivatives exceeds a treshold value χ_r. By default, the χ function used in PLUTO adopts a criterion based on the second derivative error norm (see [228]), as

$$\chi(\mathcal{U}) = \sqrt{\frac{\sum_d |\Delta_{d,+1/2}\,\varphi - \Delta_{d,-1/2}\,\varphi|^2}{\sum_d \left(|\Delta_{d,+1/2}\,\varphi| + |\Delta_{d,-1/2}\,\varphi| + \epsilon\,\varphi_{d,ref}\right)^2}}, \tag{2.58}$$

where $\varphi = \varphi(\mathcal{U})$ is a user-defined function of the conserved variables, ϵ is a constant, $\Delta_{d,\pm1/2}\,\varphi$ are defined in the position i along the direction d as $\Delta_{d,\pm1/2}\,\varphi = \pm(\varphi_{i\pm1} - \varphi_i)$, and $\varphi_{d,ref} = |\varphi_{i+1}| + 2|\varphi_i| + |\varphi_{i-1}|$.

Refinement is achieved by defining a set of nonoverlapping boxes in the computational domain, in such a way that all cells that verify $\chi > \chi_r$ are covered by the boxes. Within these, zones are evenly divided by a factor r_l along each direction. After doing so, new conserved variables are assigned to the newly created zones by interpolating values from the surrounding cells, following schemes that maintain the conservative properties of the solutions (see [201]). Once this step is finished, the already-refined cells can continue to be divided recursively a maximum number l_{max} of times, thus creating a hierarchy of refinement levels. The refinement factors r_l depend in general on the current level l, and can be chosen by the user for every particular setup. In this way, the equivalent resolution of the grid, i.e., the resolution that would be needed using an uniform grid to achieve the smallest cell size of the adaptive grid, is equal to $\prod_{l=1}^{l_{max}} (r_l)^D \prod_{d=1}^{D} N_d$, where D denotes the number of dimensions, and N_d is the initial ($l = 0$) resolution along the direction d.

Parallelization is achieved by using the Message Passing Interface (MPI) standard[5]. The implementation in PLUTO divides the global domain into n maximally cubic subdomains, being n the number of processors that are used. In this way, computations are run in parallel using one processor per each subdomain. When AMR is used, each refinement level is divided for parallelization in the already-created boxes, which are solved individually using at most one processor per box.

[5]https://www.mpi-forum.org/

Chapter 3

Simulations of the BdHN model

The dynamics of an expansive baryon-loaded e^-e^+ plasma in the fireshell model has been extensively studied in [139–142, 144, 145, 229, 230] by means of one-dimensional computations based on the assumption that most of the energy is contained within a shell of constant width. This simplified approach suffices to compute the temporal evolution of the expansive pulse in regimes of low baryon loading, and is able to fastly produce time-dependent spectra and light curves that can be readily compared with observations. However, this method is unable to capture the dynamical properties of the expansive wave in situations where such geometrical description is inaccurate, typically occurring in the BdHN model when the plasma encounters regions of high density in the SN ejecta.

This chapter focuses on several implementations of the just described HRSC methods made throughout the last three years in an attempt to provide a description of so far inexplored processes proposed to occur in the BdHN model. We start by making a comparison of the hydrodynamical approach and the mentioned constant-width approximation, part of which has been published in [56, 161]. We then explore the plausibility and observational consequences of the BdHN model for X-ray flares, summarizing the approach followed in [56, 161, 170] and showing some of the results there included. Finally, we study the dynamics and observational properties of the radiation emitted at reflected waves produced by the impact of the plasma onto the SN ejecta. This interaction is studied both by means of a simplified analytical model and a 2D RHD simulation, recently submitted for publication [231].

3.1 The fireshell model

In the BdHN model, the dynamics of the interaction between the expanding e^-e^+ plasma and the SN material depends on the amount of baryonic matter encountered by the plasma along each expansion direction. To parametrize this quantity, we define a direction-dependent

baryon load B as the ratio $Mc^2/E_{e^-e^+}$, where $E_{e^-e^+}$ is the total internal energy of the plasma and M is the mass of an object whose density profile $\rho(r)$ corresponds to the profile along the selected direction. In general, for $B \ll 1$, the structure of the shell is not affected by the distribution of matter swiped during its evolution. Contrarily, bigger values of B can lead to a dependence of the dynamics on the particular form of $\rho(r)$, and produce a spatial broadening of the plasma pulse or reflected waves. We explore such limit in Sections 3.2 and 3.3, whereas for now we focus on the $B \ll 1$ case.

It has ben proposed in [140] that most of the pulse's mass and energy can be assumed to be contained in a region of constant width as long as[1] $B \leq 10^{-2}$. This conclusion results from a series of 1D hydrodynamical simulations in which the RHD equations are solved in spherical coordinates following Wilson's approach (see Chapter 1). In the same paper, a simplified code that makes use of this assumption is introduced, in which the plasma is assumed to be contained in a slab of constant width. Within this slab, the mass density, the pressure, and the velocity are assumed to be homogeneous, and their evolution is entirely determined by the conservation of total energy-momentum, entropy, and baryon number. In addition, baryonic matter is assumed to be initially contained in a region $r \in [r_{\rm in}, r_{\rm out}]$, and to interact inelastically with the expanding slab, reaching instantaneous thermal equilibrium. This approximate code has been used to model the expansion of the pulse in the low-B directions of the SN material and its posterior interaction with the CBM, with the aim of predicting the observed light curves and spectra (see, e.g., [160, 229]).

As mentioned in Chapter 1, it is known today that the numerical schemes used in [140] are highly diffusive, and fail to produce accurate solutions if high Lorentz factors ($\gamma \gtrsim 2$) are involved. We have therefore attempted to reproduce the same results by applying the shock-capturing methods explained in Chapter 2. To this purpose, we have performed a series of simulations choosing B values slightly under and above 10^{-2}. As in [140], we have solved the RHD equations assuming spherical symmetry, thus describing the radial evolution of the fluid along selected directions. This approach is valid as long as the described region is far enough from the BH to neglect any curvature effect. In our simulations, the left boundary of the computational domain is set at $r \sim 10^8$ cm, which largely exceeds the typical Schwarzschild radius for the BdHN model ($\sim 10^5$ cm).

As long as photons are trapped in the expanding plasma, which is controlled by computing its optical depth, we can safely apply the hydrodynamical approach. Since the fluid is radiation–dominated throughout most of its evolution, we implement the constant-Γ EoS given in Eq. (2.9) with $\Gamma = 4/3$, as in [140]. A discussion of the applicability of this EoS to radiation–

[1] This baryon load is also consistent with the observational constraint given by the compactness problem; see Section 1.2.1.

dominated e^-e^+–baryon plasmas is given in Appendix B. We have chosen initial conditions similar to those used in [140], defined as

$$\begin{aligned} \rho(r) &= \rho_0 + \rho_1\, e^{-(r-r_0)^2/2\sigma_\rho^2} \\ p_g(r) &= p_0 + p_1\, e^{-(r-r_1)^2/2\sigma_p^2} \\ v_r(r) &= v_0\, e^{-(r-r_1)^2/2(4\sigma_p)^2}\,. \end{aligned} \tag{3.1}$$

In the starting point of these simulations, the shell is already formed, and its internal energy is initially concentrated around a radius r_1. The initial velocity of the wave front is fixed by setting a velocity v_0 in a region that contains most of the pulse energy. This has been set using a smooth velocity profile to prevent the formation of unphysical reflection waves due to the initial relaxation of the system. The value of v_0 is expressed as a function of the initial Lorentz factor of the pulse γ_0, as $v_0 = 1/\sqrt{1-(1/\gamma_0)^2}$. On the other hand, the SN ejecta is modelled by setting an initially still density profile centered at a given radius $r_0 > r_1$. For both the density and the pressure profiles, we have fixed the minimum values ρ_0 ($\ll \rho_1$) and p_0 ($\ll p_1$) since the methods described in Chapter 2 require that both fields are positive in the whole domain. In particular, we have chosen $\rho_0/\rho_1 = 10^{16}$, in such a way that the integral of ρ_0 in the whole domain is 10^9 times smaller than the mass of the ejecta. Simulations have been run on a 1D uniform grid of 10^5 zones.

The acceleration of the shell is driven by the conversion of internal into kinetic energy, and therefore its evolution is characterized by a transition between an initial radiation–dominated expansive phase and a final matter–dominated coasting phase. The dynamical properties of both regimes can be simply derived from the conservation of total energy-momentum, and are consequently the same as those of relativistic fireballs, described in [75, 77]. In the radiation–dominated regime, the mean Lorentz factor of the pulse increases as $\gamma \propto r$, whereas in the matter–dominated regime it approaches a constant value given approximately by $1/B$. In Fig. 3.1, we have represented the mean γ value of the pulse as a function of its radial position, for a simulation with $\mathcal{E}_{\rm int} = 5 \times 10^{50}$ erg and $B = 6.7 \times 10^{-3}$. We have calculated this quantity as the radial average of γ using as weighting function the energy density $\mathcal{E}$ defined in Eq. (2.8). As expected, the shell is initially accelerated as $\gamma \propto r$. As in [140], this expansion is slowed down as the mass in the SN ejecta is engulfed, and the behavior $\gamma \propto r$ is recovered as soon as this process ends. Our simulations are stopped during the transition from the radiation– to matter–dominated regimes, which occurs while the plasma is still optically thick. We have compared these results with a simulation produced with the mentioned approximate code, which is carried until the transparency moment (see Fig. 3.1), defined as the time when the optical depth across the shell is 1. The curves of $\gamma(r)$ obtained with both methods show a high degree of consistency, and are also consistent with

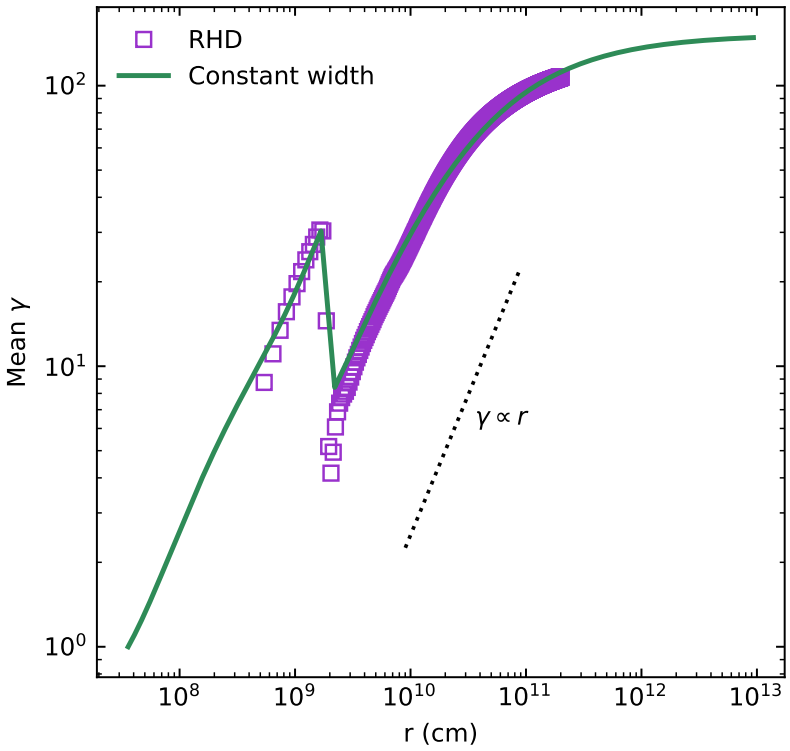

Fig. 3.1 Evolution of the mean Lorentz γ factor of the expanding shell, obtained by solving the 1D spherically symmetric RHD equations using the PLUTO code (violet squares), and with the 1D approximate code (green curve). The slope of $\gamma \propto r$, expected during the initial radiation–dominated stage, is shown for comparison. Reproduced from [56] with modifications.

the expected asymptotic value of γ (~ 150) in the matter–dominated phase. However, these results depend on the conservation of the total integrated energy-momentum in the shell, which is guaranteed even if its width is not constant.

To check the validity of the constant width approximation, we have studied the form of the pulse during its propagation. Radial profiles of the laboratory frame density $\rho\gamma$, internal energy density (computed as $\mathcal{E}_{\rm int} = \mathcal{E}|_{\rho=0}$), and γ obtained in the formerly described simulation are shown in Fig. 3.2 for different evenly spaced times between 0 and 0.14 s. In Fig. 3.3, we show the same profiles resulting from a different simulation where we have increased the total baryonic mass, in such a way that $B = 6.7 \times 10^{-2}$. In the latter case, the shape of the pulse is significantly changed after it interaction with the SN material, and an inward-traveling reflected wave is produced. As the baryon load is further increased, the plasma departs even more from its initial shell-like geometry, as we will show in Sections 3.2 and 3.3. Contrarily, in the simulations made with $B = 6.7 \times 10^{-3}$ and lower (not shown here), we have seen that the geometry of the plasma remains that of a sharp pulse. These

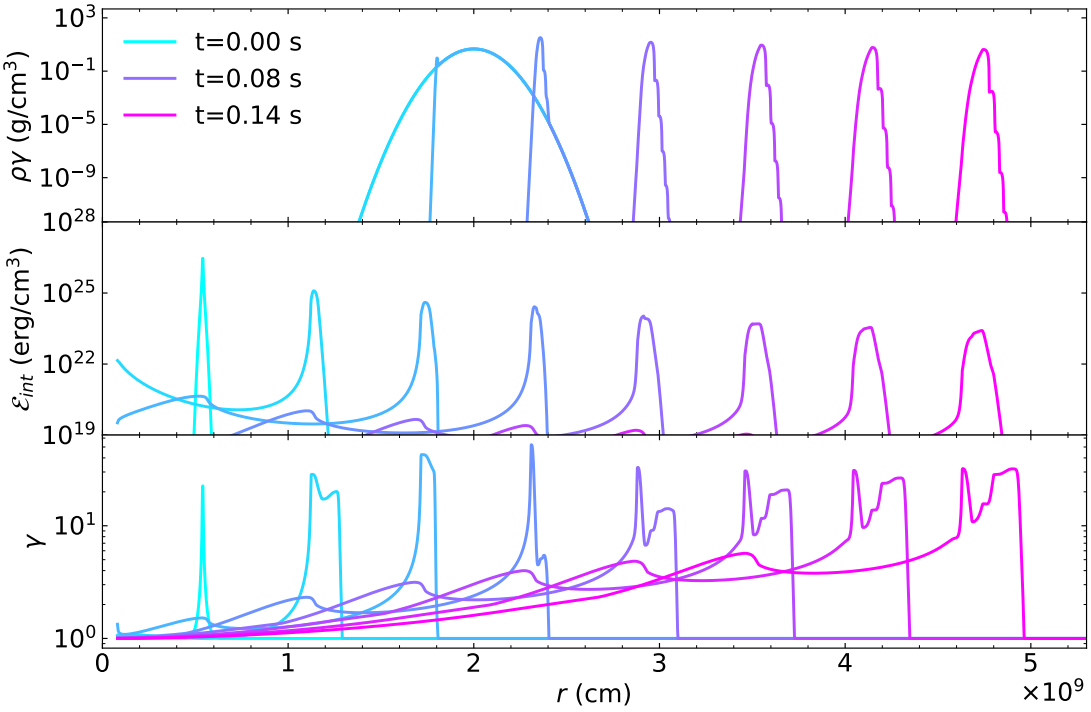

Fig. 3.2 Laboratory frame density, internal energy density, and Lorentz factor profiles for the simulation with $B = 6.7 \times 10^{-3}$, for $0 < t < 0.14$ s.

results are consistent with the mentioned limiting value of $B = 10^{-2}$ proposed in [140]. In both cases, it can be seen in Figures 3.2 and 3.3 that the $\mathcal{E}_{\rm int}$ profile broadens as the SN ejecta is swiped, which is in contradiction with the constant width approximation.

We have studied the broadening of the pulse once the baryonic matter has been completely swiped by plotting a series of profiles in different moments of the expansion, between $t = 0.67$ s (when the pulse has already engulfed the surrounding matter) and $t = 6$ s (close to the end of the simulation). In Fig. 3.4a, we show $r^2\mathcal{E}$ profiles[2] obtained from the simulation with $B = 6.7 \times 10^{-3}$. To compare the shape of these profiles, we have overlapped them by plotting them as functions of $(r - ct)$, since the pulse expands with $v_r \sim c$. The resulting profiles show that the pulse gets broader with time. Measuring its width along the fixed value given by $r^2\mathcal{E} = 10^{42}$ erg cm^{-1}, we obtain a 30% growth between $t = 0.67$ and 6 s.

One possible cause of this broadening is the numerical diffusion introduced by our solving scheme, which should decrease if the resolution is increased. We have therefore run a new simulation with $B = 6.7 \times 10^{-3}$, this time locally increasing the resolution around the pulse by applying the AMR techniques described in Section 2.3.4. We have used a grid of 10^5

[2]The reason why we multiply the energy by r^2 is that, for constant width, $\mathcal{E}$ should decrease as $1/r^2$, which follows from conservation of energy; e.g., it can be seen by integrating Eq. (2.5) in a region that contains the pulse.

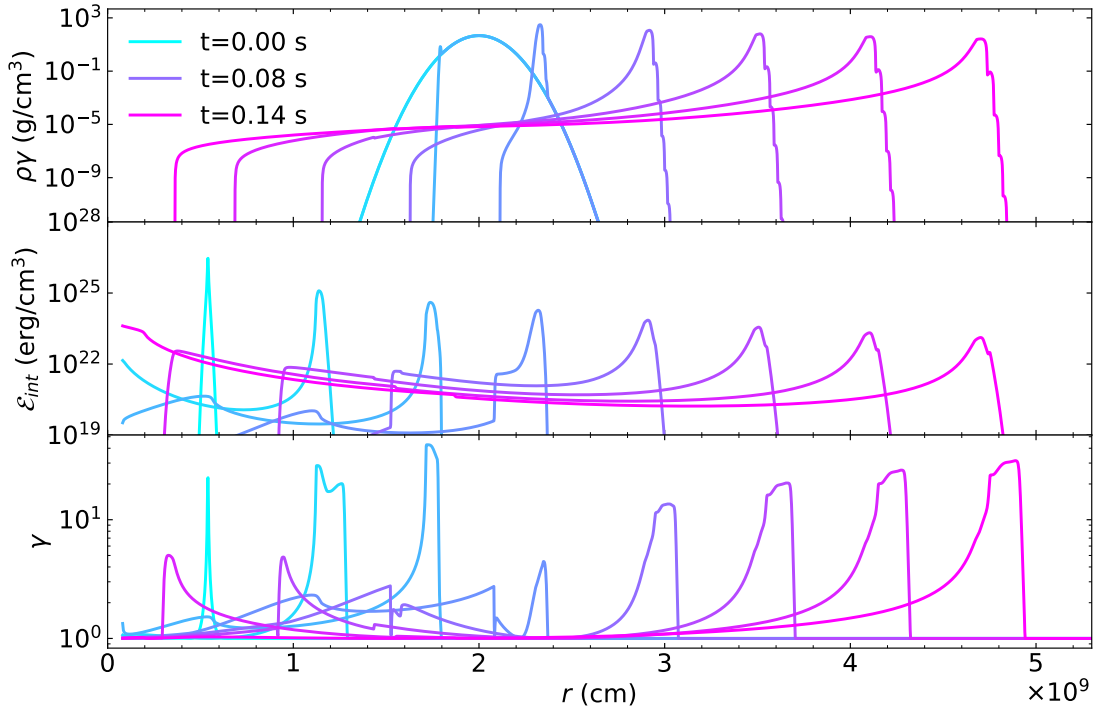

Fig. 3.3 Same as Fig. 3.2, for the simulation with $B = 6.7 \times 10^{-2}$.

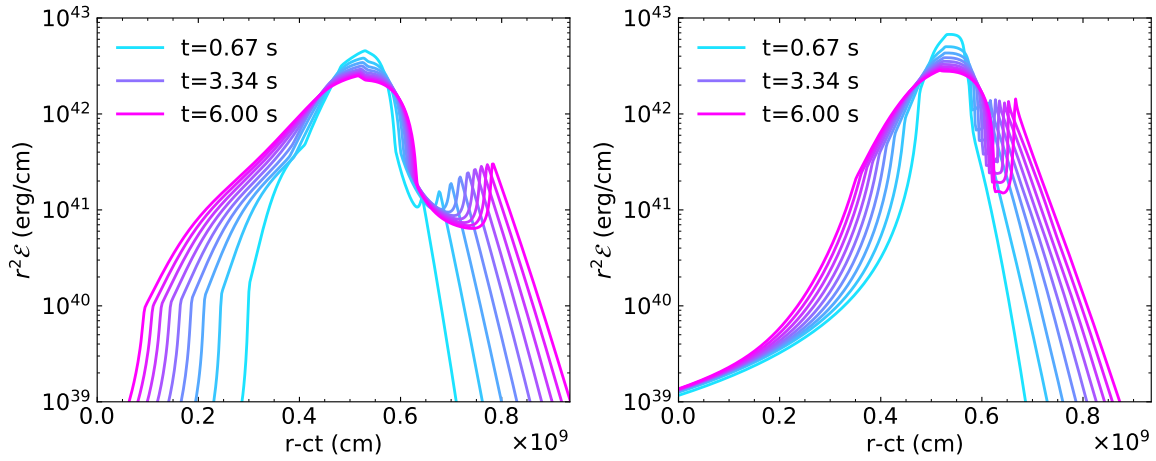

(a) (b)

Fig. 3.4 Snapshots of $r^2\mathcal{E}$ between $t = 0.67$ s and $t = 6$ s taken every 0.67 s, represented as a function of $r - ct$ to compare their shape. Results are shown for the simulations made with uniform (a) and adaptive (b) grids, with $B = 6.7 \times 10^{-3}$.

zones at level 0 with 4 refinement levels and a refinement ratio $r_l = 2$ for each of them, so that the resolution at the location of the pulse is 16 times larger than in the rest of the spatial domain. To follow the pulse, we have set $\varphi(\mathcal{U}) = \mathcal{E}$ as refinement variable (see Eq. (2.58)).

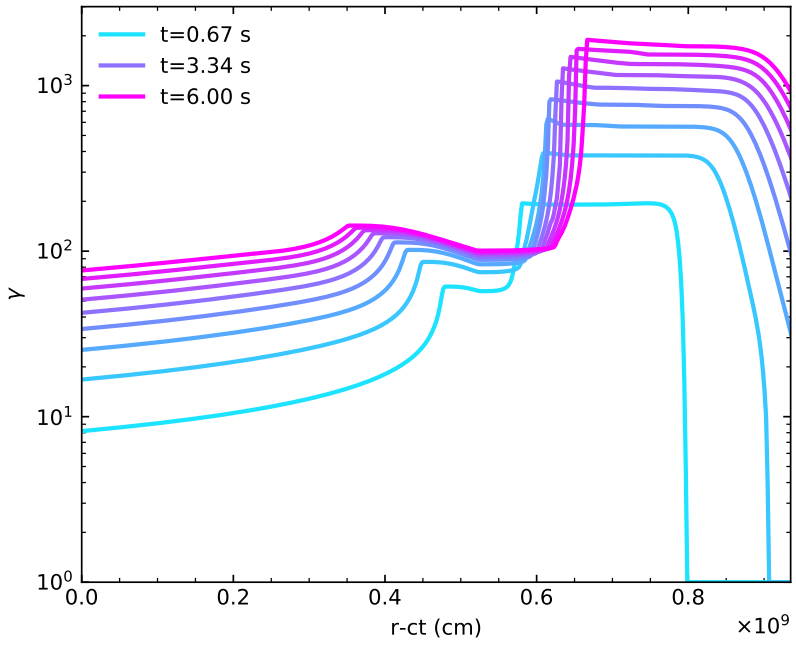

Fig. 3.5 Lorentz γ profiles between $t = 0.67$ s and $t = 6$ s as functions of $(r - ct)$, computed in the AMR simulation with $B = 6.7 \times 10^{-3}$.

The $r^2\mathcal{E}$ profiles resulting from these simulations are shown in Fig. 3.4b. In that figure, it can be seen that the pulse at $t = 0.67$ s is thinner than in the simulations made with an uniform grid, which means that the pulse's broadening when crossing the SN ejecta is reduced when the resolution is increased. However, at $t = 6$ s, the widths obtained in both simulations are comparable.

Physical reasons for this broadening are studied in [232], where it is shown that thermal spreading is in general negligible for typical parametres of GRBs when compared to the hydrodynamical spreading of the pulse. The latter phenomenon occurs due to the variation of $\gamma(r)$ across the pulse, being most important in regions with increasing γ. In [88, 233], it is shown that the thickness l of such regions increases as

$$l(R) = R_0 + \frac{R}{2}\left(\frac{1}{\gamma_i^2} - \frac{1}{\gamma_e^2}\right) , \tag{3.2}$$

where R is the radial position of the pulse, R_0 its initial width, and γ_i and γ_e are respectively the Lorentz factors at the internal and external boundaries of the region, with $\gamma_e > \gamma_i$. In this model, the pulse's width remains constant as long as $R \ll 2R_0\left(\frac{1}{\gamma_i^2} - \frac{1}{\gamma_e^2}\right)$. The variation of γ across the pulse can be seen in Fig. 3.5, where we have represented γ as a function of $(r - ct)$ for the simulation made with an adaptive grid. These profiles have two increasing

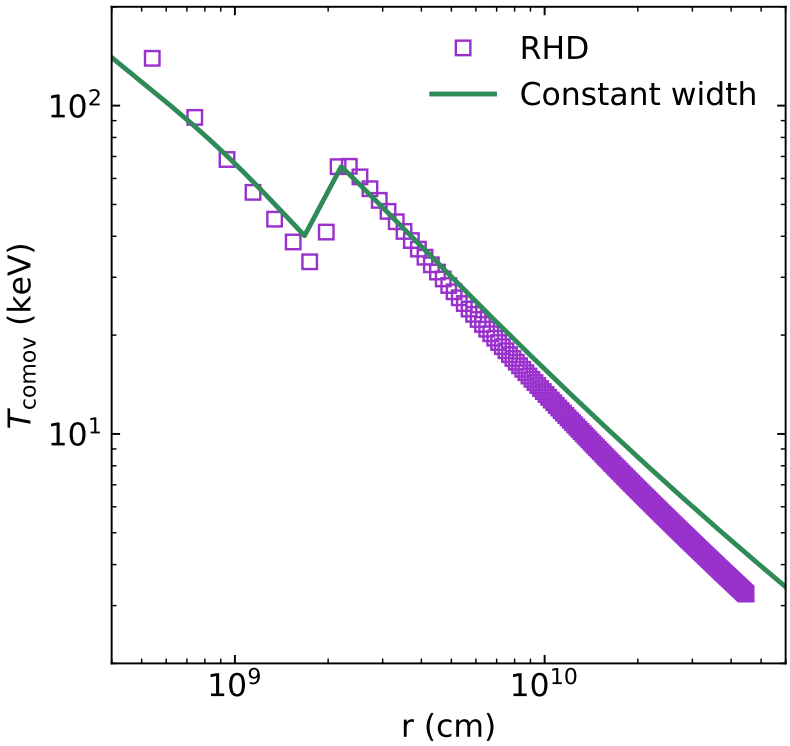

Fig. 3.6 Mean comoving temperature as a function of r for the RHD (violet squares) and constant-width (green curve) simulations with $B = 6.7 \times 10^{-3}$. RHD simulations show a faster decrease of T_{comov} than predicted by the approximate code.

regions separated by a slightly decreasing plateau. The overall growth of γ observed in this plot is therefore consistent with a physical broadening of the pulse.

The hydrodynamical spreading of the pulse has an impact on intensive quantities such as the matter density and the total pressure, that should in consequence decrease faster than predicted by the constant-width model. In Fig. 3.6, we show the variation of the pulse's mean temperature T_{comov} measured in the fluid's comoving frame, computed with both the RHD and the approximate codes (we have used a static uniform grid in the first case). We can see in this plot that T_{comov} decreases faster in the hydrodynamical code than in the approximate one, although the difference of both values is smaller than 20% in the considered range. This is due to the fact that the main variation of the pulse's volume is due to its radial expansion, whereas its broadening occupies a second order of importance. We therefore conclude that the constant-width assumption is reasonable as a first approximation and can accurately reproduce the γ factors obtained with the RHD code for $B \leq 10^{-2}$, although it can overestimate intensive quantities such as the comoving temperature in the late stages of the expansion (in particular, at the time of the emission).

3.2 Early X-ray flares in GRBs

3.2.1 Observational data and theoretical models

Since its launch in November 2004, the *Swift* satellite has provided data of numerous GRBs with unprecedented reaction times. Moreover, the Burst Alert Telescope (BAT) and the XRT on board of this satellite are able to provide measurements in the X-ray bands $15 - 150$ keV and $0.3 - 10$ keV, respectively [34]. This led in 2005 to the discovery of flares in the X-ray afterglow of some GRBs (see Fig. 3.7). These X-ray flares, which are observed in roughly $1/3$ of all GRBs, can occur between $30 - 10^5$ s after the burst trigger [234] (typically within a few hundred seconds, as shown in [235]), exhibit a significant re-brightening of the observed flux (up to a factor of 500), and are associated with the release of large isotropic equivalent energies, sometimes comparable to the energy released during the prompt phase. Because of their fast rise/decay time, the most widely accepted explanation for the occurrence of X-ray flares is a late central engine activity [33, 236–243]. Other possible explanations for their origin include delayed magnetic dissipation activity as the ejecta decelerates [244] and strongly anisotropic emission in the comoving frame of the emitting material [245].

A different model of this phenomenon has been presented in [161], where it was proposed that X-ray flares can be emitted in BdHNe due to the breakout of shocks created in high-denity regions of the SN ejecta due to their interaction with the expanding e^-e^+ plasma. In this picture, both the prompt emission and the flares are emitted towards the observer due to the system's rotation (see Fig. 3.8). This model is supported by the significant thermal component found in the spectra of 7 of the 16 GRBs included in the sample considered in that work, which were fitted as a sum of blackbody and power-law functions. The sample considered in [161] was constructed excluding GRBs with flares having a low (< 20) signal-to-noise ratio, those with X-ray flares which coincide with gamma-ray flares, those in which the integrated energy of the flares observed by *Swift*/XRT is higher than the gamma-ray energy observed by *Swift*/BAT, which would point to an incomplete coverage of the prompt emission, and those with late X-ray flares observed at $t > 300$ s (in the rest frame) after the triggering. Apart from having in general a low signal-to-noise ratio [241], such late X-ray flares cannot be explained by the BdHN model, since the dimensions of the system required to explain such times largely exceed those of the SN ejecta in BdHNe. All of the 16 GRBs satisfying these conditions were identified as BdHNe I, as they are all long GRBs with $E_{\rm iso} \gtrsim 10^{52}$ erg. Apart from characterizing these flares by obtaining correlations between $E_{\rm iso}$ and the energy of the flares, their occurrence time and their duration, the thermal component of their spectra was studied in detail to obtain the velocity of the emitting region. A special attention is paid in that article to GRB 081008, observed at $z = 1.967$ with an isotropic

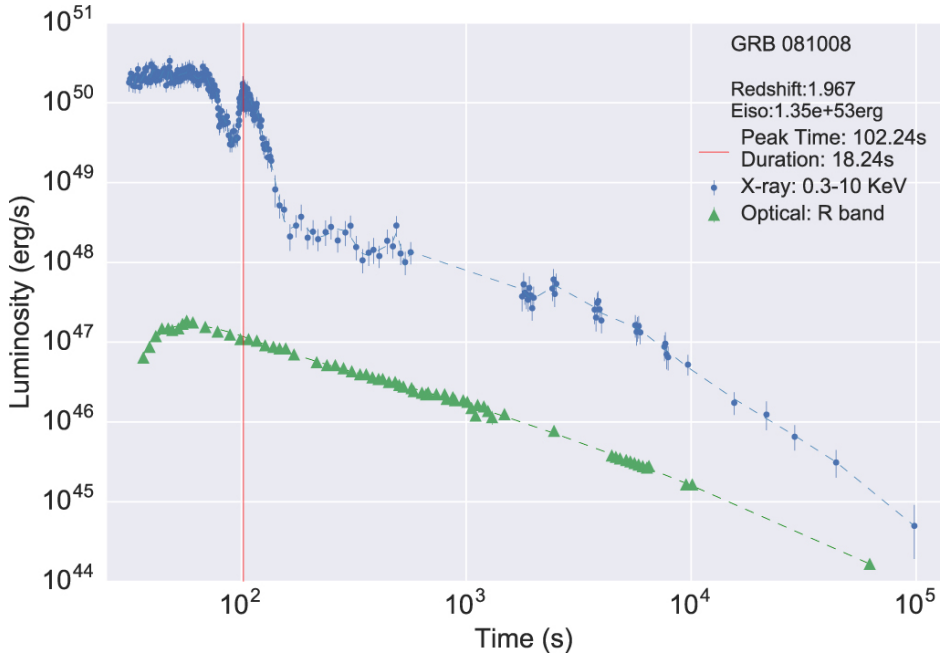

Fig. 3.7 Light curve of GRB 081008 measured by *Swift*/XRT, reproduced from [161]. This source has a redshift $z = 1.967$, as reported by VLT [246]. Optical data are from [247].

energy of $E_{\rm prompt} = (1.35 \pm 0.66) \times 10^{53}$ erg in the prompt phase and an X-ray flare with $E_{\rm iso,f} = (6.56 \pm 0.60) \times 10^{51}$ erg [161] (see Fig. 3.7). The thermal component of this flare is computed in [161] to be between 20% and 30% of $E_{\rm iso,f}$, which translates into at least 1% of $E_{\rm prompt}$ (see Fig. 3.9). Assuming that this radiation is produced by a spherically symmetric blackbody emitter, the temporal variation of the luminosity and the observed temperature has been used to infer an emitting radius of $10^{11} - 10^{12}$ cm in the source's rest frame, and a mildly relativistic Lorentz factor $\gamma \lesssim 4$ for the emitting region. Such dimensions are consistent with those predicted by the BdHN model [167].

Due to the large B values involved in the propagation of the $e^- e^+$ plasma in the high-density regions of the SN ejecta (see [161, 167]), the constant-width approximation cannot be applied to this process. In the following subsections we show a series of RHD simulations of this model, and explore its observational consequences.

3.2.2 Numerical approach

Our description of the SN ejecta is based on the simulations made in [167] in the context of the IGC. In these, the evolution of the SN ejecta is described by means of N-body Newtonian simulations (see Fig. 3.8), together with a description of the accretion process onto the NS based on the Bondi formalism (recently these simulations were improved via the SPH

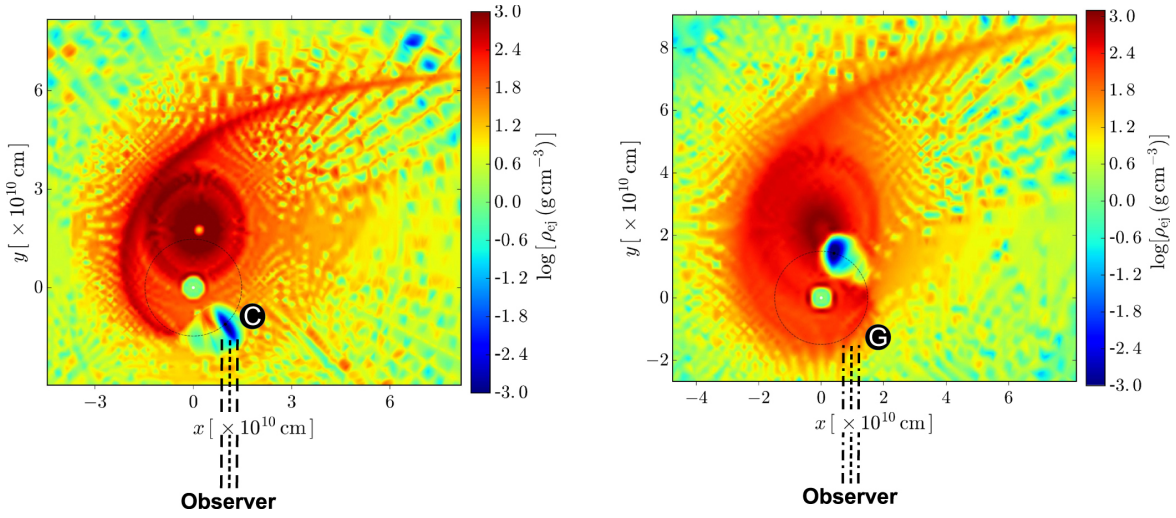

Fig. 3.8 Two snapshots of the matter distribution in the equatorial plane of the progenitor's binary system. The panel on the left corresponds to the moment in which the BH is formed and a large portion of the e^-e^+ plasma starts to self-accelerate in a low-density environment ($B \lesssim 10^{-2}$) towards the observer, producing the GRB prompt emission. The panel on the right corresponds to the moment when the shock created by the plasma inside the high-density SN ejecta ($B \sim 10^1 - 10^2$) breaks out and produces an X-ray emission, which is directed toward the observer due to the rotation of the ejecta in the equatorial plane. This figure, reproduced from [161], was made with data from the simulations shown in [167].

formalism; see [168]). To obtain typical parameters of this process, we have used the results of a simulation made considering a NS with an initial mass of $2\ M_\odot$ and a $\mathrm{CO_{core}}$ obtained from a progenitor with a zero-age main-sequence mass $M_{\mathrm{ZAMS}} = 30\ M_\odot$, which leads to a total ejecta mass of $7.94\ M_\odot$. The orbital period of this system is of 5 minutes, with a binary separation of 1.5×10^{10} cm. For these parameters, the NS reaches the critical mass and collapses to form a BH. Two snapshots of this simulation are shown in Fig. 3.8 at the moment of the collapse and 100 s after it.

Due to the asymmetry of the SN ejecta, the e^-e^+ plasma engulfs different amounts of baryonic mass in each expansion direction. We have produced 1D spherically symmetric RHD simulations[3] of this process which represent the propagation of the e^-e^+ along one direction at a time, and therefore cannot reproduce effects due to the system's rotation. As before, we ignore the gravitational effects of the newly formed BH, and follow a purely special relativistic approach. Given these considerations, we can describe both the plasma and the SN ejecta following a single-fluid approach, applying the RHD equations.

[3]The Thomson optical depth along the directions of propagation studied here is of the order of $10^7 - 10^{10}$, so radiation remains trapped in the SN ejecta throughout the entire propagation of the shock. Since the energy of photons largely exceeds that of material particles in the shocked region, a hydrodynamical description is possible even in regions which are transparent to absorption but opaque to scattering (see Chapter 5).

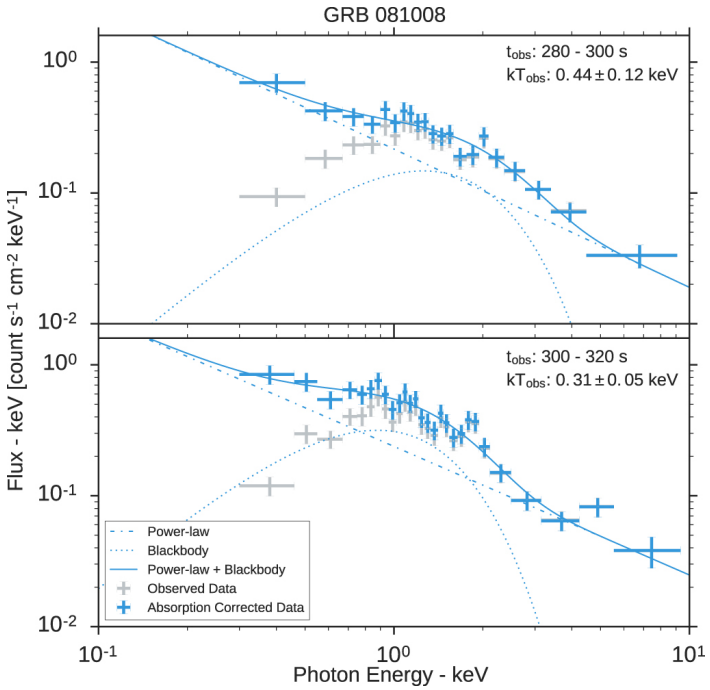

Fig. 3.9 Thermal evolution of GRB 081008 ($z = 1.967$) in the observer frame. The X-ray flare of this GRB peaks at $304(\pm 17)$ s. Upper panel: *Swift*/XRT spectrum from 280 s to 300 s. Lower panel: *Swift*/XRT spectrum from 300 to 320 s. The gray points are the observed data, while the blue points are corrected for hydrogen absorption. The data are fit with a combination of power-law (dotted–dashed lines) and blackbody (dotted lines) spectra. The power-law + blackbody spectra are shown as solid curves. The temperature decreases from ~ 0.44 keV to ~ 0.31 keV, but the ratio of the thermal component rises from $\sim 20\%$ to $\sim 30\%$. Reproduced from [161].

The EoS of an equilibrium $e^- e^+$–baryon plasma is studied in Appendix B. For the radiation– and matter–dominated regimes ($p_g \gg \rho$ and $p_g \ll \rho$, respectively), this EoS predicts an effective polytropic index $\Gamma_{\rm eff}$ of $4/3$ and $5/3$ in each of these cases respectively. The simulations presented in this section have been made using the EoS given in Eq. (2.9), with $\Gamma = 4/3$. The reason to do this is that we have set an initially negligible pressure in the SN ejecta, and therefore the only regions of space where the enthalpy density h is significantly affected by the choice of the EoS are the shocked ones, which verify $\Gamma_{\rm eff} = 4/3$ during the whole evolution. For consistency, we have verified this claim applying the EoS derived in Appendix B to the computed pressure and density profiles, obtaining that $\Gamma_{\rm eff} = 4/3$ with a maximum error of 0.2% in all shocked regions.

Initial conditions have been set consistently with the parameters of the BdHN model and GRB 081008. At the initial time, the $e^- e^+$ plasma has an energy $E_{e^- e^+} = 1.35 \times 10^{53}$ erg, a negligible baryon load, and is distributed homogeneously within a region of radii of the order

of $10^8 - 10^9$ cm. The surrounding SN ejecta has a mass density radial profile given by

$$\rho \propto (R_0 - r)^\alpha \tag{3.3}$$

where the parameters R_0 and α, with $2 < \alpha < 3$, as well as the normalization constant, are chosen to fit the profiles obtained in [167] and represented in Fig. 3.8. In this way, the initial spatial dimension of the SN ejecta is determined by the parameter R_0, set in this case as 4×10^{11} cm. The initial radial velocity is set as $v_r \propto r$ in order to reproduce the homologous expansion of the SN ejecta before its interaction with the expanding plasma. The computational domain is set as $[0, 3.6 \times 10^{12}]$ cm, with reflective and outflow conditions in the inner and outer boundaries, respectively. The simulations are run on an adaptive grid of 1.5×10^5 zones at the coarsest level, using 3 refinement levels with a refinement ratio of 2 for each of them, and choosing $\varphi(\mathcal{U}) = \mathcal{E}$ (see Section 2.3.4).

3.2.3 General results

The evolution from these initial conditions leads to the formation of a shock which expands until reaching the outermost part of the SN ejecta; that moment is marked as the shock breakout. After an initial expansion where γ may reach values of several tenths, the shock rapidly elgulfs enough mass to decelerate and reach a nonrelativistic velocity, typically in $t < 1$ s. The transition to the matter–dominated regime originates an inward-moving reflected wave, while the frontal shock continues to move outwards with $\beta = v_r/c \lesssim 0.1$. Such nonrelativistic expansion is maintained until the breakout, in which the sudden decrease of the density causes the shock to reach relativistic velocities, as shown in Fig. 3.10. From then on, the entire mass of the ejecta keeps expanding while cooling down. In Fig. 3.10, we show two radial distribution profiles of the velocity and laboratory frame mass density, computed for $B = 200$ at two selected values of the laboratory time. The velocity distribution peaks at the shock front, behind which the accelerated ejecta expands with $10^{-3} \lesssim \beta \lesssim 1$.

As the shock propagates, photons are trapped inside the SN ejecta. Contrarily, at the breakout, the shock reaches the ejecta's photosphere and photons begin to diffuse out, thus breaking the assumptions of RHD in that region. In this model, such photon emission is later measured as an X-ray flare. Since the Lorentz factor estimated in [161] is that of the emitter's photosphere, we must determine the location of that region in the simulations in order to make any comparison with observations. As shown, e.g., in [153], most photons are lastly scattered close to the *photospheric radius* $R_{\rm ph}$, namely the radius at which the optical depth τ calculated from the observer's line of sight equals 1. Therefore, we can estimate the

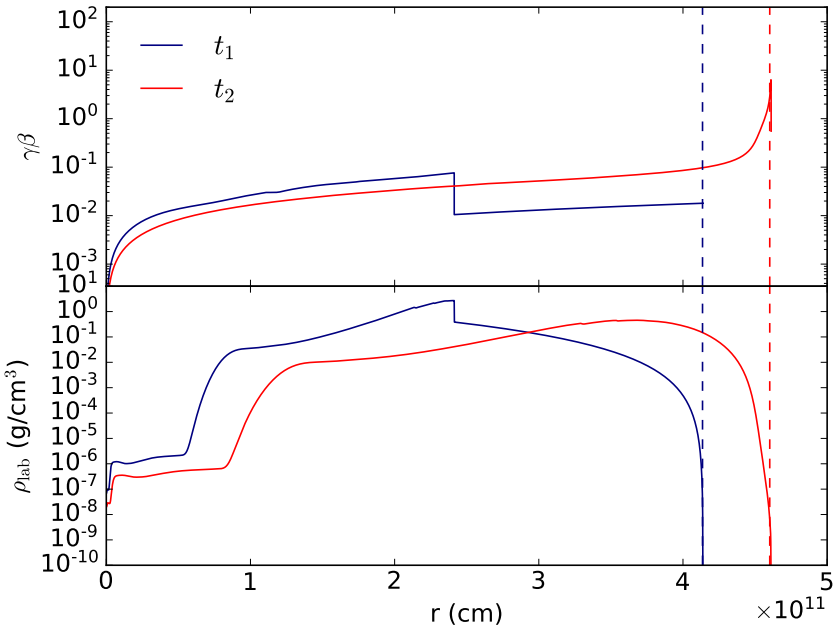

Fig. 3.10 Top panel: distribution of the velocity inside the SN ejecta at the two fixed values of the laboratory times t_1 (during the propagation of the shock within the SN ejecta) and t_2 (the breakout time). We have plotted the quantity $\gamma\beta$, recalling that $\gamma\beta \sim \beta$ when $\beta \ll 1$, and $\gamma\beta \sim \gamma$ when $\beta \sim 1$. Bottom panel: corresponding distribution of the mass density of the SN ejecta in the laboratory frame ($\rho_{\rm lab} \equiv \rho\gamma$). These particular profiles have been made using a baryon load $B = 200$. The dashed vertical lines indicate the location at each time of the photospheric radius $R_{\rm ph}$, defined as $\tau(R_{\rm ph}) = 1$. This figure is an update of the one appeared in [161].

observed γ factor in our simulations as $\gamma(R_{\rm ph})$. In this calculation, we consider that Thomson scattering constitutes the main source of opacity in the photosphere (see Chapter 5).

In a still medium, the scattering opacity of photons emitted at a radius r and observed at infinity can be computed as

$$\tau_{(v=0)} = \int_r^\infty \sigma_T \, n_e \, dl \, , \tag{3.4}$$

where $\sigma_T = 6.65 \times 10^{-25}$ cm^2 is the Thomson cross-section, and n_e is the electron density. The latter can be obtained in terms of the mass density as $n_e = Z\rho/m_a$, where m_a and Z are, respectively, the mean nuclear mass and atomic number, while the mass of electrons is neglected. We assume $Z = 1$ and $m_a = m_p$, where m_p is the proton mass. This computation is more complicated for moving matter distributions, as it requires the integration of $d\tau$ along individual photon paths while taking into account the material's motion. In particular, τ is Lorentz-invariant, as the number of scattering events along a same wordline must be the same

for different observers. A Lorentz-invariant definition of this quantity is given in [248] (see also [249]) as $d\tau = -\sigma_T j_\mu dx^\mu$, where j^μ is the four-current of particles and dx^μ is measured along the photon wordline. We can make use of this property by first considering a thin slab of constant width ΔR_0 (in the laboratory frame) and uniform electron density, moving at constant speed. In the slab's comoving frame, where the width is $\Delta R'$, the optical depth of a photon that crosses the slab from side to side is $\tau = \sigma_T\, n_e\, \Delta R'$, where n_e is the comoving electron density. The path ΔR crossed by the photon in the laboratory frame is related to $\Delta R'$ as $\Delta R = \gamma\,(1-\beta)\Delta R'$, which yields $\tau = \sigma_T\, n_e \gamma\,(1-\beta)\Delta R$ (see, e.g., [250]). On the other hand, ΔR is related to the slab's width ΔR_0 as $\Delta R_0 = (1-\beta)\Delta R$, from which $\tau = \sigma_T n_e \gamma\, \Delta R_0$. Therefore, under the condition that the ejecta's density does not change considerably along the photons' path, we estimate the optical depth of photons emitted at a given instant at a radius r (in the laboratory frame) as

$$\tau(r) = \int_r^\infty \sigma_T\, n_e\, \gamma\, dl\,, \tag{3.5}$$

and estimate at each time the radius of last scattering by inverting the implicit relation $\tau(R_{\rm ph}) = 1$.

The values of $\gamma(R_{\rm ph})$ obtained in this way are shown from the breakout time in Fig. 3.11 as a function of the observation time, for several values of B corresponding to the expansion of the e^-e^+ plasma along several different directions inside the SN ejecta. Following [141], the arrival time of photons emitted at t in the source's rest frame is computed as

$$t_{\rm obs} = t_0 + (1+z)(t - r(t)/c)\,, \tag{3.6}$$

where $r(t)$ is the position of the shock and t_0 is the arrival time of the prompt emission peak due to the expansion in the low-B directions, taken here as $t_0 = 0$. From this analysis we conclude that, in order to obtain observed γ values smaller than 4 with the chosen parameters, B must be greater than ~ 50. This result is as well approximately valid for other $E_{\rm e^-e^+}$ values, since γ is scale invariant. Thus, $\gamma(R_{\rm ph})$ depends solely on the location of $R_{\rm ph}$ at the breakout, and its value is roughly maintained if the length and mass scales are changed in such a way to maintain B constant.

To exemplify the way this model is being used to study GRBs in which multiple flares are observed, we now show the results of an ongoing analysis of GRB 160625B. The light curve of this GRB shows in its prompt emission a structure of three peaks, observed at $t_0 =$ 190, 198, and 205 s (see Fig. 3.12a, extracted from [251]), followed by a series of three X-ray flares (XRF1, XRF2, and XRF3) at $t_{\rm obs} \approx 527$, 580, and 660 s (see Fig. 3.12b). The total energies of these bursts, measured by the detectors on board of the *Fermi* and *Swift*

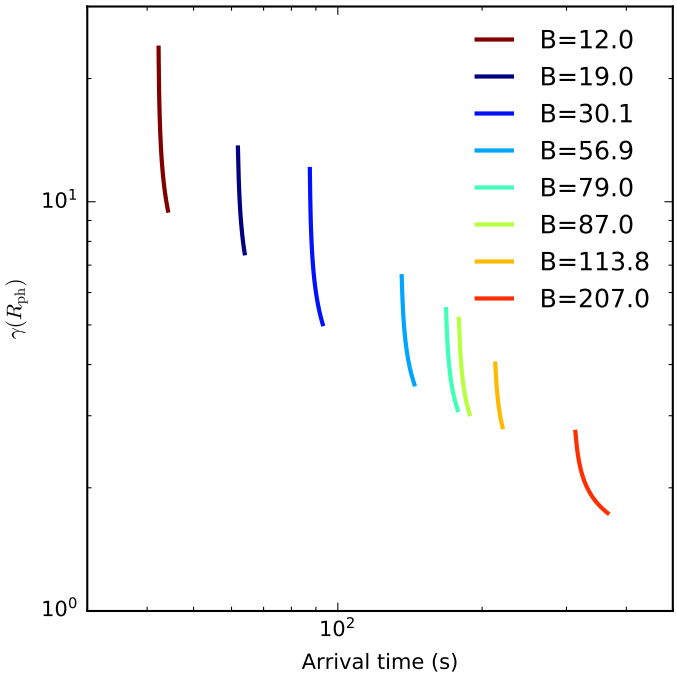

Fig. 3.11 Lorentz γ factor at the photospheric radius as a function of the arrival time for $E_{e^-e^+} = 1.35 \times 10^{53}$ erg and various selected values of the baryon load B, corresponding to the expansion along different directions inside the SN ejecta. This figure is an update of the ones appeared in [56, 161].

satellites, were determined as $E_{\rm prompt} = (3.05 \pm 0.01) \times 10^{54}$ for the prompt phase and $E_{\rm f} = (2.87 \pm 0.01) \times 10^{53}$ for the flares [251]. In the BdHN IV model, a possible explanation for these features is given by the emission of three separate bursts from the BH. In this scenario, the shocks created in each of these emission episodes expand in high-B directions within the SN ejecta, consequently emitting three X-ray flares.

For each of the three flares, we have made an independent simulation like the ones already described in this section. In each of them, the initial plasma energy is set as $E_{\rm prompt}/3$. For consistency with the parameters of the BdHN model, the proportionality constant in Eq. (3.3) is fixed for each R_0 in such a way that the equivalent isotropic mass of the density profile is $M = 6.7\ M_\odot$, and hence $B = 12$ for each shock. For each simulation, R_0 is fixed in such a way to reproduce the observed times, which are computed from Eq. (3.6) with a redshift $z = 1.406$ [251]. In this way, we obtain constraints on the system size and the observed Lorentz factors. The breakout radius r_b, defined as the shock's position at the breakout, and the observed Lorentz factor at the breakout are shown for each flare in Table 3.1, together with the corresponding values of R_0.

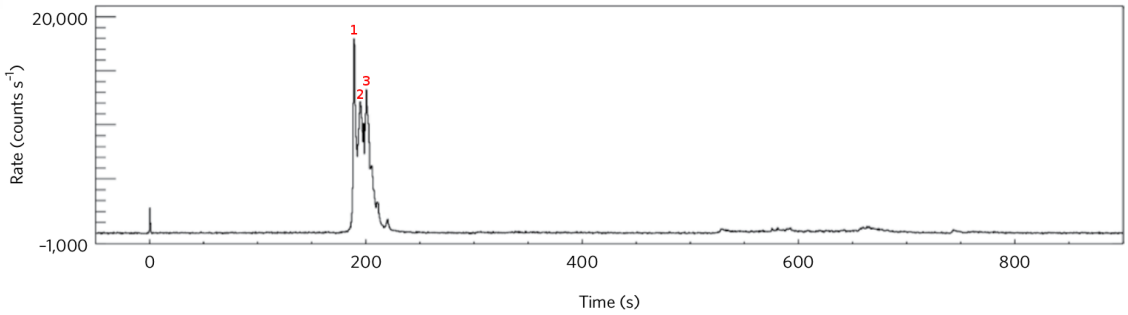

(a)

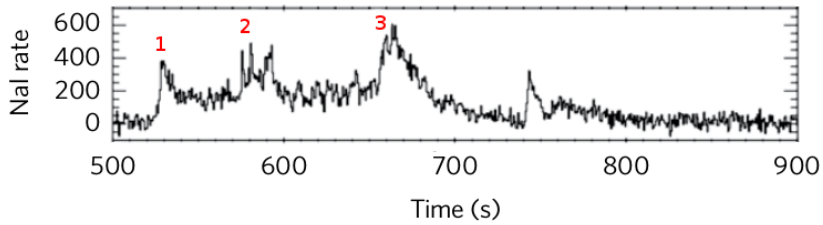

(b)

Fig. 3.12 Fermi/GBM NaI ($8-1000$ keV) light curve of GRB 160625B (extracted from [251]), where we have indicated the three flares considered by our analysis, and their corresponding peaks in the prompt phase (red characters). (a): Full light curve, including the precursor, the prompt emission, and the X-ray flares. (b): Detail of the X-ray flares.

This analysis method has the disadvantage of relying on the manual identification of the origin of the different peaks observed in the light curves (see, e.g., [170], where the same approach is followed). For instance, the three peaks in the prompt emission are here interpreted as originated in the irregular activity of the central engine, whereas in other GRBs they are interpreted as being originated in the interaction of a single emitted shell with an irregularly shaped CBM (see [229]). Furthermore, no explanation is yet given by this model for what could be identified as a fourth X-ray flare at $t_{\rm obs} \approx 743$ s (see Fig. 3.12b). Therefore, the above analysis must be regarded as a consistency check of the model depending on an ad-hoc assumption made for the shape of the light curve.

3.2.4 Observed radiation

Since radiation decouples from matter at the photosphere, a large fraction of photons diffuses out instead of staying in equilibrium and accelerating the outermost regions of the SN ejecta up to relativistic speeds. Since radiation is the main source of pressure in the shocked region, we could expect matter in the photosphere to be accelerated to smaller Lorentz factors than those predicted by our hydrodynamical computations. Therefore, the obtained γ factors at $R_{\rm ph}$

Flare	R_0 ($\times 10^{12}$ cm)	$r_{\rm b}$ ($\times 10^{12}$ cm)	$\gamma_{\rm obs}$
XRF1	3.78	3.92	3.43
XRF2	4.28	4.44	3.40
XRF3	5.10	5.30	3.38

Table 3.1 Values of the initial radius of the SN ejecta (R_0), the breakout radius ($r_{\rm b}$) and the observed Lorentz factor ($\gamma_{\rm obs} = \gamma(R_{\rm ph})$) resulting from the 1D RHD simulations of the X-ray flares in GRB 160625B.

must be regarded as an upper limit[4]. However, we can make some additional observational estimations with the data from the already-made simulations.

A key element of this model is the assumption that the described breakout process produces a Doppler-shifted blackbody spectrum given by Planck's law,

$$N_{\rm BB}(E) \propto \frac{E^2}{e^{E/k_{\rm B}T_{\rm obs}} - 1}\,, \tag{3.7}$$

where $N \equiv d\mathcal{N}/dE$ is the number $\mathcal{N}$ of photons measured in the energy interval $(E, E+dE)$. The observed temperature $T_{\rm obs}$ is related to the comoving temperature $T_{\rm comov}$ as

$$T_{\rm obs} = \frac{T_{\rm comov}}{\gamma(1-\beta)(1+z)} \tag{3.8}$$

(see, e.g., [142]), where z is the redshift of the source. The panorama gets more complicated when considering emission from different points of a radiating surface, in which case we should observe a multicolor blackbody. This effect is not considered in [161], where the fitting of the thermal component is made using a blackbody law to give an estimate of the comoving temperature. Under this assumption, we can estimate the observed temperatures from the RHD simulations by approximating $T_{\rm comov} = T(R_{\rm ph})$ in Equation (3.8). In Fig. 3.13 we have plotted this quantity from the breakout time for the parameters of GRB 081008, as a function of the arrival time. The observed temperature of this GRB is (0.32 ± 0.03) keV, which is consistent with the values predicted for $B \gtrsim 50$. The temperatures reported in [161] are in the range $0.32 - 0.92$ keV for similar values of $E_{\rm iso}$, which are in good agreement with the values shown in Fig. 3.13.

The spectrum produced by the shock breakout depends in general on the processes occurring in the photosphere before photons are lastly scattered. Since in that region scattering

[4]In Chapter 5, it is shown how this γ estimation is likely to be accurate even if radiation transport is considered.

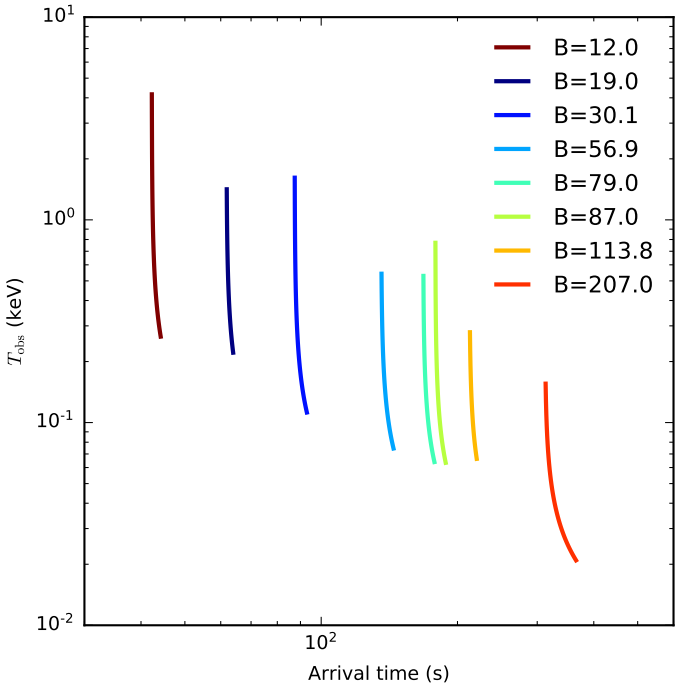

Fig. 3.13 Observed temperature as a function of the arrival time for $E_{e^-e^+} = 3.16 \times 10^{53}$, $z = 1.967$, and various selected values of the baryon load B.

is the main source of opacity, an initial thermal-like photon distribution can be significantly modified by incoherent Compton scattering (i.e., involving energy transfer; see Section 4.1.3). This is studied, e.g., in [252] for mildly relativistic shock breakouts in supernovae, and in [153, 253] for highly relativistic outflows. A main feature of these models is that the departure from a blackbody spectrum should be more important for matter–dominated than for radiation–dominated flows, since in the latter case the energy budget of heating through this process is negligible compared with the total thermally distributed photon energy. Due to the high baryon loads considered in this model, the shocked regions are always matter–dominated at the breakout, even for the lowest values of B and the highest initial energies. Thus, it is likely that the emitted spectrum is modified by Compton scattering, which can increase the peak energy of the observed distribution (see, e.g., [253]). Hence, more precise computations of this process (e.g., Monte Carlo simulations) are required in order to compute the emitted spectra at the breakout. On the other hand, Comptonization tends to significantly reduce the slope of the low-energy part of the spectrum if the emitting flow is relativistic (see [253]), which can be fitted as a power law

$$N(E) \propto E^{\alpha}\,, \tag{3.9}$$

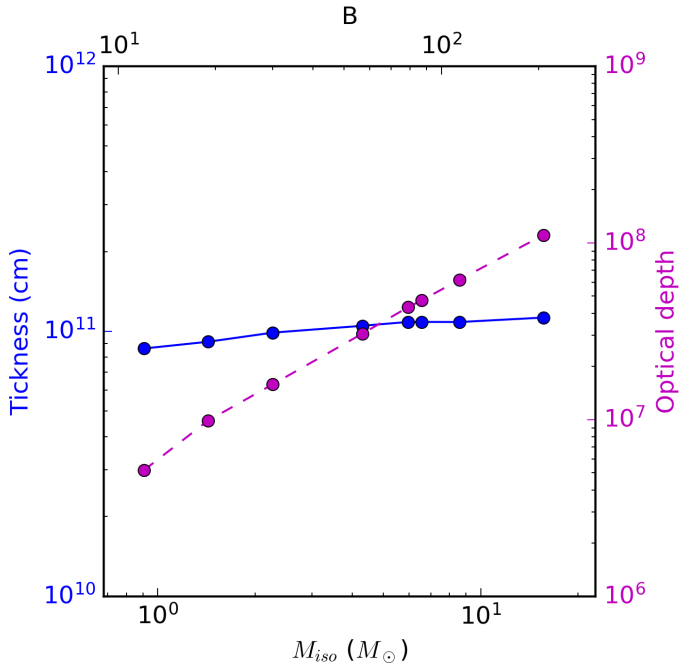

Fig. 3.14 Thickness (blue circles) and optical depth (purple circles) at the breakout time of the region containing 1% of $E_{\rm prompt}$ in the simulation of the X-ray flare of GRB 081008, plotted as a function of the total isotropic mass $M_{\rm iso}$. The corresponding values of the baryon load B used in each case are shown in the upper axis.

where α is the low-energy photon index. The determination of α can provide useful information of the processes occurring in the emitting region, as it can be used to distinguish departures from the $\alpha = 1$ value predicted by the Rayleigh-Jeans law ($N_{\rm BB}(E) \propto E$ for $E \ll k_{\rm B}T$). However, in this case, the low-energy parts of the measured spectra are dominated by the power-law component arising from other processes (e.g., synchrotron emission; see e.g. [162]), and therefore this phenomenon cannot be observed.

On average, the total energy emitted in X-ray flares is 10% of the energy emitted in the $15 - 150$ keV band during the prompt phase [243]. In some cases, a large fraction of this energy is in the observed thermal component [161]. An example is given by GRB 081008, for which the energy in the flaring phase is at least 1% of $E_{\rm prompt}$. Using the above-described shock breakout model, we can estimate the time in which this energy is emitted by computing the diffusion timescale $t_{\rm diff}$ due to photon scattering. We estimate this quantity as

$$t_{\rm diff} \approx \frac{3\tau l}{c} \tag{3.10}$$

(see, e.g., [254]), where l and τ are, respectively, the width and optical depth of the region in which 1% of the injected energy is contained. For $B = 50$, we obtain $l \approx 10^{11}$ cm

and $\tau \approx 3 \times 10^7$, which gives $t_{\rm diff} \approx 3 \times 10^8$ s. Similar values are obtained for different values of B, since both l and τ stay within the same orders of magnitude for different initial configurations, as shown in Fig. 3.14. This time can be compared to the dynamical timescale of the expansion, in particular with the time during which the emission takes place. In our simulations, the spectral peak energy associated to the observed temperature falls under the observable limit of *Swift*/XRT (~ 0.3 keV) approximately 10 s after the breakout, due to the adiabatic cooling of the material. In that entire time, the optical depth of the region containing 1% of $E_{\rm prompt}$ remains of the order of 10^7. Therefore, the material remains opaque, and most of the internal energy is converted into the kinetic energy of the outflow instead of being radiated. This conclusion is supported by the preliminary radiative transfer computations shown in Chapter 5. Conversely, we can estimate the energy emitted at the breakout by computing the energy contained in the photosphere at that moment. This gives an energy $E \sim 10^{46}$ erg, and a diffusion time of $t_{\rm diff} \sim 10^{-2}$ s, which is much smaller than the dynamical times. We should therefore expect an initial emitted power of 10^{48} erg/s lasting $\sim 10^{-2}$ s, followed by a fast decay and a posterior slow diffusion of the photons from the inner layers of the ejecta. We conclude that an additional mechanism must be included in this model to explain the complete thermal emission observed in X-ray flares. Possible alternatives, still unexplored in this model, are the reheating of the ejecta due to its interaction with energetic particles emitted from the BH, the emission of photons due to proton-proton interaction within the ejecta, and different mechanisms for the reignition of the central engine.

3.3 Model of the prompt emission in GRB 190114C

We now explore a model for the particular form of the light curve of GRB 190114C in its prompt phase. The isotropic energy of this GRB in the range 1 keV$-$10 MeV has been determined as $E_{\rm iso} = (2.48 \pm 0.22) \times 10^{53}$ erg [107], and its redshift as $z = (0.4245 \pm 0.0005)$ [255]. The light curve of GRB 190114C measured by the Gamma-ray Burst Monitor (GBM) of the *Fermi* satellite is shown in Fig. 3.15, where two emission events can be distinguished. Within the first structured spike (between 0 and 6 s in the observer's frame), the emission between $t = 2.7$ and 6 s is interpreted in the BdHN model as being originated by the expansion of the $e^- e^+$ plasma in the low-B directions of the SN ejecta, and its posterior interaction with the CBM. The isotropic energy of this last interval is $E'_{\rm iso} = (1.47 \pm 0.2) \times 10^{53}$ erg in the mentioned energy range [256]. On the other hand, we see a second spike that starts after 16 s and lasts for 13 s, whose isotropic energy is 5% of $E_{\rm iso}$. The time-integrated spectrum of this spike is best-fitted by a cut-off power law $N(E) = (E/E_{\rm piv})^\alpha e^{-E/E_0}$, with $\alpha \lesssim -1.6$ [107].

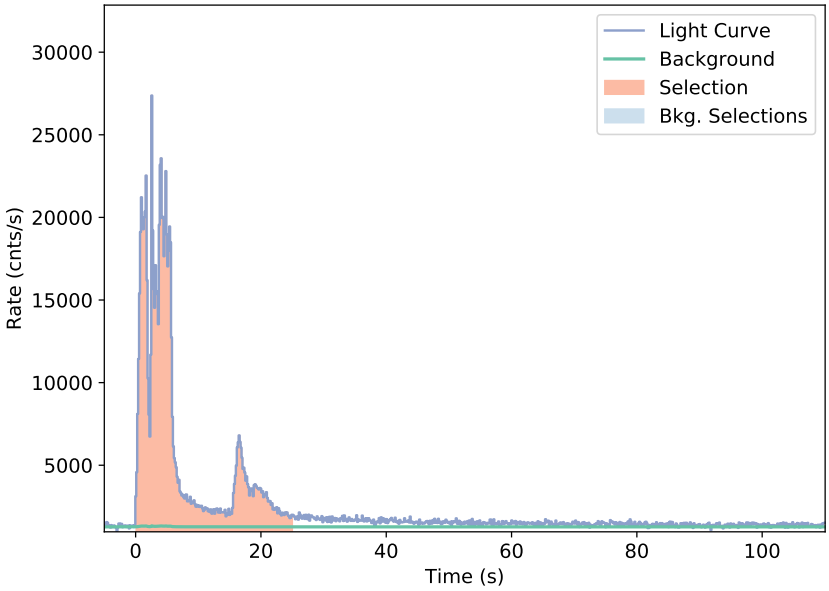

Fig. 3.15 Count light curve of the prompt phase of GRB 190114C measured by *Fermi*/GBM (8 keV−30 MeV), extracted from [107].

As mentioned in Chapter 1, such α values are below the fast-cooling limit of synchrotron shock models.

As well as X-ray flares, the occurrence of irregular spikes in the prompt emission is commonly explained in the literature as being originated in the irregular activity of the central engine (see, e.g., [257]). A different interpretation of this particular spike is given by the BdHN model [231]. Numerical simulations of the interaction between the SN ejecta and the NS (see [167]) in BdHNe I show that, just prior to the BH formation, the accreting NS is surrounded by a low-density cavity (see Fig. 3.8). Once the NS has collapsed, the e^-e^+ plasma expands inside this cavity and eventually impacts its walls, producing a significant increase of their temperature. This process creates a reflected wave that propagates from the cavity walls towards its interior. Since the cavity is transparent to radiation, thermal radiation emitted at its walls escapes in the observer's direction. The emission of most of the internal energy of the reflected wave is thus proposed in this model to produce the mentioned second spike. In Section 3.3.1 we provide a simplified analytical description of this process and obtain an estimate of the temperature reached by the cavity walls after the collision. In Section 3.3.2, we show the results of an RHD simulation of the same process, and discuss some observational consequences of this model.

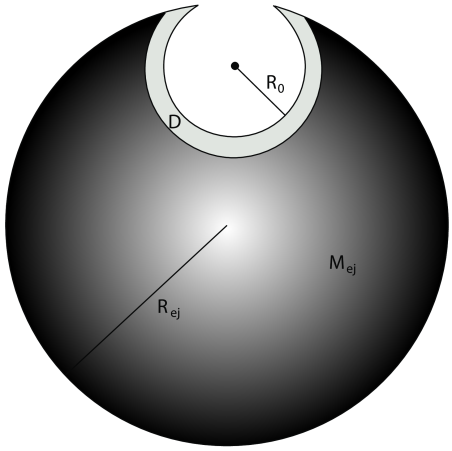

Fig. 3.16 Schematic representation of the cavity in the SN ejecta surrrounding the newly formed BH in the BdHN model. Reproduced from [231].

3.3.1 Simplified model of the interaction of the e^-e^+ plasma and the SN ejecta

We now show a simplified model of the cavity within the SN ejecta, and its interaction with the e^-e^+ plasma. A spherical cavity of initial radius R_0 is located close to the outermost regions of a spherical matter distribution of radius $R_{\rm ej}$ and total mass $M_{\rm ej}$, which here represents the SN ejecta (see Fig. 3.16). The cavity has an opening, which is in this model directed towards the observer (see the left panel of Fig. 3.8). The e^-e^+ plasma, initially located in the center of the cavity, expands isotropically as a blast wave due to its own internal pressure (see Section 3.1). Part of this outburst is directed towards the observer, whereas the portion of the plasma that is emitted towards the SN goes through the cavity and reaches its walls. When the impact occurs, a strong shock wave forms and propagates inside the SN ejecta while decelerating, until it stalls at a radius R. Through this process, the kinetic energy of the e^-e^+ plasma is converted into internal energy in the ejecta. The temperature of the shocked region can be estimated by using conservation of energy-momentum, as we now show.

Assuming that the density of the SN ejecta is uniform, its value can be estimated as

$$\rho = \frac{3M_{ej}}{4\pi R_{ej}^3}\,, \tag{3.11}$$

We model the interaction between the e^-e^+ plasma and the SN ejecta as an inelastic collision. Assuming that no energy is lost in radiation during this interaction, we can integrate the energy-momentum conservation laws (Eqs. (2.5) and (2.6)) in a volume $\mathcal{D}$ that contains the shocked region. This yields the following conservation equations:

$$\begin{aligned} \frac{d}{dt}\left(M\gamma + W\gamma\right) &= 0 \\ \frac{d}{dt}\left(M\gamma v + W\gamma v + W'\gamma v\right) &= 0\,, \end{aligned} \tag{3.12}$$

where $\gamma = 1/\sqrt{1-v^2}$ is the Lorentz factor of the shocked material, v its bulk velocity (assumed to be uniform in $\mathcal{D}$), M is the mass of the ejecta swept up by the shock wave, and W and W' are defined as

$$\begin{aligned} W &= \frac{1}{\gamma}\int_{\mathcal{D}} \left[(\epsilon + p)\gamma^2 - p\right]\, dV \\ W' &= \frac{1}{\gamma}\int_{\mathcal{D}} p\, dV\,, \end{aligned} \tag{3.13}$$

where ϵ and p are, respectively, the comoving internal energy density and pressure of the expanding material. For simplicity, we neglect W' as a first approximation, since $W'/W \sim 1/\gamma^2$ for large γ. On the other hand, $W\gamma$ gives the value of the integrated covariant internal energy of the plasma. We can now use (3.12) to compare two states: one where matter is at rest and the radiation–dominated plasma approaches the walls at $v \sim c$, and a posterior one after the walls of the cavity have been impacted. This yields

$$E + Mc^2 = \left(Mc^2 + W\right)\gamma, \tag{3.14}$$

$$E\,c = \left(Mc^2 + W\right)\gamma v\,, \tag{3.15}$$

where E is the initial energy of the e^-e^+ plasma. We now introduce the new variables

$$B = \frac{Mc^2}{E}, \qquad \omega = \frac{W}{Mc^2}, \qquad u = \gamma\frac{v}{c} \tag{3.16}$$

and rewrite the energy-momentum conservation as

$$B^{-1} = (\omega + 1)\sqrt{u^2 + 1} - 1, \tag{3.17}$$

$$B^{-1} = (\omega + 1)\, u. \tag{3.18}$$

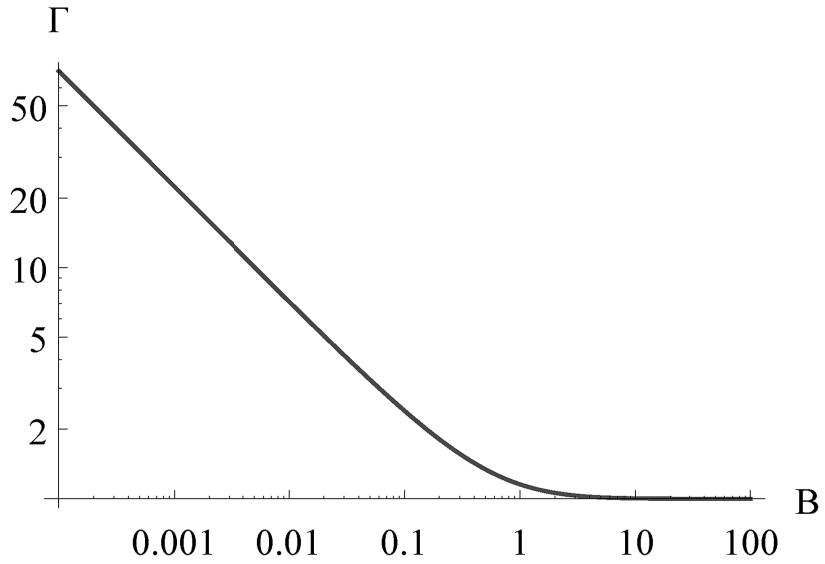

Fig. 3.17 Lorentz γ factor of the shock wave generated by the impact of the $e^- e^+$ pulse on the walls of the cavity as a function of the engulfed mass, parametrized by $B = Mc^2/E$. Reproduced from [231].

The solution to this system reads [254]

$$u = \left(B \sqrt{1 + \frac{2}{B}} \right)^{-1} , \qquad \frac{W}{E} = \omega B = \frac{1}{u} - B. \tag{3.19}$$

The bulk Lorentz factor can be computed from this expression as $\gamma = \sqrt{1 + u^2}$. The resulting function $\gamma(B)$ is shown in Fig. 3.17, from where it is clear that the shock wave becomes nonrelativistic when

$$E = Mc^2. \tag{3.20}$$

Assuming that the ejecta has a constant density, the radius R at which this happens can be computed by inverting the following relation:

$$M = \frac{4\pi}{3} \rho \left(R^3 - R_0^3 \right) , \tag{3.21}$$

from where

$$R = R_{\rm ej} \left[\left(\frac{R_0}{R_{\rm ej}} \right)^3 + \frac{E}{M_{\rm ej} c^2} \right]^{1/3} . \tag{3.22}$$

For the typical parameters of the model, we have $(R_0/R_{\rm ej})^3 \ll E/M_{\rm ej}c^2$, which gives the following stalling radius:

$$R \simeq 2.7\times10^{11}\left(\frac{E}{10^{53}\,\rm erg}\right)^{1/3}\left(\frac{M_{ej}}{4M_\odot}\right)^{-1/3}\frac{R_{ej}}{10^{12}\,\rm cm}\,\rm cm\,. \tag{3.23}$$

Finally, considering that at that radius all of the internal energy is uniformly contained within a region of thickness $l \ll R$, we can estimate the temperature of the shocked region as

$$\begin{aligned} T &= \left(\frac{W}{4\pi a_R R^2\, l}\right)^{1/4} \\ &\simeq 17\left(\frac{E}{10^{53}\,\rm erg}\right)^{1/12}\left(\frac{R_{\rm ej}}{10^{12}\,\rm cm}\right)^{-1/2}\left(\frac{M_{\rm ej}}{4M_\odot}\right)^{-1/6}\left(\frac{l}{10^{10}\,\rm cm}\right)^{-1/4}\rm keV. \end{aligned} \tag{3.24}$$

where a_R is the radiation constant and we have taken $W \simeq E$ (see Eq. (3.14)). In particular, these results are independent of R_0 under the condition $(R_0/R_{\rm ej})^3 \ll E/M_{\rm ej}c^2$, which means that they also hold in the particular case in which there is no initial cavity ($R_0 = 0$). In that case, the mentioned reflected wave should also be formed due to the interaction of the expanding plasma with the SN material. Since a low-density region is formed in either case by the blast wave itself, the results of this model do not depend on the existence of a cavity before the expansion of the e^-e^+ plasma.

3.3.2 RHD simulation

We have studied the above-described model in more detail by performing a 2D RHD simulation, where the initial conditions have been set following the simplified model shown in Fig. 3.16. Given the axial symmetry of this setup, we have solved the RHD equations in cylindrical coordinates, using a uniform grid of resolution 2048×1024. For this approach to be valid, we must assume local thermal equilibrium between photons and material particles during the time of the simulation. As in Section 3.2, we have self-consistently verified that applying the EoS for an e^-e^+–baryon plasma (see Appendix B) is equivalent to assuming a constant polytropic index $\Gamma = 4/3$ in all regions occupied by the plasma and $\Gamma = 5/3$ in all unshocked regions. This time we impose this by applying the Taub-Mathews EoS (Eq. (2.10)).

We consider a SN ejecta in initial homologous expansion with a radial velocity of $3\times10^{-3}\,c$. This matter distribution is assumed to have an initial homogeneous density, in such a way that the total mass of the ejecta is $M_{\rm ej} = 4\ M_\odot$. We locate a spherical cavity centered at a distance of 1.4×10^{11} cm from the edge of the SN ejecta, so that the latter has an opening, as

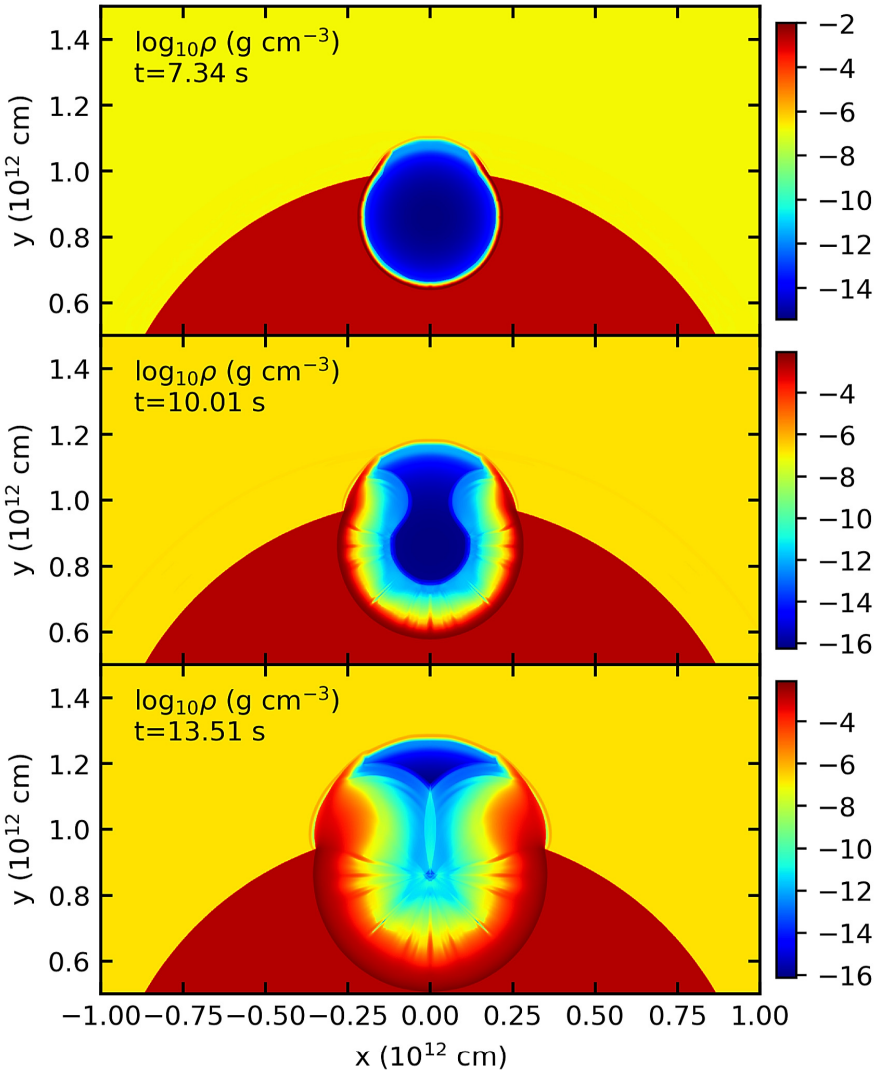

Fig. 3.18 Spatial distribution of matter density at different instants of time: the formation of a reflected wave at $t \approx 7.3$ s due to the impact of the $e^- e^+$ plasma on the cavity walls (top), the propagation of this wave at $t = 10$ s (middle), and the moment it reaches the origin at $t = 13.5$ s (bottom). Reproduced from [231].

portraited in Fig. 3.16. The initial radii of the cavity and the ejecta are set as $R_0 = 1.7 \times 10^{11}$ cm and $R_{\rm ej} = 10^{12}$ cm respectively. These values are chosen in such a way to reproduce the timing of the second spike in the considered light curve. Outside the ejecta and within the cavity, a minimum initial density is fixed as $\rho_{\rm cav} = 10^{-7}$ g/cm^3. As in Section 3.2, the $e^- e^+$ plasma is represented as an initially still uniform energy distribution located in a region of radius 10^{10} cm around the center of the cavity, in such a way that its total energy is $E_0 = 10^{53}$ erg.

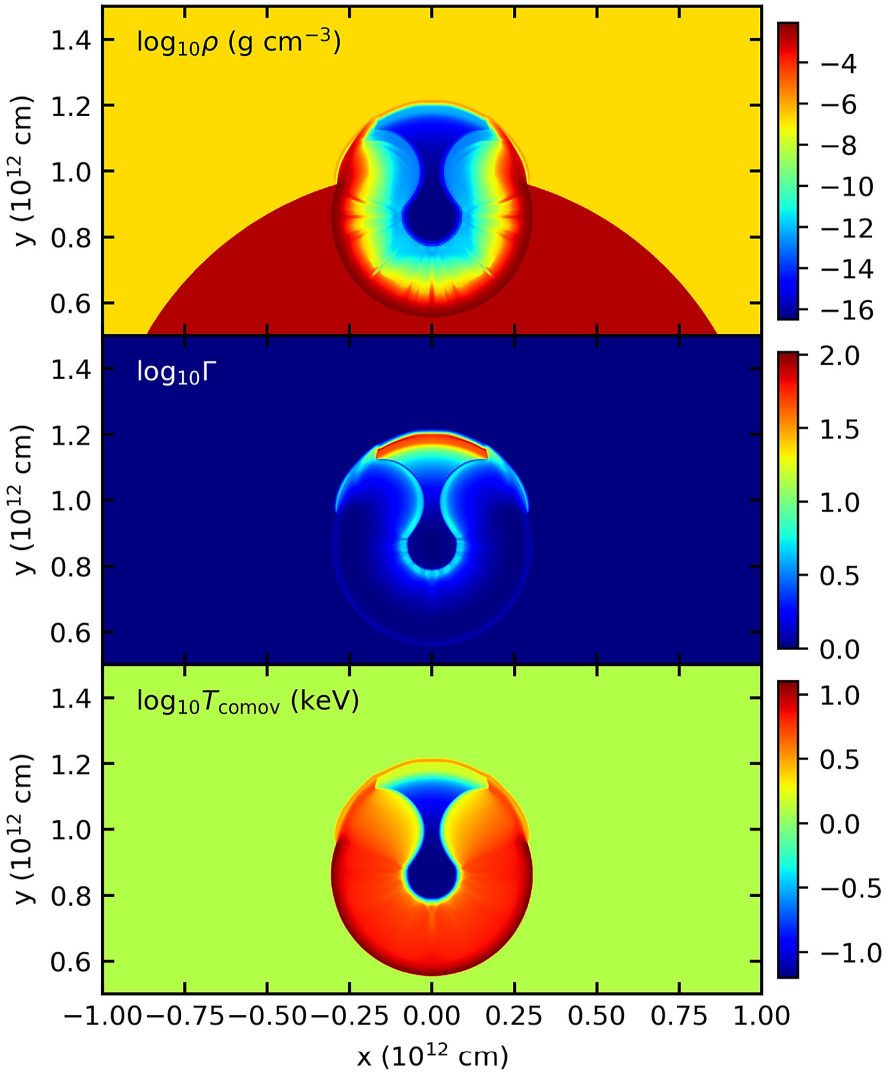

Fig. 3.19 Spatial distributions of matter density (top), Lorentz factor (middle) and comoving temperature (bottom) at $t = 11$ s, showing the mildly relativistic reflection wave propagating in the cavity, as well as the ultrarelativistic e^-e^+ plasma wave propagating outside of it. A shock wave propagating inside the SN material can also be seen. Reproduced from [231].

Since the baryon load in the cavity is small ($B \sim 10^{-4}$), the e^-e^+ plasma expands and reaches a bulk Lorentz factor of a few tenths before it impacts on the walls of the cavity at $t_{imp} = 4.5$ s. The baryons inside the cavity are swept by the expanding plasma, which reduces its matter density to $\rho \sim 10^{-14}$ g/cm^3, as shown in Fig. 3.18. The portion of the plasma that expands towards the opening continues to accelerate to $\gamma \sim 100$ as described in Section 3.1, and produces in this scenario the initial stages of the prompt emission. This process can be seen in Fig. 3.19, where we have plotted the Lorentz factor, matter density, and comoving temperature distributions at $t = 11$ s in a plane that contains the axis of symmetry. Due to the

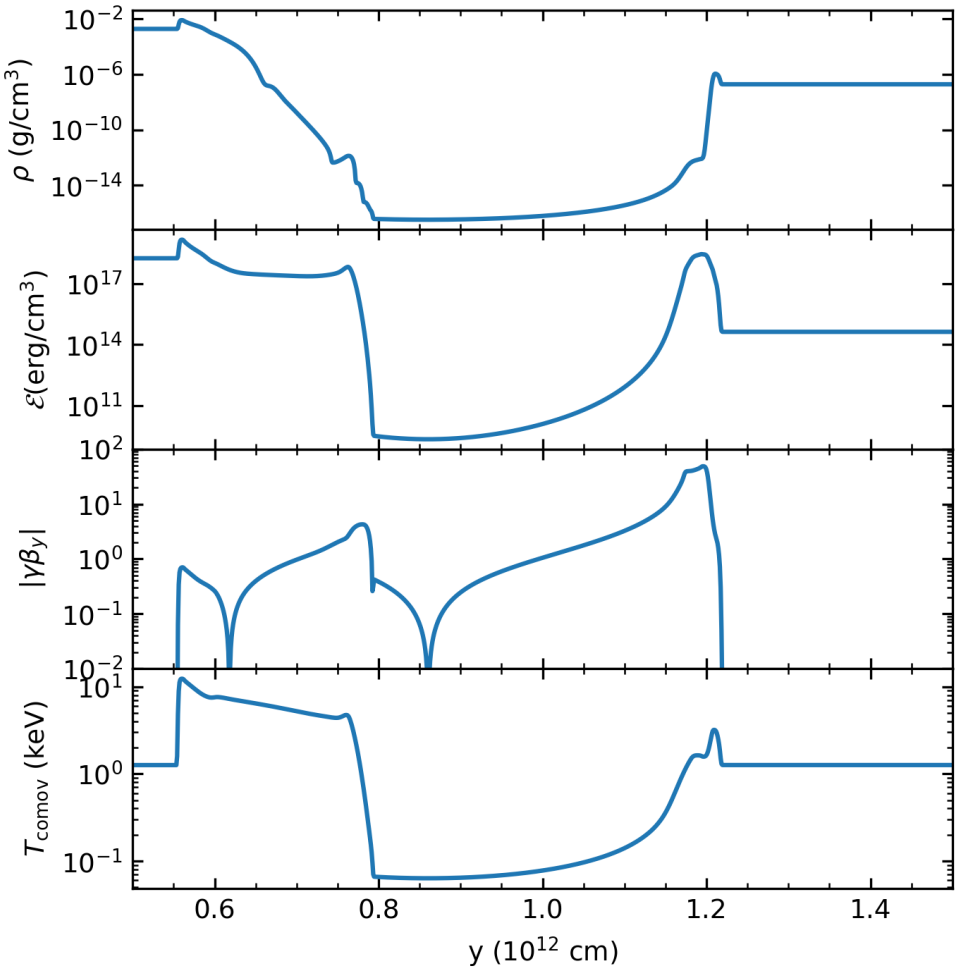

Fig. 3.20 Spatial distributions along the axis of matter density, total energy $\mathcal{E}$, $|\gamma\beta_y|$ and comoving temperature at $t = 11$ s. At $y \approx 6 \times 10^{11}$ cm, the shock created by the collision between the plasma and the SN ejecta propagates with $|\gamma\beta_y| \sim 1$, with a comoving temperature $T_{\rm comov} \approx 12$ keV. A reflected wave with a maximum Lorentz factor of ~ 4 and maximum $T_{\rm comov} \approx 5$ keV propagates towards the observer at $y \lesssim 7.9 \times 10^{11}$ cm. Between 8×10^{11} and 1.2×10^{12} cm, baryons have been evacuated by the e^-e^+ plasma, which at that time has been accelerated to a maximum bulk Lorentz factor of about 60 in the low-density regions at $y \approx 1.2 \times 10^{12}$ cm. Reproduced from [231].

impact of the e^-e^+ plasma onto the cavity walls, the temperature of the SN material rises up to 14.5 keV in a region of width of the order of $\sim 10^{10}$ cm, in agreement with the analysis made in Section 3.3.1. This collision produces a shock wave that propagates inside the SN material (see Figs. 3.18 and 3.19). The bulk speed of this wave remains relativistic ($\gamma \sim 10 - 30$) until $t \approx 7.3$ s, when the shock stalls. This occurs once the shock has propagated a distance $R \approx 2.2$ cm from its origin, which is slightly under the value estimated in Section 3.3.1 (see

Eq. (3.23)). From that moment, most of the energy in this shock continues to be transported inside the SN ejecta with $\gamma \sim 1$, as shown in Fig. 3.20, where we have plotted ρ, $\mathcal{E}$, $\gamma\beta$ and the comoving temperature of the material along the axis of symmetry. At that time, part of the shock's energy is converted into a radiation–dominated reflected wave (see Figs. 3.18–3.20), that propagates towards the interior of the cavity. This wave, initially nonrelativistic, accelerates up to $\gamma \sim 5$ due to its own internal pressure and reaches the center of the cavity at $t = 13.5$ s, maintaining throughout this evolution a comoving temperature of ~ 5 keV.

Since the interior of the cavity is transparent to radiation (its optical depth along the symmetry axis between $y = 7.5 \times 10^{11}$ and 1.15×10^{12} cm drops to 10^{-3} at $t = 11$ s), radiation can freely stream in it from the front of the reflected wave. In this model, this marks the beginning of the secondary photon emission observed in the light curve. At that moment, the separation of the outward-moving relativistic shock and the cavity walls along the axis of symmetry is equal to R_0. Since the expansion of the plasma occurs at $v \sim c$, $\Delta t_{\rm obs}$ can be computed as

$$\Delta t_{\rm obs} = (1+z)\, R_0/c \approx 16\,{\rm s}, \tag{3.25}$$

which justifies the choice of the R_0 parameter. On the other hand, we estimate the emitted energy by computing the total internal energy contained in the cavity once the reflected wave reaches its center, which gives a value of $E_r = 8.3 \times 10^{51}$ erg. Provided a large fraction of this energy is emitted towards the observer through the opening, the total emitted energy in this event roughly agrees with the energy in the second spike in the light curve in Fig. 3.15.

If we assume that photons are thermal near the front of the reflected wave, we can expect the radiated spectrum to correspond to a Doppler-shifted blackbody with a peak energy of $T_p = \frac{3k_{\rm B}T_{\rm comov}}{\gamma(1-\beta)} \sim 50$ keV. However, in that region, matter is moving relativistically towards the observer with a nonnegligible scattering optical depth. Consequently, the radiation generated by the walls of the cavity will experience inverse Compton scattering on the relativistically moving matter, which shifts the peak energy towards higher values. If this process is dominant with respect to the free-streaming of thermal photons, we can expect the observed spectrum to be similar to a Comptonized blackbody (see [253]), peaked at $E_p \sim \gamma^2 3kT \simeq 200 - 300$ keV.[5] This qualitatively agrees with the observed time-integrated spectrum of the second spike of GRB190114C, which has a peak energy $E_p = 252$ keV [259]. On the other hand, as shown in [253], Comptonization can also explain the low-energy photon index $\alpha \lesssim -1.6$ inferred for this spike. Furthermore, the time-resolved spectrum shows a decreasing tendency of the peak energy, in agreement with the cooling of the expanding walls of the cavity (see [107]).

[5] This comes from the fact that inverse Compton scattering increases the photon energy by a factor of the order of γ^2 [258].

The above model has been proposed in [231, 259] to explain a series of spikes observed in the light curves of GRBs 090926A, 130427A, and 160625B. These light curves have a rather complex structure, and the identification of the emission produced by the reflected wave is entirely manual. A systematic analysis of more sources with a similar behavior is thus required in order to support the plausibility of this model, and further theoretical developments are required in order to produce observables that help distinguish this scenario from other possible explanations (for instance, internal shocks in relativistic fireballs).

We finally recall that, since the cavity becomes transparent due to the expansion of the e^-e^+ plasma, LTE cannot be assumed in its interior, which renders the hydrodynamical description inapplicable in that region of space. Yet, we can safely expect that this does not significantly affect matter dynamics inside the cavity, since at those times most energy is contained in the SN ejecta. However, since the cavity walls irradiate part of their energy, the reflected wave could in principle have smaller speeds than predicted by our adiabatic model.

3.4 Conclusions

We have studied three different processes occurring in the BdHN model: (I) the expansion of an e^-e^+ plasma from the BH in low-density regions of the SN ejecta, proposed to be responsible for the prompt emission; (II) the breakout of shocks in regions of high density, proposed to produce X-ray flares; and (III) the creation of reflected waves due to the interaction of the plasma and the SN ejecta in high-density regions, proposed to emit secondary bursts in some GRB light curves.

We studied the validity of the constant-width approach by making 1D RHD simulations of the accelerating (radiation–dominated) stages of the e^-e^+ plasma in a low-B regime. We have compared these results with a simplified simulation made assuming that all energy is contained in a shell of constant width. In both approaches a similar bulk Lorentz factor is obtained at all instants of the pulse's evolution, owing to the conservation of total energy-momentum. Contrarily, intensive quantities like the mass density and the pressure have a sharper decrease in the RHD approach due to the spreading of the pulse. We have studied the pulse's shape using different resolutions, obtaining that this spreading is caused partially by numerical diffusion. On top of this, the velocity gradients across the pulse are consistent with the occurrence of some hydrodynamical spreading, in accordance with previous studies of this process. In particular, we have shown that the constant-width approximation tends to underestimate the decrease of the plasma's comoving temperature.

We have explored the BdHN model for X-ray flares through a series of 1D RHD simulations. The initially relativistic shock created by the expansion of the e^-e^+ plasma is slowed

down typically in $t < 1$ s, producing a nonrelativistic shock that crosses the SN ejecta. The shock's velocity is increased again at its breakout, reaching a bulk Lorentz γ factor of a few tenths. For the parameters of GRB 081008, the values of γ at the ejecta's photosphere are consistent with those estimated in [161] ($\gamma \lesssim 4$) if the direction of expansion is such that $B \gtrsim 50$. We have used this same approach to make an estimation of the dimensions of the SN ejecta in GRB 160625B needed to reproduce the observed times of three X-ray flares observed in its light curve. We have discussed the observational properties of this model, concluding that the emitted spectrum should exhibit a significant degree of Comptonization. Assuming perfect Blackbody emission, we have estimated the observed temperature obtaining values consistent with GRB 081008 and other GRBs studied in [161] with similar values of $E_{\rm iso}$. We have shown that, despite this model can self-consistently explain the observed times and temperatures of the flares, it cannot produce an efficient energy emission in the required timescales, due to the opacity of the SN ejecta. Hence, additional processes must be considered in the BdHN model in order to better explain the observed thermal emission.

We have studied an emission mechanism for a peak observed 16 s after the main episode in the light curve of GRB 190114C, consisting in the creation of a reflected wave in the SN ejecta due to its interaction with the expansive e^-e^+ plasma. We have made a simplified analytical estimation of the maximum temperature at the shocked region in the ejecta, obtaining a value of $T \sim 17$ keV for typical parameters. We have performed a 2D RHD simulation of this process that confirms this estimation, where we have fixed the system's dimensions in such a way to explain the observed times while being consistent with typical BdHN parameters. In it, the expansive e^-e^+ plasma creates a low-density cavity that becomes optically thin, and allows the photons emitted at the cavity walls to stream towards a distant observer. Provided that a large fraction of the internal energy contained in the cavity when the reflected wave reaches its center is emitted, this model explains the total energy of the second peak in the light curve. Additionally, the observed peak spectral energy and low-energy photon index can be explained by assuming the emitted radiation is highly Comptonized. A systematic analysis of more sources is needed in order to support the plausibility of this model, as well as the development of new theoretical predictions that enable a search for more precise signatures of this process.

Chapter 4

Radiative transfer

While ideal fluid dynamics provides a strong, versatile framework able to deal with multiple physical systems by means of conservation laws, its applicability is limited when describing systems out of LTE. In the previous chapters we have seen how this is the case in astrophysical flows when particle densities are low enough to allow for free transport of photons. We introduce in this chapter a numerical code for Rad-RMHD able to deal with such phenomena, built as a module within the PLUTO code. We first discuss the assumptions that lead to the form of the Rad-RMHD equations used in the code, after which we explain the implemented numerical methods, focusing on the description of the included IMEX schemes and the new HLLC Riemann solver for radiation transport. The algorithm performance is later demonstrated through a series of numerical benchmarks by investigating various different configurations with a particular emphasis on the behavior of the solutions in the free-streaming and diffusion limits. Finally, we study the scalability of the code. All of the results shown in this chapter have been published in [260], and the presented module will be included in the future releases of PLUTO.

4.1 Radiation hydrodynamics

4.1.1 The radiative transfer equation

We begin this section by outlining the main properties of the radiative transfer equation, from which the Rad-RMHD equations will be derived in the following subsections.

The radiative transfer approach consists in a statistical description of systems of many photons. In this approach, the system's state is completely determined by the *radiation specific intensity* I_ν, defined as the amount of energy per unit area transported in a time interval dt through an infinitesimal solid angle around the direction given by $\mathbf{n}$, in a range of frequencies

between ν and $\nu + \mathrm{d}\nu$. In general, I_ν is a function of time, space, photon frequency, and the direction of propagation $\mathbf{n}$. An intuitive definition of this quantity can be given in terms of the *photon distribution function* f_R, defined such that $f_R(t, \mathbf{x}, \mathbf{p})\mathrm{d}^3p$ is the number of photons per unit volume at $(\mathbf{x}, t)$ with momenta in the range $(\mathbf{p}, \mathbf{p} + \mathrm{d}\mathbf{p})$ (see [179]). If this function is known, I_ν can be obtained by multiplying it by the energy transported per photon per unit time (equal to $h_P \nu c$, where h_P is the Planck constant). This yields the following relation:

$$I_\nu(t, \mathbf{x}, \mathbf{n}) = \frac{h_P^4 \nu^3}{c^2} f_R(t, \mathbf{x}, (h\nu/c)\mathbf{n}), \tag{4.1}$$

where the term ν^3 on the right-hand side comes from the product of the photon energy and a factor ν^2 arising from d^3p. This description in terms of distribution functions of pointlike particles is entirely analogous to the approach followed in the kinetic theory of gases. In particular, the temporal dependence of I_ν can be obtained as a Boltzmann equation for photon transport (see, e.g., [179]) that can in turn be transformed into the radiative transfer equation in the following form:

$$\frac{\partial I_\nu}{\partial t} + \mathbf{n} \cdot \nabla I_\nu = \eta_\nu - \kappa_\nu \, I_\nu - \sigma_\nu \, I_\nu + \int_0^\infty \mathrm{d}\nu' \oint \mathrm{d}\Omega' \, \hat{\sigma}(\nu, \nu', \mathbf{n}, \mathbf{n}', t, \mathbf{x}) I_{\nu'}(t, \mathbf{x}, \mathbf{n}') \, . \tag{4.2}$$

This Lorentz-covariant equation describes the temporal variation of I_ν in terms of photon transport, accounted for by the second term on the left-hand side, and radiation–matter interaction, computed by the different terms on the right-hand side. The first of these, known as emissivity, represents the rate of energy release by the material due to spontaneous processes. These can be, for example, the occupation of a bound state in an atom by a previously unbound electron which emits a photon in the process (radiative recombination); the emission of a photon due to the interaction between an unbound electron and an ionized atom, giving as a result an unbound electron in a lower energy state (bremsstrahlung); and the transition of an electron between bound states in an atom due to its collision with another particle, in which a photon is emitted (collisional de-excitation). The inverse processes (respectively, bound-free, free-free, and bound-bound absorption) are considered in the second term, which accounts for the energy removed from the radiation field and turned into thermal motion in the material[1]. Scattering losses are taken into account in the third term, which as well as the second one, is proportional to I_ν. The proportionality coefficients, κ_ν and σ_ν, are known respectively as the frequency-dependent absorption and scattering coefficients. Finally, the last term in Eq. (4.2) represents the change in $I_\nu(t, \mathbf{x}, \mathbf{n})$ due to photons that are scattered

[1] A more comprehensive description of the absorption and emission processes taken into account in Eq. (4.2) is given in [261].

to the direction $\mathbf{n}$ with frequency ν from all other directions and frequencies $(\mathbf{n}', \nu')$. The function $\hat{\sigma}(\nu, \nu', \mathbf{n}, \mathbf{n}', t, \mathbf{x})$ is related to σ_ν as

$$\sigma_\nu = \int_0^\infty \mathrm{d}\nu' \oint \mathrm{d}\Omega' \, \hat{\sigma}(\nu, \nu', \mathbf{n}, \mathbf{n}', t, \mathbf{x}) \,, \tag{4.3}$$

where the $\oint$ sign represents integration over all solid angles.

In general, solving Equation (4.2) in the presented form is rather problematic, since integration must be carried out over multiple variables by concurrently taking into account changes in the material. As well, a precise knowledge of the functions η_ν, κ_ν, σ_ν, and $\hat{\sigma}_\nu$ is required, including effects due to the material's motion such as the anisotropy caused by the Doppler shift. Instead of attempting a full solution, we adopt a frequency-integrated moment-based approach: we integrate Equation (4.2) over the frequency domain and compute convenient averages of I_ν in angle and frequency (the moments) that can be naturally introduced in the equations of RHD and RMHD. This procedure is described in the next two subsections.

4.1.2 Energy-momentum conservation and moment formalism

We now explicitly derive a set of conservation laws describing the coupled evolution of matter, EM, and radiation fields. Although in this approach photons are treated as pointlike particles, net EM fields are here regarded as classical fields. While RMHD quantities and radiation fields are calculated in the laboratory frame, absorption and scattering coefficients are best obtained in the comoving frame, following the mixed-frame formalism described in [179]. The convenience of this choice relies on the fact that the opacity coefficients can be easily averaged without taking into account anisotropies due to the fluid's velocity, while the hyperbolic form of the conservation equations is kept. In this formalism, we split the total energy-momentum stress $T^{\mu\nu}$ into matter, EM, and radiative contributions, as

$$T^{\mu\nu} = T_g^{\mu\nu} + T_{em}^{\mu\nu} + T_r^{\mu\nu} \,. \tag{4.4}$$

The first two of these have been defined in Eqs. (2.1) and (2.13), while $T_r^{\mu\nu}$ can be written in terms of the specific intensity as

$$T_r^{\alpha\beta} = \int_0^\infty \mathrm{d}\nu \oint \mathrm{d}\Omega \; I_\nu(t, \mathbf{x}, \mathbf{n}) \, n^\alpha n^\beta, \tag{4.5}$$

where $n^\mu \equiv (1, \mathbf{n})$ denotes the direction of propagation, $\mathrm{d}\nu$ the differential frequency, and $\mathrm{d}\Omega$ the differential solid angle around $\mathbf{n}$. This expression is by definition covariant, since it is the

integral over all angles and frequencies of the outer product of the photon four-momemtum (equal to $h_P \nu n^\mu$ in units such that $c = 1$) with itself, multiplied by the invariants $I_\nu \nu^{-3}$ and $\nu \mathrm{d}\nu \mathrm{d}\Omega$ (see e.g. [179]). The components of $T^{\mu\nu}$ can be easily interpreted using the notation

$$T_r = \begin{pmatrix} E_r & F_r^i \\ F_r^j & P_r^{ij} \end{pmatrix}, \tag{4.6}$$

where

$$E_r = \int_0^\infty \mathrm{d}\nu \oint \mathrm{d}\Omega \; I_\nu(t, \mathbf{x}, \mathbf{n}) \tag{4.7}$$

$$F_r^i = \int_0^\infty \mathrm{d}\nu \oint \mathrm{d}\Omega \; I_\nu(t, \mathbf{x}, \mathbf{n}) \, n^i \tag{4.8}$$

$$P_r^{ij} = \int_0^\infty \mathrm{d}\nu \oint \mathrm{d}\Omega \; I_\nu(t, \mathbf{x}, \mathbf{n}) \, n^i \, n^j \tag{4.9}$$

are the first three moments of the radiation field, namely, the radiation energy density, the flux, and the pressure tensor. In our scheme, we follow separately the evolution of E_r and F_r^i, and define the pressure tensor in terms of these fields by means of a closure relation, described in Section 4.1.4.

Following these definitions, and imposing conservation of matter and total energy and momentum, we have

$$\nabla_\mu (\rho u^\mu) = 0 \tag{4.10}$$

and

$$\nabla_\mu T^{\mu\nu} = 0. \tag{4.11}$$

From equations (4.4) and (4.11), we immediately obtain

$$\nabla_\mu \left(T_g^{\mu\nu} + T_{em}^{\mu\nu} \right) = -\nabla_\mu T_r^{\mu\nu} \, . \tag{4.12}$$

The desired connection with the radiative transfer equation can thus be obtained from the right-hand side of this equation, by noting that integrating the left-hand side of Eq. (4.2) leads to:

$$\int_0^\infty \mathrm{d}\nu \oint \mathrm{d}\Omega \left(\frac{\partial I_\nu}{\partial t} + \mathbf{n} \cdot \nabla I_\nu \right) n^\alpha = \nabla_\mu T_r^{\mu\alpha} \, . \tag{4.13}$$

The equations of Rad-RMHD can then be obtained combining Eq. (4.12) with Eq. (4.2) by defining the radiation–matter interaction terms as

$$G^\mu = -\int_0^\infty \mathrm{d}\nu \oint \mathrm{d}\Omega \, (\cdots) \, n^\mu \, , \tag{4.14}$$

where the term in parentheses contains the right-hand side of Eq. (4.2). Thus, this four-vector satisfies

$$\nabla_\mu \left(T_g^{\mu\nu} + T_{em}^{\mu\nu}\right) = G^\mu \tag{4.15}$$

$$\nabla_\mu T_r^{\mu\nu} = -G^\mu \,, \tag{4.16}$$

from which the equations of Rad-RMHD can be derived. The interaction terms can be simplified provided some conditions are met, as we show in the next section.

4.1.3 Interaction terms

We now derive an expression for G^μ in the comoving frame, from which we can compute its components in the laboratory frame by means of a Lorentz boost. The covariant form of the equations guarantees that, in the comoving frame, this four-vector can also be expressed as in Equation (4.14), replacing all quantities by their comoving values. From now on, and except for the opacity coefficients, which are always understood to be measured in the comoving frame, we label all comoving quantities with a tilde.

In this work we assume coherent scattering, which means that the photon frequency remains unchanged in scattering events, and hence the function $\hat{\sigma}$ is proportional to $\delta(\nu - \nu')$. This is a valid assumption, for instance, for Thomson scattering. We are here neglecting any anisotropy due to the fluid's mean velocity, since we are computing all quantities in the comoving frame. As well, Doppler shifts caused by thermal motion of particles in the fluid can be safely neglected as long as the typical thermal velocities are much smaller than c. We also assume isotropic scattering, which in the comoving frame means that $\hat{\sigma}$ is independent of both $\mathbf{n}$ and $\mathbf{n}'$. This means that, after a scattering event, all emission directions are equally likely regardless of the direction of the incident photon. If that is not the case, the angular dependence can be accounted for by introducing a *phase function* $\Phi_\nu(\mathbf{n}, \mathbf{n}')$, defined in such a way that $\Phi_\nu(\mathbf{n}, \mathbf{n}')\mathrm{d}\Omega/4\pi$ is the probability for a photon of frequency ν of changing its direction from $\mathbf{n}'$ to $\mathbf{n}$, as measured in the scattering center's comoving frame (see, e.g., [184]). Therefore, this function must be normalized as

$$\frac{1}{4\pi} \oint \mathrm{d}\Omega' \, \Phi_\nu(\mathbf{n}, \mathbf{n}') = 1, \tag{4.17}$$

which turns the last term in Eq. (4.2) into

$$\frac{\sigma_\nu}{4\pi} \oint \mathrm{d}\Omega' \, \Phi_\nu(\mathbf{n}, \mathbf{n}') \tilde{I}_\nu(t, \mathbf{x}, \mathbf{n}') \,. \tag{4.18}$$

For Thomson scattering, for instance, the phase function is

$$\Phi_\nu(\mathbf{n},\mathbf{n}')_{\text{Thomson}} = \frac{3}{4}\left(1+(\mathbf{n}\cdot\mathbf{n}')^2\right) \tag{4.19}$$

(see e.g. [262]), whose minimum and maximum values are, respectively, $3/4$ and $3/2$. The anisotropy of this function can be safely ignored in the chosen moment approach, as we now show. When computing the zeroth component of $\tilde{G}^\mu$, we must integrate Eq. (4.18) over all frequencies and solid angles, as

$$\int_0^\infty \mathrm{d}\nu \oint \mathrm{d}\Omega\, \frac{\sigma_\nu}{4\pi} \oint \mathrm{d}\Omega'\, \Phi_\nu(\mathbf{n},\mathbf{n}')\tilde{I}_\nu(t,\mathbf{x},\mathbf{n}')\,. \tag{4.20}$$

If the product $\Phi_\nu(\mathbf{n},\mathbf{n}')\tilde{I}_\nu(t,\mathbf{x},\mathbf{n}')$ is a continuous function of $\mathbf{n}$ and $\mathbf{n}'$, we can exchange the order of the angle integrals (see, e.g., [263]), which yields

$$\int_0^\infty \mathrm{d}\nu \oint \mathrm{d}\Omega'\, \sigma_\nu \left(\frac{1}{4\pi}\oint \mathrm{d}\Omega\, \Phi_\nu(\mathbf{n},\mathbf{n}')\right)\tilde{I}_\nu(t,\mathbf{x},\mathbf{n}') = \int_0^\infty \mathrm{d}\nu \oint \mathrm{d}\Omega'\, \sigma_\nu\, \tilde{I}_\nu(t,\mathbf{x},\mathbf{n}')\,, \tag{4.21}$$

where we have used the normalization of Φ_ν (Eq. (4.17)). This is the same result that would be obtained with an isotropic phase function, and hence the zeroth component of G^μ can be obtained assuming isotropic scattering. Since we have not used the precise form of the Thomson phase function, this results holds in general for any phase function that allows for the exchange of the angular integrals. On the other hand, the computation of the spatial components of G^μ involves the evaluation of

$$\int_0^\infty \mathrm{d}\nu \oint \mathrm{d}\Omega\, \mathbf{n}\frac{\sigma_\nu}{4\pi} \oint \mathrm{d}\Omega'\, \Phi_\nu(\mathbf{n},\mathbf{n}')\tilde{I}_\nu(t,\mathbf{x},\mathbf{n}')\,. \tag{4.22}$$

Reordering the integrals in the same way as before, we obtain that this expression is equal to

$$\int_0^\infty \mathrm{d}\nu \oint \mathrm{d}\Omega'\, \sigma_\nu\, \tilde{I}_\nu(t,\mathbf{x},\mathbf{n}')\,\mathbf{g}_\nu\,, \tag{4.23}$$

where we have defined $\mathbf{g}_\nu$, the first moment of the phase function, as

$$\mathbf{g}_\nu = \frac{1}{4\pi}\oint \mathrm{d}\Omega'\, \Phi_\nu(\mathbf{n},\mathbf{n}')\,\mathbf{n}'\,. \tag{4.24}$$

Since $\mathbf{g}_\nu = 0$ for the Thomson phase function, the result of the whole integral is zero, which again coincides with the result that would be obtained with an isotropic phase function. In conclusion, the equations of Rad-RMHD are the same for isotropic and Thomson scattering.

Furthermore, this procedure gives a method to include the effects of anisotropic scattering in the equations. Since phase functions depend on $\mathbf{n} \cdot \mathbf{n}'$, i.e., they are axially symmetric around $\mathbf{n}$, we can see using Eq. (4.24) that the perpendicular components to $\mathbf{n}$ are null, and therefore $\mathbf{g}_\nu$ is of the form $g_\nu \mathbf{n}$. Inserting this expression in the definition of G^μ, it is straightforward to show that the resulting interaction terms correspond to those obtained for isotropic scattering, with an effective scattering coefficient equal to $(1 - g_\nu)\sigma_\nu$. This shows that the form of the equations of Rad-RMHD is maintained even in the case of highly anisotropic scattering[2].

Using Eq. (4.2) under the aforementioned assumptions, we arrive to the following expression for the interaction terms in the comoving frame:

$$\tilde{G}^\mu = \int_0^\infty \mathrm{d}\nu \oint \mathrm{d}\Omega \left(\chi_\nu \tilde{I}_\nu - \sigma_\nu \tilde{J}_\nu - \tilde{\eta}_\nu \right) n^\mu \,, \tag{4.25}$$

where $\tilde{J}_\nu$ is the angle-averaged value of $\tilde{I}_\nu$, and we have defined the frequency-dependent total opacity coefficient as

$$\chi_\nu = \kappa_\nu + \sigma_\nu \,. \tag{4.26}$$

We must now assume a form for $\tilde{\eta}_\nu$. If matter and radiation are in LTE in the comoving frame, then $\tilde{I}_\nu$ becomes isotropic, and the radiative transfer equation is reduced to

$$\tilde{\eta}_\nu = \kappa_\nu \tilde{I}_\nu \,. \tag{4.27}$$

Hence, in LTE, the amount of energy absorbed by the material equals the energy it emits, for every frequency and direction. In this state, $\tilde{I}_\nu$ corresponds to its equilibrium value given by the Planck's spectral radiance,

$$B_\nu(T) = \frac{2h_P \nu^3 / c^3}{e^{h_P \nu / k_B T} - 1} \,, \tag{4.28}$$

[2] When studying radiative transfer in other frameworks, isotropic scattering ($\Phi_\nu(\mathbf{n}, \mathbf{n}') \equiv 1$) cannot be assumed unless the directional dependence of Φ_ν is considered to be weak enough to be neglected. In astrophysical contexts (see e.g. [264], [153]), this is often assumed for simplicity. However, the error introduced by this approximation is smaller the more opaque the material is due to such processes, since multiple scattering events tend to randomize the direction of photons. For instance, using Eq. (4.19), we can see that the phase function for two consecutive Thomson scatterings is proportional to $(1 + \cos(2\theta)/27) \approx 1$, where θ is the angle a photon is deviated after both events. On the other hand, in optically thin materials, matter and radiation dynamics are advection-dominated, and scattering plays a secondary role. Hence, in general, the error of assuming isotropic scattering is mostly important in intermediate regions, where the average number of scattering events per photon is approximately 1; for instance, in stellar photospheres. An interesting comparison of the effects of isotropic and Thomson scattering in the context of relativistic outflows is given in [153], where the function I_ν is computed through Monte Carlo simulations in different opacity regimes.

where T is the equilibrium temperature and k_B the Boltzmann constant. Therefore, we can compute the equilibrium value of $\tilde{\eta}_\nu$ as

$$\tilde{\eta}_{\nu,\mathrm{LTE}} = \kappa_\nu B_\nu(T)\,, \tag{4.29}$$

which is known as the *Kirchhoff-Plack relation*. This relation can be assumed whenever gradients of physical properties over a photon destruction length are very small [179]. Although its validity is assumed in most codes for radiation HD, in reality it can lead to significant errors when free transport of radiation occurs. However, to describe possible departures from equilibrium due to radiative or inelastic collisional processes, we would need to solve non-LTE rate equations for all interactions relevant in the problem at hand, which would radically increase the complexity of the method. Such procedure would also require a different treatment for matter dynamics, since LTE of material particles is also one of the assumptions of HD. In this work, we shall assume the validity of Eq. (4.29) regarding it as a first approximation.

We are now in conditions to carry out the angle integrals in Eq. (4.25), which yields

$$\tilde{G}^0 = 4\pi \int_0^\infty \mathrm{d}\nu\, \kappa_\nu \left(\tilde{J}_\nu - B_\nu(T)\right) \tag{4.30}$$

$$\tilde{G}^i = \int_0^\infty \mathrm{d}\nu\, \chi_\nu \tilde{F}^i_\nu\,, \tag{4.31}$$

where $\tilde{\mathbf{F}}_\nu = \oint \mathrm{d}\Omega\, \tilde{I}_\nu \mathbf{n}$. These expressions can be easily integrated if the material behaves as a *grey body*, i.e., if the opacities are independent of the photon frequency, which most times is not the case. Depending on which source of opacity is dominant, opacity coefficients can be substantially different in different bandwidths[3]. An approximate solution to this issue, followed in our work, is the replacement of the frequency-dependent opacities by a set of effective frequency-averaged values. Even though this procedure does not give an exact solution, since a correct averaging of the opacity coefficients would require the knowledge of $\tilde{J}_\nu$ and $\tilde{\mathbf{F}}_\nu$, it provides a reasonable first approximation to the problem of transfer of total energy and momentum densities. An option for doing so is the replacement of κ_ν and χ_ν by

[3]For LTE free-free transitions, the absorption coefficient depends on the frequency roughly as $\kappa_\nu \propto \nu^{-3}$ [265]. In the case of photoionization processes, κ_ν is zero for all frequencies below a threshold value, after which κ_ν also decays as ν^{-3} [265]. For bound-bound transitions, κ_ν is zero except for a narrow band centered in $\nu = \Delta E/h_P$, where ΔE is the energy difference between both bound levels. On the other hand, for Thomson scattering, σ_ν is frequency-independent [262].

their *Planck* and *Rosseland* mean values, given respectively by

$$\kappa_P = \frac{\displaystyle\int_0^\infty \mathrm{d}\nu\, \kappa_\nu B_\nu(T)}{\displaystyle\int_0^\infty \mathrm{d}\nu\, B_\nu(T)}\,, \quad \chi_R = \frac{\displaystyle\int_0^\infty \mathrm{d}\nu\, \left(\frac{\partial B_\nu(T)}{\partial T}\right)}{\displaystyle\int_0^\infty \mathrm{d}\nu\, \chi_\nu^{-1} \left(\frac{\partial B_\nu(T)}{\partial T}\right)}\,. \tag{4.32}$$

The first of these values is particularly accurate in optically thin materials, whereas the second one tends to its correct limit in the diffusion regime [179]. We thus arrive to the final form of the interaction terms in the comoving frame:

$$\tilde{G}^\mu = \rho \left[\kappa \left(\tilde{E}_r - 4\pi B(T)\right),\, \chi \tilde{\mathbf{F}}_r\right]\,, \tag{4.33}$$

where $B(T) = \sigma_{\mathrm{SB}} T^4/\pi$ is the integrated value of $B_\nu(T)$, σ_{SB} is the Stefan–Boltzmann constant, and κ, σ, and $\chi = \kappa + \sigma$ are the values of the mentioned frequency-averaged opacities per unit density. In the code, these can either be set as constants, or defined by the user as functions of any set of local fields (for instance, ρ and T). The temperature can be in turn determined from the ideal gas law,

$$T = \frac{\mu\, m_p\, p_g}{k_B\, \rho}, \tag{4.34}$$

where μ is the material's mean molecular weight and m_p is the proton mass.

Once $\tilde{G}^\mu$ is known in the comoving frame, its components in the laboratory frame can be computed as

$$G^\mu = \Lambda^\mu{}_\alpha(\mathbf{v})\, \tilde{G}^\alpha\,, \tag{4.35}$$

where $\Lambda^\mu{}_\alpha(\mathbf{v})$ is the tensor representation of a Lorentz boost in the fluid's velocity $\mathbf{v}$. In this expression, $\tilde{G}^\alpha$ still depends on the radiation fields in the comoving frame, which can be expressed as functions of the fields in the laboratory frame by means of the transformation law

$$\tilde{T}_r^{\mu\nu} = \Lambda_\alpha{}^\mu(\mathbf{v}) \Lambda_\beta{}^\nu(\mathbf{v})\, T^{\alpha\beta} = \Lambda^\mu{}_\alpha(-\mathbf{v}) \Lambda^\nu{}_\beta(-\mathbf{v})\, T^{\alpha\beta}\,, \tag{4.36}$$

which yields

$$\tilde{E}_r = \gamma^2 \left(E_r - 2 v_i F_r^i + v_i v_j P_r^{ij} \right) \tag{4.37}$$

$$\tilde{F}_r^i = -\gamma^2 v^i E_r + \gamma \left[\delta_j^i + \left(\frac{\gamma - 1}{v^2} + \gamma \right) v^i v_j \right] F_r^j - \gamma \left(\delta_k^i + \frac{\gamma - 1}{v^2} v^i v_k \right) v_j P^{jk} \tag{4.38}$$

$$\begin{aligned} \tilde{P}_r^{ij} = {} & \gamma^2 v^i v^j E_r - \gamma \left(v^i \delta_k^j + v^j \delta_k^i + 2 \frac{\gamma - 1}{v^2} v^i v^j v_k \right) F_r^k \\ & + \left(\delta_k^i + \frac{\gamma - 1}{v^2} v^i v_k \right) \left(\delta_l^j + \frac{\gamma - 1}{v^2} v^j v_l \right) P_r^{kl} \,, \end{aligned} \tag{4.39}$$

where δ_j^i is the Kronecker delta. Finally, using the transformation laws given in Eqs. (4.35)–(4.39), we obtain the following interaction terms in the Eulerian frame:

$$\begin{aligned} G^0 = {} & -4\pi\rho\kappa\gamma B(T) + \rho\gamma \left(\kappa - \sigma ||\mathbf{u}||^2 \right) E_r \\ & - \rho \left[\kappa - \sigma \left(\gamma^2 + ||\mathbf{u}||^2 \right) \right] u_j F_r^j - \rho\sigma\gamma u_j u_k P^{jk} \,, \end{aligned} \tag{4.40}$$

$$\begin{aligned} G^i = {} & -4\pi\rho\kappa u^i B(T) - \rho\sigma\gamma^2 u^i E_r \\ & + \rho\gamma \left[\chi \delta_j^i + 2\sigma u_j u^i \right] F_r^j - \rho \left(\chi u_j \delta_k^i + \sigma u^i u_j u_k \right) P^{jk} \,, \end{aligned} \tag{4.41}$$

which, using Eq. (4.6), can be summarized as

$$G^\mu = -\kappa\rho \left(T_r^{\mu\alpha} u_\alpha + 4\pi B(T) u^\mu \right) - \sigma\rho \left(T_r^{\mu\alpha} u_\alpha + T_r^{\alpha\beta} u_\alpha u_\beta u^\mu \right) . \tag{4.42}$$

However intricate and nonlinear in both radiation and matter fields, these terms count with the advantage of depending exclusively on local values of these fields, and hence they can be computed locally as any other source term in the code.

4.1.4 Rad-RMHD under the M1 closure

Under the assumptions summarized in Sections 2.1.1 and 2.1.2, the explicit form of the left-hand side of Eq. (4.15) can be extracted from Eqs. (2.17) and (2.18). Together with Eqs. (2.16), (4.16), (4.40), and (4.41), we obtain the equations of Rad-RMHD in quasi-conservative

form:

$$\frac{\partial\left(\rho\gamma\right)}{\partial t}+\nabla\cdot\left(\rho\gamma\mathbf{v}\right)=0 \tag{4.43}$$

$$\frac{\partial\mathcal{E}}{\partial t}+\nabla\cdot\left(\mathbf{m}-\rho\gamma\mathbf{v}\right)=G^{0} \tag{4.44}$$

$$\frac{\partial\mathbf{m}}{\partial t}+\nabla\cdot\left(\rho h\gamma^{2}\mathbf{v}\mathbf{v}-\mathbf{B}\mathbf{B}-\mathbf{E}\mathbf{E}\right)+\nabla p=\mathbf{G} \tag{4.45}$$

$$\frac{\partial\mathbf{B}}{\partial t}+\nabla\times\mathbf{E}=0 \tag{4.46}$$

$$\frac{\partial E_{r}}{\partial t}+\nabla\cdot\mathbf{F}_{r}=-G^{0} \tag{4.47}$$

$$\frac{\partial\mathbf{F}_{r}}{\partial t}+\nabla\cdot P_{r}=-\mathbf{G}, \tag{4.48}$$

where, as in Chapter 2, we assume the relation $\mathbf{E}=-\mathbf{v}\times\mathbf{B}$. In our current scheme, these equations can be solved in Cartesian, cylindrical or spherical coordinates. The precise form that these equations take in curvilinear coordinates is detailed in Appendix C.

A further closure relation is needed for the radiation fields, i.e., an equation relating P_r^{ij} to E_r and $\mathbf{F}_r$. The simplest choice we can make is the *Eddington approximation*, which consists in assuming $\tilde{P}_r^{ij}=(\tilde{E}_r/3)\,\delta^{ij}$. However, this is a good approximation only in the case where I_ν is quasi-isotropic in the fluid frame, which is only verified in general in optically thick media. Instead, we have chosen to implement the M1 closure, proposed by [199], which is able to handle both the optically thick and optically thin regimes. In this closure, it is assumed that I_ν is isotropic in some inertial frame, to which we shall refer as *radiation frame*. Under this assumption, we can use the covariance of Eq. (4.5) to carry out the angular integrals in the radiation frame, obtaining $\bar{T}_r^{\mu\nu}=\mathrm{diag}(\bar{E}_r,\bar{E}_r/3,\bar{E}_r/3,\bar{E}_r/3)$, where we have indicated fields measured in the radiation frame with an upper bar. This expression is enough to determine P_r^{ij} as a function of E_r and F_r^i, as we now show following the procedure described in [190]. Defining u_R^μ as the components of the four-velocity of the radiation frame measured in the laboratory frame, we can write $\bar{T}_r^{\mu\nu}$ as

$$\bar{T}_r^{\mu\nu}=\frac{4}{3}\bar{E}_r\bar{u}_R^\mu\bar{u}_R^\nu+\frac{1}{3}\bar{E}_r\eta^{\mu\nu}\,. \tag{4.49}$$

Applying a Lorentz boost in the radiation frame's velocity, this tensor can be written in the laboratory frame as

$$T_r^{\mu\nu}=\frac{4}{3}\bar{E}_r u_R^\mu u_R^\nu+\frac{1}{3}\bar{E}_r\eta^{\mu\nu}\,, \tag{4.50}$$

from which we get the following relations:

$$\begin{aligned} \eta_{\mu\nu} T_r^{t\mu} T_r^{t\nu} &= \frac{\bar{E}_r^2}{9} \left(\eta^{tt} - 8 \left(u_R^t \right)^2 \right) \\ T_r^{tt} &= \frac{\bar{E}_r^2}{3} \left(\eta^{tt} + 4 \left(u_R^t \right)^2 \right) . \end{aligned} \tag{4.51}$$

Since the left-hand sides of Eqs. (4.51) are functions of $(E_r, \mathbf{F}_r)$, this defines a system of two equations in two unknowns, $\bar{E}_r$ and u_R^t. Once these are determined, the spatial components of u_R^μ can be found from T_r^{ti} using Eq. (4.50), and thus we can write all components of $T_r^{\mu\nu}$ as functions of $(E_r, \mathbf{F}_r)$. This procedure yields the desired closure relation, which is defined through the following equations:

$$P_r^{ij} = D^{ij} E_r, \tag{4.52}$$

$$D^{ij} = \frac{1-\xi}{2} \delta^{ij} + \frac{3\xi - 1}{2} n^i n^j, \tag{4.53}$$

$$\xi = \frac{3 + 4f^2}{5 + 2\sqrt{4 - 3f^2}}, \tag{4.54}$$

where now $\mathbf{n} = \mathbf{F}_r / ||\mathbf{F}_r||$, and $f = ||\mathbf{F}_r|| / E_r$. Since the choice of the laboratory frame is arbitrary, these equations are covariant and hold in any reference frame once the existence of the radiation frame is assumed. As well, they are well behaved, as Eqs. (4.7) and (4.8) provide an upper limit to the flux, namely

$$||\mathbf{F}_r|| \leq E_r, \tag{4.55}$$

and therefore $0 \leq f \leq 1$.

In the diffusion limit, namely, if $||\mathbf{F}_r|| \ll E_r$, the M1 closure leads to $P_r^{ij} = (\delta^{ij}/3)\, E_r$, which corresponds to an isotropic specific intensity, i.e., the Eddington limit. Likewise, in the free-streaming limit given by $||\mathbf{F}_r|| = E_r$, the pressure tensor tends to $P_r^{ij} = E_r\, n^i n^j$, which corresponds to a delta-like I_ν pointing in the same direction and orientation as $\mathbf{F}_r$. However, the above derivation is not valid in that case, since the existence of the radiation frame would imply $||\mathbf{v}_R|| = c$ and $\bar{E}_r = 0$. Nonetheless, since Equations (4.52)–(4.54) yield the correct free-streaming limit, such case can be simply regarded as the limit when $||\mathbf{v}_R|| \to c$ of this assumption.

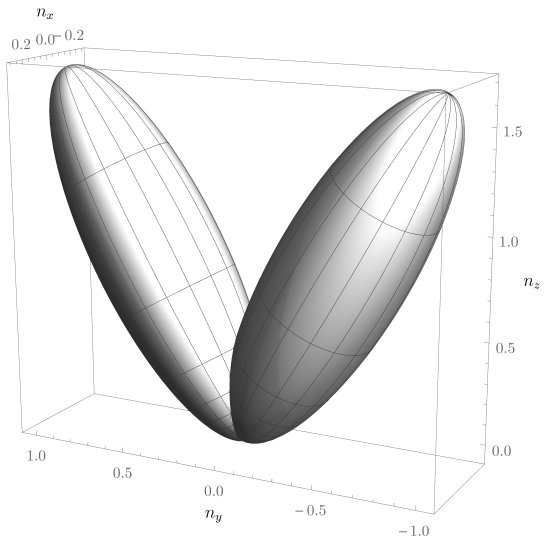

(a) Radiation intensity resulting from the contributions of two anisotropic beams.

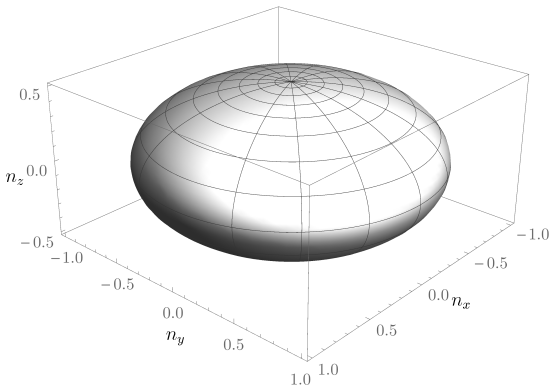

(b) Axially symmetric distribution for which the Eddington factor is lower than 1/3.

Fig. 4.1 Angular distribution of the radiation intensity I_ν as a function of the emission direction $\mathbf{n}$ for two cases where the M1 closure is not exact.

We point out that, even though both the free-streaming and diffusion limits are reproduced correctly, the M1 closure may fail in cases where there is no reference frame in which I_ν is isotropic; for instance, if I_ν is not axially symmetric. An example of this is shown in Fig. 4.1a, which shows the directional dependence of a given I_ν produced by two anisotropic beams. In that case, the M1 closure causes both beams to interact wherever they converge, which can lead to unphysical instabilities [190, 191]. Another example where the M1 is inaccurate is given by the axially symmetric distribution shown in Fig. 4.1b, where it can be seen that there is no boost that can render the radiation intensity isotropic. A consequence of this can be measured through the *Eddington factor*, defined for axially symmetric distributions as P_r^{zz}/E_r, where we have taken z to be the axis of symmetry. In this case, the M1 closure yields $P_r^{zz}/E_r = \chi(f)$, which can only take values in the interval $[\frac{1}{3}, 1]$, where the minimum value corresponds to an isotropic distribution. However, the distribution shown in Fig. 4.1b gives an Eddington factor of 0.27, which is below the minimum value allowed by the M1 closure. This may be verified in radiative shocks, as studied in [266], where it is shown by means of a direct solution of the radiative transfer equation that the Eddington factor can be slightly under $1/3$ close to the emitting layer, provided that photons in that region have a larger mean free path in the parallel directions to the shock front than in the normal one. Thus, in such cases, the M1 closure is only approximate.

4.2 Numerical scheme

As in Chapter 2, the Rad-RMHD equations can be summarized as

$$\frac{\partial \mathcal{U}}{\partial t} + \nabla \cdot \mathsf{F}(\mathcal{U}) = \mathcal{S}(\mathcal{U}) \,, \tag{4.56}$$

where now $\mathcal{U} \equiv (\rho\gamma,\, \mathcal{E},\, \mathbf{m},\, \mathbf{B},\, E_r,\, \mathbf{F}_r)^\intercal$ are the conserved fields, $\mathsf{F}(\mathcal{U})$ is the flux tensor and $\mathcal{S} \equiv (0, G^0, \mathbf{G}, \mathbf{0}, -G^0, -\mathbf{G})^\intercal$ contains the radiation–matter interaction terms. The explicit expressions of F can be extracted from Equations (4.43)–(4.48).

Equation (4.56) differs from the RMHD equations in the inclusion of the radiation fields and the source terms. To solve this new system, the new Rad-RMHD module maintains several convenient features of PLUTO, such as its parallelization and AMR capabilities, and its adaptability to different coordinate systems. In this section, we will describe the additional numerical techniques implemented to solve the Rad-RMHD equations.

In particular, the introduction of source terms poses a numerical challenge due to the fact that radiation–matter interaction may occur in timescales that are much smaller than any dynamical characteristic time. Thus, an explicit integration of $\mathcal{S}$ would either lead to instabilities or to excessively large computing times. For this reason, we discretize Equations (4.56) in time by means of IMEX–Runge-Kutta (IMEX–RK) schemes [204], as described in Section 4.2.1. In this approach, fluxes and geometrical source terms are integrated explicitly in the *explicit step* by means of Godunov-type solvers, as detailed in Section 4.2.2. Within this stage, we have included a new Riemann solver for radiation transport, which we introduce in Section 4.2.3. On the other hand, the integration of G^μ is performed implicitly in a separate step (the *implicit step*), as described in Section 4.2.4.

4.2.1 Implemented IMEX schemes

IMEX schemes consist in prescriptions for the integration of differential equations in which some terms are integrated explicitly and others implicitly. These methods are of great utility for solving equations with *stiff* source terms, i.e., terms that cause the described problem to undergo processes that occur in highly disparate timescales. In the Rad-RMHD equations, such is the case of the radiation–matter interaction terms.

In our approach, we have implemented two different IMEX–RK schemes, which are built by combining implicit and explicit Runge-Kutta methods. In general, the convergence and overall stability of these schemes are strongly dependent on details such as the ordering and number of substeps, and the coefficients used on each of them for the integration prescriptions.

One of the IMEX–RK methods we have implemented is the commonly used second-order IMEX–SSP2(2,2,2) scheme by [204]. When applied to (4.56), this method results in the following discrete scheme:

$$\begin{aligned}
\mathcal{U}^{(1)} &= \mathcal{U}^n + a\Delta t^n \mathcal{S}^{(1)} \\
\mathcal{U}^{(2)} &= \mathcal{U}^n + \Delta t^n \mathcal{R}^{(1)} + \Delta t^n \left[(1-2a)\mathcal{S}^{(1)} + a\mathcal{S}^{(2)}\right] \\
\mathcal{U}^{n+1} &= \mathcal{U}^n + \frac{\Delta t^n}{2}\left[\mathcal{R}^{(1)} + \mathcal{R}^{(2)}\right] + \frac{\Delta t^n}{2}\left[\mathcal{S}^{(1)} + \mathcal{S}^{(2)}\right].
\end{aligned} \tag{4.57}$$

Here we maintain the notation used in Chapter 2: $\mathcal{U}$ represents an array of volume averages inside the zone i, j, k (indices have been again omitted), n denotes the current step number, Δt^n is the time step, $a = 1 - \sqrt{2}/2$, and the operator $\mathcal{R}$, which approximates the contribution of $(-\nabla \cdot \mathsf{F})$, is computed in an explicit fashion as detailed in Sections 2.3.3 and 4.2.2. Potentially stiff terms (i.e., those proportional to κ and σ) are included in the operator $\mathcal{S}$, which is solved implicitly during the first and second stages in Eq. (4.57). In short, terms on the right-hand side of these equations whose step indices coincide with those on the left-hand side are solved implicitly, while the rest of them are integrated explicitly.

An alternative scheme which we also consider in the present context is the following scheme (IMEX1 henceforth):

$$\begin{aligned}
\mathcal{U}^{(1)} &= \mathcal{U}^n + \Delta t^n \mathcal{R}^n + \Delta t^n\, \mathcal{S}^{(1)} \\
\mathcal{U}^{(2)} &= \mathcal{U}^{(1)} + \Delta t^n \mathcal{R}^{(1)} + \Delta t^n\, \mathcal{S}^{(2)} \\
\mathcal{U}^{n+1} &= \frac{1}{2}\left(\mathcal{U}^n + \mathcal{U}^{(2)}\right),
\end{aligned} \tag{4.58}$$

This method is an extension to the second-order RK2 method shown in Section 2.3.3, where we have just added an implicit step after every flux integration. In the same way, we have included in the code a third-order version of this scheme that extends the third-order Runge-Kutta scheme by [220]. Both the second- and third-order versions of this method are similar to those described in [193].

Using general methods for IMEX–RK schemes [204], it can be shown that IMEX–SSP2(2,2,2) and IMEX1 are of order 2 and 1 in time and L- and A-stable respectively[4], which makes IMEX–SSP2(2,2,2) a seemingly better option when it comes to the schemes'

[4] In the theory of implicit Runge-Kutta methods (see, e.g., [267]), some stability criteria can be obtained for a particular scheme by applying it to the equation $\frac{dy}{dt} = \lambda y$, with $\lambda \in \mathbb{C}$. For $\mathrm{Re}(\lambda) < 1$, the exact solution of this equation approaches zero as $t \to \infty$. It is therefore desirable that the numerical solution satisfies the same property, and that it does not grow between time steps. With this in mind, if the numerical solution verifies $|y^{n+1}/y^n| \leq 1$ for $\mathrm{Re}(\lambda) \leq 1$, the method is called *A-stable*. Furthermore, if it also satisfies the property that $|y^{n+1}/y^n|$ approaches 0 for $\lambda \to \infty$, it is called *L-stable*. In general, both properties favor the overall stability of a given method.

stability. However, as we have observed when testing the module, the explicit addition of previously-calculated source terms in the last step of IMEX–SSP2(2,2,2) can cause inaccuracies whenever interaction terms are stiff and there are large differences in the orders of magnitude of matter and radiation fields (see Sections 4.3.5 and 4.3.6). Contrarily, IMEX1 seems to have better positivity-preserving properties and a higher accuracy in those cases. In general, as it is shown in Section 4.3, we have obtained equivalent results with both methods in every other case. Whenever source terms can be neglected, both methods reduce to RK2, which makes them second-order accurate in time for optically thin transport.

4.2.2 Explicit step

Each explicit step in the IMEX1 and IMEX–SSP2(2,2,2) methods consists in an explicit integration of the fluxes in Eq. (4.56), taking $\mathcal{S} \equiv 0$. Therefore, we can apply the same methods for homogeneous hyperbolic systems used for RHD and RMHD in Section 2.3, with a few modifications owing to the particular form of the Rad-RMHD equations. We now describe such changes.

Firstly, we define the set of primitive fields as

$$\mathcal{V} = (\rho,\, p_g,\, \mathbf{v},\, \mathbf{B},\, E_r,\, \mathbf{F}_r)^{\intercal}\,. \tag{4.59}$$

These are just the RMHD variables with the addition of the radiation fields, which remain equal to the conserved ones. The conversion between $\mathcal{U}$ and $\mathcal{V}$ can then be achieved by applying the same methods used for RMHD, leaving the radiation components unchanged. Furthermore, this choice for $\mathcal{V}$ makes it possible to straightforwardly enforce Equation (4.55) during the reconstruction step, in addition to the constraints mentioned in Section 2.3.1. As we have verified in tests, this condition is essential to guarantee the stability of the solutions.

As in Section 2.3.2, fluxes are computed by approximately solving local Riemann problems at cell interfaces. Since we are taking $\mathcal{S} \equiv 0$, the Rad-RMHD equations can be divided into two independent systems, one corresponding to RMHD (Eqs. (4.43)–(4.46)) and the other one to radiation transport (Eqs. (4.47)–(4.48)). In particular, RMHD fluxes are independent of the radiation variables, and vice versa. Consequently, the Jacobian matrices of the full system are block-diagonal, and characteristic wave speeds can be obtained from the eigenvalues of each block (the details of this computation are shown in Appendix A). In principle, we can expect the maximum and minimum signal speeds of both systems to be, in the frozen limit[5], different. We therefore solve the two subsystems separately, using for each of them the set of

[5] In the theory of stiff relaxation systems, the frozen limit refers to the small time step regime, when the effect of source terms on the characteristic waves is still negligible.

characteristic speeds obtained from each corresponding block. In this manner, as it is pointed out in [190], we avoid the excessive numerical diffusion that occurs when the same signal speeds are used to update both radiation and RMHD fields. This has been verified in our tests.

To compute the RMHD fluxes, we can apply any of the Riemann solvers mentioned in Section 2.3.2. On the other hand, radiation fluxes can be computed using either the LFR solver (Eq. (2.50)), the HLL solver (Eq. (2.45)), or the HLLC solver introduced in [260], which will be shown in the next section. Once fluxes are computed, the explicit integration step can be applied following the prescription in Equation (2.53) to compute the operator $\mathcal{R}$.

4.2.3 HLLC solver for radiation transport

We now present a novel Riemann solver for the solution of the homogenous subsystem formed by Eqs. (4.47)–(4.48) with $G^\mu = 0$. To this purpose, we restrict our attention to a single direction chosen to be the x-axis, without loss of generality. In Cartesian coordinates, the resulting equations take the form

$$\frac{\partial \mathcal{U}_r}{\partial t} + \frac{\partial \Phi}{\partial x} = 0 \tag{4.60}$$

where $\mathcal{U}_r = (E,\, \mathbf{F})^\intercal$ while $\Phi = (F_x,\, P_{xx},\, P_{yx},\, P_{zx})^\intercal$ and we have omitted the subscripts r for clarity purposes (we shall maintain that convention throughout this section). From the analysis carried out in Appendix A, we know that the Jacobian J_x of this system has three different eigenvalues $\{\lambda_1, \lambda_2, \lambda_3\}$, satisfying $\lambda_1 \leq \lambda_2 \leq \lambda_3$. Since the system is hyperbolic, the breaking of an initial discontinuity will involve the development of (at most) as many waves as the number of different eigenvalues (see Chapter 2). On this basis, we have implemented a three-wave Riemann solver.

Following [268], we define the following fields:

$$\begin{aligned} \beta_x &= \frac{3\xi - 1}{2} \frac{F_x}{||\mathbf{F}||^2} E \\ \Pi &= \frac{1-\xi}{2} E\,, \end{aligned} \tag{4.61}$$

where ξ is given by Eq. (4.54). With these definitions, the fluxes in Eq. (4.60) can be written as

$$\Phi = \begin{pmatrix} F_x \\ F_x\,\beta_x + \Pi \\ F_y\,\beta_x \\ F_z\,\beta_x \end{pmatrix}, \tag{4.62}$$

and F_x can be shown to satisfy $F_x = (E + \Pi)\,\beta_x$. These expressions are similar to those of RHD, where β_x, Π and $\mathbf{F}$ play, respectively, the role of v_x, p_g and $\mathbf{m}$ while E tantamounts to total energy. With the difference that there is no field corresponding to mass density, the equations are exactly the same as those corresponding to energy-momentum conservation of a fluid, with a different closure relation.

With this in mind, we follow analogous steps to those in [203] in order to construct a HLLC solver for the system defined by Equations (4.60). In this case, instead of the intermediate constant state considered in the HLL solver, we include an additional noncompressive middle wave of speed λ^* that separates two intermediate states $\mathcal{U}_L^*$ and $\mathcal{U}_R^*$, where

$$\lambda_L \leq \lambda^* \leq \lambda_R\,. \tag{4.63}$$

In this way, the full approximate solution verifies

$$\mathcal{U}_r(0,t) = \begin{cases} \mathcal{U}_{r,L} & \text{if } \lambda_L > 0 \\ \mathcal{U}^*_{r,L} & \text{if } \lambda_L \leq 0 < \lambda^* \\ \mathcal{U}^*_{r,R} & \text{if } \lambda^* \leq 0 \leq \lambda_R \\ \mathcal{U}_{r,R} & \text{if } \lambda_R < 0\,. \end{cases} \tag{4.64}$$

The corresponding fluxes are

$$\Phi_{hllc}(0,t) = \begin{cases} \Phi_L & \text{if } \lambda_L > 0 \\ \Phi^*_L & \text{if } \lambda_L \leq 0 < \lambda^* \\ \Phi^*_R & \text{if } \lambda^* \leq 0 \leq \lambda_R \\ \Phi_R & \text{if } \lambda_R < 0\,. \end{cases} \tag{4.65}$$

States and fluxes are related by the Rankine-Hugoniot jump conditions across the outermost waves, λ_S ($S = L, R$),

$$\lambda_S\,(\mathcal{U}^*_{r,S} - \mathcal{U}_{r,S}) = \Phi^*_S - \Phi_S\,. \tag{4.66}$$

A similar condition must also hold across the middle wave, so that when Equation (4.66) is applied to all three waves, one has a system of 12 equations for the 17 unknowns ($\mathcal{U}^*_{r,L}$, $\mathcal{U}^*_{r,R}$, Φ^*_L, Φ^*_R, and λ^*), and therefore further assumptions must be made. From the results of the tests performed with the HLL solver, we have verified that β_x and Π are conserved along the intermediate noncompressive mode for all of the obtained solutions. This property is proven in [269]. Since $\lambda_2(E, \mathbf{F}) = \beta_x(E, \mathbf{F})$, we impose the constraints $\lambda^* = \beta^*_{x,L} = \beta^*_{x,R}$ and $\Pi^*_L = \Pi^*_R$. These conditions are analogous to those satisfied by the contact discontinuity in RHD, across which p_g and v_x are conserved, and where the latter coincides with the propagation speed (we hence apply the term *contact wave* to this mode). Following [203], we assume that Φ^* can be written in terms of the five variables $(E^*, \Pi^*, \beta^*_x, F^*_y, F^*_z)$ in the following way:

$$\Phi^* = \begin{pmatrix} F^*_x \\ F^*_x\,\beta^*_x + \Pi^* \\ F^*_y\,\beta^*_x \\ F^*_z\,\beta^*_x \end{pmatrix}, \tag{4.67}$$

where, for consistency, we have defined $F^*_x \equiv (E^* + \Pi^*)\beta^*_x$. Under these constraints, the jump conditions across the middle wave are automatically satisfied, and Eq. (4.66) is reduced to the following system of 8 equations in 8 unknowns:

$$\begin{aligned} E^*(\lambda - \lambda^*) &= E(\lambda - \beta_x) + \Pi^*\lambda^* - \Pi\,\beta_x \\ F^*_x(\lambda - \lambda^*) &= F_x(\lambda - \beta_x) + \Pi^* - \Pi \\ F^*_y(\lambda - \lambda^*) &= F_y(\lambda - \beta_x) \\ F^*_z(\lambda - \lambda^*) &= F_z(\lambda - \beta_x)\,, \end{aligned} \tag{4.68}$$

which holds for both subscripts L and R (we shall maintain this convention in what follows). The first two equations in Eq. (4.68) can be turned into the following quadratic expression, from which λ^* can be obtained:

$$(A_L\lambda^* - B_L)(1 - \lambda_R\lambda^*) = (A_R\lambda^* - B_R)(1 - \lambda_L\lambda^*), \tag{4.69}$$

with

$$A = \lambda E - F_x \tag{4.70}$$

$$B = (\lambda - \beta_x)F_x - \Pi. \tag{4.71}$$

Once λ^* is known, we can compute Π^* as

$$\Pi^* = \frac{A\,\lambda^* - B}{1 - \lambda\,\lambda^*}, \tag{4.72}$$

and the remaining fields from Eq. (4.68). Similar to the RHD counterpart, among the two roots of Equation (4.69) we must choose the only one that guarantees $\lambda^* \in [-1, 1]$, which in our case corresponds to that with the minus sign. As shown in Appendix D, this definition of λ^* satisfies Eq. (4.63). We have also numerically checked that the intermediate states $\mathcal{U}_L^*$ and $\mathcal{U}_R^*$ constructed in this way satisfy Equation (4.55), which guarantees the positivity of our HLLC scheme. However, unlike the RHD case, the coefficients $\{A_L, B_L, A_R, B_R\}$ defined in Equations (4.70) and (4.71) can simultaneously be equal to zero, meaning that λ^* can no longer be determined from Equation (4.69). This happens under the conditions $||\mathbf{F}|| = E$ for both L and R, and $F_{xL}/||\mathbf{F}_L|| \leq F_{xR}/||\mathbf{F}_R||$, in which case the jump conditions lead to the formation of vacuum-like intermediate states. We overcome this issue by switching the solver to the standard HLL whenever these conditions are met.

As for the HLL solver, signal velocities must be limited when describing radiation transfer in highly opaque materials in order to reduce numerical diffusion (see Appendix A). Whenever this occurs, we also switch to the standard HLL solver, and limit λ_L and λ_R according to Equation (A.10). Hence, we can only expect the HLLC solver to improve the accuracy of the obtained solutions in optically thin regions of space, whereas the results should be the same for both HLL and HLLC everywhere else. Finally, although the use of the HLLC solver can reduce the numerical diffusion when compared to the HLL solver, this can cause spurious oscillations around shocks that would be damped with a more diffusive method. As for the HLLC solver for RHD and RMHD included in `PLUTO`, this problem can be reduced by implementing an additional flattening in the vicinity of strong shocks [203].

4.2.4 Implicit step

We now describe the algorithm employed for the implicit integration of the radiation–matter interaction terms. A typical implicit step of an IMEX scheme (see Eqs. 4.57 and 4.58) takes the form

$$\mathcal{U} = \mathcal{U}' + s\,\Delta t^n\,\mathcal{S}\,, \tag{4.73}$$

where s is a constant and primed terms denote some intermediate state value. Equation (4.73) shows that the mass density, computed as $\rho\gamma$, as well as the total energy and momentum densities, defined as $E_{tot} = \mathcal{E} + E_r$ and $\mathbf{m}_{tot} = \mathbf{m} + \mathbf{F}_r$, must be conserved during this partial update owing to the particular form of the source terms. This yields the following

implicit relations between $\mathcal{V}$ and $\mathcal{U}_r$:

$$\begin{aligned} \mathcal{E}(\mathcal{V}) &= E_{tot} - E_r \\ \mathbf{m}(\mathcal{V}) &= \mathbf{m}_{tot} - \mathbf{F}_r. \end{aligned} \tag{4.74}$$

We can then solve Eq. (4.73) in terms of the following reduced system:

$$\mathcal{U}_r = \mathcal{U}_r' - s\,\Delta t^n\,\mathcal{G}\,, \tag{4.75}$$

with $\mathcal{G} \equiv (G^0, \mathbf{G})^\intercal$, where G^μ is given in Eqs. (4.40) and (4.41). In Eq. (4.75), radiation fields can be regarded as functions of the RMHD fields and vice versa by means of Eq. (4.74), and therefore the system can be solved in terms of either one of these.

In order to solve Equation (4.75), we have implemented and compared three different multidimensional root finder algorithms, which we now describe.

1. *Fixed-point method.* This method (originally proposed in [192]) is based on iterations of $\mathcal{U}_r$ and follows essentially the same approach outlined in [270] in the context of resistive RMHD. In this scheme, all of the RMHD primitive variables, as well as D^{ij}, are written at a previous iteration with respect to $\mathcal{U}_r$. In that manner, $\mathcal{G}$ can be written at a given iteration m as

$$\mathcal{G}^{(m)} = \mathcal{M}^{(m)}\mathcal{U}_r^{(m+1)} + b^{(m)}, \tag{4.76}$$

   where $\mathcal{M}$ is a matrix and b is a column vector, both depending on $\mathcal{V}$ and D^{ij}, and the numbers in parentheses indicate the iteration in which the fields are evaluated. Inserting this into Equation (4.75), the updated conserved fields can be computed as

$$\mathcal{U}_r^{(m+1)} = \left(\mathcal{I} + s\,\Delta t^n \mathcal{M}^{(m)}\right)^{-1}\left(\mathcal{U}_r' - s\,\Delta t^n\, b^{(m)}\right), \tag{4.77}$$

   after which primitive fields can be updated using Eq. (4.74).

2. *Newton's method for radiation fields*, implemented in [190] and [193]. This scheme consists in finding the roots of the nonlinear multidimensional function

$$\mathcal{Q}(E_r, \mathbf{F}_r) = \mathcal{U}_r - \mathcal{U}_r' + s\,\Delta t^n\,\mathcal{G}, \tag{4.78}$$

   updating the radiation variables on each iteration as

$$\mathcal{U}_r^{(m+1)} = \mathcal{U}_r^{(m)} - \left[\mathcal{J}^{(m)}\right]^{-1}\mathcal{Q}^{(m)}, \tag{4.79}$$

where we have defined the Jacobian matrix $\mathcal{J}$ as $\mathcal{J}_{ij} = \partial \mathcal{Q}_i / \partial \mathcal{U}_r^j$. The elements of $\mathcal{J}$ are computed numerically, taking small variations of the iterated fields. As in the fixed-point method, matter fields are computed from $\mathcal{U}_r$ for each step by means of an inversion of Eq. (4.74).

3. *Newton's method for matter fields*, implemented in [193]. This procedure is identical to the previous one, with the difference that in this case the iterated fields are the fluid's pressure and the spatial components of its four-velocity, which we denote as $\mathcal{W} = (p_g, \mathbf{u})^\intercal$. These are updated as

$$\mathcal{W}^{(m+1)} = \mathcal{W}^{(m)} - \left[\mathcal{J}^{(m)}\right]^{-1} \mathcal{Q}^{(m)}, \tag{4.80}$$

where now $\mathcal{J}_{ij} = \partial \mathcal{Q}_i / \partial \mathcal{W}^j$ and $\mathcal{Q}$ is regarded as a function of $\mathcal{W}$. This scheme is much faster than the previous one, since the computation of $\mathcal{U}_r$ from $\mathcal{W}$ by means of Eq. (4.74) is now straightforward and no longer requires a cumbersome inversion of conserved to primitive fields.

For each of these methods, iterations are carried out until convergence is reached, which is controlled by means of some error function. In the first of them, this function is chosen as the norm of the relative differences between successive values of $\mathcal{V}$, whereas in the last two of them it is defined as the norm of $\mathcal{Q}^{(m+1)}$. If $\mathcal{E} \ll E_r$, the errors of the matter fields can be large even when radiation fields converge, since Eq. (4.74) implies that $\mathcal{E}$ and E_r have the same absolute error, as well as $\mathbf{m}$ and $\mathbf{F}_r$. Therefore, having small relative differences of E_r does not guarantee the same for $\mathcal{E}$, which can lead to nonnegligible inaccuracies if the second method is used. Equivalently, the same problem can occur whenever $\mathcal{E} \gg E_r$ if method 3 is chosen [193]. To overcome this issue, we have included in the code the option of adding to the convergence function the norm of the relative differences of $\mathcal{E}$ when using the second method and of E_r when using the third one. We have seen in the performed tests that the fixed-point method converges rather fast, meaning that the number of iterations that it requires frequently coincides with that obtained with the last two methods. This scheme has sufficed to perform all of the tests carried out in this work and has often been the fastest one when compared to the other two, having been overcome only by method 3 in a few cases.

4.3 Numerical benchmarks

We show in this section a series of numerical benchmarks to verify the code performance, as well as the correctness of the implementation under different physical regimes and choices of

coordinates. Unless otherwise stated, we employ the HLLC solver introduced in Section 4.2.3; the domain is discretized using a fixed uniform grid, and outflow boundary conditions are imposed for all fields. Magnetic fields are neglected in all of the considered problems, except in Section 4.3.7. Furthermore, all of the tests have been run with both the IMEX–SSP2(2,2,2) and IMEX1 methods, obtaining equivalent results unless indicated otherwise.

4.3.1 Riemann problem for optically thin radiation transport

We first validate the implemented radiation transport schemes when any interaction with matter is neglected. To this end, we have run several 1D Riemann problems, setting all of the interaction terms to zero and focusing only on the evolution of the radiation fields. The initial setup of these consists of two regions of uniform E_r and $\mathbf{F}_r$, separated by a discontinuity at $x = 0$. The full domain is defined as the interval $[-20, 20]$. We show here two of such tests, exploring the case $||\mathbf{F}_r|| < E_r$ (test 1) and the free-streaming limit, $||\mathbf{F}_r|| \simeq E_r$ (test 2).

In the first test, initial states are assigned at $t = 0$ as

$$(E_r,\, F_r^x,\, F_r^y)_{L,R} = \begin{cases} \left(1,\, 0,\, \frac{1}{2}\right) & \text{for} \quad x < 0 \\ (1,\, 0,\, 0) & \text{for} \quad x > 0 \end{cases} \tag{4.81}$$

The solution, plotted in Fig 4.2 at $t = 20$ with a resolution of 2^{14} zones (solid black line), shows a three-wave pattern, as it is expected from the eigenstructure of the radiation transport equations (see Section 4.2.3 and Appendix D). The left and right outermost waves are, respectively, a left-facing shock and a right-going expansion wave, while the middle wave is the analogous of a contact wave. The fields Π and β_x, defined in Section 4.2.3, are constant across the contact mode. In the same Figure, we show the solution obtained with the HLL and HLLC solvers at the resolution of 256 zones using a first-order reconstruction scheme [see 203]. As expected, the employment of the HLLC solver yields a sharper resolution of the middle wave.

For the second test, the initial condition is defined as

$$(E_r,\, F_r^x,\, F_r^y)_{L,R} = \begin{cases} \left(\frac{1}{10},\, \frac{1}{10},\, 0\right) & \text{for} \quad x < 0 \\ (1,\, 0,\, 1) & \text{for} \quad x > 0 \end{cases} \tag{4.82}$$

Results obtained with the first-order scheme and the HLL and HLLC solvers are plotted in Fig. 4.3 together with the reference solution (solid black line) at $t = 20$. As for the previous case, a three-wave pattern emerges, formed by two left- and right-going shocks and a middle contact wave. It can also be seen that Π and β_x are again continuous across the contact wave.

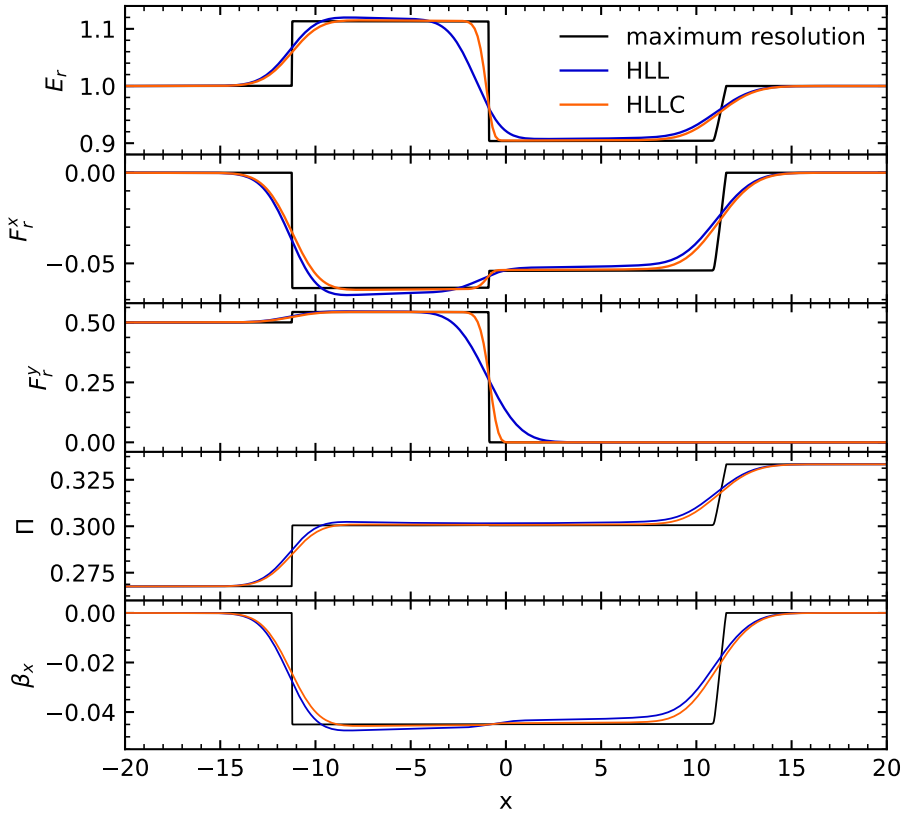

Fig. 4.2 Radiation fields in the optically thin Riemann test 1 at $t = 20$. Two solutions obtained with the HLL solver (solid blue line) and the HLLC solver (solid orange line), computed using 2^8 zones in both cases, are compared to a reference solution obtained with 2^{14} zones. These show a left shock at $x \approx -11$, a right expansion wave at $x \approx 11$, and a central contact discontinuity at $x \approx -1$, along which the fields Π and β_x are continuous. Reproduced from [260].

Differences between HLLC and HLL are less pronounced than the previous case, with the HLL (HLLC) overestimating the left-going shock position by 50% (30%).

For both tests, we have conducted a resolution study covering the range $[2^6, 2^{10}]$ using first-order as well as second-order reconstructions making use of the second-order harmonic mean limiter by [271]. In Figure 4.4, we plot the L_1-norm error of E_r (computed with respect to the reference solution) as functions of the resolution. The Courant number is $C_a = 0.4$ for both cases. Overall, the HLLC yields smaller errors when compared to the HLL, as expected. This discrepancy is more evident in the first-order case and it is mitigated in the case of a second-order interpolant (a similar behavior is also found in [203]).

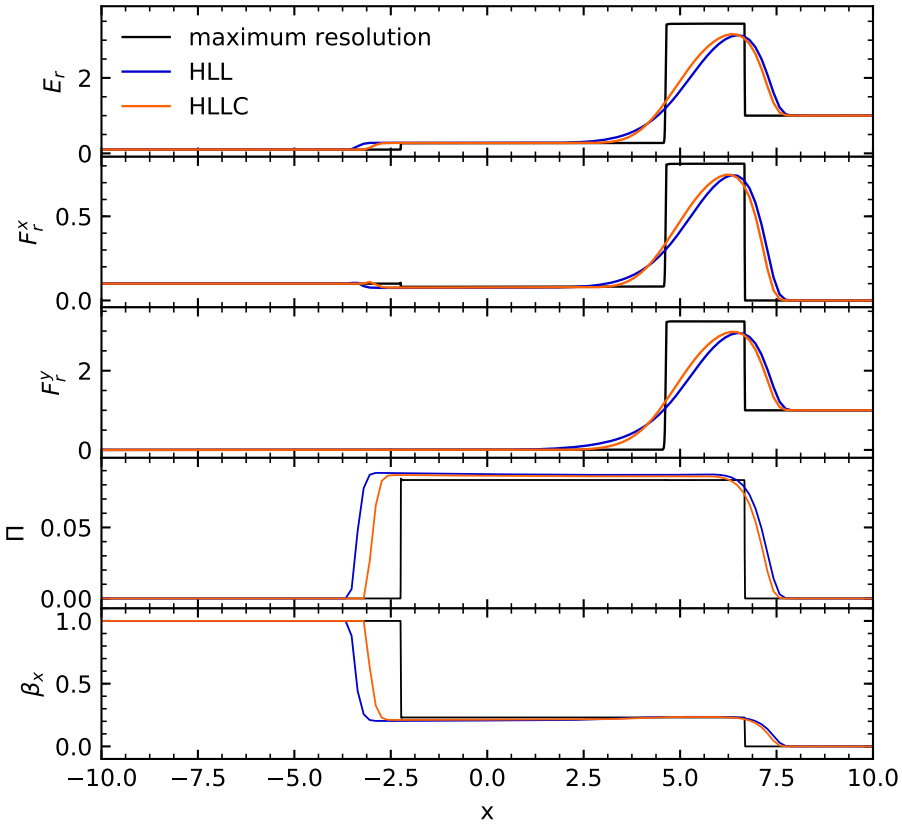

Fig. 4.3 Same as Fig. 4.2, but for the optically thin Riemann test 2. The solutions exhibit a leftward-moving shock, a contact discontinuity, and a rightward-moving shock at $x \approx -2.2$, 4.5, and 7, respectively. Reproduced from [260].

4.3.2 Free-streaming beam

A useful test to investigate the code's accuracy for multidimensional transport is the propagation of a radiation beam oblique to the grid (see, e.g., [187, 272]). This problem is also useful to quantify the numerical diffusion that may appear when the fluxes are not aligned with the axes. We again neglect the gas–radiation interaction terms and solely follow the evolution of the radiation fields.

The initial setup consists of a square Cartesian grid of side $L = 5$ cm, where the radiation energy density is set to $E_{r,0} = 10^4$ erg cm^{-3}. At the $x = 0$ boundary, a radiation beam is injected by fixing $E_r = 10^8\, E_{r,0}$ and $\mathbf{F}_r = (1/\sqrt{2}, 1/\sqrt{2})\, E_r$ for $y \in [0.30, 0.44]$ cm. Thus, the injected beam satisfies the equality $||\mathbf{F}_r|| = E_r$, which corresponds to the free-streaming limit. Outflow conditions are imposed on the remaining boundaries.

Again, we compare the performance of the HLL and HLLC solvers, this time using the fourth-order linear slopes by [273] and resolutions of 150×150 and 300×300 zones. The

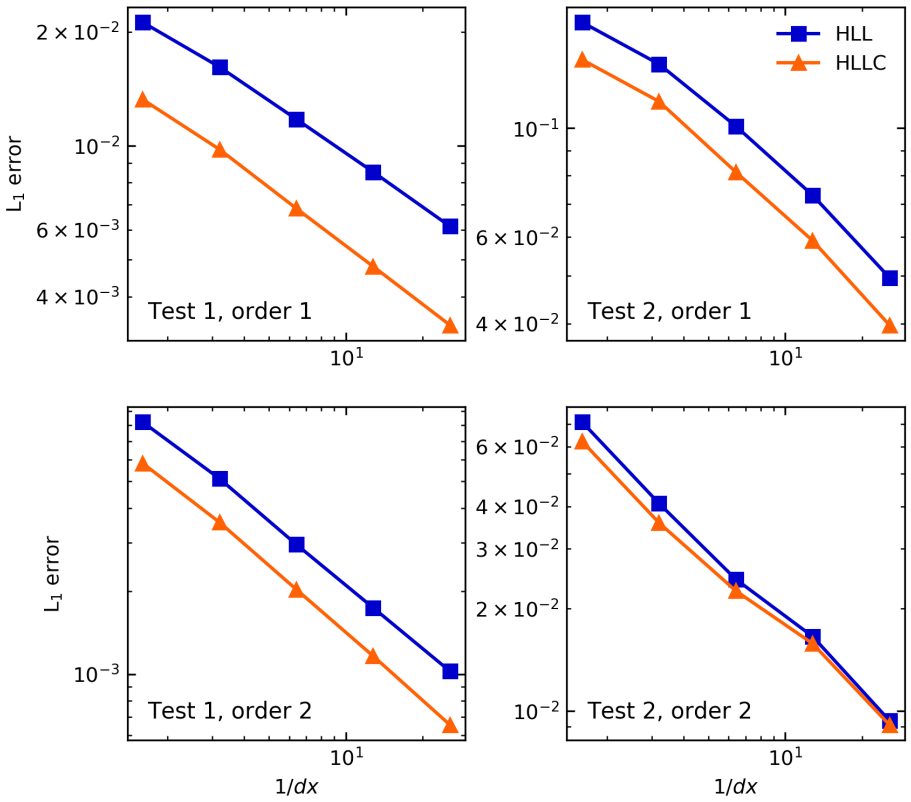

Fig. 4.4 L_1 error of E_r in the optically thin Riemann tests 1 and 2, computed in each case with respect to a reference solution obtained using 2^{14} zones. The errors are plotted for several resolutions as a function of $1/dx$, where dx is the cell's width in each case. Different results are shown using first-order (upper panels) and second-order (lower panels) reconstruction schemes. Reproduced from [260].

Courant number is $C_a = 0.4$. The energy density distribution obtained with the HLLC solver at the largest resolution is shown in Fig. 4.5 at $t = 5 \times 10^{-10}$ s. In every case, a beam forms and reaches the upper boundary between $x = 4$ and 5 cm, after crossing a distance equivalent to roughly 64 times its initial width. Since no interaction with matter is considered, photons should be transported in straight lines. As already mentioned, the free-streaming limit corresponds to a delta-like specific intensity parallel to $\mathbf{F}_r$. Hence, photons are injected in only one direction, and the beam's structure should be maintained as it crosses the computational domain. However, in the simulations, the beam broadens due to numerical diffusion before reaching the upper boundary. For this particular test, due to its strong discontinuities, we have seen that this effect is enhanced by the flattening applied during the reconstruction step in order to satisfy Equation (4.55), which is necessary for stability reasons.

In order to quantify this effect and its dependency on the numerical resolution, we have computed several time-averaged $E_r(y)$ profiles along vertical cuts at different x values. As an

indicator of the beam's width, we have computed for each x the standard deviation of these profiles as

$$\sigma_y = \sqrt{\int_0^L \left[y - \overline{y}\right]^2 \varphi(y)\,\mathrm{d}y}\,, \tag{4.83}$$

with

$$\overline{y} = \int_0^L \varphi(y)\, y\,\mathrm{d}y\,, \tag{4.84}$$

where the weighting function $\varphi(y)$ is defined as

$$\varphi(y) = \overline{E}_r(y) \Big/ \int_0^L \overline{E}_r(y)\,\mathrm{d}y\,, \tag{4.85}$$

being $\overline{E}_r$ the time-averaged value of E_r. We have then divided the resulting values of σ_y by $\sigma_{y0} \equiv \sigma_y(x=0)$ in order to show the relative growth of the dispersion. The resulting values of σ_y/σ_{y0} are shown in Fig. 4.5, where it can be seen that the beam's dispersion grows with x. The difference between σ_y/σ_{y0} and its ideal value ($\sigma_y/\sigma_{y0} \equiv 1$) gets reduced by a factor between 2 and 2.5 when the highest resolution is used. In the same figure, it can be seen that the dispersion is only slightly reduced when the HLLC solver is used instead of HLL. A similar plot of σ_y/σ_{y0} is obtained with the second-order limiter by [271], where the values of the relative dispersion increase roughly between 30% and 40%, showing as in Section 4.3.1 that the accuracy of these methods not only depends on the chosen Riemann solver but is also extremely sensitive to the chosen reconstruction scheme.

4.3.3 Radiation–matter coupling

In order to verify the correct integration of the interaction terms, we have run a test proposed in [274], in which matter and radiation approach thermal equilibrium in a homogeneous system. This is achieved by solving the radiation RHD (Rad-RHD) equations in a single-cell grid, thus removing any spatial dependence. In this configuration, due to the form of Equations (4.43)–(4.48), all fields but the energy densities of both radiation and matter remain constant for $t > 0$. Using conservation of total energy, the resulting equation for the evolution of the gas energy density (in cgs units) is

$$\frac{1}{c}\frac{d\mathcal{E}}{dt} = \rho\kappa\left(E_r - 4\pi B\left(T\right)\right). \tag{4.86}$$

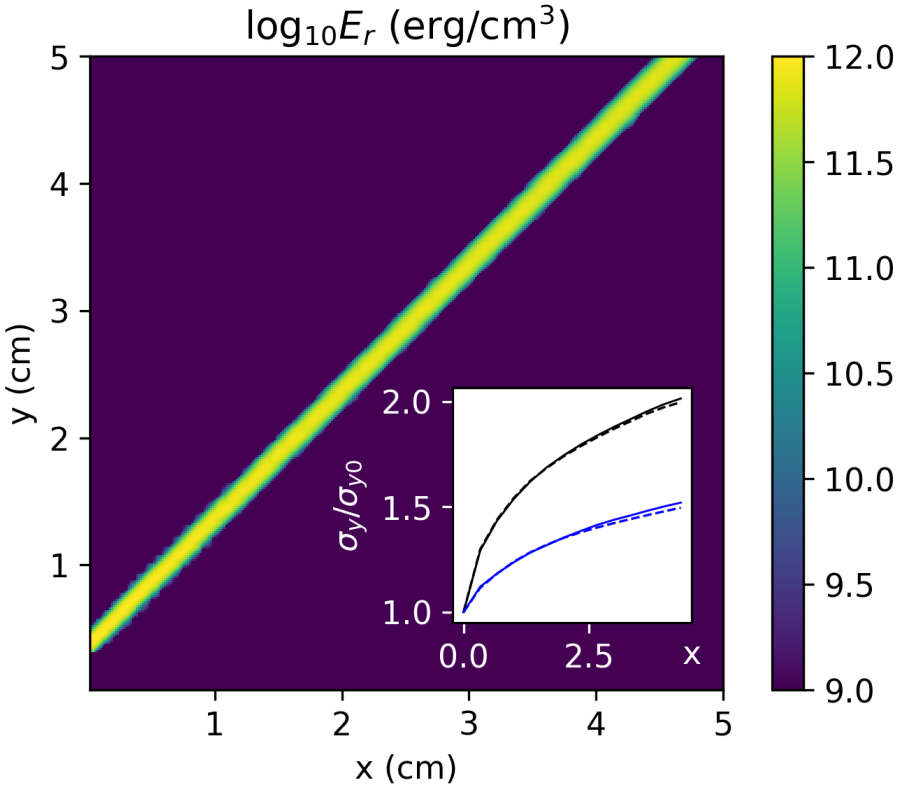

Fig. 4.5 Free-streaming beam test. A radiation beam is introduced in a 2D grid from its lower left boundary, at $45°$ with respect to the coordinate axes. The values of $\log_{10} E_r$ obtained with the HLLC solver using a resolution of 300×300 zones are plotted as a function of (x, y) at $t = 5 \times 10^{-10}$ s (color scale). The relative dispersion σ_y/σ_{y0} along the y-direction is shown in the lower-right corner as a function of x (cm) for the selected resolutions of 150×150 (black lines) and 300×300 (blue lines). In both cases, the solid and dashed lines correspond respectively to the results obtained with the HLL and the HLLC solvers. Reproduced from [260].

This can be simplified if the chosen initial conditions are such that E_r is constant throughout the system's evolution. In that case, Equation (4.86) can be solved analytically, leading to an implicit relation between $\mathcal{E}$ and t that can be inverted using standard methods.

We have run this test for two different initial conditions, using in both cases $\rho = 10^{-7}$ g cm^{-3}, $E_r = 10^{12}$ erg cm^{-3}, opacities $\kappa = 0.4$ cm^2 g^{-1} and $\sigma = 0$, and a mean molecular weight $\mu = 0.6$. A constant-gamma EoS has been assumed, with $\Gamma = 5/3$. We have chosen the initial gas energy density to be either $\mathcal{E} = 10^{10}$ erg cm^{-3} or $\mathcal{E} = 10^2$ erg cm^{-3}, which are, respectively, above and below the final equilibrium value of around 7×10^7 erg cm^{-3}.

The gas energy density is plotted as a function of time for both conditions in Fig. 4.6. Simulations are started with an initial time step $\Delta t = 10^{-10}$ s. An additional run for $t \leq 10^{-10}$

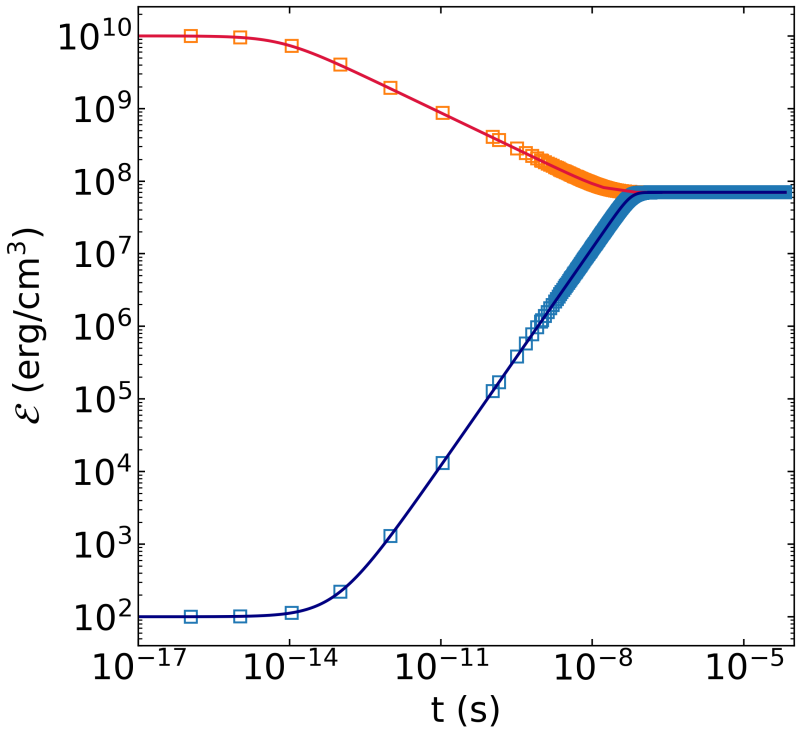

Fig. 4.6 radiation–matter coupling test. The gas energy density $\mathcal{E}$ is plotted as a function of time for the two chosen initial conditions, until thermal equilibrium is reached. The obtained numerical values (empty squares) are shown here to match the analytical solutions (solid lines) for both initial conditions. Reproduced from [260].

s is done for each initial condition with an initial $\Delta t = 10^{-16}$ s, in order to show the evolution in the initial stage. In every case, the gas radiation energy goes through an initial constant phase that lasts until $t \sim 10^{-14}$ s, after which it varies towards the equilibrium value. Equilibrium occurs when the condition $E_r = 4\pi B(T)$ is reached (see Eq. (4.86)), i.e., when the power emitted by the gas equals its energy absorption rate. This happens around $t \approx 10^{-7}$ s for both initial conditions. As shown in Fig. 4.6, the numerical solutions match the analytical ones in the considered time range.

4.3.4 Shock waves

We now study the code's ability to reproduce general shock-like solutions without neglecting the interaction terms. To this purpose, we have reproduced a series of tests proposed in [275]. As in Section 4.3.1, we place a single initial discontinuity at the center of the 1D domain defined by the interval $[-20, 20]$. At $t = 0$, both matter and radiation fields are constant on each side of the domain and satisfy the condition for LTE between matter and

Test	ρ_L	$p_{g,L}$	u^x_L	$E_{r,c,L}$	ρ_R	$p_{g,R}$	u^x_R	$E_{r,c,R}$	Γ	κ
1	1.0	3.0×10^{-5}	0.015	1.0×10^{-8}	2.4	1.61×10^{-4}	6.25×10^{-3}	2.51×10^{-7}	5/3	0.4
2	1.0	4.0×10^{-3}	0.25	2.0×10^{-5}	3.11	0.04512	0.0804	3.46×10^{-3}	5/3	0.2
3	1.0	60.0	10.0	2.0	8.0	2.34×10^{3}	1.25	1.14×10^{3}	2	0.3
4	1.0	6.0×10^{-3}	0.69	0.18	3.65	3.59×10^{-2}	0.189	1.3	5/3	0.08

Table 4.1 Parameters used in the shock tests, in code units. The subscripts R and L correspond, respectively, to the initial conditions for $x > 0$ and $x < 0$.

radiation, that is, $\tilde{E}_r = 4\pi B(T)$. Additionally, the fluxes on each side obey $\tilde{F}^x_r = 0.01 \times \tilde{E}_r$. A constant-gamma EoS is assumed, scattering opacity is neglected, and a Courant factor $C_a = 0.25$ is used.

Initial conditions are chosen in such a way that the system evolves until it reaches a final stationary state. Neglecting time derivatives, Equations (4.43)–(4.48) lead to

$$\partial_x \left(\rho u^x\right) = 0 \tag{4.87}$$

$$\partial_x \left(m^x_{tot}\right) = 0 \tag{4.88}$$

$$\partial_x \left(m^x v^x + p_g + P^{xx}_r\right) = 0 \tag{4.89}$$

$$\partial_x \left(F^x_r\right) = -G^0 \tag{4.90}$$

$$\partial_x \left(P^{xx}_r\right) = -G^x. \tag{4.91}$$

A time-independent solution demands that quantities under derivative in Equations (4.87)–(4.89) remain constant, and this condition must also be respected by the initial states. In addition, Equations (4.90) and (4.91) show that the final F^x_r and P^{xx}_r must be continuous, although their derivatives can be discontinuous. This does not necessarily imply that the final E_r profile must also be continuous, since any value of $P^{xx}_r(E_r, F^x_r)$ can correspond to up to two different E_r values for fixed F^x_r. However, in the particular case where $F^x_r < P^{xx}_r$, it can be shown using Eqs. (4.52)–(4.54) that the inversion of $P^{xx}_r(E_r, F^x_r)$ in terms of E_r leads to unique solutions, and thus E_r must be continuous. In the same way, we have verified that this condition is equivalent to $F^x_r/E_r < 3/7$.

We have performed four tests for different physical regimes. All of the initial values are chosen to coincide with those in [275]. In that work, as in several others where the same tests are performed (see, e.g., [190, 200, 276]), the Eddington approximation, given by $\tilde{P}^{xx}_r = \tilde{E}_r/3$, is used instead of the M1 closure. Therefore, our results are not comparable with these unless the final state satisfies $\tilde{P}^{xx}_r \simeq \tilde{E}_r/3$ in the whole domain. We now outline the main features of each test, whose parameters are summarized in Table 4.1:

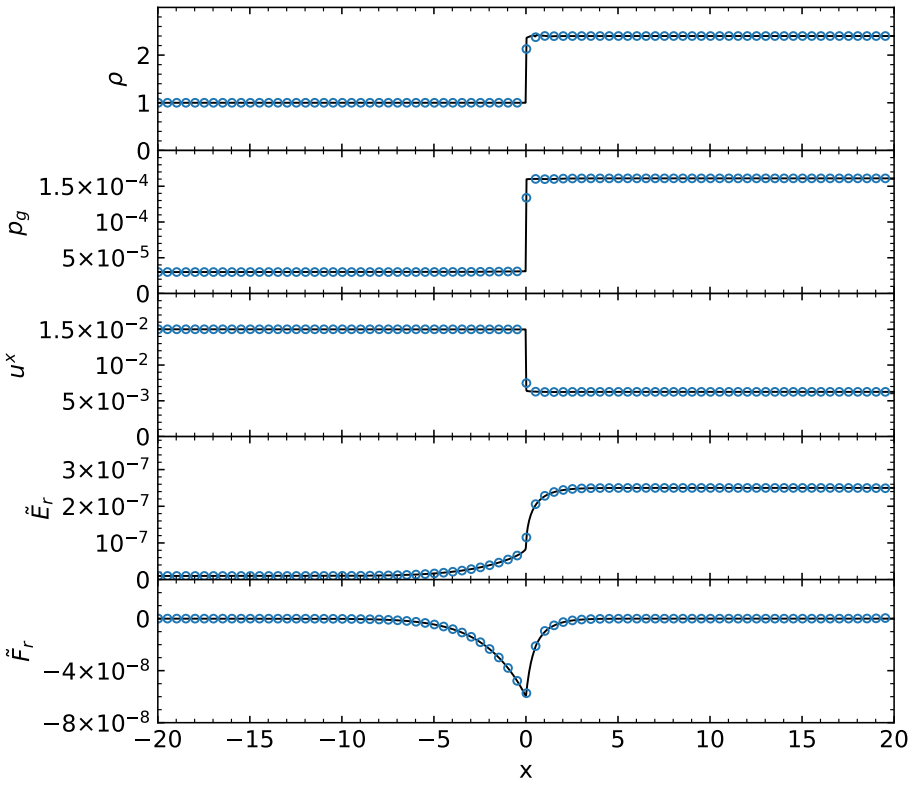

Fig. 4.7 Final profiles of the nonrelativistic strong shock test obtained using 3200 zones (solid black line) and 800 zones (open blue circles; plotted every 10 values). Reproduced from [260].

1. *Nonrelativistic strong shock*. A gas-pressure–dominated shock moves at a nonrelativistic speed in a cold gas ($p_g \ll \rho$), with a maximum u^x of 0.015. The final profiles of ρ, p_g, u^x, $\tilde{E}_r$, and $\tilde{F}_r^x$ are shown in Fig. 4.7. As in the nonradiative case, the first three show an abrupt change at $x = 0$, while radiation fields seem continuous.

2. *Mildly relativistic strong shock*. The conditions are similar to the previous test, with the difference that a mildly relativistic velocity ($u^x \leq 0.25$) is chosen. The final profiles (see Fig. 4.8) look similar to those in Fig. 4.7, with the difference that $\tilde{E}_r$ exhibits a small discontinuity close to $x = 0$.

3. *Highly relativistic wave*. The initial conditions are those of a highly relativistic gas-pressure–dominated wave ($u^x \leq 10$, $\rho \ll \tilde{P}_r^{xx} < p_g$). In this case, as it can be seen in Fig. 4.9, all profiles are continuous.

4. *Radiation-pressure–dominated wave*. In this case we study a situation where the radiation pressure is much higher than the gas pressure, in a shock that propagates

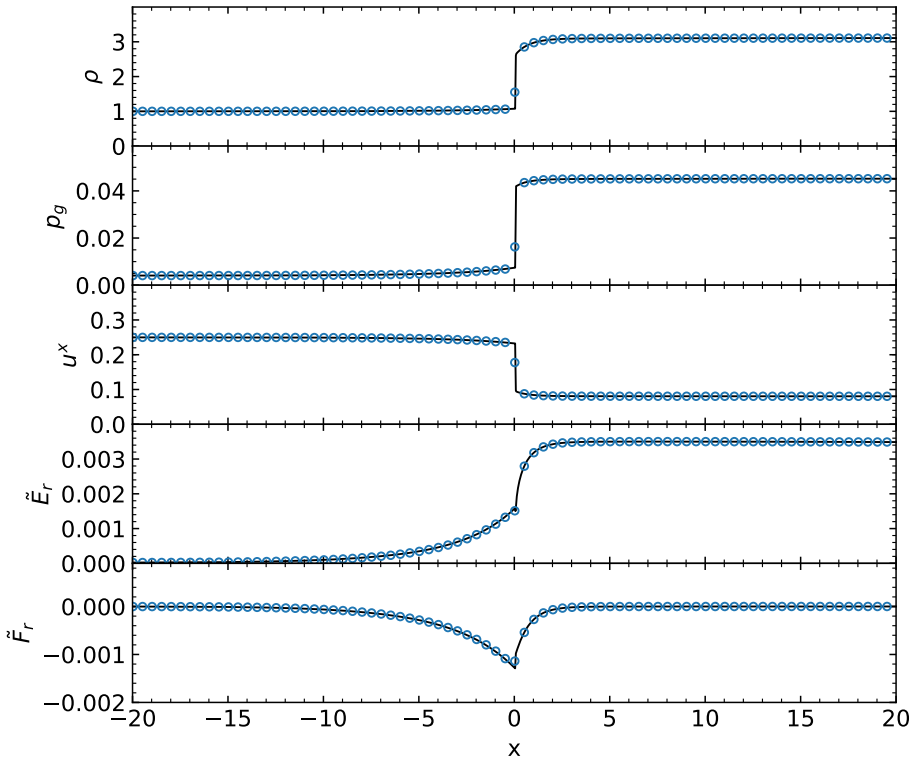

Fig. 4.8 Same as Fig. 4.7, but for the mildly relativistic shock test. Reproduced from [260].

at a mildly relativistic velocity ($u^x \leq 0.69$). As in the previous case, there are no discontinuities in the final profiles (see Fig. 4.10).

In order to test the convergence of the numerical solutions, we have performed each simulation twice, dividing the domain into 800 and in 3200 zones. In every case, as shown in Figs. 4.7-4.10, both solutions coincide. However, our results do not coincide with those obtained in the references mentioned above. The most noticeable case is the test shown in Fig. 4.8, where the ratio $\tilde{P}_r^{xx}/\tilde{E}_r$ reaches a maximum value of 0.74 close to the shock, instead of the value of $1/3$ that would be obtained within the Eddington approximation. The result is a much smoother $\tilde{E}_r$ profile than the one shown in, for instance, [275]. Yet, our results show a good agreement with those in [192], where the tests are also performed assuming the M1 closure.

We point out that, in the nonrelativistic strong shock case, the characteristic fluid speeds are ~ 35 times smaller than those corresponding to radiation transport. Still, the computations do not show a significant increase of numerical diffusion owing to such scale disparity. The same conclusion holds if the computations are done in the downstream reference frame (not shown here).

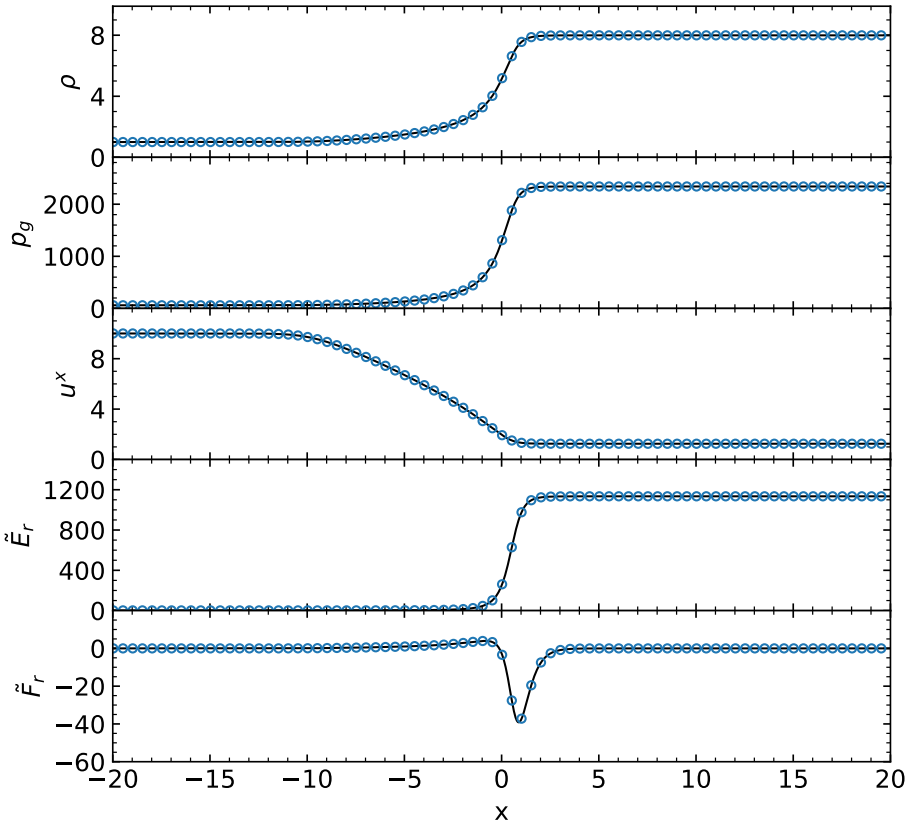

Fig. 4.9 Same as Fig. 4.7, but for the highly relativistic wave test. Reproduced from [260].

4.3.5 Radiation pulse

Following [190], we have tested the evolution of a radiation pulse in the optically thin and optically thick limits. These two regimes allowed us to assess, respectively, the code performance when choosing different coordinate systems and its accuracy in the diffusion limit, as summarized below.

Optically thin case

We considered an initial spherically symmetric radiation energy distribution contained around the center of a 3D box of side $L = 100$. Radiation energy is initially set as $E_r = 4\pi B(T_r)$, with

$$T_r = T_0 \left(1 + 100\, e^{-r^2/w^2}\right), \tag{4.92}$$

where r is the spherical radius, while $T_0 = 10^6$ and $w = 5$. Similarly, gas pressure is set in such a way that $T(\rho, p_g) = T_0$, which means that the system is initially in thermal equilibrium far from the pulse. We also set $\rho = 1$, $v^x = 0$ and $F_r^x = 0$ in the whole domain, $\Gamma = 5/3$,

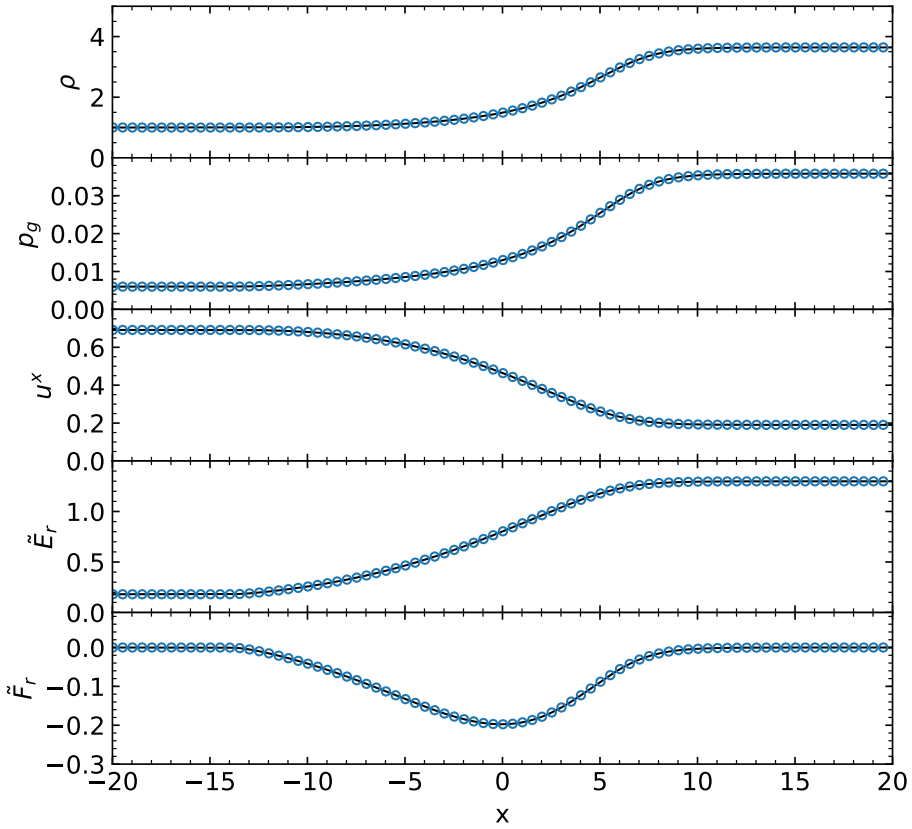

Fig. 4.10 Same as Fig. 4.7, but for the radiation-pressure–dominated wave test. Reproduced from [260].

$C_a = 0.4$, $\kappa = 0$, and a small scattering opacity $\sigma = 10^{-6}$. In this way, the total optical depth of the box from side to side is $\tau = \rho\,\sigma L = 10^{-4} \ll 1$; i.e., the box is transparent to radiation.

We have computed the departure from these conditions using 1D spherical and 3D Cartesian coordinates. In the Cartesian case, we have employed a uniform grid resolution of $200 \times 200 \times 200$ zones. On the other hand, in spherical geometry, our domain is the region $r \in [0, L/2]$ using a uniformly spaced grid of 100 zones, in order to have a comparable resolution with the 3D simulations. In this last case, reflective boundary conditions have been set at $r = 0$.

As shown in Fig. 4.11, the pulse expands and forms a nearly isotropic blast wave, which slightly deviates from the spherical shape in the Cartesian case due to grid noise. The evolution of the radiation energy profiles in both simulations is shown in the two upper panels of Figure 4.12. Since no absorption in the material is considered, the total radiation energy is conserved, and thus the maximum energy density of the formed expanding wave decreases as $1/r^2$. As it can be seen in Fig. 4.12, this dependence is effectively verified once the blast wave

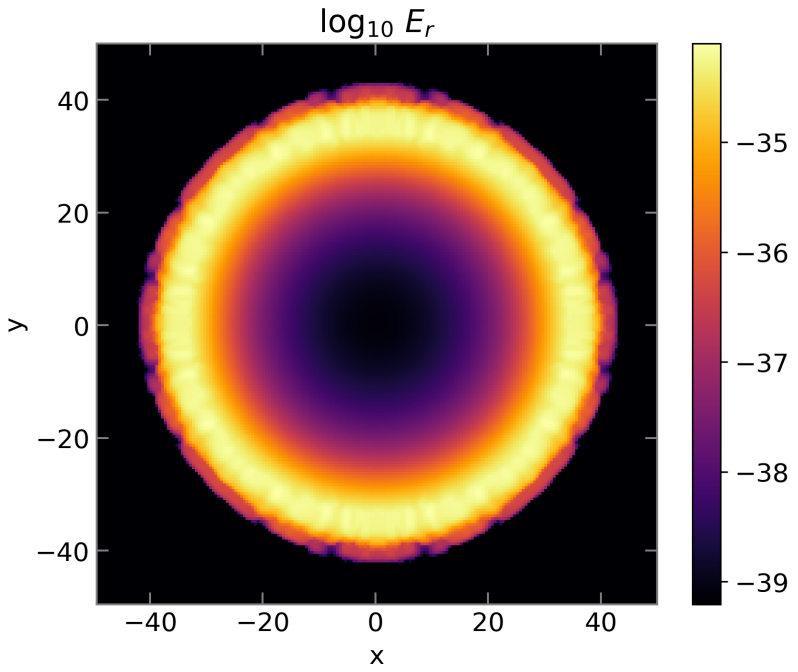

Fig. 4.11 Radiation energy density map of the optically thin radiation pulse computed using a $200 \times 200 \times 200$ uniform Cartesian grid. Values of $\log_{10} E_r$ on the plane $z = 0$ are shown at $t = 35$, when the blast wave has already been formed. Reproduced from [260].

is formed. The same kind of analysis is possible if radiation is contained entirely on the plane $z = 0$. In this case, the maximum energy density decreases as $1/R$, with $R = \sqrt{x^2 + y^2}$. We have verified this behavior in 1D cylindrical and 2D Cartesian coordinates, employing uniform grids of 100 zones in the first case and 200×200 in the second (see the two lower panels in Fig. 4.12). In every case, the same simulations performed with different coordinate systems show a good agreement.

Optically thick case

We now consider the case where the scattering opacity is nine orders of magnitude larger than in the previous simulations, i.e., $\sigma = 10^3$, and all other parameters remain unchanged. In that situation, the optical thickness of the box from side to side is $\tau = 10^5 \gg 1$, which means that the box is largely opaque to radiation. Here we solve the evolution equations on a Cartesian 1D grid with uniform spacing. Using a resolution of 101 zones, the optical thickness of a single cell is $\tau \sim 10^3$. For this reason, signal speeds are always limited according to Eq. (A.10).

Under these conditions, the system evolves in such a way that $|\partial_t F_r^x| \ll |\partial_x P_r^{xx}|$ and $|F_r^x| \ll E_r$, and therefore $P_r^{xx} \simeq E_r/3$, as pointed out in Section 4.1.4. Neglecting the

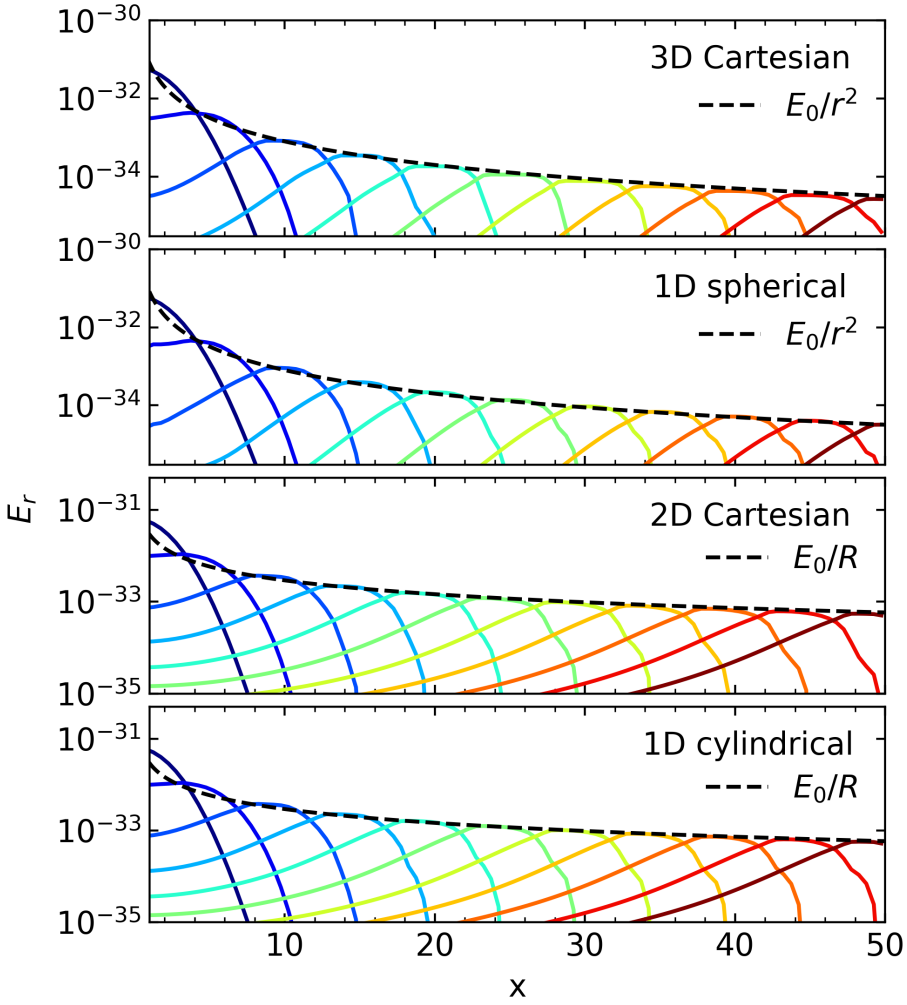

Fig. 4.12 Radiation energy density profiles in the optically thin pulse test (solid colored lines), computed at $y = z = 0$. From top: profiles obtained using 3D Cartesian, 1D spherical, 2D Cartesian and 1D cylindrical coordinates, shown every $\Delta t = 5.0$. The dependence of the maximum energy on $1/r^2$ ($1/R$) is shown with dashed black lines in the first (last) two cases. Reproduced from [260].

term $\partial_t F_r^x$ in Eq. (4.48) and assuming $P_r^{xx} = E_r/3$, the radiation flux can be written as $F_r^x = -\partial_x E_r/3\rho\chi$. Hence, assuming the density remains constant, the radiation energy density should evolve according to the following diffusion equation:

$$\frac{\partial E_r}{\partial t} = \frac{1}{3\rho\chi}\frac{\partial^2 E_r}{\partial x^2}. \tag{4.93}$$

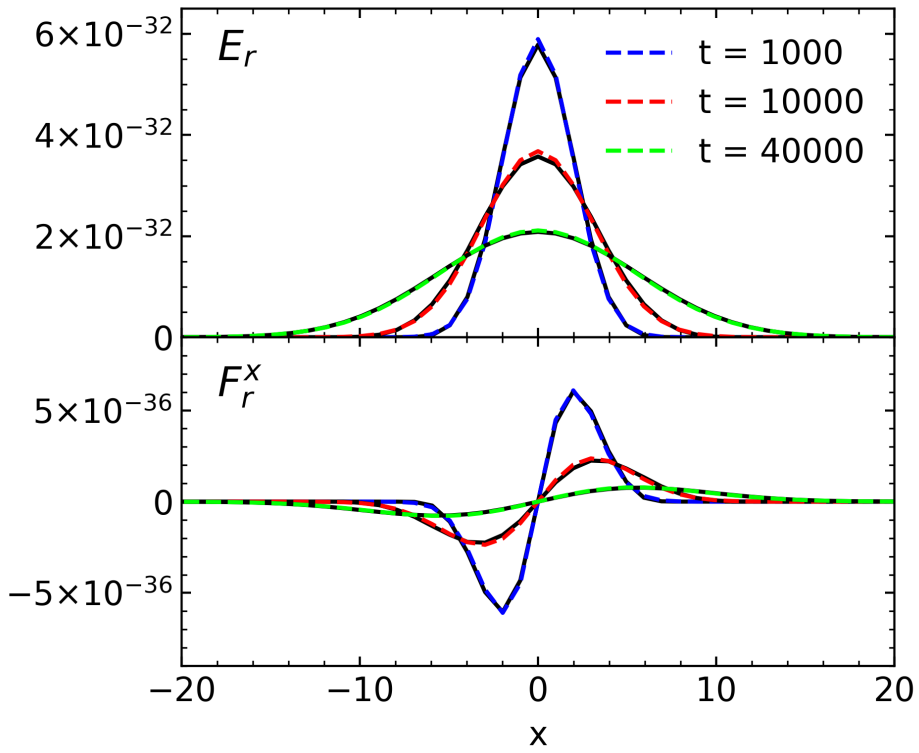

Fig. 4.13 Radiation energy density and flux profiles in the optically thick pulse test shown at $t = 10^3, 10^4$ and 4×10^4 (solid black lines). The analytical solution of the diffusion equation (Eq. (4.93)) is superimposed (dashed colored lines). Reproduced from [260].

With the chosen initial conditions, this equation can be solved analytically, e.g., by means of a Fourier transform in the spatial domain. The exact and numerical solutions are shown in Fig. 4.13. Our results show a good agreement between the analytical and numerical solutions. Furthermore, we have verified that, if radiation–matter interaction is not taken into account for the signal speed calculation, i.e., if the limiting given by Eq. (A.10) is not applied, the pulse gets damped much faster than what it should be expected from Eq. (4.93), due to the numerical diffusion that occurs when signal speeds are overestimated.

Finally, we have seen that this test leads to inaccurate values of F_r^x if IMEX–SSP2(2,2,2) is used, although the values of E_r remain close to the analytical ones. This problem lies in the fact that both the gradient of the flux of F_r^x and its source term largely exceed F_r^x and are not compensated in the last explicit step of the method (see Eq. (4.57)). When these conditions are met, we have observed that IMEX–SSP2(2,2,2) can lead to inaccuracies and instabilities due to failure in preserving energy positivity (see Section 4.3.6). On the contrary, IMEX1 shows better performance in those cases, as the flux and the source terms are more accurately balanced during the implicit steps (see Eq. (4.58)).

The limiting scheme in Eq. (A.10) depends on the optical depth of individual cells, which is inversely proportional to the resolution. Therefore, when AMR is used, there can be situations where this limiting is applied at the coarser levels but not at the finer ones. Furthermore, when using HLLC, the solver is replaced by HLL for every zone where Eq. (A.10) is enforced. To study the code's performance under these conditions, we have run this test on a static AMR grid using 128 zones at the coarsest level with 6 levels of refinement with a jump ratio of 2, yielding an equivalent resolution of 8192 zones. We choose $\sigma = 50$ so that levels 0–4 are solved with the HLL solver limiting the maximum signal speeds according to Eq. (A.10), while levels 5 and 6 are solved using the HLLC solver. The solution thus obtained converges to the analytic solution of Eq. (4.93) at all refinement levels (see Fig. 4.14).

However, we have observed the formation of spurious overshoots at the boundaries between refinement levels. These artifacts are drastically reduced if the order of the reconstruction scheme is increased—for instance, if the weighted essentially nonoscillatory (WENO) method of [277] or the piecewise parabolic method (PPM) of [278] are used, as shown in Fig. 4.14. We argue that such features, which are not uncommon in AMR codes [279, 280], can be attributed to the refluxing process[6] needed to ensure correct conservation of momentum and total energy (see [201]). In addition, the presence of source terms requires additional care when solving the Riemann problem between fine-coarse grids due to temporal interpolation [281]. We do not account here for such modifications and defer these potential issues to future investigations.

4.3.6 Shadows

One of the most important features of the M1 closure is its ability to reproduce the behavior of physical systems in which the angular distribution of the radiation specific intensity has strong spatial variations. One such example is a system where a free-streaming radiation field encounters a highly opaque region of space, casting a shadow behind it. To test the code performance when solving such problems, we have performed a test in which a shadow is formed behind a high-density elliptic cylinder, following [282] and using the same parameters as in [187].

Computations are carried out in the 2D domain given by $\{(x, y) \in [-0.5, 0.5]\ \text{cm} \times [0, 0.6]\,\text{cm}\}$. Reflective boundary conditions are imposed at $y = 0$. A constant density $\rho_0 = 1$ g cm^{-3} is fixed in the whole space, except in the elliptic region, where $\rho = \rho_1 = 10^3$ g cm^{-3}. In order

[6] At the boundary between two different levels l and $l + 1$, fluxes at the level $l + 1$ must be averaged in space and time before being used for the time integration at level l.

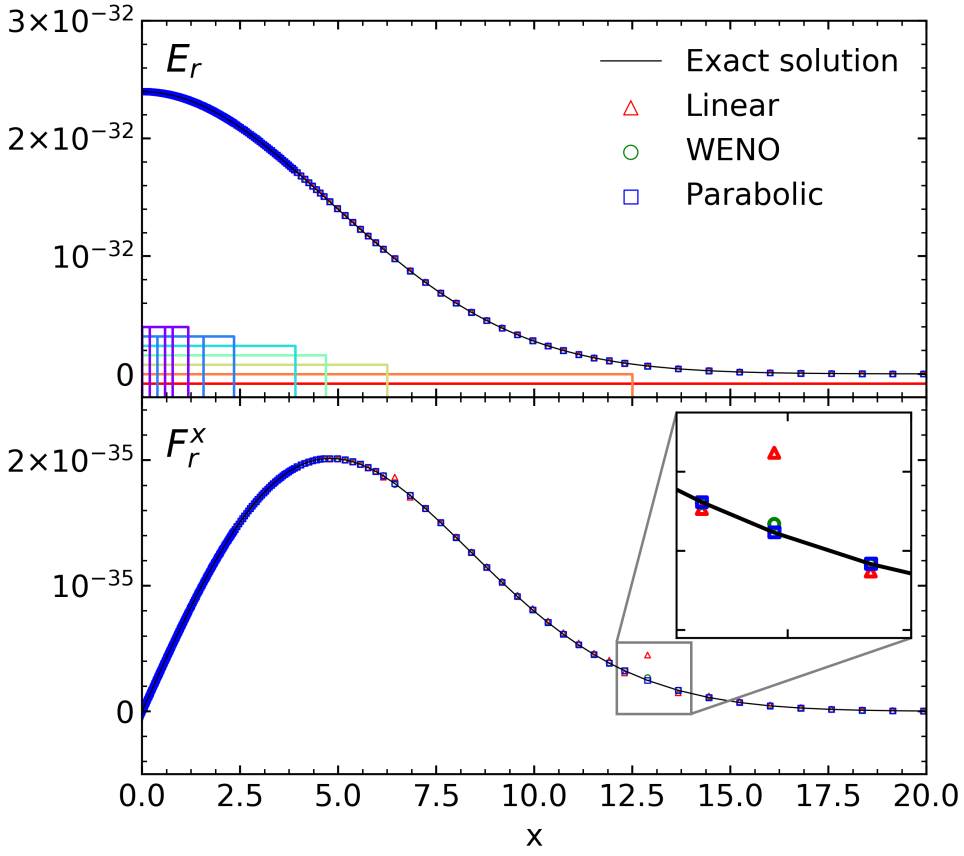

Fig. 4.14 Radiation energy density (top) and flux (bottom) profiles in the optically thick pulse test with $\sigma = 50$ using a static AMR grid with six refinement levels. Solutions are shown at $t = 1500$ using linear reconstruction (red triangles), WENO (green circles), and PPM (blue squares). Refinement levels are marked by colored boxes (top panel), with red corresponding to the base level grid. The analytical solution of Eq. (4.93) is plotted for comparison, while a close-up view of the interface between the first two grid levels is shown in the bottom panel. Reproduced from [260].

to have a smooth transition between ρ_0 and ρ_1, the initial density field is defined as

$$\rho\left(x,y\right) = \rho_0 + \frac{\rho_1 - \rho_0}{1 + e^{\Delta}}, \tag{4.94}$$

where

$$\Delta = 10\left[\left(\frac{x}{x_0}\right)^2 + \left(\frac{y}{y_0}\right)^2 - 1\right], \tag{4.95}$$

with $(x_0, y_0) = (0.10, 0.06)$ cm. In such a way, the region with $\rho = \rho_1$ is approximately contained in an ellipse of semiaxes (x_0, y_0). Initially, matter is set in thermal equilibrium with radiation at a temperature $T_0 = 290$ K, and fluxes and velocities are initialized to

zero. The absorption opacity in the material is computed according to Kramers' law, i.e., $\kappa = \kappa_0 \left(\frac{\rho}{\rho_0}\right) \left(\frac{T}{T_0}\right)^{-3.5}$, with $\kappa_0 = 0.1$ g^{-1}cm^2, while scattering is neglected. Therefore, the cylinder's optical thickness along its largest diameter is approximately $\tau \approx 2 \times 10^4$, which means that its width exceeds $\tau \gg 1$ times the photons' mean free path in that region. On the contrary, above $y > y_0$, the optical thickness is $\tau = 0.1$, so that the exterior of the cylinder is transparent to radiation while its interior is opaque.

Radiation is injected from the left boundary at a temperature $(c\,E_r/4\,\sigma_{SB})^{1/4} = 1740$ K $> T_0$, with a flux $\mathbf{F}_r = c\,E_r\,\hat{\boldsymbol{e}}_x$. Hence, the radiation field is in initially in the free-streaming limit and should be transported at the speed of light in the transparent regions.

We have initially computed the system's evolution in a fixed uniform grid of resolution 280×80, using a fourth-order reconstruction scheme with a Courant factor $C_a = 0.4$, and with $\Gamma = 5/3$. Simulations show a radiation front that crosses the space at light speed from left to right, producing a shadow behind the cylinder. After interacting with it, the shadow settles into a final stable state that is ideally maintained until the matter distribution is modified due to its interaction with radiation. The radiation energy density distribution is shown in the upper panel of Fig. 4.15 at $t = 10\,t_c$, where $t_c = 1\,\text{cm}/c = 3.336 \times 10^{-11}$ s is the light-crossing time, namely, the time it takes light to cross the domain horizontally in the transparent region. Behind the cylinder, the radiation energy density is roughly equal to its initial equilibrium value of $(4\,\sigma_{SB}/c)\,T_0^4$. This value is slightly affected by small waves that are produced in the upper regions of the cylinder, where the matter distribution stops being opaque to radiation along horizontal lines. Above the cylinder, the radiation field remains equal to the injected one. The transition between the shadowed and transparent regions is abrupt, as can be seen in Fig. 4.15. The shape of the E_r profile along vertical cuts is roughly maintained as radiation is transported away from the central object.

When IMEX–SSP2(2,2,2) is used, we have noticed that E_r frequently goes below zero on the left edge of the cylinder, where the radiation field impacts it. Still, the obtained solutions are stable and convergent as long as E_r is floored to a small value whenever this occurs. As in Section 4.3.5, the radiation flux is much smaller in those zones than both its flux and the source terms, and the problem does not occur if IMEX1 is used.

We have used this same problem to test the code's performance when AMR is used in a multidimensional setup. In this case, we have run the same simulation using an initially coarse grid of resolution 80×16 set to adapt to changes in E_r and ρ [see 201]. We have used 5 refinement levels, in every case with a grid jump ratio of 2, which gives an equivalent resolution of 2560×512. The resulting energy profiles are plotted in the lower panels of Figure 4.15, for $t = 0.2\,t_c$, $0.6\,t_c$, and $10\,t_c$, and agree with those computed using a fixed grid. In each panel, we have superimposed the refinement level.

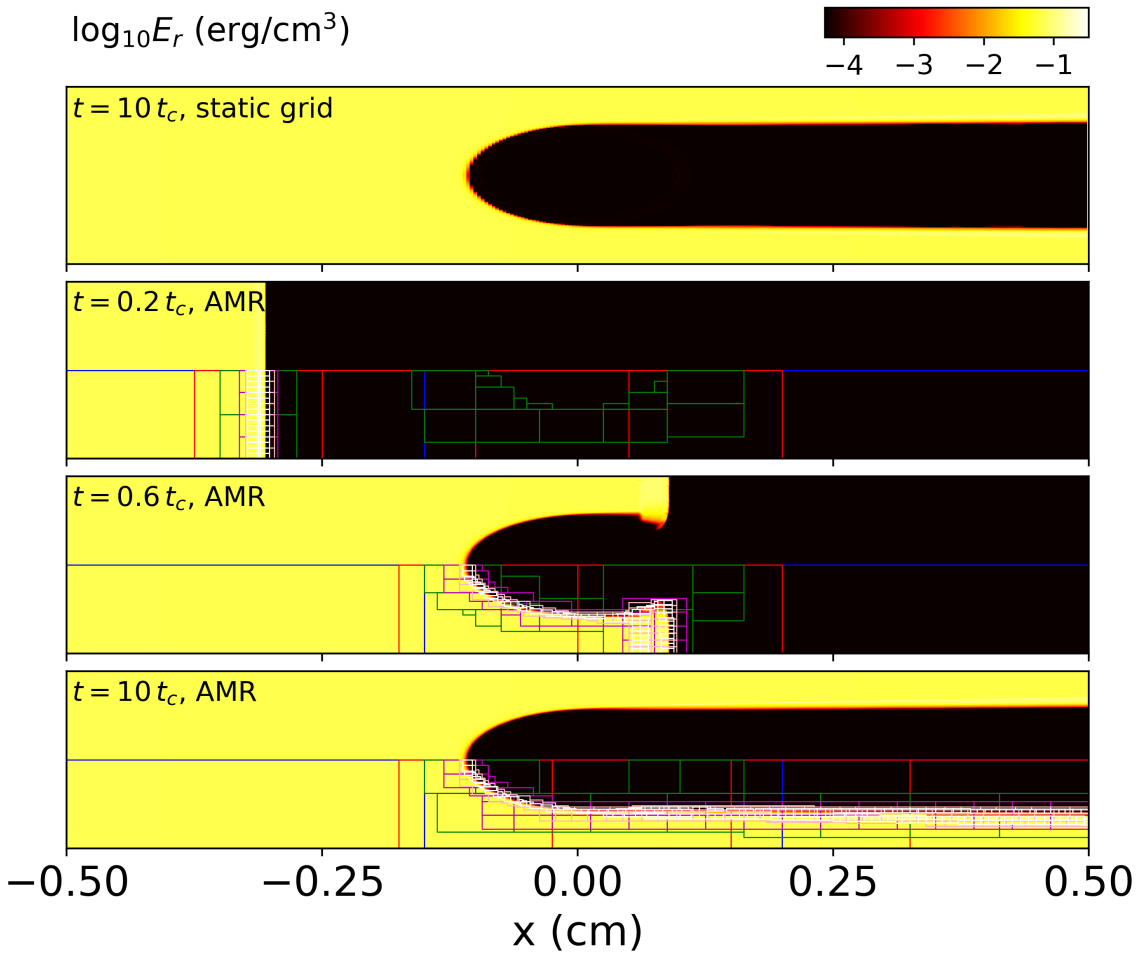

Fig. 4.15 Radiation energy density maps obtained in the shadow test. *Upper panel*: radiation energy at $t = 10\,t_c$, obtained with a fixed uniform grid of resolution 280×80. The radiation front crosses the domain from left to right, casting a shadow behind an elliptic cylinder centered at $(0, 0)$. From top to bottom, we show the numerical solutions obtained, respectively, on a static uniform grid with resolution 280×80 at $t = 10\,t_c$ and on the AMR grid (80×16 zones on the base level) at $t = 0.2\,t_c$, $0.6\,t_c$, and $10\,t_c$. The radiation front crosses the domain at the speed of light in the transparent regions. Refinement levels are superimposed with colored lines in the lower halves of these figures, corresponding to $l = 0$ (blue), 1 (red), 2 (green), 3 (purple), 4 (pink), and 5 (white), where l is the refinement level. Reproduced from [260].

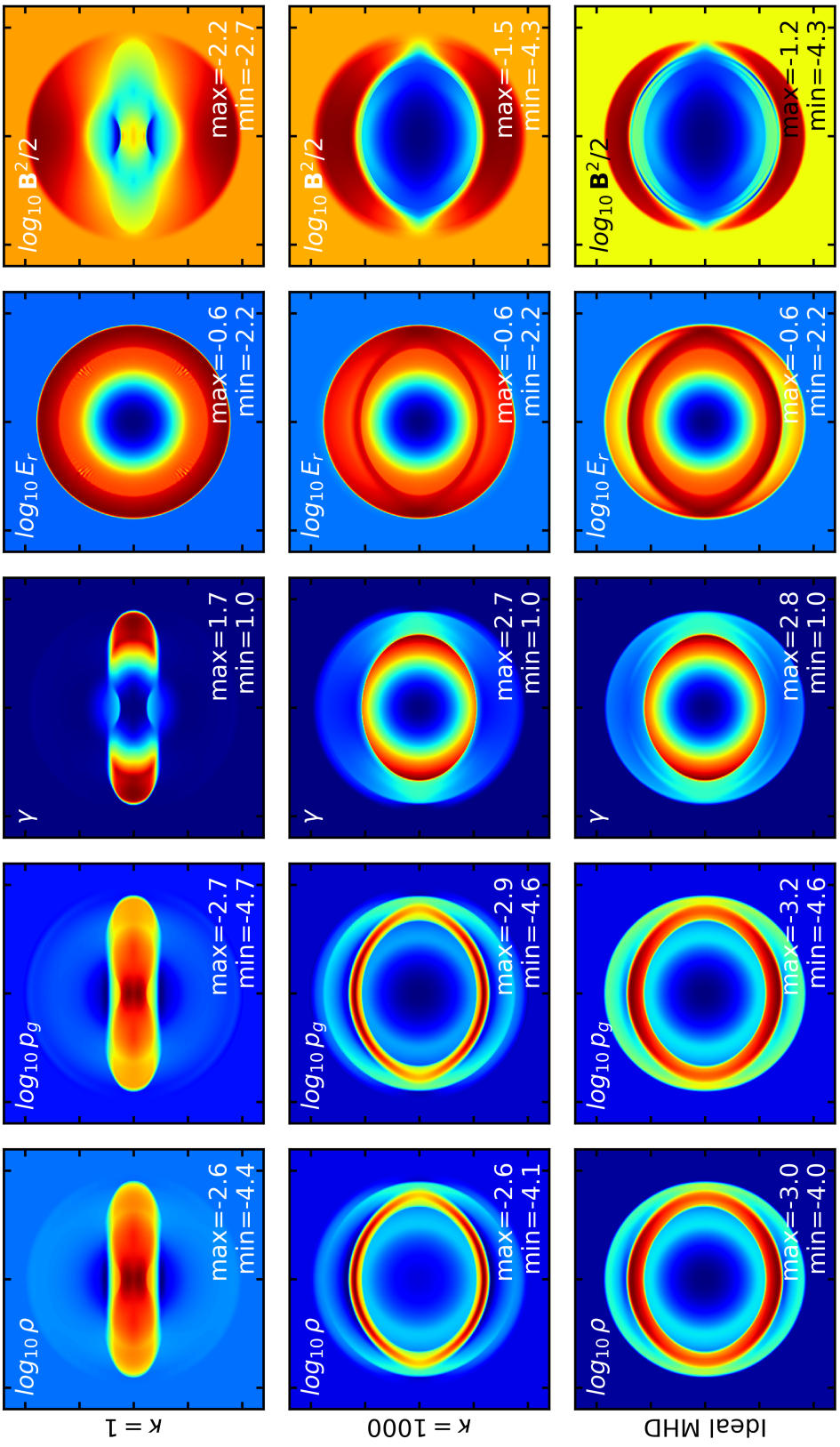

Fig. 4.16 Density maps at $t = 4$ in the magnetized cylindrical blast-wave test, corresponding to $\kappa = 1$ (top row), $\kappa = 1000$ (middle row), and ideal RMHD (bottom row). Reproduced from [260].

4.3.7 Magnetized cylindrical blast wave

We now examine a case in which matter is affected by both radiation and large-scale EM fields. We consider the case of a cylindrical blast wave, represented in a 2D Cartesian grid as in the planar configurations described in Section 4.3.5. In the context of MHD, this kind of problem was formerly used to check the robustness of the employed methods when handling relativistic magnetized shocks, as well as their ability to deal with different kinds of degeneracies (see, e.g., [216, 283]). In our case, we draw on this configuration as an example system that can switch from radiation–dominated to magnetically dominated regimes, depending on the material's opacity. To this end, we set up a cylindrical explosion from an area where the magnetic pressure is of the same order as the gas pressure and both are smaller than the radiation pressure. Under this condition, matter dynamics is magnetically dominated when the opacities are low and radiation–dominated in the opposite case. The latter case also serves to investigate the high-absorption regime in which both the diffusion approximation and LTE are valid.

We consider a square domain defined as $(x, y) \in [-6, 6] \times [-6, 6]$, initially threaded by a uniform magnetic field, $\mathbf{B} = B_0\, \hat{\boldsymbol{e}}_x$, with $B_0 = 0.1$. Gas pressure and density are initially set as follows:

$$\begin{pmatrix} p \\ \rho \end{pmatrix} = \begin{pmatrix} p_1 \\ \rho_1 \end{pmatrix} \delta + \begin{pmatrix} p_0 \\ \rho_0 \end{pmatrix} (1 - \delta) \tag{4.96}$$

where $p_0 = 3.49 \times 10^{-5}$ and $\rho_0 = 10^{-4}$ are the ambient values, while $p_1 = 1.31 \times 10^{-2}$ and $\rho_1 = 10^{-2}$ identify the overpressurized region. Here $R = \sqrt{x^2 + y^2}$ is the cylindrical radius, while $\delta \equiv \delta(R/R_0)$ is a taper function that decreases linearly for $R_0 < R \leq 1$ (we use $R_0 = 0.8$). The ideal EoS with $\Gamma = 4/3$ is used throughout the computations.

A radiation field is initially introduced in equilibrium with the gas. Since $\mathbf{v} = \mathbf{0}$ in the whole domain, the condition of LTE is initially satisfied if $E_r = 4\pi B(T)$ and $\mathbf{F}_r = \mathbf{0}$. These conditions are chosen in such a way that, close to the center of the domain, $p_g \sim \mathbf{B}^2/2 < E_r/3$, where $\mathbf{B}^2/2$ gives the initial magnetic contribution to the total pressure (see Eq. (2.20)). To guarantee the condition $\nabla \cdot \mathbf{B} = 0$, necessary for the solutions' stability, we have implemented in every case the constrained transport method.

Figure 4.16 shows a set of 2D color maps representing the fields' evolution at $t = 4$, using a resolution of 360×360 zones. The two upper rows correspond to computations using $\sigma = 0$ and $\kappa = 1$ (top row) or 1000 (middle row). For $\kappa = 1$, the initial optical depth along the central sphere is $\tau \approx \rho_1 \kappa \Delta x = 0.02 \ll 1$, and therefore the material's expansion should not be noticeably affected by the radiation field. Indeed, in this case, the radiation energy profile expands spherically, as in Section 4.3.5. The dynamic is magnetically dominated, and

matter is accelerated up to $\gamma \sim 1.7$ along the magnetic field lines along the x-axis, which is why the hydrodynamic variables are characterized by an elongated horizontal shape.

The middle row of Fig. 4.16 shows analog results obtained with $\kappa = 1000$, where $\tau \approx 20 \gg 1$. In this case, the interaction of the radiation field with the gas during its expansion produces a much more isotropic acceleration. This acceleration is still maximal along the x-direction, due to the joint contributions of the magnetic field and the radiation pressure. This is why the Lorentz factor is larger in this case, reaching $\gamma \sim 2.7$. Gas density and pressure reach their maxima along an oblated ring, instead of the previous elongated distributions obtained with $\kappa = 1$. As shown in the same figures, the magnetic field lines are pushed away from the center as matter is radially accelerated, producing a region of high magnetic energy density around the area where γ is highest, and a void of lower magnetic energy inside. Also different from the previous case, the radiation energy distribution is no longer spherically symmetric due to its interaction with the matter distribution.

For high values of $\rho\kappa$, it is expected that the radiation reaches LTE with matter, as Eqs. (4.33), (4.47), and (4.48) lead to $\tilde{E}_r \to 4\pi B(T)$ and $\tilde{F}_r^i \to 0$ for smooth field distributions that do not vary abruptly in time. In this limit, Eqs. (4.43)–(4.48) can be reduced to those of RMHD, redefining the total gas pressure as

$$p_{\rm tot} = p_g' + \frac{\mathbf{E}^2 + \mathbf{B}^2}{2}, \tag{4.97}$$

with $p_g' = p_g + \tilde{p}_r$, and the enthalpy density as

$$\rho h_{\rm tot} = \rho h_g + \tilde{E}_r + \tilde{p}_r, \tag{4.98}$$

where $\tilde{P}_r^{ij} = \tilde{p}_r\, \delta^{ij}$, which follows from the M1 closure in this limit. Taking a constant-Γ EoS with $\Gamma = 4/3$ in every case, the EoSs of both systems of equations coincide in the large-opacity limit and therefore the results obtained with both of them are comparable.

The bottom row of Fig. 4.16 shows the results of an ideal RMHD simulation performed in such a way, using the same initial conditions as before. To compute the gas pressure represented herein, it was assumed that $p_g' \simeq \tilde{p}_r = 4\pi B(T)/3$, from where it is possible to extract T and then p_g. Following the same idea, an effective E_r was computed boosting its comoving value, assumed to be equal to $4\pi B(T)$, and taking $\tilde{F}_r^i = 0$. The resulting plots thus obtained are in fact similar to those computed with $\kappa = 1000$, with slight differences that can be explained by taking into account that κ has a finite value and that close to the shocks the fields do not satisfy the conditions of being smooth and varying slowly with time. Consequently, the value of $\tilde{E}_r$ can be different than $4\pi B(T)$ in the regions of space that are close to discontinuities, which means that the hypothesis of LTE, assumed by ideal RMHD,

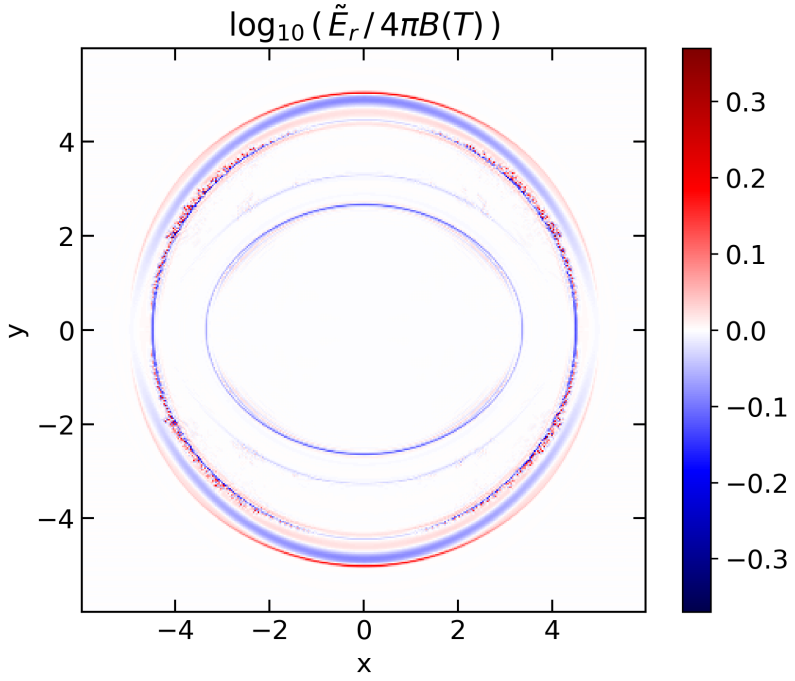

Fig. 4.17 Values of $\log_{10}\left(\tilde{E}_r/4\pi B(T)\right)$ in the cylindrical blast wave for $\kappa = 1000$, computed at at $t = 4$. The condition for LTE is here verified except in the closest regions to the shocks (see Fig. 4.16). Reproduced from [260].

is not satisfied in the whole domain. This is verified in Figure 4.17, where it is shown that, for $\kappa = 1000$, the ratio $\tilde{E}_r/4\pi B(T)$ differs from 1 only in the regions that are close to shocks, shown in Fig. 4.16.

4.3.8 Parallel Performance

Parallel scalability of our algorithm has been investigated in strong scaling through 2D and 3D computations. For simplicity, we have chosen the (unmagnetized) blast-wave problem of Section 4.3.7 with $\kappa = 10$ leaving the remaining parameters unchanged. For reference, computations have been carried out with and without the radiation field on a fixed grid of 2304^2 (in 2D) and 288^3 (in 3D) zones, a constant time step, and the solver given by Eq. (2.50). The number of processors—Intel Xeon Phi7250 (KnightLandings) at 1.4 GHz—has been varied from $N_{\rm CPU} = 8$ to $N_{\rm CPU} = 1024$.

The corresponding speed-up factors are plotted in Fig. 4.18 as a function of $\mathrm{N_{CPU}}$ (solid lines with symbols), together with the ideal scaling-law curve $\propto N_{\rm CPU}$. We compute the speed-up factors as $S = T_{\rm ref}/T_{\mathrm{N_{CPU}}}$ where $T_{\rm ref}$ is a normalization constant while $T_{\mathrm{N_{CPU}}}$ is the total running time for a simulation using $N_{\rm CPU}$ processors.

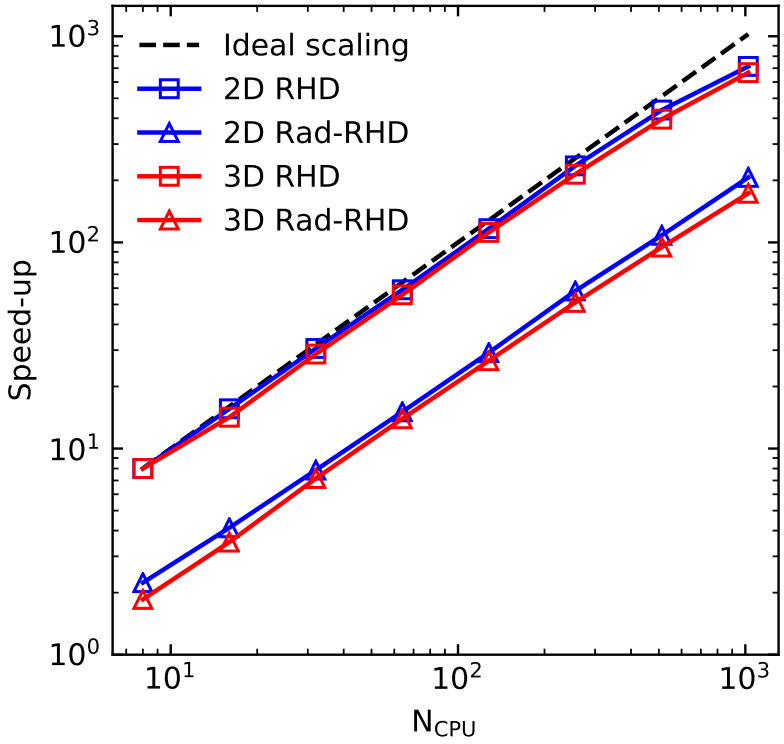

Fig. 4.18 Speed-up for the 2D (blue) and 3D (red) blast-wave tests, with and without radiation fields (triangles and squares) as a function of the number of processors. The ideal scaling law (dashed black line) is shown for comparison. Reproduced from [260].

Overall, favorable scaling properties are observed in two and three dimensions with efficiencies that remain above 90% up to 256 cores and drop to $\sim 70\%$ when $N_{\rm CPU} = 1024$. Slightly better results are achieved when radiation is included, owing to the additional computational overhead introduced by the implicit part of the algorithm that uses exclusively local data without requiring additional communication between threads.

Note that, for convenience, we have normalized the curves to the corresponding running time without the radiation field. This demonstrates that, by including radiation, the code is (approximately) four times more expensive than its purely hydro counterpart, regardless of the dimensionality.

4.4 Conclusions

We have presented a relativistic radiation transfer code, designed to function within the PLUTO code. Our implementation can be used together with the RHD and RMHD modules of PLUTO to solve the equations of radiation transfer under the gray approximation. Integration is

achieved through one of two possible IMEX schemes, in which source terms due to radiation–matter interaction are integrated implicitly and flux divergences, as well as every other source term, are integrated explicitly. The transition between optically thick and thin regimes is controlled by imposing the M1 closure on the radiation fields, which allows us to handle both the diffusion and free-streaming limits. Opacity coefficients can be arbitrarily defined, depending on the problem at hand, as functions of the primitive variables.

In our implementation, a novel HLLC Riemann solver for radiation transport has been introduced. The new solver is designed to improve the accuracy of the solutions with respect to it predecessors (such as HLL) in optically thin regions of space. The module has been designed to function with either Cartesian, cylindrical, or spherical coordinates in multiple spatial dimensions, and it is suitable for either serial or parallel computations. Extension to adaptive grids, based on the standard implementation of the `CHOMBO` library within the code, has also been presented.

We have performed a series of numerical benchmarks to assess the module performance under different configurations, including handling of radiation transport, absorption, and emission in systems with different characteristics. Our results demonstrate excellent stability properties under the chosen parameters in both the free-streaming and diffusion limits. In the latter case, numerical diffusion is successfully controlled by limiting the signal speeds of the radiation transport equations whenever the material is opaque across single grid cells. Overall, the transition between both regimes has been properly captured by the code in all of the considered cases. For optically thin transport, our HLLC solver produces more accurate solutions when compared to HLL. Regarding the implemented IMEX schemes, we have seen a similar performance of both IMEX–SSP2(2,2,2) and IMEX1 except in tests where the order of magnitude of the radiation flux is much smaller than both its source terms and the divergence of its own flux, in which IMEX1 seems to have better stability and positivity-preserving properties. When AMR is used, the obtained solutions exhibit a similar overall behavior to those computed using a fixed grid. Good agreement is also shown with standard tests whenever the comparison is possible. Finally, parallel performance tests show favorable scaling properties that are comparable to those of the RHD module of `PLUTO`.

Chapter 5

Ongoing work and perspectives

In this chapter, we show some preliminary results of an ongoing application of the radiative transfer module presented in Chapter 4, in the context of the model of shock breakouts in BdHNe described in Chapter 3. After discussing these results, we briefly outline a different ongoing application in the context of the fireshell model, and conclude by mentioning a few lines of research to be followed in the near future.

5.1 Shock breakouts in BdHNe

In Chapter 3 we have shown RHD simulations of relativistic shock breakouts in the context of a model for X-ray flares within the BdHN scenario. There we have mentioned two aspects of the dynamics of this process that are not described by the hydrodynamical approach: firstly, the LTE assumption does not allow us to compute the amount of radiation that escapes the SN ejecta; secondly, the feedback on matter dynamics of radiative losses is also not considered, and consequently the fluid's bulk Lorentz factor could be in principle overestimated close to the photosphere. In this section we show a series of preliminary calculations aimed to address these issues through the application of the module for radiative transfer described in Chapter 4.

As shown in Section 3.2.4 (see Fig. 3.14), the total optical depth of the SN ejecta in the regions of interest for this model can be as large as $\tau \sim 10^7$. This renders the source terms in the Rad-RHD equations too large to be stably handled by the IMEX schemes shown in Section 4.2, unless prohibitively large resolutions are used.[1] However, we can still apply these

[1] Generally, for such large opacities, flux-limited diffusion (FLD) techniques are preferred to the M1 approach (see, e.g., [188]). In these, the magnitude of the flux is computed as $\mathbf{F}_r = -D\,\nabla E_r$, where D is a function of the radiation fields built in such a way to reproduce both the free-streaming and diffusion limits. However, despite this method is particularly accurate in optically thick regions of space, it depends on an ad-hoc definition

methods to study this process if we reduce the computational domain to a region near to the photosphere and start the simulations in the moments prior to the breakout. To obtain the initial conditions, we use the results of the simulations of GRB 160625B shown in Section 3.2.3, choosing an initial ejecta radius $R_0 = 3.78 \times 10^{12}$ cm.

The new 1D spherically symmetric Rad-RHD simulation starts at a time $t_i = 268.8$ s after the beginning of the shock's expansion, when the homologous expansion of the ejecta has increased its radius up to $R_{\mathrm{ej},i} = 3.923 \times 10^{12}$ cm, while the shock is located at $R_{\mathrm{s},i} = 3.865 \times 10^{12}$ cm. The lower boundary of the domain is set at $R_{\mathrm{ej},i}$, while the upper boundary is set at 4.05×10^{12} cm. Initial conditions are chosen in such a way that the initial mass profile coincides with that in the RHD simulation, while E_r and p_g are fixed to small values ($\ll \rho c^2$). The expansive shock is introduced into the system by setting all of the conserved fields at the lower boundary to their values in the shocked region computed with the RHD code. To obtain the separate values of the comoving pressure of both matter and radiation, we assume them to be at LTE in the injected flow. Assuming this, the total pressure p_{tot} computed in the RHD simulation equals the sum of the LTE values of p_g and $\tilde{p}_r$ (such that $\tilde{P}_r^{ij} = \tilde{p}_r \delta^{ij}$) computed at the same temperature. As in section 4.3.7, the fact that p_g is much smaller than $\tilde{p}_r$ simplifies the computation of the temperature, which can be obtained by inverting the relation $p_{\mathrm{tot}} \simeq a_R T^4/3$ and then used to compute p_g. Although we know that LTE is in general not satisfied in the vicinity of shocks, this is a reasonable first approximation since the shock is radiation–dominated, and hence the accurate determination of p_g plays no role in the dynamics of the system as long as its value is much smaller than p_{tot}. Once these comoving values are determined, the radiation fields injected at the lower boundary are computed as

$$\begin{aligned} E_r &= \gamma^2 \left(3 + v^2\right) \tilde{p}_r \\ F_r &= 4 \gamma^2 \tilde{p}_r \, v \end{aligned} \tag{5.1}$$

(see Eqs. (4.37) and (4.38)), where F_r is the radial component of the radiation flux and v is the initial radial velocity of the fluid, computed in terms of the Lorentz γ factor of the shocked material as $v(r) = \sqrt{1 - \gamma^{-2}}$, with $\gamma = 1.54$. This expression is obtained by setting $\tilde{F}_r = 0$, which follows from the limit $\sigma \to \infty$ in the Rad-RHD equations (see Eq. (4.33)).

Equation (5.1) is based on the assumption that matter and radiation are tightly coupled due to Thomson scattering. This is justified by the fact that the mean free path due to this

of D, which can make it inaccurate in optically thin regions. An intermediate approach is given in [284] in the context of neutrino transport in NS–BH mergers, where fluxes are computed with the M1 closure and replaced by their values in the difussion limit in optically thick regions. Although this method can be applied to systems with high optical depths ($\sim 10^{10}$), we are not certain that it ensures an accurate handling of energy-momentum transport.

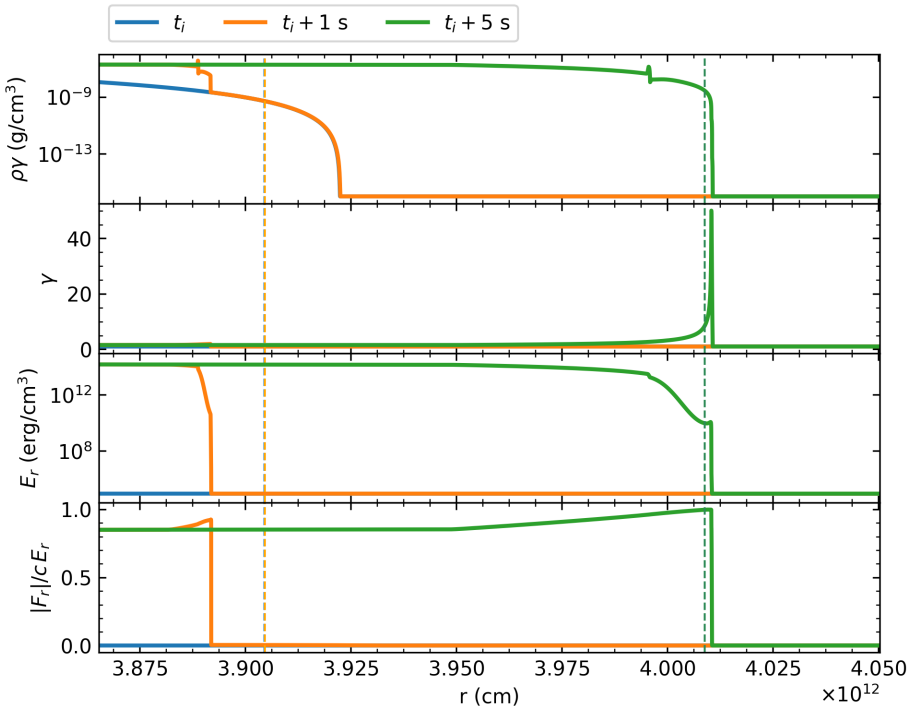

Fig. 5.1 Profiles obtained in the Rad-RHD simulation of a shock breakout, shown at $t = t_i$, $t_i + 1$ s and $t_i + 5$ s with blue, orange, and green solid lines respectively. From top to bottom: comoving mass density $\rho\gamma$, Lorentz γ factor, radiation energy density E_r, and ratio $|F_r|/cE_r$ between the radiation flux and energy density, normalized by the speed of light. Dashed lines mark the location of the photospheric radius at each time (indicated with the same colors).

process is $\lambda_T \sim 10^3$ cm in the shocked region, which is much smaller than any length of interest in this problem. In particular, the Thomson optical depth along a path that crosses the SN ejecta from the shock's radius is $\tau_T = 68$ at $t = t_i$. Additionally, we can estimate the absorption coefficient in the shocked region by using its value for free-free absorption, since there the temperature (~ 1 keV) is well above the ionization energies of both H and He, both of the order of 10 eV (see Appendix B). The Rosseland mean of this coefficient is $\kappa_R \approx 7.4 \times 10^{22}\, \rho\, T^{-7/2}$ for a pure hydrogen ionized gas.[2] For the temperatures and densities of the shocked region, this gives $\kappa_R/\sigma \sim 10^{-8}$, where σ is the scattering coefficient in g^{-1} cm^2, computed in terms of the Thomson cross section and the proton mass as $\sigma = \sigma_T/m_p$. On the other hand, we cannot use this expression to compute the absorption opacity of the unshocked region, since we do not count with an estimation of the temperature of the SN ejecta coming from the BdHN model. In the simulations, we simply assume that Thomson scattering is the only source of opacity in the described part of the ejecta, and set $\kappa = 0$.

[2]This usual expression can be obtained by applying the second of Eqs. (4.32) to the frequency-dependent free-free opacity coefficient given, e.g., in [265].

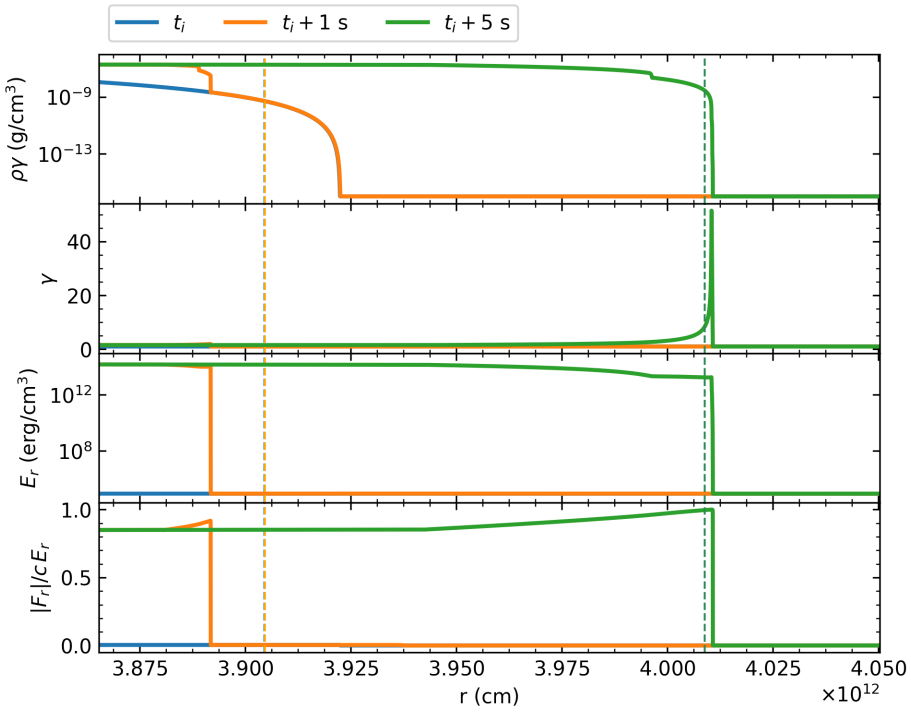

Fig. 5.2 Same as Fig. 5.1, for the RHD simulation of the same process.

We have computed the system's evolution using a fixed uniform grid of 50000 zones. The resulting profiles are shown in Fig. 5.1 at $t = t_i$, $t_i + 1$ s and $t_i + 5$ s. For comparison, we have run a similar simulation with the RHD module, where we inject at the left boundary a fluid with total pressure $p_{\rm tot} = p_g + \tilde{p}_r$. The profiles obtained in this RHD simulation are shown in Fig. 5.2, where we have computed equivalent values of E_r and F_r by using their expressions in the $\sigma \to \infty$ limit given by Eq. (5.1). A comparison between these figures shows that the profiles obtained with both approaches are almost identical in the entire domain, since most of the expanding flow is contained below the photosphere. This is illustrated in both figures by showing at each time the location of the photospheric radius $R_{\rm ph}$, computed as in Section 3.2.3 by inverting the relation $\tau(R_{\rm ph}) = 1$. In both cases, the radiation flux tends to its free-streaming limit ($F_r = c\,E_r$) as r approaches the shock's radius R_s. In the RHD simulation, as well as in the Rad-RHD one far below the photosphere, this occurs because the tight coupling of matter and radiation fields causes the latter to be transported at the fluid's velocity, which approaches the speed of light close to R_s. Because of this large opacity, photons remain trapped in the SN ejecta throughout its evolution; hence, the energy of the radiation field is mainly converted into the bulk kinetic energy of the material, in agreement with the preliminary analysis made in Section 3.2.4. On the other hand, the resulting γ

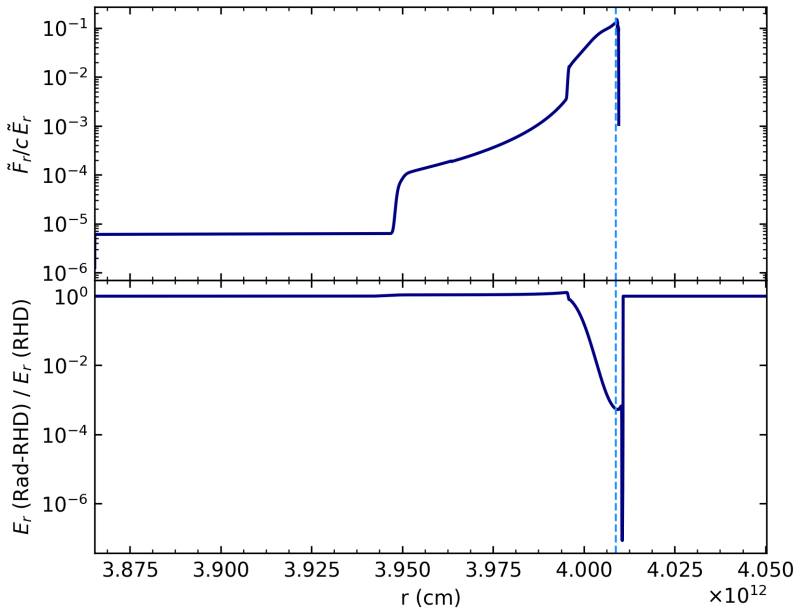

Fig. 5.3 Top: profile of $\tilde{F}_r/c\,\tilde{E}_r$ at $t = t_i + 5$ s in the Rad-RHD shock breakout simulation. Bottom: ratio between the values of E_r computed in the Rad-RHD and RHD simulations, plotted as a function of r at the same time. The vertical dashed line indicates the position of $R_{\rm ph}$.

profiles are identical in both simulations (their relative difference is always below 1%), which validates the values of $\gamma(R_{\rm ph})$ computed in the RHD simulations shown in Section 3.2.

As expected, the main differences between the profiles obtained with the two considered approaches can be observed close to the photosphere, where E_r is significantly smaller in the Rad-RHD simulation that its estimated value in the RHD one. This is a consequence of the fact that the scattering opacity has a finite value, and hence the coupling between matter and radiation is not perfect. As a result, the comoving value of the radiation flux can differ from zero, and therefore Eq. 5.1 is not verified in the whole domain. This can be seen in Fig. 5.3, where it is shown that $\tilde{F}_r/c\,\tilde{E}_r \sim 10^{-1}$ at the photosphere in the Rad-RHD simulation. Because of this, a transition zone is created near the photosphere, in which the radiation fields smoothly vary between their downstream and upstream values.[3] In particular, in this transition zone, adiabatic compression at the shock front causes the matter pressure to be higher than the radiation pressure before the latter rises to its scattering–dominated value within the ejecta (see Fig. 5.4). Contrarily, in the RHD approach, the LTE value of the radiation pressure (estimated as $\tilde{p}_r \approx p_{\rm tot}$) rises abruptly, which causes the observed disparity between the values of E_r in Figures 5.1 and 5.2. The ratio between the E_r values

[3]Transition zones are a general feature of radiative shocks (see, e.g., [285, 286]). They can also be seen in the shock tests shown in Section 4.3.4 (see Figs. 4.7–4.10).

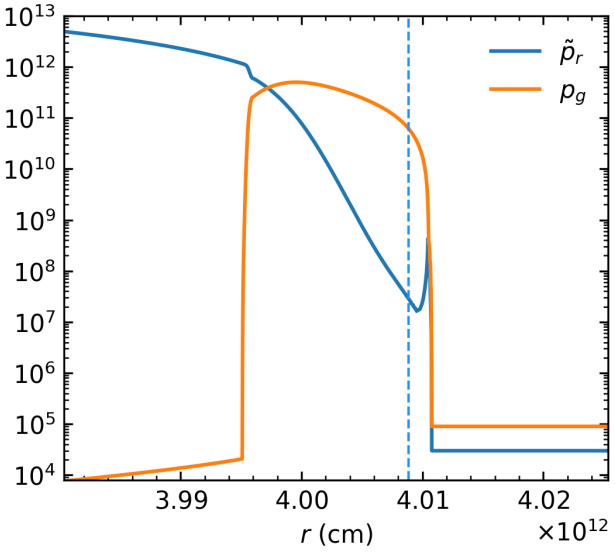

Fig. 5.4 Comoving values in dyn cm^{-2} of the radiation ($\tilde{p}_r$) and gas (p_g) pressures close to the shock boundary, obtained at $t = t_i + 5$ s in the Rad-RHD simulation of the shock breakout. The dashed line indicates the position of $R_{\rm ph}$.

computed in both simulations is shown in Fig. 5.3 as a function of r, where it can be seen that, at $R_{\rm ph}$, E_r is overestimated in the RHD approach by a factor of $\sim 10^3$. Therefore, the results of these simulations point to a possible overestimation of the observed temperatures in the RHD approach if blackbody emission is assumed, even if it is considered that not all emitted photons are lastly scattered at $R_{\rm ph}$. However, since free-free absorption provides an additional coupling between radiation and matter that brings the gas pressure closer to its LTE value, it remains to be seen in the future how this result changes if $\kappa \neq 0$.

5.2 Discussion and future projects

We have made RHD and Rad-RHD simulations of shock breakouts in the BdHN model, produced when the shock created by the expansion of the e^-e^+–baryon plasma reaches the outermost regions of the SN ejecta. The chosen parameters in these simulations correspond to the expansion along a direction such that $B = 12$, which is among the lowest values considered by the model for X-ray flares studied in Chapter 3. On top of this, the initial plasma energy of 10^{54} erg is of the highest order of magnitude considered in this model. Despite both of these choices are the most favorable ones for the emission of radiation in this scenario, the results of the Rad-RHD simulation show that radiation remains tightly coupled to the SN material throughout its entire evolution; in particular, the obtained profiles are

almost identical to those in the RHD simulation. In agreement with the discussion made in Section 3.2.4, these results indicate that the scattering opacity of the SN ejecta is too high to allow for the observed energy release in the considered X-ray flares, which consequently cannot be explained by this model alone in its current form. Therefore, these results encourage the exploration of additional scenarios, such as the reheating of the SN ejecta due to energetic particles coming from the BH, the photon emission due to proton-proton interactions in the SN ejecta, and the reignition of the central engine. On the other hand, the radiation energy density at the photosphere is significantly lower in the Rad-RHD simulation than in the RHD one. However, the additional coupling between radiation and matter caused by free-free absorption should bring the radiation and gas pressures closer to their LTE values. This can be studied in the future by using the temperature profiles obtained in SPH simulations of the SN ejecta (see, e.g., [168]) to compute realistic values of the absorption coefficients. Further improvements can be made by considering a time-dependent energy and mass injection at the lower boundary, in order to represent the variation of these quantities behind the shock front. Finally, the expansion of the shock along different directions could be better described by running simulations in a higher number of dimensions, which could also describe effects due to the system's rotation that cannot be accounted for in the 1D approach.

Apart from the simulations shown in this chapter, we are currently running 1D spherically symmetric Rad-RHD simulations of the evolution of the ultrarelativistic e^-e^+–baryon plasma in the fireshell model. These computations are aimed to obtain a better description of the shell during the emission of the P-GRB, and to compute approximate frequency-averaged lightcurves if possible. The main caveat of this approach is that it depends on a description of the shell's expansion along distances that exceed its initial width by many orders of magnitude (between 6 and 8), which means that a wide range of length scales must be covered. Even with the aid of AMR, computing the pulse's expansion throughout long distances (and consequently using a large number of time steps) introduces a considerable amount of numerical diffusion unless very large resolutions are employed. Since the geometry of the shell is largely influenced by this effect, the timescale of the emitted light curve is unphysically prolonged, and the luminosities consequently reduced. Furthermore, due to the mentioned resolution requirements and our current computational capabilities, so far we have not integrated the equations for a long enough time to see a detachment of the radiation from the shell, nor to reach optical depths smaller than 1 by at least one order of magnitude.

Finally, apart from these applications, it is our intention to keep making changes to the numerical methods implemented in the radiative transfer module. The immediate next step will be to develop a nonrelativistic version of this code, applicable to lower-energy physical systems such as star atmospheres and protoplanetary disks. This poses a new velocity scale

disparity, as the described velocities in such systems are much smaller than the speed of light. To overcome this issue, one possibility is to change our formalism by including an artificially reduced value of the speed of light, similarly to the approaches followed in [287, 288]. In general, this technique can be applied to nonrelativistic systems only if describing the free transport of radiation at its actual speed is of no importance for the desired results. On the other hand, we are also interested in modifying the AMR scheme in such a way to take into account the influence of the source terms on the fluxes employed in the refluxing step, in order to avoid inaccuracies at the boundaries between different levels when large opacities and small resolutions are used (see Section 4.3.5). Such an approach is followed in [281, 289], where source terms are integrated explicitly. In our case, we would like to develop a similar method that can be integrated to the IMEX schemes presented in Section 4.2.1.

References

[1] D. D. Frederiks, K. Hurley, D. S. Svinkin, V. D. Pal'shin, V. Mangano, S. Oates, R. L. Aptekar, S. V. Golenetskii, E. P. Mazets, P. P. Oleynik, A. E. Tsvetkova, M. V. Ulanov, A. A. Kokomov, T. L. Cline, D. N. Burrows, H. A. Krimm, C. Pagani, B. Sbarufatti, M. H. Siegel, I. G. Mitrofanov, D. Golovin, M. L. Litvak, A. B. Sanin, W. Boynton, C. Fellows, K. Harshman, H. Enos, R. Starr, A. von Kienlin, A. Rau, X. Zhang, and J. Goldstein. *ApJ*, 779:151, 2013.

[2] X.-Y. Wang, Z. Li, Z.-G. Dai, and P. Mészáros. *ApJL*, 698:L98–L102, 2009.

[3] J. E. Rhoads. *ApJ*, 525:737–749, 1999.

[4] R. Sari, T. Piran, and J. P. Halpern. *ApJL*, 519:L17–L20, 1999.

[5] S. B. Cenko, D. A. Frail, F. A. Harrison, S. R. Kulkarni, E. Nakar, P. C. Chandra, N. R. Butler, D. B. Fox, A. Gal-Yam, M. M. Kasliwal, J. Kelemen, D.-S. Moon, E. O. Ofek, P. A. Price, A. Rau, A. M. Soderberg, H. I. Teplitz, M. W. Werner, D. C.-J. Bock, J. S. Bloom, D. A. Starr, A. V. Filippenko, R. A. Chevalier, N. Gehrels, J. N. Nousek, and T. Piran. *ApJ*, 711:641–654, 2010.

[6] S. Dong, B. J. Shappee, J. L. Prieto, S. W. Jha, K. Z. Stanek, T. W.-S. Holoien, C. S. Kochanek, T. A. Thompson, N. Morrell, I. B. Thompson, U. Basu, J. F. Beacom, D. Bersier, J. Brimacombe, J. S. Brown, F. Bufano, P. Chen, E. Conseil, A. B. Danilet, E. Falco, D. Grupe, S. Kiyota, G. Masi, B. Nicholls, F. Olivares E., G. Pignata, G. Pojmanski, G. V. Simonian, D. M. Szczygiel, and P. R. Woźniak. *Science*, 351:257–260, 2016.

[7] P. P. Povinec. *Journal of Analytical Science & Technology*, 3(1):42–71, 2012.

[8] Govert Schilling. *Flash!: the hunt for the biggest explosions in the universe*. Cambridge University Press, 2002.

[9] R. W. Klebesadel, I. B. Strong, and R. A. Olson. *ApJL*, 182:L85, 1973.

[10] S. A. Colgate. *Canadian Journal of Physics*, 46:S476–S480, 1968.

[11] C. A. Meegan, G. J. Fishman, R. B. Wilson, W. S. Paciesas, G. N. Pendleton, J. M. Horack, M. N. Brock, and C. Kouveliotou. *Nature*, 355:143–145, 1992.

[12] S. Mao and B. Paczynski. *ApJL*, 388:L45–L48, 1992.

[13] T. Piran. *ApJL*, 389:L45–L48, 1992.

[14] E. E. Fenimore, R. I. Epstein, C. Ho, R. W. Klebesadel, C. Lacey, J. G. Laros, M. Meier, T. Strohmayer, G. Pendleton, G. Fishman, C. Kouveliotou, and C. Meegan. *Nature*, 366:40–42, 1993.

[15] P. Kumar and B. Zhang. The physics of gamma-ray bursts & relativistic jets. *Physics Reports*, 561:1–109, 2015.

[16] S. D. Barthelmy et al. *GCN Circular 10251*, 2010.

[17] E. Costa, F. Frontera, J. Heise, M. Feroci, J. in't Zand, F. Fiore, M. N. Cinti, D. Dal Fiume, L. Nicastro, M. Orlandini, E. Palazzi, M. Rapisarda#, G. Zavattini, R. Jager, A. Parmar, A. Owens, S. Molendi, G. Cusumano, M. C. Maccarone, S. Giarrusso, A. Coletta, L. A. Antonelli, P. Giommi, J. M. Muller, L. Piro, and R. C. Butler. *Nature*, 387:783–785, 1997.

[18] J. S. Bloom, S. G. Djorgovski, and S. R. Kulkarni. *ApJ*, 554:678–683, 2001.

[19] A. Pe'er. *Advances in Astronomy*, 2015, 2015.

[20] J. S. Bloom. *What are gamma-ray bursts?*, volume 2. Princeton University Press, 2011.

[21] W. S. Paciesas, C. A. Meegan, A. von Kienlin, P. N. Bhat, E. Bissaldi, M. S. Briggs, J. M. Burgess, V. Chaplin, V. Connaughton, R. Diehl, G. J. Fishman, G. Fitzpatrick, S. Foley, M. Gibby, M. Giles, A. Goldstein, J. Greiner, D. Gruber, S. Guiriec, A. J. van der Horst, R. M. Kippen, C. Kouveliotou, G. Lichti, L. Lin, S. McBreen, R. D. Preece, A. Rau, D. Tierney, and C. Wilson-Hodge. *ApJS*, 199:18, 2012.

[22] C. Kouveliotou, C. A. Meegan, G. J. Fishman, N. P. Bhat, M. S. Briggs, T. M. Koshut, W. S. Paciesas, and G. N. Pendleton. *ApJL*, 413:L101–L104, 1993.

[23] W. S. Paciesas, C. A. Meegan, G. N. Pendleton, M. S. Briggs, C. Kouveliotou, T. M. Koshut, J. P. Lestrade, M. L. McCollough, J. J. Brainerd, J. Hakkila, W. Henze, R. D. Preece, V. Connaughton, R. M. Kippen, R. S. Mallozzi, G. J. Fishman, G. A. Richardson, and M. Sahi. *ApJS*, 122:465–495, 1999.

[24] T. J. Galama, P. M. Vreeswijk, J. van Paradijs, C. Kouveliotou, T. Augusteijn, H. Böhnhardt, J. P. Brewer, V. Doublier, J.-F. Gonzalez, B. Leibundgut, C. Lidman, O. R. Hainaut, F. Patat, J. Heise, J. in't Zand, K. Hurley, P. J. Groot, R. G. Strom, P. A. Mazzali, K. Iwamoto, K. Nomoto, H. Umeda, T. Nakamura, T. R. Young, T. Suzuki, T. Shigeyama, T. Koshut, M. Kippen, C. Robinson, P. de Wildt, R. A. M. J. Wijers, N. Tanvir, J. Greiner, E. Pian, E. Palazzi, F. Frontera, N. Masetti, L. Nicastro, M. Feroci, E. Costa, L. Piro, B. A. Peterson, C. Tinney, B. Boyle, R. Cannon, R. Stathakis, E. Sadler, M. C. Begam, and P. Ianna. *Nature*, 395:670–672, 1998.

[25] J. Hjorth, J. Sollerman, P. Møller, J. P. U. Fynbo, S. E. Woosley, C. Kouveliotou, N. R. Tanvir, J. Greiner, M. I. Andersen, A. J. Castro-Tirado, J. M. Castro Cerón, A. S. Fruchter, J. Gorosabel, P. Jakobsson, L. Kaper, S. Klose, N. Masetti, H. Pedersen, K. Pedersen, E. Pian, E. Palazzi, J. E. Rhoads, E. Rol, E. P. J. van den Heuvel, P. M. Vreeswijk, D. Watson, and R. A. M. J. Wijers. *Nature*, 423:847–850, 2003.

[26] K. Z. Stanek, T. Matheson, P. M. Garnavich, P. Martini, P. Berlind, N. Caldwell, P. Challis, W. R. Brown, R. Schild, K. Krisciunas, M. L. Calkins, J. C. Lee, N. Hathi, R. A. Jansen, R. Windhorst, L. Echevarria, D. J. Eisenstein, B. Pindor, E. W. Olszewski, P. Harding, S. T. Holland, and D. Bersier. *ApJL*, 591:L17–L20, 2003.

[27] S. Campana, V. Mangano, A. J. Blustin, P. Brown, D. N. Burrows, G. Chincarini, J. R. Cummings, G. Cusumano, M. Della Valle, D. Malesani, P. Mészáros, J. A. Nousek, M. Page, T. Sakamoto, E. Waxman, B. Zhang, Z. G. Dai, N. Gehrels, S. Immler, F. E. Marshall, K. O. Mason, A. Moretti, P. T. O'Brien, J. P. Osborne, K. L. Page, P. Romano, P. W. A. Roming, G. Tagliaferri, L. R. Cominsky, P. Giommi, O. Godet, J. A. Kennea, H. Krimm, L. Angelini, S. D. Barthelmy, P. T. Boyd, D. M. Palmer, A. A. Wells, and N. E. White. *Nature*, 442:1008–1010, 2006.

[28] E. Pian, P. A. Mazzali, N. Masetti, P. Ferrero, S. Klose, E. Palazzi, E. Ramirez-Ruiz, S. E. Woosley, C. Kouveliotou, J. Deng, A. V. Filippenko, R. J. Foley, J. P. U. Fynbo, D. A. Kann, W. Li, J. Hjorth, K. Nomoto, F. Patat, D. N. Sauer, J. Sollerman, P. M. Vreeswijk, E. W. Guenther, A. Levan, P. O'Brien, N. R. Tanvir, R. A. M. J. Wijers, C. Dumas, O. Hainaut, D. S. Wong, D. Baade, L. Wang, L. Amati, E. Cappellaro, A. J. Castro-Tirado, S. Ellison, F. Frontera, A. S. Fruchter, J. Greiner, K. Kawabata, C. Ledoux, K. Maeda, P. Møller, L. Nicastro, E. Rol, and R. Starling. *Nature*, 442:1011–1013, 2006.

[29] B. E. Cobb, J. S. Bloom, D. A. Perley, A. N. Morgan, S. B. Cenko, and A. V. Filippenko. *ApJL*, 718:L150–L155, 2010.

[30] R. L. C. Starling, K. Wiersema, A. J. Levan, T. Sakamoto, D. Bersier, P. Goldoni, S. R. Oates, A. Rowlinson, S. Campana, J. Sollerman, N. R. Tanvir, D. Malesani, J. P. U. Fynbo, S. Covino, P. D'Avanzo, P. T. O'Brien, K. L. Page, J. P. Osborne, S. D. Vergani, S. Barthelmy, D. N. Burrows, Z. Cano, P. A. Curran, M. de Pasquale, V. D'Elia, P. A. Evans, H. Flores, A. S. Fruchter, P. Garnavich, N. Gehrels, J. Gorosabel, J. Hjorth, S. T. Holland, A. J. van der Horst, C. P. Hurkett, P. Jakobsson, A. P. Kamble, C. Kouveliotou, N. P. M. Kuin, L. Kaper, P. A. Mazzali, P. E. Nugent, E. Pian, M. Stamatikos, C. C. Thöne, and S. E. Woosley. *MNRAS*, 411:2792–2803, 2011.

[31] K. Maeda and K. Nomoto. *ApJ*, 598:1163–1200, 2003.

[32] J. D. Lyman, D. Bersier, P. A. James, P. A. Mazzali, J. J. Eldridge, M. Fraser, and E. Pian. *MNRAS*, 457(1):328–350, 2016.

[33] B. Zhang, Y. Z. Fan, J. Dyks, S. Kobayashi, P. Mészáros, D. N. Burrows, J. A. Nousek, and N. Gehrels. *ApJ*, 642(1):354, 2006.

[34] N. Gehrels, G. Chincarini, P. Giommi, K. O. Mason, J. A. Nousek, A. A. Wells, N. E. White, S. D. Barthelmy, D. N. Burrows, L. R. Cominsky, et al. The swift gamma-ray burst mission. *ApJ*, 611(2):1005, 2004.

[35] N. Gehrels, E. Ramirez-Ruiz, and D. B. Fox. *Annual Review of Astronomy and Astrophysics*, 47(1):567–617, 2009.

[36] J. A. Nousek, C. Kouveliotou, D. Grupe, K. L. Page, J. Granot, E. Ramirez-Ruiz, S. K. Patel, D. N. Burrows, V. Mangano, S. Barthelmy, A. P. Beardmore, S. Campana, M. Capalbi, G. Chincarini, G. Cusumano, A. D. Falcone, N. Gehrels, P. Giommi, M. R. Goad, O. Godet, C. P. Hurkett, J. A. Kennea, A. Moretti, P. T. O'Brien, J. P. Osborne, P. Romano, G. Tagliaferri, and A. A. Wells. *ApJ*, 642(1):389, 2006.

[37] G. Stratta, B. Gendre, J. L. Atteia, M. Boër, D. M. Coward, M. De Pasquale, E. Howell, A. Klotz, S. Oates, and L. Piro. *ApJ*, 779(1):66, 2013.

[38] Y.-D. Hu, E.-W. Liang, S.-Q. Xi, F.-K. Peng, R.-J. Lu, L.-Z. Lü, and B. Zhang. Internal Energy Dissipation of Gamma-Ray Bursts Observed with Swift: Precursors, Prompt Gamma-Rays, Extended Emission, and Late X-Ray Flares. *ApJ*, 789:145, 2014.

[39] T. M. Koshut, C. Kouveliotou, W. S. Paciesas, J. van Paradijs, G. N. Pendleton, M. S. Briggs, G. J. Fishman, and C. A. Meegan. *ApJ*, 452:145, 1995.

[40] D. Lazzati. *MNRAS*, 357:722–731, 2005.

[41] D. Burlon, G. Ghirlanda, G. Ghisellini, J. Greiner, and A. Celotti. *A&A*, 505(2):569–575, 2009.

[42] D. Band, J. Matteson, L. Ford, B. Schaefer, D. Palmer, B. Teegarden, T. Cline, M. Briggs, W. Paciesas, G. Pendleton, G. Fishman, C. Kouveliotou, C. Meegan, R. Wilson, and P. Lestrade. *ApJ*, 413:281–292, 1993.

[43] A. Goldstein, J. M. Burgess, R. D. Preece, M. S. Briggs, S. Guiriec, A. J. van der Horst, V. Connaughton, C. A. Wilson-Hodge, W. S. Paciesas, C. A. Meegan, et al. *ApJS*, 199(1):19, 2012.

[44] W. B. Atwood, A. A. Abdo, M. Ackermann, et al. *ApJ*, 697(2):1071–1102, 2009.

[45] B.-B. Zhang, B. Zhang, E.-W. Liang, Y.-Z. Fan, X.-F. Wu, A. Pe'er, A. Maxham, H. Gao, and Y.-M. Dong. *ApJ*, 730(2):141, 2011.

[46] S. Guiriec, C. Kouveliotou, F. Daigne, B. Zhang, R. Hascoët, R. S. Nemmen, D. J. Thompson, P. N. Bhat, N. Gehrels, M. M. Gonzalez, Y. Kaneko, J. McEnery, R. Mochkovitch, J. L. Racusin, F. Ryde, J. R. Sacahui, and A. M. Ünsal. *ApJ*, 807:148, 2015.

[47] J. P. Norris, G. H. Share, D. C. Messina, B. R. Dennis, U. D. Desai, T. L. Cline, S. M. Matz, and E. L. Chupp. *ApJ*, 301:213–219, 1986.

[48] S. V. Golenetskii, E. P. Mazets, R. L. Aptekar, and V. N. Ilinskii. *Nature*, 306:451–453, 1983.

[49] A. A. Abdo, M. Ackermann, M. Arimoto, K. Asano, W. B. Atwood, M. Axelsson, L. Baldini, J. Ballet, D. L. Band, G. Barbiellini, and et al. Fermi Observations of High-Energy Gamma-Ray Emission from GRB 080916C. *Science*, 323:1688, 2009.

[50] M. Ackermann, K. Asano, W. B. Atwood, et al. *ApJ*, 716:1178–1190, 2010.

[51] Tsvi Piran. The physics of gamma-ray bursts. *Reviews of Modern Physics*, 76(4):1143–1210, 2004.

[52] J. Goodman. *New Astronomy*, 2:449–460, 1997.

[53] J. I. Katz and T. Piran. *ApJ*, 490:772–778, 1997.

[54] G. B. Taylor, D. A. Frail, E. Berger, and S. R. Kulkarni. *ApJL*, 609:L1–L4, 2004.

[55] G. Cavallo and M. J. Rees. *MNRAS*, 183:359–365, 1978.

[56] J. D. Melon Fuksman, L. Becerra, C. L. Bianco, M. Karlica, M. Kovačević, R. Moradi, M. Muccino, G. B. Pisani, D. Primorac, J. A. Rueda, R. Ruffini, G. V. Vereshchagin, and Y. Wang. In *European Physical Journal Web of Conferences*, volume 168, page 04009, 2018.

[57] C. Thompson. *MNRAS*, 270:480–498, 1994.

[58] E. Waxman. *Plasma Physics and Controlled Fusion*, 48(12B):B137–B151, 2006.

[59] A. M. Beloborodov. *MNRAS*, 407:1033–1047, 2010.

[60] D. Giannios and H. C. Spruit. Spectra of poynting-flux powered grb outflows. *A&A*, 430:1–7, 2005.

[61] Andrei M. Beloborodov. *ApJL*, 585(1):L19–L22, 2003.

[62] J. L. Racusin, E. W. Liang, D. N. Burrows, A. Falcone, T. Sakamoto, B. B. Zhang, B. Zhang, P. Evans, and J. Osborne. *ApJ*, 698:43–74, 2009.

[63] P. Mészáros and M. J. Rees. *MNRAS*, 306(3):L39–L43, 1999.

[64] A. Panaitescu and P. Mészáros. *ApJ*, 526(2):707–715, 1999.

[65] W. Zhang and A. MacFadyen. *ApJ*, 698(2):1261–1272, 2009.

[66] F. A. Harrison, J. S. Bloom, D. A. Frail, R. Sari, S. R. Kulkarni, S. G. Djorgovski, T. Axelrod, J. Mould, B. P. Schmidt, M. H. Wieringa, R. M. Wark, R. Subrahmanyan, D. McConnell, P. J. McCarthy, B. E. Schaefer, R. G. McMahon, R. O. Markze, E. Firth, P. Soffitta, and L. Amati. 523:L121–L124, 1999.

[67] K. Z. Stanek, P. M. Garnavich, J. Kaluzny, W. Pych, and I. Thompson. *ApJL*, 522:L39–L42, 1999.

[68] M. De Pasquale, P. Evans, S. Oates, M. Page, S. Zane, P. Schady, A. Breeveld, S. Holland, P. Kuin, and M. Still. *MNRAS*, 392(1):153–169, 2009.

[69] H. J. van Eerten and A. I. MacFadyen. *ApJL*, 733(2):L37, 2011.

[70] P. A. Curran, A. J. van der Horst, and R. A. M. J. Wijers. *MNRAS*, 386(2):859–863, 2008.

[71] G. B. Pisani, R. Ruffini, Y. Aimuratov, C. L. Bianco, M. Kovačević, R. Moradi, M. Muccino, A. V. Penacchioni, J. A. Rueda, S. Shakeri, and Y. Wang. *ApJ*, 833(2):159, 2016.

[72] J. A. Rueda, R. Ruffini, and Y. Wang. *Universe*, 5:110, May 2019.

[73] P. Mészáros. *Rep. Prog. Phys.*, 69:2259–2321, 2006.

[74] J. Goodman. *ApJL*, 308:L47–L50, 1986.

[75] B. Paczynski. *ApJL*, 308:L43–L46, 1986.

[76] A. Shemi and T. Piran. *ApJL*, 365:L55–L58, 1990.

[77] M. J. Rees and P. Meszaros. *ApJL*, 430:L93–L96, 1994.

[78] G. V. Vereshchagin. *International Journal of Modern Physics D*, 23(03):1430003, 2014.

[79] Asaf Pe'er and Felix Ryde. *International Journal of Modern Physics D*, 26(10):1730018, 2017.

[80] A. M. Beloborodov and P. Mészáros. *Space Science Reviews*, 207(1-4):87–110, 2017.

[81] L.-X. Li. *MNRAS*, 380:621–636, 2007.

[82] E. Ramirez-Ruiz, A. I. MacFadyen, and D. Lazzati. *MNRAS*, 331:197–202, 2002.

[83] Davide Lazzati and Mitchell C. Begelman. *ApJ*, 629(2):903–907, 2005.

[84] X.-Y. Wang and P. Mészáros. *ApJ*, 670(2):1247–1253, 2007.

[85] D. Burlon, G. Ghirlanda, G. Ghisellini, D. Lazzati, L. Nava, M. Nardini, and A. Celotti. *ApJL*, 685:L19, 2008.

[86] A. Gomboc. *Contemporary Physics*, 53:339–355, 2012.

[87] E. Waxman. *Gamma-Ray Bursts: The Underlying Model*, volume 598, pages 393–418. 2003.

[88] P. Meszaros, P. Laguna, and M. J. Rees. *ApJ*, 415:181–190, 1993.

[89] A. Spitkovsky. *ApJL*, 682(1):L5, 2008.

[90] Andrei M. Beloborodov. *ApJL*, 539(1):L25–L28, 2000.

[91] S. Kobayashi and R. Sari. *ApJ*.

[92] P. Mészáros and M. J. Rees. *ApJ*, 476:232–237, 1997.

[93] R. Sari and T. Piran. *MNRAS*, 287(1):110–116, 1997.

[94] R. Sari and T. Piran. *ApJ*, 485:270–273, 1997.

[95] R. Sari and T. Piran. *A&AS*, 138:537–538, 1999.

[96] R. Sari, T. Piran, and R. Narayan. *ApJL*, 497:L17–L20, 1998.

[97] Dipankar Bhattacharya. *Bulletin of the Astronomical Society of India*, 29:107–114, 2001.

[98] E. Waxman. *ApJL*, 489:L33–L36, 1997.

[99] E. Waxman. *ApJL*, 485:L5–L8, 1997.

[100] P. Mészáros, M. J. Rees, and R. A. M. J. Wijers. *ApJ*, 499:301–308, 1998.

[101] P. Meszaros and M. J. Rees. *ApJL*, 418:L59, 1993.

[102] J. I. Katz. *ApJ*, 422:248, 1994.

[103] E. Cohen, J. I. Katz, T. Piran, R. Sari, R. D. Preece, and D. L. Band. *ApJ*, 488:330–337, 1997.

[104] J. M. Burgess, R. D. Preece, V. Connaughton, M. S. Briggs, A. Goldstein, P. N. Bhat, J. Greiner, D. Gruber, A. Kienlin, C. Kouveliotou, S. McGlynn, C. A. Meegan, W. S. Paciesas, A. Rau, S. Xiong, M. Axelsson, M. G. Baring, C. D. Dermer, S. Iyyani, D. Kocevski, N. Omodei, F. Ryde, and G. Vianello. *ApJ*, 784(1):17, 2014.

[105] J. M. Burgess. In *Proceedings of the 7th International Fermi Symposium*, page 74, 2017.

[106] R. D. Preece, M. S. Briggs, R. S. Mallozzi, G. N. Pendleton, W. S. Paciesas, and D. L. Band. *ApJL*, 506:L23–L26, 1998.

[107] Y. Wang, L. Li, R. Moradi, and R. Ruffini. *arXiv preprint arXiv:1901.07505*, 2019.

[108] G. B. Rybicki and A. P. Lightman. *Radiative Processes in Astrophysics*. John Wiley & Sons, 1986.

[109] J. Granot, T. Piran, and R. Sari. *ApJL*, 534(2):L163–L166, 2000.

[110] J. Granot and R. Sari. *ApJ*, 568:820–829, 2002.

[111] M. Vietri. *PRL*, 78:4328–4331, 1997.

[112] M. Böttcher and C. D. Dermer. *ApJL*, 499:L131–L134, 1998.

[113] H. C. Spruit, F. Daigne, and G. Drenkhahn. *A&A*, 369:694–705, 2001.

[114] G. Drenkhahn. *A&A*, 387:714–724, 2002.

[115] P. Mészáros and M. J. Rees. *ApJL*, 733(2):L40, 2011.

[116] P. Goldreich and W. H. Julian. *ApJ*, 60:971, 1970.

[117] Bing Zhang and Shiho Kobayashi. *ApJ*, 628(1):315–334, 2005.

[118] P. Mimica, D. Giannios, and M. A. Aloy. *A&A*, 494(3):879–890, 2009.

[119] P. Mimica and M. A. Aloy. *MNRAS*, 401(1):525–532, 2010.

[120] P. Kumar and R. Narayan. *MNRAS*, 395(1):472–489, 2009.

[121] B. Zhang and H. Yan. *ApJ*, 726(2):90, 2011.

[122] Shuang-Nan Zhang, Merlin Kole, Tian-Wei Bao, Tadeusz Batsch, Tancredi Bernasconi, Franck Cadoux, Jun-Ying Chai, Zi-Gao Dai, Yong-Wei Dong, Neal Gauvin, Wojtek Hajdas, Mi-Xiang Lan, Han-Cheng Li, Lu Li, Zheng-Heng Li, Jiang-Tao Liu, Xin Liu, Radoslaw Marcinkowski, Nicolas Produit, Silvio Orsi, Martin Pohl, Dominik Rybka, Hao-Li Shi, Li-Ming Song, Jian-Chao Sun, Jacek Szabelski, Teresa Tymieniecka, Rui-Jie Wang, Yuan-Hao Wang, Xing Wen, Bo-Bing Wu, Xin Wu, Xue-Feng Wu, Hua-Lin Xiao, Shao-Lin Xiong, Lai-Yu Zhang, Li Zhang, Xiao-Feng Zhang, Yong-Jie Zhang, and Anna Zwolinska. *Nature Astronomy*, 3:258–264, 2019.

[123] J. M. Burgess, M. Kole, F. Berlato, J. Greiner, G. Vianello, N. Produit, Z. H. Li, and J. C. Sun. *A&A*, 627:A105, 2019.

[124] R. Narayan, T. Piran, and P. Kumar. *ApJ*, 557(2):949–957, 2001.

[125] B. P. Abbott, R. Abbott, T. D. Abbott, F. Acernese, K. Ackley, C. Adams, T. Adams, P. Addesso, R. X. Adhikari, V. B. Adya, and et al. *ApJL*, 848:L12, 2017.

[126] W.-X. Chen and A. M. Beloborodov. *ApJ*, 657(1):383–399, 2007.

[127] I. Zalamea and A. M. Beloborodov. *MNRAS*, 410(4):2302–2308, 2011.

[128] R. D. Blandford and R. L. Znajek. *MNRAS*, 179:433–456, 1977.

[129] D. A. Uzdensky and A. I. MacFadyen. *ApJ*, 647(2):1192–1212, 2006.

[130] N. Bucciantini, E. Quataert, J. Arons, B. D. Metzger, and T. A. Thompson. *MNRAS*, 383(1):L25–L29, 2008.

[131] N. Bucciantini, E. Quataert, B. D. Metzger, T. A. Thompson, J. Arons, and L. Del Zanna. *MNRAS*, 396(4):2038–2050, 2009.

[132] B. D. Metzger, D. Giannios, T. A. Thompson, N. Bucciantini, and E. Quataert. *MNRAS*, 413(3):2031–2056, 2011.

[133] D. M. Siegel, R. Ciolfi, and L. Rezzolla. *ApJL*, 785(1):L6, 2014.

[134] W. Kluźniak and M. Ruderman. *ApJL*, 505(2):L113–L117, 1998.

[135] M. A. Ruderman, L. Tao, and W. Kluźniak. *ApJ*, 542(1):243–250, 2000.

[136] Z. G. Dai, X. Y. Wang, X. F. Wu, and B. Zhang. *Science*, 311, 2006.

[137] S. Dall'Osso, G. Stratta, D. Guetta, S. Covino, G. De Cesare, and L. Stella. *A&A*, 526:A121, 2011.

[138] T. Damour and R. Ruffini. *PRL*, 35:463–466, 1975.

[139] R. Ruffini, J. D. Salmonson, J. R. Wilson, and S.-S. Xue. *A&A*, 350:334–343, 1999.

[140] R. Ruffini, J. D. Salmonson, J. R. Wilson, and S.-S. Xue. *A&A*, 359:855–864, 2000.

[141] R. Ruffini, C. L. Bianco, F. Fraschetti, S.-S. Xue, and P. Chardonnet. *ApJ*, 555(2):L113, 2001.

[142] C. L. Bianco, R. Ruffini, and S.-S. Xue. *A&A*, 368(2):377–390, 2001.

[143] R. Ruffini, C. L. Bianco, P. Chardonnet, F. Fraschetti, L. Vitagliano, and S.-S. Xue. In *Cosmology and Gravitation*, 2003, editor = Novello, Mario and Perez Bergliaffa, Santiago E., series = American Institute of Physics Conference Series, volume = 668, pages = 16-107.

[144] C. L. Bianco and R. Ruffini. *ApJL*, 620(1):L23–L26, 2005.

[145] C. L. Bianco and R. Ruffini. *ApJL*, 633(1):L13–L16, 2005.

[146] R. Ruffini, M. G. Bernardini, C. L. Bianco, L. Caito, P. Chardonnet, M. G. Dainotti, F. Fraschetti, R. Guida, M. Rotondo, G. Vereshchagin, L. Vitagliano, and S.-S. Xue. In *XIIth Brazilian School of Cosmology and Gravitation*, volume 910 of *American Institute of Physics Conference Series*, pages 55–217, Jun 2007.

[147] J. Schwinger. *Physical Review*, 82:664–679, 1951.

[148] G. Preparata, R. Ruffini, and S.-S. Xue. *A&A*, 338:L87–L90, 1998.

[149] R. Ruffini, G. Vereshchagin, and S.-S. Xue. *Physics Reports*, 487(1-4):1–140, 2010.

[150] D. N. Page. *ApJ*, 653:1400–1409, 2006.

[151] R. M. Wald. *Phys. Rev. D*, 10:1680–1685, 1974.

[152] R. Ruffini, J. A. Rueda, R. Moradi, Y. Wang, S. S. Xue, L. Becerra, C. L. Bianco, Y. C. Chen, C. Cherubini, S. Filippi, M. Karlica, J. D. Melon Fuksman, D. Primorac, N. Sahakyan, and G. V. Vereshchagin. *arXiv e-prints*, Nov 2018.

[153] A. M. Beloborodov. *ApJ*, 737(2):68, 2011.

[154] M. M. Shara, D. R. Zurek, R. E. Williams, D. Prialnik, R. Gilmozzi, and A. F. J. Moffat. *The Astronomical Journal*, 114:258, 1997.

[155] L. Ducci, L. Sidoli, S. Mereghetti, A. Paizis, and P. Romano. *MNRAS*, 398(4):2152–2165, 2009.

[156] W. D. Arnett and C. Meakin. *ApJ*, 733(2):78, 2011.

[157] C. D. Dermer and K. E. Mitman. *ApJL*, 513:L5–L8, 1999.

[158] R. Ruffini, C. L. Bianco, S.-S. Xue, P. Chardonnet, F. Fraschetti, and V. Gurzadyan. *International Journal of Modern Physics D*, 13:843–851, 2004.

[159] S. I. Blinnikov, A. V. Kozyreva, and I. E. Panchenko. *Astronomy Reports*, 43(11):739–747, 1999.

[160] B. Patricelli, M. G. Bernardini, C. L. Bianco, L. Caito, G. de Barros, L. Izzo, R. Ruffini, and G. V. Vereshchagin. *The Astrophysical Journal*, 756(1):16, 2012.

[161] R. Ruffini, Y. Wang, Y. Aimuratov, U. Barres de Almeida, L. Becerra, C. L. Bianco, Y. C. Chen, M. Karlica, M. Kovačević, L. Li, J. D. Melon Fuksman, R. Moradi, M. Muccino, A. V. Penacchioni, G. B. Pisani, D. Primorac, J. A. Rueda, S. Shakeri, G. V. Vereshchagin, and S.-S. Xue. *ApJ*, 852(1):53, 2018.

[162] R. Ruffini, M. Karlica, N. Sahakyan, J. A. Rueda, Y. Wang, G. J. Mathews, C. L. Bianco, and M. Muccino. *ApJ*, 869(2):101, 2018.

[163] Y. Wang, J. A. Rueda, R. Ruffini, L. Becerra, C. Bianco, L. Becerra, L. Li, and M. Karlica. *ApJ*, 874(1):39, 2019.

[164] J. A. Rueda and R. Ruffini. *ApJL*, 758(1):L7, 2012.

[165] C. L. Fryer, J. A. Rueda, and R. Ruffini. *ApJL*, 793(2):L36, 2014.

[166] L. Becerra, F. Cipolletta, C. L. Fryer, J. A. Rueda, and R. Ruffini. *ApJ*, 812(2):100, 2015.

[167] L. Becerra, C. L. Bianco, C. L. Fryer, J. A. Rueda, and R. Ruffini. *ApJ*, 833, 2016.

[168] L. Becerra, C. L. Ellinger, C. L. Fryer, J. A. Rueda, and R. Ruffini. *ApJ*, 871(1):14, 2019.

[169] K. A. Postnov and L. R. Yungelson. *Living Reviews in Relativity*, 17(1):3, 2014.

[170] R. Ruffini, L. Becerra, C. L. Bianco, Y. C. Chen, M. Karlica, M. Kovačević, J. D. Melon Fuksman, R. Moradi, M. Muccino, G. B. Pisani, D. Primorac, J. A. Rueda, G. V. Vereshchagin, Y. Wang, and S.-S. Xue. *ApJ*, 869(2):151, 2018.

[171] J. R. Wilson. *ApJ*, 173:431, 1972.

[172] J. R. Wilson. A numerical method for relativistic hydrodynamics. In L. L. Smarr, editor, *Sources of Gravitational Radiation*, pages 423–445, 1979.

[173] J. R. Wilson and G. J. Mathews. *Relativistic numerical hydrodynamics*. Cambridge University Press, 2003.

[174] J. Centrella and J. R. Wilson. *ApJS*, 54:229–249, 1984.

[175] C. L. Fryer, G. Rockefeller, and M. S. Warren. *ApJ*, 643(1):292–305, 2006.

[176] J. M. Martí and E. Müller. Numerical hydrodynamics in special relativity. *Living Reviews in Relativity*, 6(1):7, 2003.

[177] S. K. Godunov. *Sbornik: Mathematics*, 47(8-9):357–393, 1959.

[178] L. Rezzolla and O. Zanotti. *Relativistic Hydrodynamics*. Oxford University Press, 2013.

[179] D. Mihalas and B. W. Mihalas. *Foundations of Radiation Hydrodynamics*. Dover Books on Physics. Dover Publications, 1999.

[180] P. A. Mazzali and L. B. Lucy. *A&A*, 279:447–456, 1993.

[181] M. Kromer and S. A. Sim. *MNRAS*, 398(4):1809–1826, 2009.

[182] O. Teșileanu, A. Mignone, and S. Massaglia. *A&A*, 488(1):429–440, 2008.

[183] S. Chandrasekhar. *Radiative transfer*. Dover Publications, 1960.

[184] M. F. Modest. *Radiative heat transfer*. Academic press, 2003.

[185] C. P. Dullemond and R. Turolla. *A&A*, 360, 2000.

[186] S. W. Davis, J. M. Stone, and Y.-F. Jiang. *ApJS*, 199(1):9, 2012.

[187] M González, E. Audit, and P. Huynh. *A&A*, 464(2):429–435, 2007.

[188] B. Commerçon, R. Teyssier, E. Audit, P. Hennebelle, and G. Chabrier. *A&A*, 529:A35, 2011.

[189] C. Roedig, O. Zanotti, and D. Alic. *MNRAS*, 426(2):1613–1631, 2012.

[190] A. Sądowski, R. Narayan, A. Tchekhovskoy, and Y. Zhu. 429(4):3533–3550, 2013.

[191] M. A. Skinner and E. C. Ostriker. *ApJS*, 206(2):21, 2013.

[192] H. R. Takahashi and K. Ohsuga. *ApJ*, 772(2):127, 2013.

[193] J. C. McKinney, A. Tchekhovskoy, A. Sądowski, and R. Narayan. *MNRAS*, 441(4):3177–3208, 2014.

[194] F. J. Rivera-Paleo and F. S. Guzmán. *MNRAS*, 459(3):2777–2786, 2016.

[195] G. C. Pomraning. *The equations of radiation hydrodynamics*. Pergamon Press, 1973.

[196] P. Mimica, M. A. Aloy, Iván Agudo, J. M. Martí, J. L. Gómez, and J. A. Miralles. *ApJ*, 696(2):1142, 2009.

[197] J. P. H. Goedbloed and S. Poedts. *Principles of Magnetohydrodynamics*. Cambridge University Press, 2004.

[198] M. González, N. Vaytet, B. Commerçon, and J. Masson. *A&A*, 578:A12, 2015.

[199] C.D. Levermore. *Journal of Quantitative Spectroscopy and Radiative Transfer*, 31(2):149–160, 1984.

[200] P. C. Fragile, A. Gillespie, T. Monahan, M. Rodriguez, and P. Anninos. *ApJS*, 201(2):9, 2012.

[201] A. Mignone, C. Zanni, P. Tzeferacos, B. van Straalen, P. Colella, and G. Bodo. The PLUTO Code for Adaptive Mesh Computations in Astrophysical Fluid Dynamics. *ApJS*, 198:7, January 2012.

[202] M. Adams et al. Chombo software package for amr applications – design document. *Lawrence Berkeley National Laboratory Technical Report*, LBNL-6616E, 2015.

[203] A. Mignone and G. Bodo. *MNRAS*, 364(1):126–136, 2005.

[204] L. Pareschi and G. Russo. *Journal of Scientific computing*, 25(1):129–155, 2005.

[205] W. G. Mathews. *ApJ*, 165:147, 1971.

[206] A. Mignone and J. C. McKinney. *MNRAS*, 378(3):1118–1130, 2007.

[207] J. P. Freidberg. *Ideal magnetohydrodynamics*. Cambridge University Press, 2014.

[208] E. F. Toro. *Riemann solvers and numerical methods for fluid dynamics: a practical introduction*. Springer Science & Business Media, 2013.

[209] R. L. Merlino, J. R. Heinrich, S. H. Kim, and J. K. Meyer. *Plasma Physics and Controlled Fusion*, 54(12):124014, 2012.

[210] J. M. Martí and E. Müller. *Journal of Fluid Mechanics*, 258:317–333, 1994.

[211] A. M. Anile and S. Pennisi. *arXiv preprint astro-ph/0206281*, 46:127, 1987.

[212] C. B. Laney. *Computational gasdynamics*. Cambridge university press, 1998.

[213] A. Mignone, G. Bodo, S. Massaglia, T. Matsakos, O. Tesileanu, C. Zanni, and A. Ferrari. *ApJS*, 170(1):228–242, 2007.

[214] A. Harten, P. D. Lax, and B. van Leer. *SIAM review*, 25(1):35–61, 1983.

[215] V. V. Rusanov. *Zhurnal Vychislitel'noi Matematiki i Matematicheskoi Fiziki*, 1(2):267–279, 1961.

[216] A. Mignone and G. Bodo. *MNRAS*, 368(3):1040–1054, 2006.

[217] A. Mignone, M. Ugliano, and G. Bodo. *MNRAS*, 393(4):1141–1156, 2009.

[218] A. Mignone. *Journal of Computational Physics*, 270:784–814, 2014.

[219] A. Harten. *Journal of Computational Physics*, 135(2):260–278, 1997.

[220] S. Gottlieb and C.-W. Shu. *NASA CR-201591 ICASE Rep. 96-50, 20 (Washington: NASA)*, 1996.

[221] R. Courant, K. Friedrichs, and H. Lewy. *Math. Ann.*, 100:32, 1928.

[222] J. U. Brackbill and D. C. Barnes. *Journal of Computational Physics*, 35, 1980.

[223] D. S. Balsara and D. S. Spicer. *Journal of Computational Physics*, 149(2):270–292, 1999.

[224] P. Londrillo and L. Del Zanna. *Journal of Computational Physics*, 195(1):17–48, 2004.

[225] A. Dedner, F. Kemm, D. Kröner, C.-D. Munz, T. Schnitzer, and M. Wesenberg. *Journal of Computational Physics*, 175(2):645–673, 2002.

[226] A. Mignone and P. Tzeferacos. *Journal of Computational Physics*, 229(6):2117–2138, 2010.

[227] A. Mignone, P. Tzeferacos, and G. Bodo. *Journal of Computational Physics*, 229(17):5896–5920, 2010.

[228] R. Löhner. *Computer Methods in Applied Mechanics and Engineering*, 61(3):323–338, 1987.

[229] R. Ruffini, C. L. Bianco, P. Chardonnet, F. Fraschetti, and S.-S. Xue. *ApJL*, 581(1):L19, 2002.

[230] C. L. Bianco, M. G. Bernardini, L. Caito, M. G. Dainotti, R. Guida, and R. Ruffini. In *AIP Conference Proceedings*, volume 966, pages 12–15. AIP, 2008.

[231] R. Ruffini, J. D. Melon Fuksman, and G. V. Vereshchagin. *arXiv preprint arXiv:1904.03163*, 2019.

[232] R. Ruffini, I. A. Siutsou, and G. V. Vereshchagin. *New Astronomy*, 27:30–33, 2014.

[233] T. Piran, A. Shemi, and R. Narayan. *MNRAS*, 263(4):861–867, 1993.

[234] P. Beniamini and P. Kumar. *MNRAS Letters*, 457(1):L108–L112, 2016.

[235] A. D. Falcone, D. Morris, J. Racusin, G. Chincarini, A. Moretti, P. Romano, D. N. Burrows, C. Pagani, M. Stroh, D. Grupe, S. Campana, S. Covino, G. Tagliaferri, R. Willingale, and N. Gehrels. *ApJ*, 671:1921–1938, 2007.

[236] D. N. Burrows, P. Romano, A. Falcone, S. Kobayashi, B. Zhang, A. Moretti, P. T. O'Brien, M. R. Goad, S. Campana, K. L. Page, et al. *Science*, 309(5742):1833–1835, 2005.

[237] K. Ioka, S. Kobayashi, and B. Zhang. *ApJ*, 631(1):429, 2005.

[238] Y.-Z. Fan and D. M. Wei. *MNRAS Letters*, 364(1):L42–L46, 2005.

[239] E.-W. Liang, B. Zhang, P. T. O'Brien, R. Willingale, L. Angelini, D. N. Burrows, S. Campana, G. Chincarini, A. Falcone, N. Gehrels, et al. *ApJ*, 646(1):351, 2006.

[240] D. Lazzati and R. Perna. *MNRAS Letters*, 375(1):L46–L50, 2007.

[241] G. Chincarini, A. Moretti, P. Romano, A. D. Falcone, D. Morris, and Racusin.

[242] A. Maxham and B. Zhang. *ApJ*, 707(2):1623, 2009.

[243] R. Margutti, C. Guidorzi, G. Chincarini, M. G. Bernardini, F. Genet, J. Mao, and F. Pasotti. *MNRAS*, 406(4):2149–2167, 2010.

[244] *A&A*, 455(1):L5–L8, 2006.

[245] A. M. Beloborodov, F. Daigne, R. Mochkovitch, and Z. L. Uhm. *MNRAS*, 410(4):2422–2427, 2011.

[246] P. D'Avanzo, V. D'Elia, and S. Covino. GRB 081008: VLT redshift confirmation. *GRB Coordinates Network*, 8350, 2008.

[247] F. Yuan, P. Schady, J. L. Racusin, R. Willingale, T. Krühler, P. T. O'Brien, J. Greiner, S. R. Oates, E. S. Rykoff, F. Aharonian, C. W. Akerlof, M. C. B. Ashley, S. D. Barthelmy, R. Filgas, H. A. Flewelling, N. Gehrels, E. Göğüş, T. Güver, D. Horns, Ü. Kızıloğlu, H. A. Krimm, T. A. McKay, M. E. Özel, A. Phillips, R. M. Quimby, G. Rowell, W. Rujopakarn, B. E. Schaefer, W. T. Vestrand, J. C. Wheeler, and J. Wren. *ApJ*, 711:870–880, March 2010.

[248] Jürgen Ehlers. In *Relativity, astrophysics and cosmology*, pages 1–125. Springer, 1973.

[249] R. Ruffini, I. A. Siutsou, and G. V. Vereshchagin. *ApJ*, 772(1):11, 2013.

[250] M. A. Abramowicz, I. D. Novikov, and B. Paczynski. *The Astrophysical Journal*, 369:175–178, 1991.

[251] B.-B. Zhang, B. Zhang, A. J. Castro-Tirado, Z. G. Dai, P.-H. T. Tam, X.-Y. Wang, Y.-D. Hu, S. Karpov, A. Pozanenko, F.-W. Zhang, et al. *Nature Astronomy*, 2(1):69, 2018.

[252] N. Sapir, B. Katz, and E. Waxman. *ApJ*, 774(1):79, 2013.

[253] A. G. Aksenov, R. Ruffini, and G. V. Vereshchagin. *MNRAS*, 436(1):L54–L58, 2013.

[254] R. Ruffini, G. V. Vereshchagin, and Y. Wang. *A&A*, 600:A131, 2017.

[255] A. Castro-Tirado et al. *GCN Circular 23708*, 2019.

[256] R. Ruffini, L. Li, R. Moradi, J. A. Rueda, Y. Wang, S.-S. Xue, C. L. Bianco, S. Campion, J. D. Melon Fuksman, C. Cherubini, S. Filippi, M. Karlica, and N. Sahakyan. *arXiv preprint arXiv:1904.04162*, 2019.

[257] S. Kobayashi, T. Piran, and R. Sari. *ApJ*, 490:92, 1997.

[258] G. R. Blumenthal and R. J. Gould. *Reviews of Modern Physics*, 42(2):237, 1970.

[259] L. Li, J. A. Rueda, R. Ruffini, and Y. Wang. Extension of the self-similarity laws and of the supernova shock breakout discovered in grb. *in preparation*.

[260] J. D. Melon Fuksman and A. Mignone. *ApJS*, 242(2):20, 2019.

[261] A. Peraiah. *An Introduction to Radiative Transfer: Methods and applications in astrophysics*. Cambridge University Press, 2002.

[262] J. D. Jackson. Classical electrodynamics, 1999.

[263] T. W. Körner. *Fourier analysis*. Cambridge university press, 1989.

[264] S. L. Shapiro. *ApJ*, 472(1):308, 1996.

[265] F. H. Shu. *The physics of astrophysics. Volume 1: Radiation*. University Science Books, Mill Valley, CA (USA), 1991, 446 p., ISBN 0-935702-64-4.

[266] M. W. Sincell, M. Gehmeyr, and D. Mihalas. *Shock Waves*, 9(6):391–402, 1999.

[267] E. Hairer and G. Wanner. *Solving ordinary differential equations II*. Springer Berlin Heidelberg, 1996.

[268] C. Berthon, J. Dubois, B. Dubroca, T.-H. Nguyen-Bui, and R. Turpault. *Adv. Appl. Math. Mech*, 2(3):259–285, 2010.

[269] T. Hanawa and E. Audit. *Journal of Quantitative Spectroscopy and Radiative Transfer*, 145:9–16, 2014.

[270] C. Palenzuela, L. Lehner, O. Reula, and L. Rezzolla. *MNRAS*, 394(4):1727–1740, 2009.

[271] B. van Leer. *Journal of computational physics*, 14(4):361–370, 1974.

[272] S. Richling, E. Meinköhn, N. Kryzhevoi, and G. Kanschat. *A&A*, 380(2):776–788, 2001.

[273] G. H. Miller and P. Colella. *Journal of computational physics*, 167(1):131–176, 2001.

[274] N. J. Turner and J. M. Stone. *ApJS*, 135(1):95, 2001.

[275] B. D. Farris, T. K. Li, Y. T. Liu, and S. L. Shapiro. *Phys. Rev. D*, 78(2):024023, 2008.

[276] O. Zanotti, C. Roedig, L. Rezzolla, and L. Del Zanna. *MNRAS*, 417(4):2899–2915, 2011.

[277] G.-S. Jiang and C.-W. Shu. *Journal of Computational Physics*, 126(1):202–228, 1996.

[278] P. Colella and P. R. Woodward. *Journal of Computational Physics*, 54(1):174–201, 1984.

[279] D.-I. Choi, J. David Brown, B. Imbiriba, J. Centrella, and P. MacNeice. Interface conditions for wave propagation through mesh refinement boundaries. *Journal of Computational Physics*, 193:398–425, January 2004.

[280] S. H. Chilton and P. Colella. Damping of spurious wave reflections from coarse-fine adaptive mesh refinement grid boundaries. In *Abstracts IEEE International Conference on Plasma Science*, 2010.

[281] M. J. Berger and R. J. LeVeque. *SIAM J. Numer. Anal.*, 35(6):2298–2316, 1998.

[282] J. C. Hayes and M. L. Norman. *ApJS*, 147(1):197, 2003.

[283] S. S. Komissarov. *MNRAS*, 303(2):343–366, 1999.

[284] F. Foucart, E. O'Connor, L. Roberts, M. D. Duez, R. Haas, L. E. Kidder, C. D. Ott, H. P. Pfeiffer, M. A. Scheel, and B. Szilagyi. *Physical Review D*, 91(12):124021, 2015.

[285] Y. B. Zel'dovich and Y. P. Raizer. *Physics of Shock Waves and High-Temperature Hydrodynamic Phenomena*. Academic Press, 1967.

[286] R. P. Drake. *Physics of Plasmas*, 14(4), 2007.

[287] Y.-F. Jiang, J. M. Stone, and S. W. Davis. *ApJS*, 199(1):14, 2012.

[288] J. Rosdahl and R. Teyssier. *MNRAS*, 449(4):4380–4403, 2015.

[289] A. S. Almgren, V. E. Beckner, J. B. Bell, M. S. Day, L. H. Howell, C. C. Joggerst, M. J. Lijewski, A. Nonaka, M. Singer, and M. Zingale. *ApJ*, 715(2):1221–1238, 2010.

[290] A. M. Anile. *Relativistic Fluids and Magneto-Fluids*. Cambridge Univ. Press, 1989.

[291] E. Audit, P. Charrier, J.-P. Chièze, and B. Dubroca. *arXiv preprint astro-ph/0206281*, 2002.

[292] A. Kramida, Yu. Ralchenko, J. Reader, and NIST ASD Team. NIST Atomic Spectra Database (ver. 5.6.1), [Online]. Available: `https://physics.nist.gov/asd` [2019, May 23]. National Institute of Standards and Technology, Gaithersburg, MD., 2018.

[293] L. D. Landau and E. M. Lifshitz. *Statistical Physics (Part 1)*. Pergamon Press Oxford New York, 1980.

Appendix A

Signal speeds

In this appendix, we describe the computation of the characteristic signal speeds used to construct approximate Riemann solvers for RHD, RMHD (Section 2.3.2), and radiation transport (Sections 4.2.2 and 4.2.3). For any homogeneous hyperbolic system of equations, these speeds can be computed for every direction d as the eigenvalues of the Jacobian matrix J_d (see Section 2.2.1). All of the Riemann solvers implemented in this work approximate maximum and minimum signal speeds as the maximum and minimum eigenvalues of J_d, although different estimations are in general possible (see e.g. [208]).

As pointed out in Section 4.2.2, the Rad-RMHD equations reduce for $\mathcal{S} \equiv 0$ to two decoupled systems of equations; one corresponding to the RMHD equations and the other one to radiation transport. The resulting J_d are block-diagonal, where the blocks correspond to the Jacobian matrices of each subsystem. Consequently, the full set of characteristic speeds can be obtained by computing the eigenvalues of each of these blocks individually. We now outline the procedures followed for this calculation.

A.1 RHD and RMHD

For a given direction d, maximum and minimum eigenvalues of the Jacobian matrix of the RHD equations can be obtained as the roots of the quadratic equation in λ

$$(\lambda - v_d)^2 = \sigma_s(1 - \lambda^2)\,, \tag{A.1}$$

where $\sigma_s = c_s^2/(\gamma^2(1-c_s^2))$, while c_s is the sound speed of the gas (see [203]). This speed can be generally computed as $c_s^2 = \left(\partial p_g/\partial e\right)\big|_S$, where e is the internal energy density and the derivative is taken at constant entropy. The result of this calculation depends on the chosen

EoS, and can take in our case one of the following two forms (see [206]):

$$c_s^2 = \begin{cases} \frac{\Gamma\Theta}{h} & \text{Constant}-\Gamma \text{ law} \\ \frac{\Theta}{3h}\frac{5h-8\Theta}{h-\Theta} & \text{Taub} - \text{Mathews} \end{cases} . \tag{A.2}$$

RMHD maximum and minimum signal speeds are computed by making use of the characteristic decomposition of the RMHD equations, which is extensively analyzed in [211] and [290]. These are obtained as the maximum and minimum roots of the following quartic equation in λ:

$$\rho h \left(1 - c_s^2\right) a^4 = \left(1 - \lambda^2\right) \left[\left(b^\mu b_\mu + \rho h c_s^2\right) a^2 - c_s^2 \mathcal{B}^2\right] , \tag{A.3}$$

where $a = \gamma\left(\lambda - v_x\right)$, $\mathcal{B} = b^x - \lambda b^0$ and we have defined the four vector

$$b^\mu = \gamma\left(\mathbf{v}\cdot\mathbf{B}, \mathbf{B}/\gamma^2 + \left(\mathbf{v}\cdot\mathbf{B}\right)\mathbf{v}\right) . \tag{A.4}$$

To find the roots of equation (A.3), we follow [203]: if the total velocity or the normal component of the magnetic field vanish, the equation is reduced, respectively, to a biquadratic or quadratic form. Otherwise, the full quartic equation is solved.

A.2 Radiation transport

The treatment needed for the radiation characteristic wave speeds is rather simpler, as a short calculation shows that, for every direction d, the radiation block depends only on the angle θ between $\mathbf{F}_r$ and $\hat{\boldsymbol{e}}_d$, and on $f = ||\mathbf{F}_r||/E_r$. This simplifies the calculation, which can be performed analytically as shown in [291] and [191]. The full set of eigenvalues of the radiation block, which we denote as $\{\lambda_{r1}, \lambda_{r2}, \lambda_{r3}\}$, can be computed as

$$\lambda_{r1} = \frac{f\cos\theta - \zeta(f,\theta)}{\sqrt{4-3f^2}}, \tag{A.5}$$

$$\lambda_{r2} = \frac{3\xi(f)-1}{2f}\cos\theta, \tag{A.6}$$

$$\lambda_{r3} = \frac{f\cos\theta + \zeta(f,\theta)}{\sqrt{4-3f^2}}, \tag{A.7}$$

where

$$\zeta(f,\theta) = \left[\frac{2}{3}\left(4 - 3f^2 - \sqrt{4-3f^2}\right) + 2\,\cos^2\theta\left(2 - f^2 - \sqrt{4-3f^2}\right)\right]^{1/2}. \tag{A.8}$$

When $f = 0$, λ_{r2} is replaced by zero, i.e., its limit when $f \to 0$. It can be seen from Equations (A.5)–(A.8) that the following inequalities hold for every value of f and θ:

$$\lambda_{r1} \leq \lambda_{r2} \leq \lambda_{r3}. \tag{A.9}$$

In the free-streaming limit ($f = 1$), all of these eigenvalues coincide and are equal to $\cos\theta$, which gives $\lambda_{rj} = \pm 1$ in the parallel direction to $\mathbf{F}_r$, and $\lambda_{rj} = 0$ in the perpendicular ones for $j = 1, 2, 3$. On the other hand, in the diffusion limit ($f = 0$), we have $(\lambda_{r1}, \lambda_{r2}, \lambda_{r3}) = (-1/\sqrt{3}, 0, 1/\sqrt{3})$ in every direction.

The above analysis can be applied to homogeneous hyperbolic systems. Although the equations of Rad-RMHD do not belong to this category, this is not a problem for small opacities and densities, and in general when radiation transport dominates over radiation–matter interaction. On the contrary, in the diffusion limit, the modules of the maximum and minimum speeds, equal to $1/\sqrt{3}$ in both cases, may be too big and lead to an excessive numerical diffusion. In those cases, the interaction terms need to be taken into account for the speed calculations. With this purpose, following [190], we include in the code the option of locally limiting the maximum and minimum speeds by means of the following transformations:

$$\begin{aligned} \lambda_{r,\,L} &\to \max\left(\lambda_{r,\,L}, -\frac{4}{3\tau}\right) \\ \lambda_{r,\,R} &\to \min\left(\lambda_{r,\,R}, \frac{4}{3\tau}\right) \end{aligned}, \tag{A.10}$$

where $\tau = \rho\,\gamma\,\chi\,\Delta x$ is the optical depth along one cell, with Δx its width in the current direction. Hence, this limiting is only applied whenever cells are optically thick. These reduced speeds are computed considering a diffusion equation with a stationary flux, with a diffusion coefficient of $1/3\chi$.

Appendix B

Equation of state of an equilibrium e^-e^+–baryon plasma

We give here the details of the obtention of an EoS of a fully ionized[1] e^-e^+–baryon plasma. Assuming LTE, we compute the total comoving internal energy and pressure by adding the contributions of electrons, positrons, photons and baryons, as

$$\epsilon = \epsilon_{e^-} + \epsilon_{e^+} + \epsilon_\gamma + \epsilon_B \tag{B.1}$$

$$p_g = p_{e^-} + p_{e^+} + p_\gamma + p_B \,. \tag{B.2}$$

The number and energy densities of the different species, as well as their pressure, can be computed in natural units ($c = \hbar = k_B = 1$) in terms of their equilibrium distribution functions as

$$n_{e^-} = A\,T^3 \int_0^\infty f(z, T, m_e, \mu_{e^-})\, z^2\, dz \tag{B.3}$$

$$n_{e^+} = A\,T^3 \int_0^\infty f(z, T, m_e, \mu_{e^+})\, z^2\, dz \tag{B.4}$$

$$\epsilon_{e^-} = A\,T^4 \int_0^\infty f(z, T, m_e, \mu_{e^-})\, \sqrt{z^2 + (m_e/T)^2}\; z^2\, dz - m_e n_{e^-} \tag{B.5}$$

$$\epsilon_{e^+} = A\,T^4 \int_0^\infty f(z, T, m_e, \mu_{e^+})\, \sqrt{z^2 + (m_e/T)^2}\; z^2\, dz - m_e n_{e^+} \tag{B.6}$$

[1] In LTE, the degree of ionization of a given species is given by the Saha equation (see, e.g., [179]). A sufficient condition for fully ionization is that the equilibrium temperature is well above all relevant ionization energies, although high degrees of ionization can still occur for lower temperatures. For instance, hydrogen is strongly ionized even in the case $\varepsilon_{\rm H}/k_B T \sim 10$, where $\varepsilon_{\rm H} = 13.6$ eV is the ionization energy of atomic hydrogen, as extracted from [292]. Other relevant values are the first and second ionization energies of helium, of 24.6 and 54.4 eV respectively.

$$p_{e^-} = A\,\frac{T^4}{3}\int_0^\infty f(z,T,m_e,\mu_{e^-})\,\frac{z^4}{\sqrt{z^2+(m_e/T)^2}}\,dz \tag{B.7}$$

$$p_{e^+} = A\,\frac{T^4}{3}\int_0^\infty f(z,T,m_e,\mu_{e^+})\,\frac{z^4}{\sqrt{z^2+(m_e/T)^2}}\,dz \tag{B.8}$$

$$\epsilon_\gamma = a_R\,T^4 \tag{B.9}$$

$$p_\gamma = \frac{a_R\,T^4}{3} \tag{B.10}$$

$$\epsilon_B = \frac{3}{2}n_B T \tag{B.11}$$

$$p_B = n_B T\,, \tag{B.12}$$

where

$$f(z,T,m,\mu) = \frac{1}{e^{\sqrt{z^2+(m/T)^2}-\mu/T}+1}, \tag{B.13}$$

is the (rescaled) Fermi-Dirac distribution at a temperature T and a chemical potential μ, m_e is the electron mass, n_B the nuclei number density, a_R is the radiation constant, and $A = 15\,a_R/\pi^4$ (see, e.g., [293]).

If the pair annihilation rate is zero, i.e., if the process $e^- + e^+ \leftrightarrows 2\gamma$ is in equilibrium, then the equality $\mu_{e^-} = -\mu_{e^+} \equiv \mu$ holds, since equilibrium photons have zero chemical potential. Besides, charge neutrality implies

$$n_{e^-}(\mu,T) - n_{e^+}(\mu,T) = Z\,n_B, \tag{B.14}$$

where Z is the average atomic number. An additional relation can be obtained by adding the contribution of all species to the total mass density, as

$$\rho = m_a n_B + m_e(n_{e^-} + n_{e^+})\,, \tag{B.15}$$

where m_a is the average nuclear mass in the plasma. Together with Equation (B.14), Eq. (B.15) completely defines the mass density as a function of (μ, T). Thus, the desired EoS that relates p_g, ϵ and ρ is defined implicitly as the parametric surface

$$\{(\rho(\mu,T),\epsilon(\mu,T),p_g(\mu,T)) :\ T>0,\ \mu\geq 0\} \tag{B.16}$$

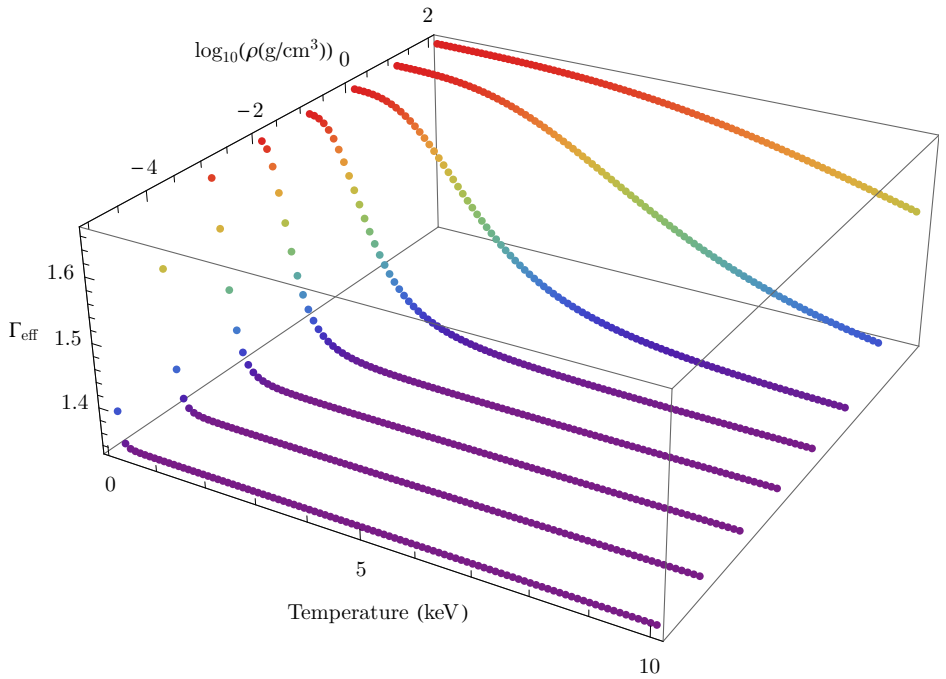

Fig. B.1 Curves of $\Gamma_{\mathrm{eff}}(\rho, T)$ at constant ρ for $\rho \in [10^{-5}, 10^{2}]$ g cm^{-3} and $T < 10$ keV.

that satisfies all of the above relations.

Departures of this EoS from the constant-Γ law (Eq. (2.9)) can be evaluated by defining an effective Γ index as

$$\Gamma_{\mathrm{eff}} = 1 + \frac{p_g}{\epsilon}. \tag{B.17}$$

In Fig. B.1, the value of Γ_{eff} obtained from Eq. (B.16) with $Z = 1$ (i.e., for pure hydrogen) is plotted as a function of T taking different values of ρ in the range $[10^{-5}, 10^{2}]$ g cm^{-3}. In every case, Γ_{eff} decreases from its nonrelativistic value $(5/3)$ to its relativistic limit $(4/3)$ as the temperature increases. For increasing values of the density, it can be seen that Γ_{eff} remains close to $5/3$ in a larger temperature range. This is due to the fact that, for higher baryon and electron densities, the total energy and pressure start being dominated by the contributions of material particles, which are nonrelativistic since we have taken $k_B T \ll m_e = 511$ keV$\ll m_{\mathrm{baryons}}$.

In the simulations shown in Sections 3.1 and 3.2, we have verified that $\Gamma_{eff} \approx 4/3$ with a maximum error of 0.2% in all regions occupied by the plasma.

Appendix C

Curvilinear coordinates

In this appendix we show the formalism used in this work to write conservation laws in spherical and cylindrical coordinates. Although we will now focus on the form taken by the radiation part of the Rad-RMHD equations (Eqs. (4.47) and (4.48)), the same procedure is applied to the RMHD subsystem.

When using curvilinear coordinates, it is convenient to write all vector and tensor fields in such a way that all of their components have the same dimensionality. With this purpose, we write them in terms of their *physical* components, defined at each point of the Minkowski space $\mathcal{M}$ as their coordinates in a chosen orthonormal basis (tetrad) of its tangent space. For a system of coordinates $\{x^\mu\}$, a basis of the tangent space of $\mathcal{M}$ is given by $\mathcal{B} = \{\partial_\mu\}$, with $\mu = 1, 2, 3, 4$. Therefore, the components of a given tetrad in this basis, denoted by $\{\epsilon_\alpha{}^\mu\}$ with $\alpha = 1, 2, 3, 4$, must satisfy the property of orthogonality given by

$$(\epsilon_\alpha|\epsilon_\beta) = g_{\mu\nu}\epsilon_\alpha{}^\mu\epsilon_\beta{}^\nu = \eta_{\alpha\beta}\,, \tag{C.1}$$

where $g_{\mu\nu}$ represents the components of the metric tensor in the basis $\mathcal{B}$. The tensor $g_{\mu\nu}$ can be in turn written in terms of the tetrad components as

$$g_{\mu\nu} = \epsilon^\alpha{}_\mu\epsilon^\beta{}_\nu\eta_{\alpha\beta}\,. \tag{C.2}$$

Using these definitions, we can write the physical components of any four-vector v and rank-2 tensor T in terms of its components in $\mathcal{B}$, as

$$v^\alpha = \epsilon^\alpha{}_\mu v^\mu \tag{C.3}$$

$$T^{\alpha\beta} = \epsilon^\alpha{}_\mu\epsilon^\beta{}_\nu T^{\mu\nu}. \tag{C.4}$$

This choice radically simplifies the calculations, since in this way inner products between spatial vectors in $\mathbb{R}^3$ such as velocities and fluxes do not require the inclusion of metric coefficients (for instance, the inner product $(\mathbf{v}|\mathbf{u})$ is just $\sum_{i=1}^{3} v_i u_i$).

Let us now consider the case where the spatial components of the Minkowski metric are writen in spherical cordinates (r, θ, ϕ), i.e.,

$$ds^2 = -dt^2 + dr^2 + r^2(d\theta^2 + \sin^2\theta\, d\phi^2)\,, \tag{C.5}$$

where θ and ϕ are, respectively, the zenithal and azimuthal angles. In this case, a tetrad is given by the basis $\{\epsilon_\alpha^{\ \mu}\}$ whose only nonzero components in $\mathcal{B}$ are

$$\epsilon_t^{\ 0} = 1\ ,\ \epsilon_r^{\ 1} = 1\ ,\ \epsilon_\theta^{\ 2} = \frac{1}{r}\ ,\ \epsilon_\phi^{\ 3} = \frac{1}{r\sin\theta}\,. \tag{C.6}$$

When projected on any constant-t hyperplane, the last three vectors in this tetrad become the basis of $\mathbb{R}^3$ given by $\mathcal{B}_s = \{\hat{\boldsymbol{e}}_r, \hat{\boldsymbol{e}}_\theta, \hat{\boldsymbol{e}}_\phi\}$. With this choice of coordinates, Equations (4.47) and (4.48) can be written in terms of physical components by projecting Eq. (4.16) onto the tetrad's vectors, as

$$\epsilon_\nu^{\ \alpha}\nabla_\mu T^{\mu\nu} = -\epsilon_\nu^{\ \alpha}\, G^\nu\,, \tag{C.7}$$

where we have omitted the subindex r to avoid confusion with the coordinate indices. The value of $\nabla_\mu T^{\mu\nu}$ can be computed by applying the usual law for the covariant derivative of rank-2 tensors,

$$\nabla_\mu T^{\mu\nu} = \partial_\mu T^{\mu\nu} + \Gamma^\mu_{\ \mu\sigma}\, T^{\sigma\nu} + \Gamma^\nu_{\ \mu\sigma}\, T^{\mu\sigma}\,, \tag{C.8}$$

where the Christoffel symbols $\Gamma^\mu_{\ \sigma\rho}$ are defined as

$$\Gamma^\mu_{\ \sigma\rho} = \frac{1}{2}\, g^{\mu\nu}\left(\partial_\sigma g_{\nu\rho} + \partial_\rho g_{\nu\sigma} - \partial_\nu g_{\sigma\rho}\right)\,. \tag{C.9}$$

Finally, writing $T^{\mu\nu}$ in terms of physical components by inverting Eq. (C.4), we arrive to the form of Equations (4.47) and (4.48) in spherical coordinates:

$$\frac{\partial E}{\partial t} + \nabla\cdot\mathbf{F} = -G^0 \tag{C.10}$$

$$\frac{\partial F^r}{\partial t} + \nabla\cdot\mathbf{P}^r = -G^r + \frac{P^{\theta\theta} + P^{\phi\phi}}{r} \tag{C.11}$$

$$\frac{\partial F^\theta}{\partial t} + \nabla\cdot\mathbf{P}^\theta = -G^\theta + \frac{\cot\theta\, P^{\phi\phi} - P^{r\theta}}{r} \tag{C.12}$$

$$\frac{\partial F^\phi}{\partial t} + \nabla^r\cdot\mathbf{P}^\phi = -G^\phi, \tag{C.13}$$

where

$$\nabla \cdot \mathbf{F} = \frac{1}{r^2}\frac{\partial(r^2 F^r)}{\partial r} + \frac{1}{r\sin\theta}\frac{\partial(\sin\theta\, F^\theta)}{\partial\theta} + \frac{1}{r\sin\theta}\frac{\partial F^\phi}{\partial\phi} \tag{C.14}$$

$$\nabla^r \cdot \mathbf{F} = \frac{1}{r^3}\frac{\partial(r^3 F^r)}{\partial r} + \frac{1}{r\sin^2\theta}\frac{\partial(\sin^2\theta\, F^\theta)}{\partial\theta} + \frac{1}{r\sin\theta}\frac{\partial F^\phi}{\partial\phi}\,, \tag{C.15}$$

and $\mathbf{P}^i = \left(P^{ir}, P^{i\theta}, P^{i\phi}\right)$.

This procedure can be applied in the same way to obtain the form these equations take in cylindrical coordinates (R, ϕ, z). In that case, spatial components are expressed in the basis $\mathcal{B}_c = \{\hat{\boldsymbol{e}}_R, \hat{\boldsymbol{e}}_\phi, \hat{\boldsymbol{e}}_z\}$, which yields

$$\frac{\partial E}{\partial t} + \nabla \cdot \mathbf{F} = -G^0 \tag{C.16}$$

$$\frac{\partial F^R}{\partial t} + \nabla \cdot \mathbf{P}^R = -G^R + \frac{P^{\phi\phi}}{R} \tag{C.17}$$

$$\frac{\partial F^\phi}{\partial t} + \nabla^R \cdot \mathbf{P}^\phi = -G^\phi \tag{C.18}$$

$$\frac{\partial F^z}{\partial t} + \nabla \cdot \mathbf{P}^z = -G^z, \tag{C.19}$$

with

$$\nabla \cdot \mathbf{F} = \frac{1}{R}\frac{\partial(RF^R)}{\partial R} + \frac{1}{R}\frac{\partial F^\phi}{\partial\phi} + \frac{\partial F^z}{\partial z} \tag{C.20}$$

$$\nabla^R \cdot \mathbf{F} = \frac{1}{R^2}\frac{\partial(R^2 F^R)}{\partial R} + \frac{1}{R}\frac{\partial F^\phi}{\partial\phi} + \frac{\partial F^z}{\partial z}\,, \tag{C.21}$$

and $\mathbf{P}^i = \left(P^{iR}, P^{i\phi}, P^{iz}\right)$. In the code, the terms that appear in the right-hand side of Equations (C.11), (C.12) and (C.17) that are not of the form $-G^\mu$ are integrated explicitly as shown in Eq. (2.53).

Appendix D

Semi-analytical proof of Equation (4.63)

In order to check the validity of Equation (4.63), we have verified the following relations:

$$\lambda_R \geq \max\left(\frac{B_R}{A_R}, \frac{B_L}{A_L}\right) \tag{D.1}$$

$$\lambda_L \leq \min\left(\frac{B_R}{A_R}, \frac{B_L}{A_L}\right). \tag{D.2}$$

As in Section 4.2.3 and Appendix C, we omit the subindex r, as it is understood that only radiation fields are considered here.

We begin by proving the positivity of A_R. From its definition in Equation (4.70), we have

$$\frac{A_R}{E_R} = \lambda_R - f_{x,R} = \max(\lambda_{3,L}, \lambda_{3,R}) - f_{x,R}\,, \tag{D.3}$$

where $\lambda_{3,L/R} = \lambda_3(f_{L/R}, \theta_{L/R})$. Since $E > 0$, we can conclude from Eq. (D.3) that $A_R \geq 0$ is automatically satisfied if

$$\lambda_3(f, \theta) \geq f\cos\theta \;\forall\,(f, \theta)\,. \tag{D.4}$$

From Eq. (A.7), this condition can be rewritten as

$$\zeta(f, \theta) \geq f\cos\theta\;(\Delta - 1)\;, \tag{D.5}$$

where $\Delta = \sqrt{4 - 3f^2}$. Taking squares at both sides and rearranging terms, this condition reads

$$X(f) + Y(f)\cos^2\theta \geq 0, \tag{D.6}$$

where $X(f) = \frac{2}{3}(4 - 3f^2 - \Delta)$ and $Y(f) = (1 - f^2)(4 - 3f^2 - 2\Delta)$. Since only the second of these terms can be smaller than zero, it is enough to prove that Eq. (D.6) holds for $\cos^2\theta = 1$, since that yields the minimum value that the left-hand side can take when $Y < 0$. Hence, it is enough to prove

$$X(f) + Y(f) = \frac{1}{3}\Delta^2(5 - 3f^2 - 2\Delta) \geq 0\,, \tag{D.7}$$

which holds, since the last term in parentheses is always greater than or equal to zero. This finishes the proof of Eq. (D.4). Using the same equations, we can see that $\lambda_3(f,\theta) - f_x = 0$ is only satisfied if $f = 1$. An analog treatment can be used for A_L, from which we arrive to the following inequalities:

$$A_R \geq 0, \text{ and } A_R > 0 \;\forall\, f \in [0,1) \tag{D.8}$$

$$A_L \leq 0, \text{ and } A_L < 0 \;\forall\, f \in [0,1). \tag{D.9}$$

We now proceed to verify Equations (D.1) and (D.2), firstly considering the case $f_L, f_R < 1$, in which $A_{L/R} \neq 0$. Under this condition, the ratio B_S/A_S depends only on $(f_L, f_R, \theta_L, \theta_R)$ as

$$\frac{B_S}{A_S} \equiv \alpha(\lambda_S, f_S, \theta_S) = \frac{(\lambda_S - \lambda_{2,S}) f_S \cos\theta_S - (1 - \xi(f_S))/2}{\lambda_S - f_S \cos\theta_S}, \tag{D.10}$$

with $S = L, R$. In order to verify Eq. (D.1), we must prove $\lambda_R \geq B_R/A_R$ and $\lambda_R \geq B_L/A_L$. Since $\lambda_R = \max(\lambda_{3,L}, \lambda_{3,R})$, we can write the first of these conditions considering the cases $\lambda_R = \lambda_{3,R}$ and $\lambda_R = \lambda_{3,L}$, as

$$\lambda_{3,R} \geq \alpha(\lambda_{3,R}, f_R, \theta_R) \;\; \forall\,(f_R, \theta_R) \tag{D.11}$$

$$\lambda_{3,L} \geq \alpha(\lambda_{3,L}, f_R, \theta_R) \;\; \forall\,(f_R, \theta_R) : \lambda_{3,R} < \lambda_{3,L} \;\forall\, \lambda_{3,L} \in [-1,1]. \tag{D.12}$$

The first of these can be verified from the graph of $\lambda_3(f,\theta) - \alpha(\lambda_3(f,\theta), f, \theta)$, where it can be seen that this function is always positive and tends to zero for $f \to 1$. Similarly, we have checked the second one numerically by plotting $\lambda_{3,L} - \alpha(\lambda_{3,L}, f_R, \theta_R)$ under the condition $\lambda_{3,R} < \lambda_{3,L}$, taking multiple values of $\lambda_{3,L}$ covering the range $[-1,1]$. The condition $\lambda_R \geq B_L/A_L$ can be proven in a similar fashion by considering the cases $\lambda_L = \lambda_{1,L}$ and $\lambda_L = \lambda_{1,R}$. Since $\lambda_R \geq \lambda_{3,L}$, it is enough to prove the following conditions:

$$\lambda_{3,L} \geq \alpha(\lambda_{1,L}, f_L, \theta_L) \;\; \forall\,(f_L, \theta_L) \tag{D.13}$$

$$\lambda_{3,L} \geq \alpha(\lambda_{1,R}, f_L, \theta_L) \;\; \forall\,(f_L, \theta_L) : \lambda_{1,R} < \lambda_{1,L} \;\forall\, \lambda_{1,R} \in [-1,1], \tag{D.14}$$

which can be verified in the same manner, finishing the proof of Eq. (D.1) for the case $f_L, f_R < 1$. The same procedure can be used to prove the validity of Eq. (D.2).

Unlike the RHD case, the maximum and minimum eigenvalues do not satisfy $\lambda_L < 0$ and $\lambda_R > 0$. However, studying the parabolas defined on both sides of Eq. (4.69), it can be shown that λ^* is always contained between B_R/A_R and B_L/A_L, regardless of the order of these two values and of the signs of λ_L and λ_R. Hence,

$$\lambda^* \in \left[\min\left(\frac{B_R}{A_R}, \frac{B_L}{A_L}\right), \max\left(\frac{B_R}{A_R}, \frac{B_L}{A_L}\right)\right]. \tag{D.15}$$

Together with Equations (D.1) and (D.2), this proves Eq. (4.63) for $f_L, f_R < 1$. These results are also valid in the cases $f_L = 1$ and $f_R = 1$ whenever the A functions differ from zero. Let us now assume $f_a = 1$ and $f_b \neq 1$. From Eqs. (4.70) and (4.71), we have $A_a \cos\theta_a = B_a$, and consequently, $A_a = 0$ implies that $B_a = 0$. If $A_a = 0$ and $A_b \neq 0$, from Eq. (4.69) we can extract that $\lambda^* = B_b/A_b$. Finally, from the above analysis, we know that Eq. $\lambda_L \leq B_b/A_b \leq \lambda_R$, from which we conclude that (4.63) holds even in this case. The only remaining case is that in which $f_L = f_R = 1$ and $A_L = A_R = 0$, already considered in Section 4.2.3, where the HLLC solver is replaced by the usual HLL solver.